Technische Universität München
Fachgebiet Strömungsmechanik

Direct and large-eddy simulation of inert and reacting compressible turbulent shear layers

Inga Mahle

Vollständiger Abdruck der von der Fakultät für Maschinenwesen der Technischen Universität München zur Erlangung des akademischen Grades eines

Doktor-Ingenieurs

genehmigten Dissertation.

Vorsitzender: Univ.-Prof. Dr.-Ing. habil. N. A. Adams
Prüfer der Dissertation:
1. Univ.-Prof. Dr.-Ing., Dr.-Ing. habil. R. Friedrich i.R.
2. Univ.-Prof. W. H. Polifke Ph.D. (CCNY)

Die Dissertation wurde am 16.4.2007 bei der Technischen Universität München eingereicht und durch die Fakultät für Maschinenwesen am 10.7.2007 angenommen.

Abstract

In the first part of the thesis, Direct Numerical Simulations (DNS) of temporally evolving, turbulent, compressible shear layers are discussed. Simulations at three different convective Mach numbers (0.15, 0.7 and 1.1) were performed for both, inert and infinitely fast reacting gases. All simulations were continued beyond the onset of a self-similar state in order to guarantee statistics of general value. Self-similarity manifested itself by a collapse of suitably normalized profiles of flow variables and a constant momentum thickness growth rate. During this state, the Reynolds number based on the vorticity thickness of the shear layers was between 10000 and 40000 and therefore in a fully turbulent regime. The relevance of the achieved results and parameter ranges for practical applications can be seen from the fact that shear (or mixing) layers develop when injecting fuel into the combustion chamber of an engine. Here, a good mixing of fuel and oxidizer is of great interest for an efficient combustion process.

The focus of the DNS data analyses was on the effects of compressibility and heat release due to combustion on turbulence and scalar mixing. Both phenomena, compressibility and heat release, were studied separately as well as in combination. Increasing compressibility, i.e. increasing convective Mach number, resulted in a stabilization of the mixing layers: Instantaneous fields of flow quantities became smoother, there were less turbulent fluctuations and the growth rate of the mixing layers reduced. The latter effect was related to a reduction in the production rate of the streamwise Reynolds stress and a reduction in the pressure-strain correlations caused by changes in the fluctuating pressure field. When heat release was present, the effects of compressibility were similar as for the inert mixing layers, but they were less distinct, e.g. the reduction of the growth rate with increasing Mach number was comparatively smaller. At first sight, heat release alone had similar consequences as compressibility: A stabilization of the shear layers, flow fields with lower levels of fluctuations and smaller spreading rates. However, when studied in more detail, it could be seen that the consequences of heat release, were mainly 'mean density effects', i.e. a result of the reduction of the mean density by the high temperatures in the vicinity of the flame sheets. This was not the case for the compressibility effects. Therefore, it is important to distinguish between compressibility and heat release effects, even though they share the property to be both detrimental for the turbulent mixing process.

In the second part of the thesis, Large Eddy Simulations (LES) of shear layers at a convective Mach number of 0.15 were performed. By a coarsening of the grid, large reductions of computational time were achieved. A deconvolution approach in the form of a single explicit filtering step was validated successfully for inert and reacting mixing layers by comparison with DNS data. For the LES with chemical reactions, two differently detailed chemistry models were used for the filtered chemical source term: one model taking into account the same infinitely fast, irreversible, global reaction as in the DNS and one flamelet model. The particular formulation of the flamelet equations allowed not only to take into account multistep Arrhenius chemistry, but also detailed diffusion mechanisms. The evaluation of the results obtained with two different descriptions of these mechanisms - one with Soret and Dufour effects as well as multicomponent diffusion and

one without - showed differences for both, laminar flamelets and turbulent mixing layers, in quantities related to the flame dynamics and in the extinction behaviour.

Acknowledgements

First of all, I would like to thank my supervisor Prof. Dr.-Ing. habil. Rainer Friedrich for the opportunity to perform this work at the 'Fachgebiet Strömungsmechanik'. He gave me constant guidance and support and was always ready to answer questions or to discuss various aspects.

I am also thankful to Prof. Dr. Joseph Mathew for giving me the opportunity to spend four months in his lab at the Indian Institute of Science in Bangalore. I appreciate his gracious hospitality and the fruitful discussions that we had. The final outcome of our joint work has been very rewarding.

I would also like to thank Prof. W. Polifke Ph.D. (CCNY) for taking over the role of the second examiner and Prof. Dr.-Ing. habil. N. Adams for leading the board of examiners.

My thanks go also to the High Performance Computing Group of the 'Leibniz Rechenzentrum' (LRZ) for providing help and support at nearly all times of the day, all days of the week. The computations of this work were performed on the Hitachi-SR8000 and the Altix 4700 of the LRZ. Financial contributions came from the Federal Ministry of Education and Research (BMBF) under grant number 03FRA1AC and from 'Bayerischer Forschungsverbund für Turbulente Verbrennung' (FORTVER).

Without my colleagues and the mutual support and encouragement within our group, this work would not have been imaginable. In this context, I would like to mention especially Dr.-Ing. Holger Foysi who gave me a lot of help and advice concerning the numerical codes and evaluation programs. I would also like to thank Prof. Alexandre Ern from CERMICS, ENPC (France) for providing the code EGlib.

Last but not least, I am deeply grateful to my family, in particular to my parents and grandparents, for supporting me throughout the process of this work and throughout all my life.

Garching, March 2007

Inga Mahle

Contents

List of Tables

List of Figures

Nomenclature

Roman symbols

A	pre-exponential factor in the Arrhenius law
A_γ	atomic weight of species γ
a_γ	elemental mass fraction
$a_{\gamma i}$	elemental diffusive flux in direction x_i
b_{ij}	shear stress anisotropy parameter
$C_{M,irct}$	effective third compound concentration in reaction $irct$
C_{SM}	Smagorinsky constant
C_z^{GR}	constant in the gradient model for the mixture fraction subgrid variance
C_α	molar concentration of species α
C_χ^{GR}	constant in the gradient model for the scalar dissipation rate
c	speed of sound, sonic speed
c_p	heat capacity of gas mixture at constant pressure
$c_{p\alpha}$	heat capacity of species α at constant pressure
c_v	heat capacity of gas mixture at constant volume
$c_{v\alpha}$	heat capacity of species α at constant volume
D	fractal dimension
D_α	diffusion coefficient of species α
$D_{\alpha,m}$	diffusion coefficient of species α in the mixture
$D_{\alpha\beta}$	multicomponent diffusion coefficient
D_2	fractal dimension in 2D
$\mathcal{D}_{\alpha\beta}$	multicomponent flux diffusion matrix
$\mathcal{D}_{\alpha\beta,appr}$	approximate flux diffusion matrix
Da	Damköhler number
$d_{\alpha i}$	Cartesian component of the diffusion vector of species α
dd	detailed diffusion
E	spectral energy (or activation energy in the Arrhenius law if specially indicated)
E_f	spectral energy of quantity f
e	specific internal energy of the gas mixture
e_α	specific internal energy of species α
F	filtered density function (fdf)
G	Green function, (or low-pass filter if specially indicated)
h	specific enthalpy of the gas mixture
h_α	specific enthalpy of species α
I	factor in the model for the filtered heat release ω
$K_{e,irct}$	equilibrium constant of reaction $irct$
K_ϵ	coefficient used in the analysis of the reduced growth rate

K_{11}	coefficient in the analysis of the reduced growth rate
k	turbulent kinetic energy (or wavenumber if specially indicated)
$k_{b,irct}$	backward constant of reaction $irct$
$k_{f,irct}$	forward constant of reaction $irct$
k_i	wavenumber in direction x_i
k_0	peak wavenumber of energy spectrum
L_i	length of computational domain in direction x_i
Le	Lewis number
l	integral length scale
l_i	integral length scale in direction x_i
l_k	Kolmogorov length scale
M	Mach number
M_c	convective Mach number
M_g	gradient Mach number
M_t	turbulent Mach number
N	number of terms taken into account for the determination of filter Q
N_i	number of grid points in direction x_i
N_P	number of particles
$N_{\alpha\gamma}$	number of γ atoms in molecule of species α
n_α	mole number of species α
P	production rate of the turbulent kinetic energy
$P(f)$	probability density function (pdf) of f
P_{ij}	production rate of $\langle\rho\rangle R_{ij}$
p	pressure
Q	heat release term, $Q = Q_p/(\gamma - 1)$ (or inverse filter of G if specially indicated)
$\mathcal{Q}$	non-dimensional heat release term
Q_e	heat release parameter
Q_p	heat release term in the pressure equation
q_i	Cartesian component of the heat flux vector
q_0	enthalpy of reaction
R	gas constant of the gas mixture
$R(f,g)$	correlation coefficient of fluctuations of quantities f and g
R_{if}	two-point correlation of quantity f in direction x_i
R_{ij}	Cartesian component of the Reynolds stress tensor
$\mathcal{R}$	universal gas constant, $\mathcal{R} = 8,314\ Jmol^{-1}K^{-1}$
Re_λ	Taylor micro-scale Reynolds number
Re_ω	Reynolds number based on δ_ω and Δu
S	shear rate
s	specific entropy
Sc	Schmidt number
Sc_t	turbulent Schmidt number
Sc_α	Schmidt number of species alpha
s	stoichiometric ratio
s_{ij}	deformation tensor, symmetric part of the strain rate tensor
sd	simplified diffusion

T	temperature (or transport term in the transport equation of k if specially indicated)
T_{ij}	transport term in the transport equation of $\langle\rho\rangle R_{ij}$
t	time
t_{vis}	time scale based on δ_{vis} and Δu
u_i	Cartesian velocity component
V_{en}	engulfed volume
V_{ml}	mixing layer volume
$V_{\alpha i}$	Cartesian diffusion velocity component of species α
W	molecular weight of the gas mixture
W_α	molecular weight of species α
w_{irct}	reaction progress rate of reaction $irct$
X_α	mole fraction of species α
x_i	Cartesian coordinate
Y_α	mass fraction of species α
Z	conserved scalar
z	mixture fraction
$(z^2)_{sg}$	subgrid variance of the mixture fraction

Greek symbols

α	filter parameter
α_z	diffusivity of the mixture fraction
β	temperature dependence coefficient in the Arrhenius law
γ	ratio of specific heats
$\gamma_{\alpha,irct}$	pre-factor in the computation of third compound effectivity
Δ	averaged grid spacing
$\Delta\mathcal{H}$	molar enthalpy change during reaction $irct$
Δh_α	standard enthalpy of formation of species α
$\Delta\mathcal{S}$	molar entropy change during reaction $irct$
Δu	difference between freestream velocities
Δx_i	grid spacing in direction x_i
δ	smoothing factor
δ_{ij}	Kronecker symbol
δ_M	shear layer thickness related to the mixing efficiency
δ_P	product shear layer thickness
δ_{vis}	visual shear layer thickness
δ_{vol}	shear layer thickness computed from mixing layer volume
δ_Y	99% scalar (mass fraction) shear layer thickness
δ_z	99% scalar (mixture fraction) shear layer thickness
δ_θ	momentum thickness
$\dot{\delta}_\theta$	normalized momentum thickness growth rate
δ_ω	vorticity thickness

ϵ	dissipation rate of k (or small parameter if specially indicated)
ϵ_d	dilatational part of the dissipation rate of k
ϵ_I	inhomogeneous part of the dissipation rate of k
ϵ_i	i-th part of the dissipation rate of k, $i = 1, 2, 3$
ϵ_{ij}	dissipation rate of $\langle\rho\rangle R_{ij}$
ϵ_s	solenoidal part of the dissipation rate of k
ϵ_Y	scalar dissipation rate of mass fraction Y
ϵ_z	scalar dissipation rate of mixture fraction z
θ_α	thermal diffusion coefficient of species α
κ	bulk viscosity
λ	heat conductivity (or Taylor micro-scale if specially indicated)
λ'	partial heat conductivity
μ	dynamic viscosity
μ_t	turbulent viscosity
μ_α	chemical potential of species α
ν	kinematic viscosity
ν_α	stoichiometric coefficient of species α
ξ	scaled wavenumber
Π	pressure dilatation
Π_{ij}	pressure-strain correlation in the transport equation of $\langle\rho\rangle R_{ij}$
Π_{Yi}	pressure-scrambling term of mass fraction Y in direction x_i
Π_{zi}	pressure-scrambling term of mixture fraction z in direction x_i
ρ	density
ρ_{en}	density of the engulfed volume
ρ_{mix}	density of the mixed volume
ρ_{ml}	mixing layer density
Σ	mass flux coupling term in the transport equation of k
Σ_{ij}	mass flux coupling term in the transport equation of $\langle\rho\rangle R_{ij}$
σ	source term of entropy
σ_α	source term of species α
τ_a	acoustic time scale
τ_d	mean distortion time scale
τ_{ij}	viscous stress tensor
τ_t	turbulent time scale
τ_ω	non-dimensional time based on δ_ω and Δu
Φ	equivalence ratio
ϕ	dissipation function
χ	scalar dissipation rate, $\chi = -\epsilon_z$
χ_α	thermal diffusion ratio of species α
ψ	mixture fraction diffusion
ω	heat release term, $\omega = -\sum_\alpha h_\alpha \omega_\alpha$ (or vorticity magnitude if specially indicated)
ω_G	global reaction rate
ω_i	Cartesian vorticity component
ω_α	mass production rate of species α

Indices

av	volume averaged quantity
B	beginning of the self-similar state
E	end of the self-similar state
F	fuel
f	fuel stream
l	lower threshold
ls	large scale quantity
m	model (if not indicated otherwise)
O	oxidizer
o	oxidizer stream
P	product (or quantity referring to particles if specially indicated)
rms	root of the mean square value
s	quantity at stoichiometric conditions
sg	subgrid quantity
u	upper threshold
Y	quantity referring to the mass fraction threshold in the particle analysis
z	quantity referring to the mixture fraction threshold in the particle analysis
ω	quantity referring to the vorticity threshold in the particle analysis
0	reference quantity (if not indicated otherwise)
1	property of the upper free stream (if not indicated otherwise)
2	property of the lower free stream (if not indicated otherwise)

Superscripts

ac	acoustic part of a quantity
en	entropic part of a quantity
m	model
rel	quantity relative to a moving shock
0	value at $T^0 = 298K$ and $p^0 = 1013.25hPa$
$*$	conjugate complex quantity

Others

$\overline{\bullet}$	low-pass filtered quantity
$\widetilde{\bullet}$	mass-weighted low-pass filtered quantity
$\breve{\bullet}$	quantity integrated in transverse direction (if not indicated otherwise)
$\hat{\bullet}$	quantity in wavenumber space
$\langle\bullet\rangle$	Reynolds averaged quantity
$\langle\bullet\rangle_f$	Favre averaged quantity
$\bullet'$	Reynolds fluctuation (if not indicated otherwise)
$\bullet''$	Favre fluctuation (if not indicated otherwise)

Abbreviations

ADM	Approximate Deconvolution Method
CMC	Conditional Moment Closure
DNS	Direct Numerical Simulation
dd	detailed diffusion
EFM	Explicit Filtering Method
fdf	filtered density function
i-f-DNS	DNS data interpolated to an LES grid and filtered
inert-XX	simulation of inert mixing layer at $M_c = XX$
inf-XX	simulation of infinitely fast reacting mixing layer at $M_c = XX$
LEM	Linear Eddy Model
LES	Large Eddy Simulation
LHS	left hand side of an equation
pdf	probability density function
RHS	right hand side of an equation
sd	simplified diffusion
TKE	turbulent kinetic energy

1 Introduction

The first successful flight of the scramjet powered airplane NASA X-43 in 2004 demonstrated the feasibility of the scramjet concept that allows to fly at hypersonic speed. Even though this and other tests of smaller rockets have shown that the operation of scramjets is practically possible, many difficulties remain still to be solved until a commercial operation can be aimed at.

A scramjet is entirely different from conventional jet engines where fuel is burnt at a relatively low speed of approximately Mach 0.2. This low speed allows a good mixing of the injected fuel with air and an efficient combustion process. Subsonic combustion is even possible when flying at supersonic speed: The high entrance velocity of the air is simply reduced in the inlet of the engine with the help of strong shocks. At the same time, the air heats up and compresses. Consequently, no compressor is necessary. In the combustion chamber, the added fuel mixes with the air stream, combusts and the burnt gases accelerate in the nozzle to high speed. This is the concept of the so-called 'ramjets': Subsonic combustion at supersonic flight. However, losses (in total pressure) are related with the slow-down of the air by shocks, and the losses increase with increasing flight velocity. Consequently, efficiency and thrust are reduced. Therefore, above Mach numbers of about 6, it makes sense to accept less efficient supersonic combustion. Then, smaller losses are caused at the inlet since the air does not have to be slowed down below the speed of sound. This is the concept of 'scramjets' with which it is theoretically possible to fly at speeds up to Mach 20.

As just indicated, an important aspect in supersonic and also subsonic combustion is the strong reduction in mixing efficiency with increasing speed. Since perfect combustion requires effective small-scale mixing, strategies to improve supersonic combustion have to be based on a full understanding of the underlying mechanisms. To contribute to this understanding, is one of the aims of the present work, in which inert and reacting, compressible turbulent shear layers are investigated with the help of numerical simulations.

Shear (or mixing) layers are generic configurations for free shear flows, i.e flows that are not bounded by walls but have mean velocity gradients perpendicular to the main flow direction. Besides their importance in many basic studies, mixing layers also appear very often in practical applications. Basically everywhere where two streams of gases or liquids with different velocities come into contact. Examples are combustion chambers where shear layers separate the core flow from the recirculation areas. In 'conventional' jet engines, as well as in ram- and scramjets, mixing layers develop between the fuel stream that is injected into the combustion chamber and the surrounding air flow.

Mixing layers are also particularly important for the study of compressibility since free stream conditions remain constant with downstream distance. Compressibility effects, i.e. density changes along fluid trajectories, appear not only in high speed gas flows, but also in unsteady processes at high frequencies (acoustics) and in meteorology, where currents span large vertical distances. However, this study is limited to the first phenomena: compressibility effects at high speeds. It is widely known that with increasing compressibility, i.e. increasing flow speed, the

growth rates of shear layers reduce. Early shear layer experiments have shown that data collapse onto the so-called 'Langley curve' when using the convective Mach number as a parameter. This stabilizing effect of compressibility is further investigated in the present work, both, as a single mechanism and as a mechanism influenced by heat release due to combustion. Hydrogen is chosen as fuel for the reacting mixing layers, since it is normally used in ram- and scramjets. One reason for this is that hydrogen has a much higher energy content than kerosene: one kilogram of fuel delivers about three times more energy. Furthermore, hydrogen has a good capability of cooling, and the combustion after mixing with air occurs rapidly. However, there are two drawbacks for its application: hydrogen must be stored in liquid state at very low temperature and its density is very low which requires voluminous tanks in order to store a certain amount of mass.

In the first part of this work, inert and reacting mixing layers at three different convective Mach numbers are studied with the help of Direct Numerical Simulations (DNS). The main questions which are addressed are:

- What are the effects of compressibility on turbulence and scalar mixing within inert mixing layers?
- How do these effects change when heat is released during combustion?
- Which effects does heat cause at different convective Mach numbers, i.e. different levels of compressibility?

DNS is the most powerful tool to predict and simulate compressible turbulent flows since it provides a complete description of the flow field. All scales from the largest to the smallest are resolved. Since this is only possible at high computational costs, simplifications, e.g. concerning transport mechanisms and chemistry must be made. In the present DNS of reacting mixing layers, an infinitely fast, irreversible global reaction and simplified diffusion mechanisms are taken into account. Nevertheless, it is also of interest what changes occur when detailed, finite-rate chemistry and detailed diffusion processes are considered. Therefore, the second part of this work is dedicated to Large Eddy Simulations (LES). This kind of simulation requires less computational effort, since only the large turbulent scales are resolved, and the smaller ones are modeled. Therefore, LES is intermediate between DNS and prediction methods based on statistically averaged transport equations.

The LES method used in the present work is a particular version of the Approximate Deconvolution Method (ADM) involving a single filtering step. It does not need any analytical modeling of subgrid terms arising from non-linearities in the transport equations of the flow variables. The only exception is the chemical source term that has to be modeled nevertheless since most of the chemical reactions occur in the unresolved small scales. The relevant questions that are answered in the second part of the study are:

- Is a realistic LES of reacting mixing layers possible with combinations of ADM (in the form of a single explicit filtering step) and different models for the chemical source term?
- What are the changes that occur in mixing layers at low convective Mach number when finite-rate chemistry and different approximations of diffusion mechanisms are taken into account?

Besides this general introduction, which is the first chapter, the thesis has four chapters. Each chapter starts with another introduction including an overview over the relevant literature. Chapters 2 and 3 form the first part of the thesis in which DNS of inert and infinitely fast reacting compressible turbulent mixing layers at three different convective Mach numbers are described and analyzed. In Chapter 4, the simulations at low convective Mach number from the previous chapters are 'repeated' as LES with the objective to check the performance of the LES method in general and the modeling of the filtered chemical source term for infinitely fast chemistry in particular. In Chapter 5, a steady flamelet model is used to improve the simulation of the filtered source term. The particular formulation of the flamelet equations allows not only to take detailed, finite-rate chemistry into account, but also detailed diffusion effects at two different levels of approximation. The aim of Chapter 5 is to contrast the results for finite-rate chemistry to those obtained with infinitely fast chemistry in the previous chapters. Furthermore, comparisons between the different diffusion models are performed. Besides summaries and conclusions that are given in each chapter individually, there is a chapter at the very end of the thesis, in which its most important results are highlighted and an outlook is given on how the work could be pursued.

2 DNS of inert compressible turbulent shear layers

2.1 Introduction and literature survey

Turbulent combustion in technical devices heavily depends on the quality of the mixing between fuel and oxidizer. This is true for combustion devices at all speeds starting from furnaces and spark ignition engines, going to rocket motors and combustion chambers of aircraft engines and up to supersonic propulsion engines (scramjet). In this chapter, turbulent mixing in inert shear layers at different speeds, i.e. convective Mach numbers, is investigated.

The shear layer or mixing layer, a kind of prototype for any free shear flow, has been subject of many theoretical, experimental and numerical studies for over half a century. Among the first authors investigating the pressure and velocity fields of the incompressible mixing layer experimentally were Spencer & Jones [172], Brown & Roshko [21] as well as Dimotakis & Brown [44] who identified the important role of coherent structures and their pairing for the mixing process. Later, comprehensive measurements were done for example by Bell & Mehta [7] who showed that their incompressible mixing layers attained a self-similar state with a constant thickness growth rate and a collapse of the spanwise averaged flow quantity profiles. The first authors who performed DNS of temporally evolving incompressible mixing layers up to a fully turbulent state and analyzed the data in detail were Rogers & Moser [152].

The mixing layer is in particular useful to study compressibility effects since, unlike the jet, which has continuously varying mean centreline velocity, the free-stream velocities are conserved in both near- and far-fields. The same applies to density and scalar concentration differences across the layer. In addition, the fluctuations do not decrease with streamwise distance. Numerical studies, using both linear stability theory and direct simulations, have shown a significant difference between the low compressibility regime (convective Mach number $M_c < 0.4$) where two-dimensional structures, like Kelvin-Helmholtz instabilites, prevail and the higher compressibility regime ($M_c > 0.6$) with oblique instability waves [81, 147] resulting in highly three-dimensional structures when it comes to non-linearity [158]. This change with increasing convective Mach number has been confirmed by several experiments [15, 27, 50, 112, 156]. Furthermore, it is well-known [6, 14, 16, 49, 126] that, when the convective Mach number increases, there is a large reduction in the thickness growth rate and the turbulent intensities of the mixing layer. The decrease of the growth rate at higher Mach numbers has important practical implications like for the quality of mixing between oxidizer and fuel in scramjet engines, and knowing the reason for the stabilizing effect allows to work on possible mixing enhancement strategies.

The first DNS of compressible mixing layers were only performed up to the early stages of vortex formation [157] and did therefore not contain very small scales of turbulence. This was improved by later DNS which included the so-called mixing transition to small-scale turbulence

[63, 64, 123, 183]. All these simulations confirmed the stabilizing effect of compressibility. Several explanations for this effect have been offered: While some authors [48, 160, 164, 192] considered the dilatational part of the total dissipation to be responsible for it and reasoned that this part would increase due to the appearance of shocklets, others pointed out the similarity with results for the linear growth rate of small disturbances in laminar compressible shear flow [157]. However, no shocklets have been observed in a 3D simulation or an experiment of a mixing layer below a convective Mach number of one, and it is also not clear why linear instability theory should apply to a turbulent, non-linearly evolving flow. Other explanations of the reduced growth rate with increasing convective Mach number, incorporated the effect of compressibility on large-scale coherent structures [27, 71, 126, 156].

A similar stabilizing effect as in the mixing layer has been observed in simulations of uniformly sheared, compressible flow [13, 164, 161]. Sarkar [161] identified the gradient Mach number $M_g = Sl/\langle c \rangle$, wherein S is the constant mean shear rate, l the integral length scale of the streamwise velocity fluctuations in the transverse shearing direction and $\langle c \rangle$ the mean speed of sound, as the crucial parameter, the increase of which is accompanied by a large reduction in the normalized growth rate of the turbulent kinetic energy (TKE). The cause of this reduction was found to be a large decrease in the normalized Reynolds shear stress which is involved in the production term of the TKE transport equation. Explicit dilatational effects, i.e. the dilatational dissipation rate and the pressure-dilatation correlation, were excluded from being the reason for the stabilization. This was confirmed by Vreman et al. [183] for the compressible mixing layer even at convective Mach numbers that lead to the occurrence of shocklets. Sarkar [161] also reasoned that the change of the pressure field and the related altering of the pressure-strain terms in the Reynolds stress equations lead to reduced levels of turbulence. By using a direct relation between the momentum thickness growth rate and the production of TKE together with the integrated equations for the Reynolds stress tensor, Vreman et al. [183] clearly showed that the decrease in pressure fluctuations, which leads to reduced pressure-strain terms, is responsible for the changes in growth rate of the compressible mixing layer. Freund et al. [63] found the quintessential element of compressibility to be the suppression of transverse turbulent length scale with increasing convective Mach number which leads to reduced pressure fluctuations, pressure-strain correlations, Reynold stresses and shear-layer growth rates with increasing convective Mach number. Recently, Pantano & Sarkar [123] derived a relation similar to Vreman et al. [183] and showed the reason for the reduction of the pressure-strain terms at high Mach number by an analysis based on the wave equation for the pressure fluctuations: The finite speed of sound in compressible flows introduces a finite time delay in the transmission of pressure-strain signals from one point to an adjacent point, and the resultant increase in decorrelation leads to a reduction in the pressure-strain correlation.

The aim of this chapter is to identify and analyze mixing processes in inert mixing layers and to verify and enhance the already gained knowledge about their alterations with increasing convective Mach number. The highly resolved and therefore computationaly demanding simulations are performed as DNS. The chapter is organized as follows: In Section 2.2, the DNS code is presented, and the relevant equations, i.e. the Navier-Stokes equations for a gas mixture, as well as important features of the numerical method are given. The subsequent section, Sect. 2.3, describes the inert mixing layer test cases, which differ mainly by their convective Mach number, i.e. the level of compressibility. Details concerning the initialization and important parameters of the corresponding DNS are given as well. The main part of this chapter is Sect. 2.4, the presentation of the simulation results and their analysis. First, the most obvious differences between

the mixing layers are identified with the help of instantaneous flow images (Sect. 2.4.1). Then, the relaxation of the mixing layer towards a self-similar state is shown (Sect. 2.4.2). Over this state, statistics are taken, which form the basis of the subsequent discussions. Before the statistical results are analyzed, the adequacy of resolutions and domain sizes is checked in Sect. 2.4.3. The effect of compressibility, first on general turbulence characteristics, e.g. statistical quantities concerning the velocity field, is investigated in Sect. 2.4.4.1. The effect of compressibility on the mixing of the inert chemical species, is the subject of Sect. 2.4.4.2. The findings there are closely related to entrainment, i.e. the way the mixing layers acquire outside fluid. Finally, the studies concerning the inert mixing layers are completed by analyzing the role of shocklets at high convective Mach number (Sect. 2.4.4.4), before a summary of the results is given and conclusions are drawn.

2.2 The DNS code for inert gas mixtures

2.2.1 Navier-Stokes equations for a gas mixture

The governing equations describing turbulent flow of gas mixtures are the unsteady, three-dimensional, compressible Navier-Stokes equations for an inert gas mixture consisting of multiple species. They consist of equations for mass, momentum, energy and species mass fracions and read in Cartesian tensor notation:

$$\frac{\partial \rho}{\partial t} + \frac{\partial \rho u_i}{\partial x_i} = 0 \tag{2.1}$$

$$\rho \frac{Du_i}{Dt} = -\frac{\partial p}{\partial x_i} + \frac{\partial \tau_{ji}}{\partial x_j} \tag{2.2}$$

$$\rho \frac{D}{Dt}\left(e + \frac{1}{2}u_i u_i\right) = \frac{\partial}{\partial x_j}\left(-p u_j + \tau_{ji} u_i - q_j\right) \tag{2.3}$$

$$\rho \frac{DY_\alpha}{Dt} = -\frac{\partial}{\partial x_i}\left(\rho Y_\alpha V_{\alpha i}\right) \tag{2.4}$$

Here and in the following, the summation convention does not apply to Greek indices (α, β,...) which denote different species. Wherever a sum over species is necessary, this is indicated by $\sum_\alpha$,$\sum_\beta$,... The species, which are also called active scalars, do not only influence the flow field by the density due to their different molecular weights, but also by the transport properties, like the viscosity and the diffusion coefficients. Density and pressure of the gas mixture are denoted by ρ and p, which are related with the temperature T via the equation of state for ideal gas mixtures

$$p = \rho \frac{\mathcal{R}}{W} T = \rho R T. \tag{2.5}$$

$\mathcal{R} = 8,314\ Jmol^{-1}K^{-1}$ is the universal gas constant, and $W = \sum_\alpha X_\alpha W_\alpha = \left(\sum_\alpha Y_\alpha / W_\alpha\right)^{-1}$ is the average molecular weight of the gas mixture, computed with the molecular weights of the individual species, W_α, and their mole or mass fractions, X_α and Y_α, respectively. An alternative expression is obtained by using the gas constant of the gas mixture, $R = \mathcal{R}/W$.

Other quantities in the Navier-Stokes equations are the velocity components u_i, the internal energy e, the components of the heat flux vector q_j and the components of the diffusion velocity of species α, $V_{\alpha i}$. The stress tensor τ_{ij} can be determined from kinetic theory as

$$\tau_{ij} = 2\mu s_{ij} + \left(\kappa - \frac{2}{3}\mu\right) s_{kk}\delta_{ij} \tag{2.6}$$

with the dynamic viscosity of the mixture μ and its bulk viscosity κ. The Kronecker symbol δ_{ij} is the unity tensor of second order and s_{ij} the symmetric part of the strain rate tensor,

$$s_{ij} = \frac{1}{2}\left(\frac{\partial u_i}{\partial x_j} + \frac{\partial u_j}{\partial x_i}\right) \tag{2.7}$$

which is also called deformation tensor.

An accurate way to compute the species diffusion flux $Y_\alpha V_{\alpha i}$ is given by

$$\begin{aligned} Y_\alpha V_{\alpha i} &= -\sum_\beta \mathcal{D}_{\alpha\beta} d_{\beta i} - Y_\alpha \theta_\alpha \frac{\partial \ln T}{\partial x_i} \\ &= -\sum_\beta \mathcal{D}_{\alpha\beta}\left(d_{\beta i} + \chi_\beta \frac{\partial \ln T}{\partial x_i}\right) \end{aligned} \tag{2.8}$$

with the diffusion vector

$$d_{\beta i} = \frac{\partial X_\beta}{\partial x_i} + (X_\beta - Y_\beta)\frac{\partial \ln p}{\partial x_i} \tag{2.9}$$

where $\mathcal{D}_{\alpha\beta}$ is the multicomponent flux diffusion matrix $\mathcal{D}_{\alpha\beta} = Y_\alpha D_{\alpha\beta}$ with the multicomponent diffusion coefficients $D_{\alpha\beta}$. The thermal diffusion coefficients are θ_α. An alternative to their use are the thermal diffusion ratios χ_α. Equations (2.8) and (2.9) consider not only the 'normal' diffusion caused by gradients in the mole fractions of the species, but also barodiffusion due to pressure gradients and thermodiffusion due to temperature gradients. The latter is also called Soret effect and causes lighter molecules to diffuse towards regions of higher temperature. By using the multicomponent diffusion matrix $D_{\alpha\beta}$, cross-diffusion effects are taken into account.

An accurate way to determine the heat flux vector is

$$\begin{aligned} q_i &= \sum_\alpha \rho h_\alpha Y_\alpha V_{\alpha i} - \lambda' \frac{\partial T}{\partial x_i} - p\sum_\alpha \theta_\alpha d_{\alpha i} \\ &= \sum_\alpha \rho h_\alpha Y_\alpha V_{\alpha i} - \lambda \frac{\partial T}{\partial x_i} + p\sum_\alpha \chi_\alpha V_{\alpha i}. \end{aligned} \tag{2.10}$$

The first term on the right hand side (RHS) is the transport of heat caused by diffusion, the second term is the heat conduction and the last term is the Dufour effect, namely the transport of heat due to gradients in the mole fractions of the species. Additionally, a barodiffusive term is considered via Eq. (2.9). λ' is the partial heat conductivity and λ the heat conductivity[1)].

[1)]The heat conductivity λ is more frequently used than the partial heat conductivity λ', because λ can be measured experimentally: Every temperature gradient leads to thermal diffusion and therefore to a gradient in the species concentration, because of which $\sum_\alpha \theta_\alpha d_{\alpha i} \neq 0$. Having an external temperature gradient and reaching an equilibrium, the diffusion velocities in a gas mixture disappear and Eq. (2.10) becomes $q_i = -\lambda\frac{\partial T}{\partial x_i}$

The specific enthalpies of the individual species, which are required to compute the heat flux (2.10) are computed by a polynomial expression [66],

$$\begin{aligned} h_\alpha(T) &= \frac{1}{W_\alpha}\left(a_{6\alpha}\mathcal{R} + \int_{T'=298\ K}^{T} c_{p_\alpha} dT'\right) \\ &= \frac{\mathcal{R}}{W_\alpha}\left(a_{6\alpha} + a_{1\alpha}T + a_{2\alpha}\frac{T^2}{2} + a_{3\alpha}\frac{T^3}{3} + a_{4\alpha}\frac{T^4}{4} + a_{5\alpha}\frac{T^5}{5}\right), \end{aligned} \tag{2.11}$$

which is obtained by the integration of the fourth-order polynomial for the specific heat capacities at constant pressure,

$$c_{p_\alpha}(T) = \frac{\mathcal{R}}{W_\alpha}\left(a_{1\alpha} + a_{2\alpha}T + a_{3\alpha}T^2 + a_{4\alpha}T^3 + a_{5\alpha}T^4\right). \tag{2.12}$$

The coefficients $a_{i\alpha}$ are taken from tables that mostly distinguish two temperature ranges: $300\ K$ to $1000\ K$ and above $1000\ K$. The integration constant $a_{6\alpha}$ in Eq. (2.11) is chosen such that the correct formation enthalpy $h_\alpha\,(T = 298\ K)$ is obtained. The specific enthalpy of the gas mixture is assembled by $h = \sum_\alpha Y_\alpha h_\alpha$ and specific heat capacity for the gas mixture by $c_p = \sum_\alpha Y_\alpha c_{p_\alpha}$. The specific heat capacity at constant volume, c_v, is obtained by $c_v = c_p - R$.

2.2.2 The numerical method

The numerical method used in the present DNS is based on the code of Sesterhenn [167], a similar version of which has also been used by Foysi [61] to simulate compressible channel flows. The Navier-Stokes equations are written in a characteristic pressure-velocity-entropy formulation which allows for an easy boundary treatment. Having various species, some adaptions of the code were necessary, and species transport equations had to be added. For a detailed explanation, including the treatment of the non-reflecting boundaries, see Appendix A. The transport equations are integrated in time with a third-order low-storage Runge-Kutta scheme [188] whereby the spatial derivatives are discretized by using sixth-order compact central schemes [99].

The primitive variables are filtered every 20th time step to prevent spurious accumulation of energy in the highest wavenumbers using a sixth-order compact filter [99]. The effect of this filtering is weak and is quantified in Sect. 2.4.3.

In the present DNS, the transport coefficients (viscosity, bulk viscosity, heat conductivity and the diffusion coefficients) are evaluated by EGlib [54]. EGlib uses an iterative method to obtain an approximate solution of the linear system of transport coefficients derived from kinetic theory. Truncation then provides, at a moderate computational cost, approximate expressions for the transport coefficients at a desired accuracy.

The code is parallelized using MPI-routines and the simulations were done on the Hitachi SR8000-F1 and the SGI Altix4700 of the Leibniz-Rechenzentrum in Munich on up to 256 processors.

2.3 Test cases

The test cases under investigation are plane mixing layers which develop between two streams of gas that have constant, but different velocities. The layers are studied in a reference frame

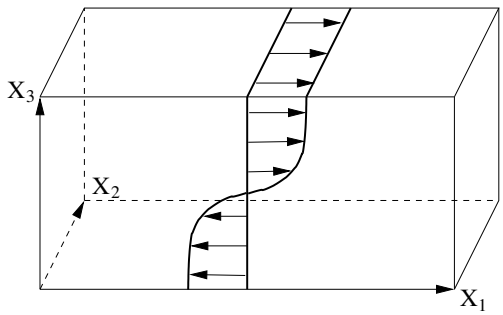

Figure 2.1: The configuration of temporally evolving shear layers

moving with the average speed of the two streams and under the parallel-flow assumption which makes them temporally evolving mixing layers. They are computationally much less demanding than spatially evolving mixing layers, but provide, nevertheless, useful insight into fundamental properties of turbulenent shear layers, since they isolate specific effects and remove some of the flow complexity.

Figure 2.1 shows the configuration of the shear layers. All test cases are 3D with x_1 and x_2 denoting the homogeneous streamwise and spanwise directions and x_3 denoting the transverse direction. The upper stream (index 1) is pure oxygen and the lower stream (index 2) pure nitrogen. At the beginning of the computations, temperature and pressure are constant. This results in an initially nearly constant density across the mixing layer due to similar molecular weight of oxygen and nitrogen.

The convective Mach number

$$M_c = \frac{\Delta u}{c_1 + c_2} \tag{2.13}$$

differs between the test cases: For the simulation called inert-0.15 it is 0.15, for inert-0.7 it is 0.7 and for inert-1.1 it is 1.1. In Eq. (2.13), the velocity difference between the two streams is denoted by Δu, and c_1 and c_2 are their sonic speeds. Strictly taken, expression (2.13), which was introduced by Bogdanoff [14], is only valid for equal γ of the two streams. As in the present cases, the ratio of the specific heats $\gamma = c_p/c_v$ differs by only 0.3% between the streams, Eq. (2.13) gives a good approximation of M_c.

The flow is initialized by a hyperbolic-tangent profile for the mean streamwise velocity and density. In order to accelerate the transition to turbulence, broadband fluctuations in the velocity components are used. This is achieved by generating an isotropic turbulence spectrum of the form

$$E(k) = \left(\frac{k}{k_0}\right)^4 \exp\left[-2\left(\frac{k}{k_0}\right)^2\right] \tag{2.14}$$

with wavenumber k and peak wavenumber k_0. k_0 is chosen in a way that there are initially 72 peak wavelengths within the streamwise box size for all simulation. The Reynolds number at the

Table 2.1: Geometrical parameters of the simulations inert-0.15, inert-0.7, inert-1.1. The computational domain has the dimensions L_1, L_2 and L_3 with N_1, N_2 and N_3 grid points, respectively. The reference vorticity thickness $\delta_\omega, 0$ is chosen such that it results in $Re_{\omega,0} = 640$.

$L_1/\delta_{\omega,0}$	$L_2/\delta_{\omega,0}$	$L_3/\delta_{\omega,0}$	N_1	N_2	N_3
129.375	32.25	96.75	768	192	576

beginning of the computations

$$Re_{\omega,0} = \frac{\Delta u \, \rho_0 \, \delta_{\omega,0}}{\mu_0} \tag{2.15}$$

is 640 in all cases. It is based on the initial vorticity thickness $\delta_{\omega,0}$, on the averaged free-stream density $\rho_0 = (\rho_1 + \rho_2)/2$ and on the viscosity $\mu_0 = (\mu_1 + \mu_2)/2$.

Grid and domain sizes are given in table 2.1 and are the same for all inert simulations. The grid-spacing is constant in all directions.

2.4 Results and analysis

2.4.1 The structure of the compressible shear layers

In the following, instantaneous images of the mixing layers at different normalized times,

$$\tau_\omega = \frac{t \cdot \Delta u}{\delta_{\omega,0}}, \tag{2.16}$$

are shown in order to contrast characteristic features of their development with each other.

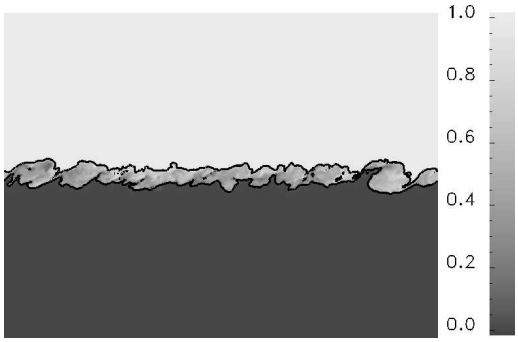

Figure 2.2: Case inert-0.15: Instantaneous mass fraction field of O_2, x_1-x_3-plane in the middle of the computational domain at $\tau_\omega = 83$, isolines $Y_{O2} = 0.1$ and 0.9 are shown

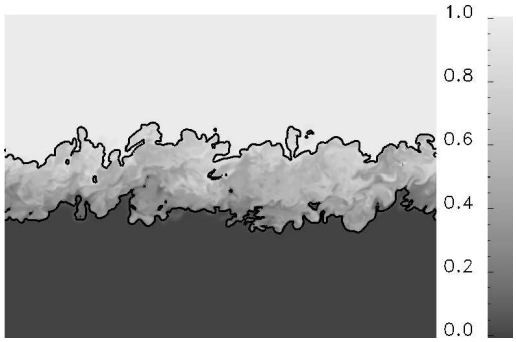

Figure 2.3: Case inert-0.15: Instantaneous mass fraction field of O_2, x_1-x_3-plane in the middle of the computational domain at $\tau_\omega = 286$, isolines $Y_{O2} = 0.1$ and 0.9 are shown

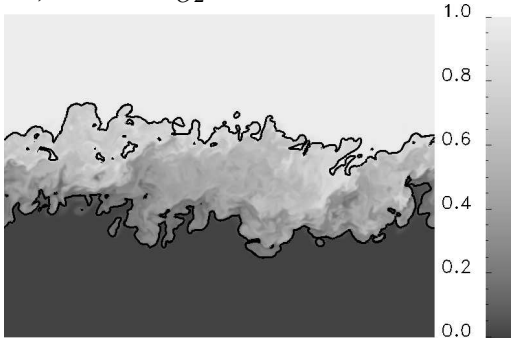

Figure 2.4: Case inert-0.15: Instantaneous mass fraction field of O_2, x_1-x_3-plane in the middle of the computational domain at $\tau_\omega = 409$, isolines $Y_{O2} = 0.1$ and 0.9 are shown

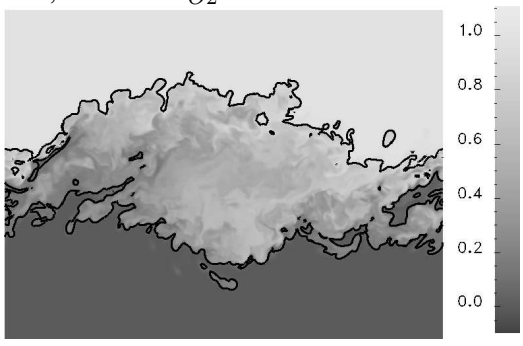

Figure 2.5: Case inert-0.15: Instantaneous mass fraction field of O_2, x_1-x_3-plane in the middle of the computational domain at $\tau_\omega = 533$, isolines $Y_{O2} = 0.1$ and 0.9 are shown

2.4.1.1 Inert shear layer at $M_c = 0.15$

Figures 2.2 to 2.5 show instantaneous distributions of the oxygen mass fraction in the central x_1-x_3-plane of the case inert-0.15 at different stages during its development. At early times (Fig. 2.2) the rotation-dominated vortices (rollers) can be easily distinguished from the strain-dominated braid regions between them, and pairings of vortices are going on, for example close to the right edge of the computational domain. However, later during the self-similar state (cf. Sect. 2.4.2) in Fig. 2.3 and Fig. 2.4, organized pairings are not the dominant mechanism that leads to the growth of the shear layer. The rollers rather merge gradually with their neigbours which is in agreement with the simulations of Rogers & Moser [152] and with the experiments of other authors who were not able to observe pairings during the fully developed turbulent state [21, 75]. A possible explanation for pairings that are observed in some experiments [18, 83] is given by [152] and refers to the disturbance environment in the experiments which may include two-dimensional or quasi-two-dimensional disturbances e.g. due to the splitter-plate tip. At very late times (Fig. 2.5) only one large structure is present in the computational domain and is interacting unphysically with itself due to box size limitations.

Instantaneous pictures of the mass fraction in x_1-x_2-planes through the middle of the domain (Figs. 2.6 to 2.9) provide more insight into the structures. It can be seen that before self-similarity is reached (Fig. 2.6), there is some two-dimensional organization of the flow with structures spanning the whole domain. This is in agreement with previous studies of incompressible mixing layers [19, 21, 27, 189]. During the self-similar state (Figs. 2.7 and 2.8) no such two-dimensionality can be observed, and the mixing layer appears irregular with no organization. While at earlier times there is a large quantity of unmixed fluid, both pure oxygen and pure hydrogen, present at the centreline, this is the case only to a minor degree at later states (Figs. 2.7 to 2.9).

Figures 2.10 to 2.13 show x_2-x_3-cuts through a braid corresponding to a pressure maximum and a roller corresponding to a pressure minimum at the different times, respectively. In the braid-region at early times (Fig. 2.10), the isolines are rolled up around the streamwise vortices which is also a characteristic feature of nonturbulent mixing layers [152]. At later times, these discrete roll-ups cannot be seen any more (Figs. 2.11 and 2.12), and braid and roller cores appear very similar since the braid-regions also contain mixed fluid and are not as clean as during the initial stage. Therefore, the only difference between braids and rollers that can be seen from the mass

Figure 2.6: Case inert-0.15: Instantaneous mass fraction field of O_2, x_1-x_2-plane in the middle of the computational domain at $\tau_\omega = 83$

Figure 2.7: Case inert-0.15: Instantaneous mass fraction field of O_2, x_1-x_2-plane in the middle of the computational domain at $\tau_\omega = 286$

Figure 2.8: Case inert-0.15: Instantaneous mass fraction field of O_2, x_1-x_2-plane in the middle of the computational domain at $\tau_\omega = 409$

Figure 2.9: Case inert-0.15: Instantaneous mass fraction field of O_2, x_1-x_2-plane in the middle of the computational domain at $\tau_\omega = 533$

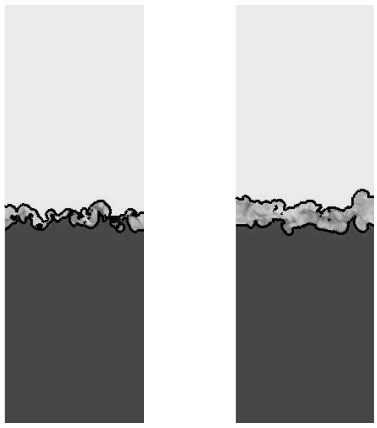

Figure 2.10: Case inert-0.15: Instantaneous mass fraction field of O_2, x_2-x_3-plane through a braid (left) and a roller (right) at $\tau_\omega = 83$, isolines $Y_{O2} = 0.1$ and 0.9 are shown

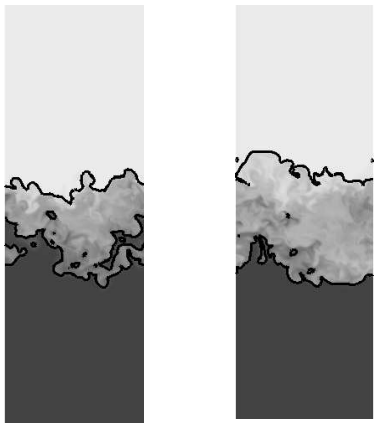

Figure 2.11: Case inert-0.15: Instantaneous mass fraction field of O_2, x_2-x_3-plane through a braid (left) and a roller (right) at $\tau_\omega = 286$, isolines $Y_{O2} = 0.1$ and 0.9 are shown

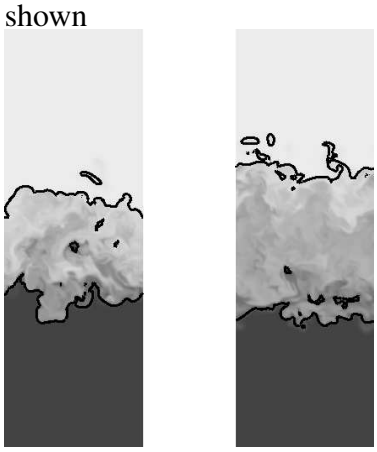

Figure 2.12: Case inert-0.15: Instantaneous mass fraction field of O_2, x_2-x_3-plane through a braid (left) and a roller (right) at $\tau_\omega = 409$, isolines $Y_{O2} = 0.1$ and 0.9 are shown

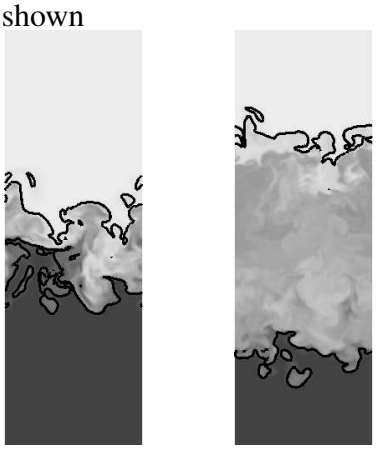

Figure 2.13: Case inert-0.15: Instantaneous mass fraction field of O_2, x_2-x_3-plane through a braid (left) and a roller (right) at $\tau_\omega = 533$, isolines $Y_{O2} = 0.1$ and 0.9 are shown

fraction field at the self-similar state is a smaller extent of the braids in the x_3-direction. At the latest state shown (Fig. 2.12), which is however not self-similar anymore, the difference between the braid- and the roller-region becomes more pronounced again.

2.4.1.2 Inert shear layer at $M_c = 0.7$

Figures 2.14 to 2.17 show instantaneous distributions of the oxygen mass fraction in the central x_1-x_3-plane at different times. Even at the earliest time shown (Fig. 2.14), no pairing of vortices is visible which is in contrast to the test case at the lower convective Mach number. As Clemens & Mungal [27] pointed out, the vortex cores at this time seem to be angular, nearly polygonial, as opposed to the more elliptical ones in Fig. 2.2. This feature can be noticed at later times, too, for example in Fig. 2.16 and in general, the structures at $M_c = 0.7$ are not very coherent with even less distinction between rollers and braids than at $M_c = 0.15$. The isolines at $Y_{O2} = 0.1$ and 0.9 that are shown in Figs. 2.14 to 2.17 and that can be considered as the edges of the mixing layer

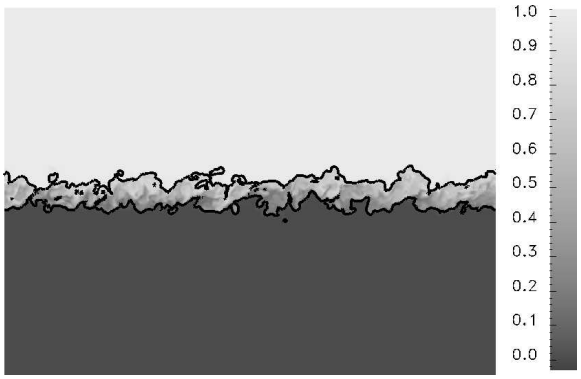

Figure 2.14: Case inert-0.7: Instantaneous mass fraction field of O_2, x_1-x_3-plane in the middle of the computational domain at $\tau_\omega = 146$, isolines $Y_{O2} = 0.1$ and 0.9 are shown

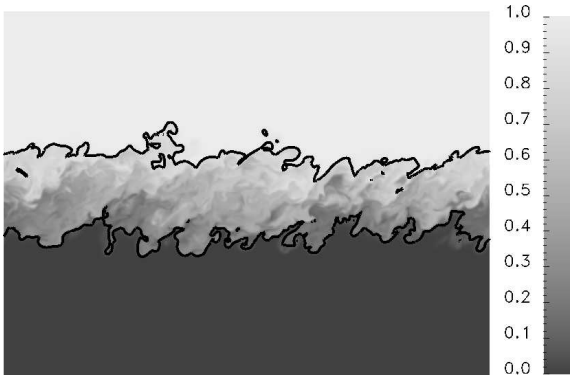

Figure 2.15: Case inert-0.7: Instantaneous mass fraction field of O_2, x_1-x_3-plane in the middle of the computational domain at $\tau_\omega = 418$, isolines $Y_{O2} = 0.1$ and 0.9 are shown

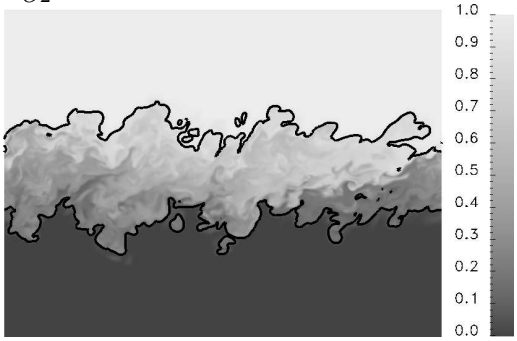

Figure 2.16: Case inert-0.7: Instantaneous mass fraction field of O_2, x_1-x_3-plane in the middle of the computational domain at $\tau_\omega = 697$, isolines $Y_{O2} = 0.1$ and 0.9 are shown

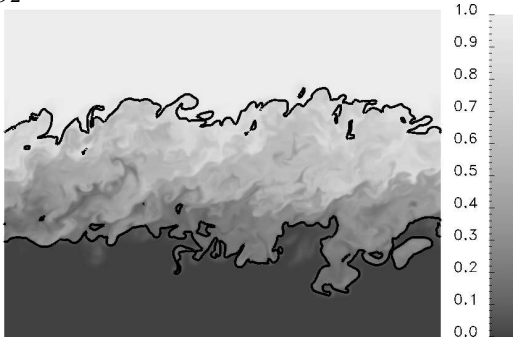

Figure 2.17: Case inert-0.7: Instantaneous mass fraction field of O_2, x_1-x_3-plane in the middle of the computational domain at $\tau_\omega = 980$, isolines $Y_{O2} = 0.1$ and 0.9 are shown

Figure 2.18: Case inert-0.7: Instantaneous mass fraction field of O_2, x_1-x_2-plane in the middle of the computational domain at $\tau_\omega = 146$

Figure 2.19: Case inert-0.7: Instantaneous mass fraction field of O_2, x_1-x_2-plane in the middle of the computational domain at $\tau_\omega = 418$

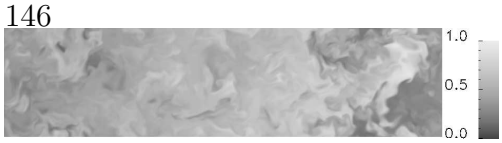

Figure 2.20: Case inert-0.7: Instantaneous mass fraction field of O_2, x_1-x_2-plane in the middle of the computational domain at $\tau_\omega = 697$

Figure 2.21: Case inert-0.7: Instantaneous mass fraction field of O_2, x_1-x_2-plane in the middle of the computational domain at $\tau_\omega = 980$

show ondulations on a larger scale than at the lower convective Mach number (Figs. 2.3 and 2.5). Especially at later times (Figs. 2.16 and 2.17), mushroom-like ejections are visible.

Cuts through the central x_1-x_2-plane (Figs. 2.18 to 2.21) reveal the highly three-dimensional nature of this mixing layer right from the beginning. The lack of any obvious spatial regularity or organization is striking [27]. Comparing Fig. 2.18 with Fig. 2.6 at $M_c = 0.15$, the structures at the higher convective Mach number are more stretched in streamwise direction than at the lower

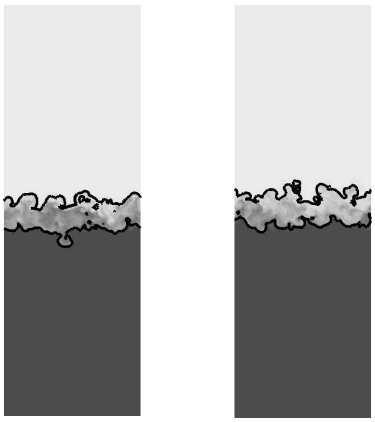

Figure 2.22: Case inert-0.7: Instantaneous mass fraction field of O_2, x_2-x_3-plane through a braid (left) and a roller (right) at $\tau_\omega = 146$, isolines $Y_{O2} = 0.1$ and 0.9 are shown

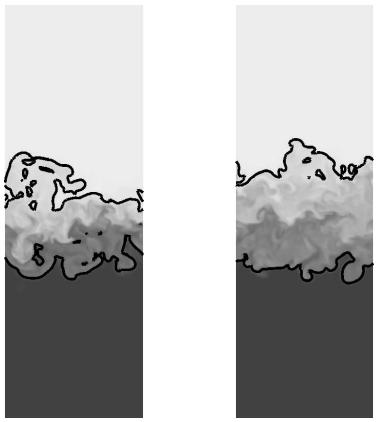

Figure 2.23: Case inert-0.7: Instantaneous mass fraction field of O_2, x_2-x_3-plane through a braid (left) and a roller (right) at $\tau_\omega = 418$, isolines $Y_{O2} = 0.1$ and 0.9 are shown

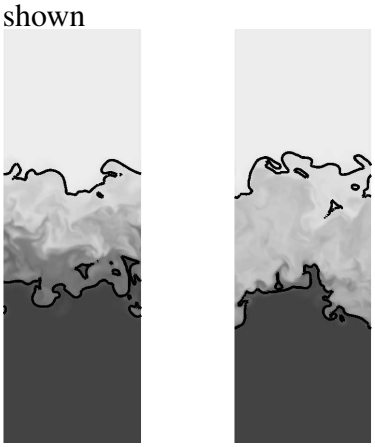

Figure 2.24: Case inert-0.7: Instantaneous mass fraction field of O_2, x_2-x_3-plane through a braid (left) and a roller (right) at $\tau_\omega = 697$, isolines $Y_{O2} = 0.1$ and 0.9 are shown

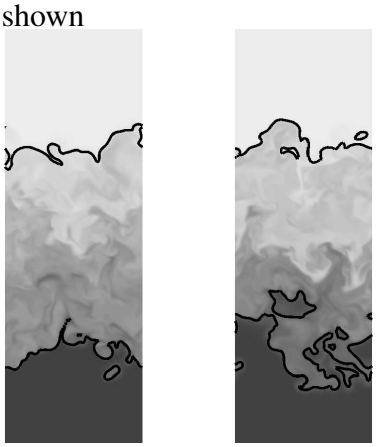

Figure 2.25: Case inert-0.7: Instantaneous mass fraction field of O_2, x_2-x_3-plane through a braid (left) and a roller (right) at $\tau_\omega = 980$, isolines $Y_{O2} = 0.1$ and 0.9 are shown

convective Mach number.

The fact that braids and rollers are not so clearly marked can also be seen when cutting through them as done in Figs. 2.22 to 2.25. Even at earlier times, it is hard to distinguish whether the structure that is cut is a braid or a roller, with the braids only being a little less extended in x_3-direction. No distinctive roll-ups of the isolines within the braids are visible as it was the case in Fig. 2.10 at $M_c = 0.15$. The larger-scale ondulations in braids and rollers as well as the mushroom-like ejections that are visible in the x_1-x_3-cuts (Figs. 2.14 to 2.17) can also be seen here.

2.4.1.3 Inert shear layer at $M_c = 1.1$

Cuts through x_1-x_3-planes of the instantaneous oxygen mass fraction distribution for the test case at $M_c = 1.1$ are shown in the Figs. 2.26 to 2.29. While the earliest state shown looks completely different from the mixing layers at lower convective Mach number and gives evidence of the

Figure 2.26: Case inert-1.1: Instantaneous mass fraction field of O_2, x_1-x_3-plane in the middle of the computational domain at $\tau_\omega = 162$, isolines $Y_{O2} = 0.1$ and 0.9 are shown

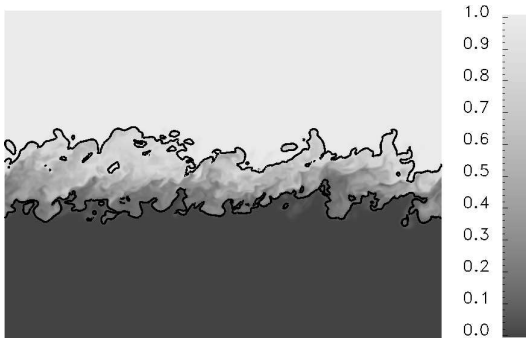

Figure 2.27: Case inert-1.1: Instantaneous mass fraction field of O_2, x_1-x_3-plane in the middle of the computational domain at $\tau_\omega = 381$, isolines $Y_{O2} = 0.1$ and 0.9 are shown

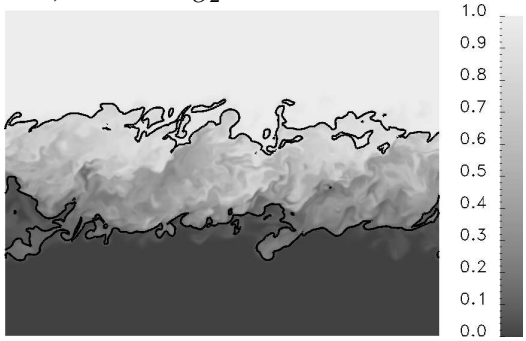

Figure 2.28: Case inert-1.1: Instantaneous mass fraction field of O_2, x_1-x_3-plane in the middle of the computational domain at $\tau_\omega = 735$, isolines $Y_{O2} = 0.1$ and 0.9 are shown

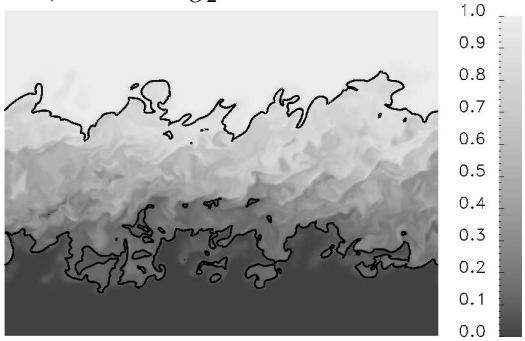

Figure 2.29: Case inert-1.1: Instantaneous mass fraction field of O_2, x_1-x_3-plane in the middle of the computational domain at $\tau_\omega = 1098$, isolines $Y_{O2} = 0.1$ and 0.9 are shown

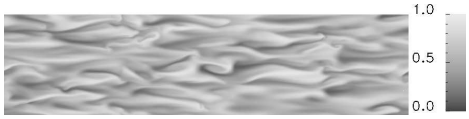

Figure 2.30: Case inert-1.1: Instantaneous mass fraction field of O_2, x_1-x_2-plane in the middle of the computational domain at $\tau_\omega = 162$

Figure 2.31: Case inert-1.1: Instantaneous mass fraction field of O_2, x_1-x_2-plane in the middle of the computational domain at $\tau_\omega = 381$

Figure 2.32: Case inert-1.1: Instantaneous mass fraction field of O_2, x_1-x_2-plane in the middle of the computational domain at $\tau_\omega = 735$

Figure 2.33: Case inert-1.1: Instantaneous mass fraction field of O_2, x_1-x_2-plane in the middle of the computational domain at $\tau_\omega = 1098$

stabilizing nature of compressibility, the later development of this mixing layer is similar to the inert-0.7 case with rather angular rollers. The isolines at $Y_{O2} = 0.1$ and 0.9 which limit the mixing layer show ondulations on even a larger scale than at $M_c = 0.7$, and the edge of the mixing layer appears more torn with many ejections going from the turbulent region into the laminar one.

While the organization of the structures at earlier times for $M_c = 0.15$ was in spanwise direction (Fig. 2.6) and had a slight tendency towards streamwise organization at $M_c = 0.7$ (Fig. 2.18), it is clearly streamwise at $M_c = 1.1$ as reveals the x_1-x_2-cut in Fig. 2.30. However, at later

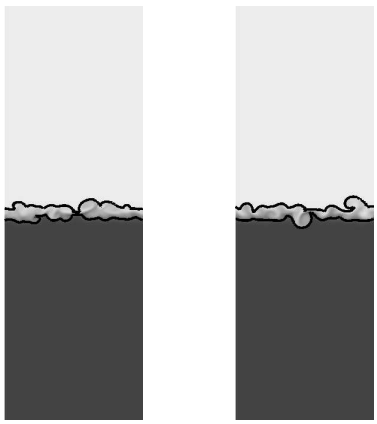

Figure 2.34: Case inert-1.1: Instantaneous mass fraction field of O_2, x_2-x_3-plane through a braid (left) and a roller (right) at $\tau_\omega = 162$, isolines $Y_{O2} = 0.1$ and 0.9 are shown

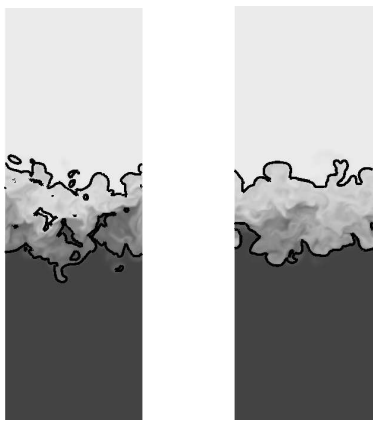

Figure 2.35: Case inert-1.1: Instantaneous mass fraction field of O_2, x_2-x_3-plane through a braid (left) and a roller (right) at $\tau_\omega = 381$, isolines $Y_{O2} = 0.1$ and 0.9 are shown

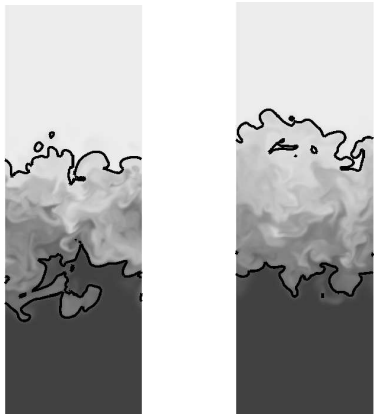

Figure 2.36: Case inert-1.1: Instantaneous mass fraction field of O_2, x_2-x_3-plane through a braid (left) and a roller (right) at $\tau_\omega = 735$, isolines $Y_{O2} = 0.1$ and 0.9 are shown

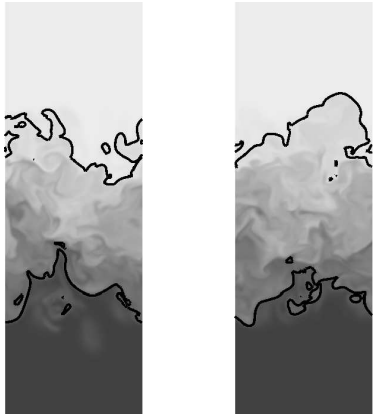

Figure 2.37: Case inert-1.1: Instantaneous mass fraction field of O_2, x_2-x_3-plane through a braid (left) and a roller (right) at $\tau_\omega = 1098$, isolines $Y_{O2} = 0.1$ and 0.9 are shown

times (Figs. 2.31 to 2.33), there is no more organization visible, and the mixing layer is highly three-dimensional. While it is obviously more three-dimensional than at $M_c = 0.15$, it is hard to say whether the three-dimensionality has increased when rising M_c from 0.7 to 1.1. In particular at the latest time shown (Fig. 2.33), there is no free-stream fluid present in the mid-plane of the mixing layer.

Cuts through braid and roller regions, which are of course hardly distinguishable from another, are shown in Figs. 2.34 to 2.37 and confirm the observations concerning the three-dimensional nature of the mixing layer. The large-scale ondulations in the isolines correspond to ejections going outwards from the mixing layer rather than inwards.

2.4.2 The self-similar state

All simulations are performed during time-intervals that are long enough to reach a self-similar state and to collect sufficient data during this state for reliable statistics. After an initial transient, constant normalized growth rates

$$\dot{\delta}_\theta = \frac{1}{\Delta u}\frac{d\delta_\theta}{dt} \tag{2.17}$$

of the momentum thickness

$$\delta_\theta = \frac{1}{\rho_0 \Delta u^2}\int_{-\infty}^{\infty}\langle\rho\rangle\left(\frac{1}{4}\Delta u^2 - \langle u_1\rangle_f^2\right)dx_3 \tag{2.18}$$

are established in all cases which can be seen from the constant slopes in Fig. 2.38. This figure reveales that with increasing compressibility it takes longer for the mixing layer to reach a fully turbulent, self-similar state which has to be attributed to the stabilizing effect of the compressibility. Following Vreman et al. [183], the normalized growth rate can be computed by

$$\dot{\delta}_\theta = \frac{2}{\rho_0 \Delta u^3}\left[\int\left(-\langle\rho u_1'' u_3''\rangle\frac{\partial\langle u_1\rangle_f}{\partial x_3}\right)dx_3 + \int\left(\langle\tau_{13}\rangle\frac{\partial\langle u_1\rangle_f}{\partial x_3}\right)dx_3\right]. \tag{2.19}$$

Quantities with brackets, like $\langle\rho\rangle$, are Reynolds averaged quantities, quantities with an additional index f, like $\langle u_1\rangle_f$, are Favre averaged quantities. Primes and double primes indicate the respective fluctuations. The first integral in Eq. (2.19) is the integrated production of the TKE. The second integral represents the molecular dissipation of the mean flow. In the turbulent regime the latter can be neglected compared to the former [183, 123], and the expression for the growth rate reduces to

$$\dot{\delta}_\theta = \frac{2}{\rho_0 \Delta u^3}\int\left(-\langle\rho u_1'' u_3''\rangle\frac{\partial\langle u_1\rangle_f}{\partial x_3}\right)dx_3. \tag{2.20}$$

The normalized time period between 286 and 409 is considered the self-similar state of the inert-0.15 case for which the nearly constant normalized growth rate of the momentum thickness computed by Eq. (2.20) is 0.0124. This lies close to the growth rate of 0.014 found by Rogers & Moser [152] for an incompressible mixing layer. By increasing the convective Mach number $\dot{\delta}_\theta$ is reduced to 0.0054 in the simulation inert-0.7 and to 0.0036 in the simulation inert-1.1. Figure 2.39 presents the so-called 'Langley Experimental Curve'obtained from growth rates found by

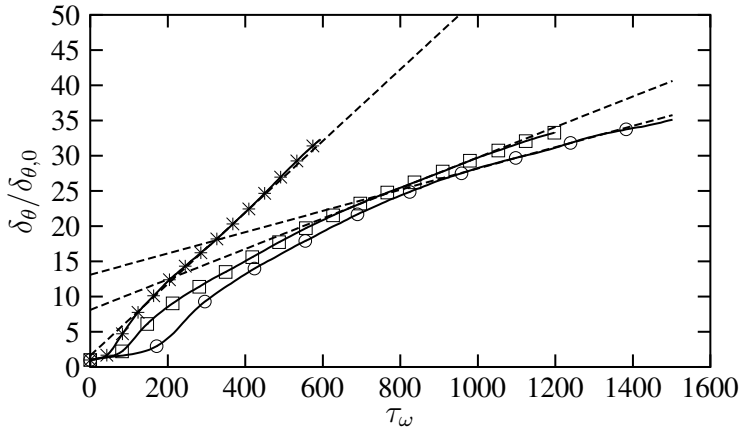

Figure 2.38: Temporal development of the momentum thickness, normalized by initial momentum thickness $\delta_{\theta,0}$, $*$: inert-0.15, $\square$: inert-0.7, $\circ$: inert-1.1, dashed lines show linear regressions for the self-similar state

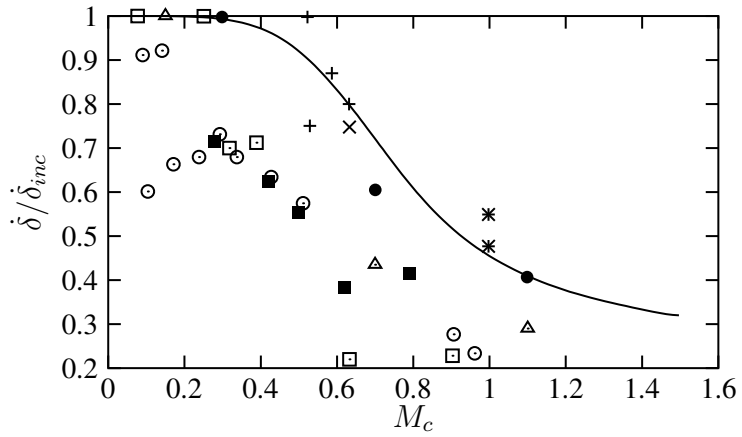

Figure 2.39: Dependence of shear layer growth rate on M_c: solid line: Langley curve, $+$: Debisschop & Bonnet [36], $\times$: Samimy & Elliot [155], $*$: Chambres, Barre & Bonnet [25], $\square$: Papamoschou & Roshko [126], $\blacksquare$: Clemens & Mungal [27], $\circ$: Hall, Dimotakis & Rosemann [71], $\bullet$: Pantano & Sarkar [123], $\triangle$: Present DNS

early air-air shear layer experimentalists along with various other experimental results, the DNS results of Pantano & Sarkar [123] and the present DNS results. Our results are lying within the region where other experiments are situated. However, they are below the DNS results of Pantano & Sarkar who did similar computations to the present ones. This fact is commented on in the course of this section.

The beginning and the end of the self-similar states, along with the corresponding Reynolds numbers

$$Re_\omega = \frac{\Delta u \, \rho_0 \, \delta_\omega}{\mu_0} \tag{2.21}$$

are summarized in table 2.2. They are based on the instantaneous vorticity thickness

$$\delta_\omega = \frac{\Delta u}{\left(\partial \langle u_1 \rangle_f / \partial x_3\right)_{max}}. \tag{2.22}$$

The peak values of the micro-scale Reynolds number,

$$Re_\lambda = 2k\sqrt{\frac{5\rho}{\nu\epsilon}}, \tag{2.23}$$

where ν is the kinematic viscosity, k the TKE and ϵ its dissipation rate (see Eq. (2.27)) are also given in table 2.2. This Reynolds number is based on the Taylor micro-scale

$$\lambda = \sqrt{\frac{10\rho\nu k}{\epsilon}}. \tag{2.24}$$

The initial ratio between the vorticity thickness and the momentum thickness is 4.0 which is due to the initialization of the vorticity by a hyperbolic-tangent profile. It increases during the initial development to values around 5.5 for all test cases but relaxes back during the self-similar state to approximately the initial value.

A normalization by the variables δ_ω, ρ_0 and Δu allows to verify if a truly self-similar state is reached by following the temporal development of profiles which are spatially averaged over the two homogeneous directions. Figures 2.40 to 2.42 show profiles of the Reynolds shear stress

$$\langle \rho \rangle R_{13} = \langle \rho u_1'' u_3'' \rangle \tag{2.25}$$

Table 2.2: Dimensionless times and Reynolds numbers at the beginning (index: B) and end (index: E) of the self-similar state

	$\tau_{\omega,B}$	$\tau_{\omega,E}$	$Re_{\omega,B}$	$Re_{\omega,E}$	$Re_{\lambda,B}$	$Re_{\lambda,E}$
inert-0.15	286	409	11540	13410	122	144
inert-0.7	626	980	15370	18014	100	105
inert-1.1	1023	1305	18586	22353	85	90

at different times for the three inert test cases, respectively. The relaxation to a self-similar state is visible. Consequently, a temporal averaging of the appropriately normalized profiles over this state is possible. A similar collapse can be observed for other profiles, e.g. those of the other Reynolds stresses, the TKE, the dissipation rate of the TKE or the variance of the mass fractions and their dissipation rate.

In Figs. 2.43 to 2.47, the mean streamwise velocity and the rms velocities computed from the turbulent stress tensor

$$\langle\rho\rangle R_{ij} = \langle\rho u_i'' u_j''\rangle \tag{2.26}$$

of case inert-0.15 are shown in comparison with other DNS and experimental values. The profiles of the numerical simulations are averaged both spatially over the two homogeneous directions

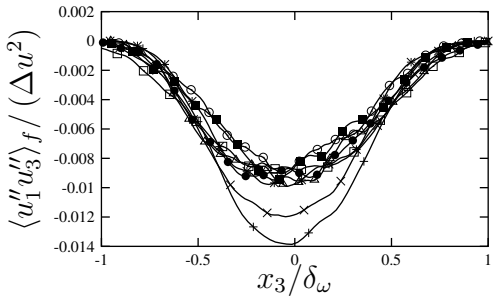

Figure 2.40: Case inert-0.15: Spatially averaged profiles of the Reynolds shear stress R_{13} at different times, $+$: $\tau_\omega = 83$, $\times$: $\tau_\omega = 123$, $*$: $\tau_\omega = 164$, $\square$: $\tau_\omega = 204$, $\blacksquare$: $\tau_\omega = 245$, $\circ$: $\tau_\omega = 286$, $\bullet$: $\tau_\omega = 327$, $\triangle$: $\tau_\omega = 368$

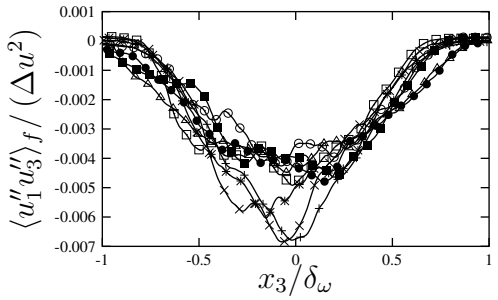

Figure 2.41: Case inert-0.7: Spatially averaged profiles of the Reynolds shear stress R_{13} at different times, $+$: $\tau_\omega = 390$, $\times$: $\tau_\omega = 474$, $*$: $\tau_\omega = 557$, $\square$: $\tau_\omega = 640$, $\blacksquare$: $\tau_\omega = 725$, $\circ$: $\tau_\omega = 809$, $\bullet$: $\tau_\omega = 866$, $\triangle$: $\tau_\omega = 923$

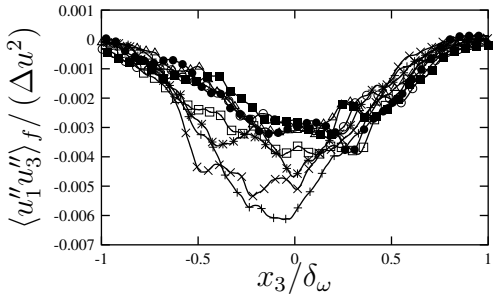

Figure 2.42: Case inert-1.1: Spatially averaged profiles of the Reynolds shear stress R_{13} at different times, $+$: $\tau_\omega = 735$, $\times$: $\tau_\omega = 807$, $*$: $\tau_\omega = 878$, $\square$: $\tau_\omega = 949$, $\blacksquare$: $\tau_\omega = 1023$, $\circ$: $\tau_\omega = 1098$, $\bullet$: $\tau_\omega = 1174$, $\triangle$: $\tau_\omega = 1248$

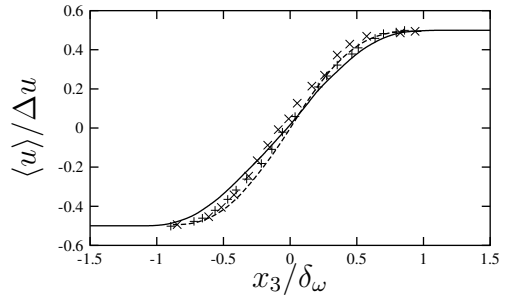

Figure 2.43: Streamwise velocity, solid line: inert-0.15, dashed line: DNS Pantano & Sarkar $M_c = 0.3$ [123], [152], $+$: Experiments Bell & Mehta [7], $\times$: Experiments Spencer & Jones [172]

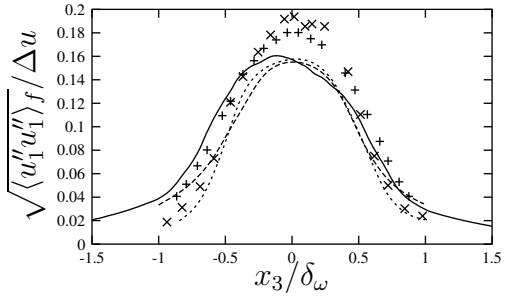

Figure 2.44: Streamwise rms velocity, solid line: inert-0.15, dashed line: DNS Pantano & Sarkar $M_c = 0.3$ [123], dotted line: DNS Rogers & Moser, [152], $+$: Experiments Bell & Mehta [7], $\times$: Experiments Spencer & Jones [172]

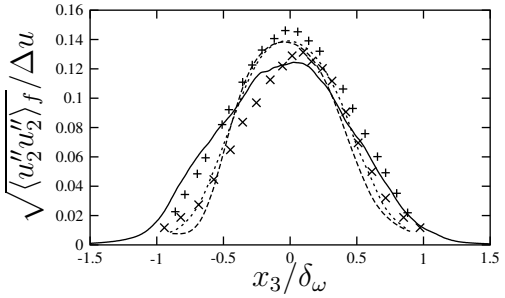

Figure 2.45: Spanwise rms velocity, curves as in Fig. 2.44

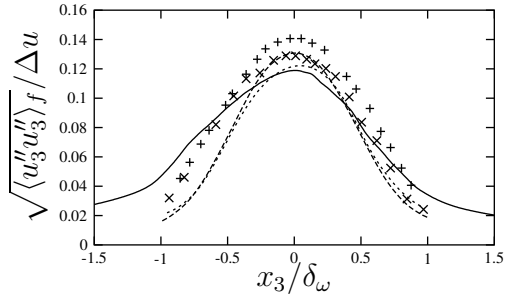

Figure 2.46: Transverse rms velocity, curves as in Fig. 2.44

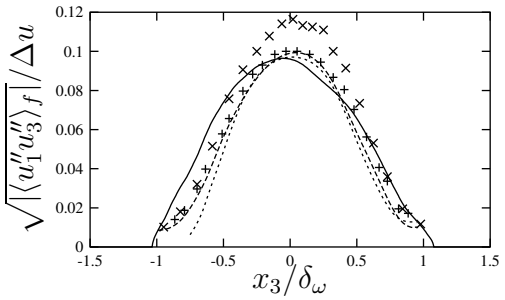

Figure 2.47: Velocity computed from Reynolds shear stress, curves as in Fig. 2.44

and temporally over the self-similar state. This is the case for all profiles in the following if not mentioned otherwise. In general, the agreement of the present profiles with the others is good which verifies the computation. However, it is interesting to note that the width of the rms velocity profiles varies which can be due to different initial developments in the time elapsed until self-similarity is reached. While Rogers & Moser [152] initialized their simulation with a turbulent field from a previous boundary layer DNS, the present DNS were initialized with laminar profiles and broadband fluctuations in the velocity components only. Pantano & Sarkar [123] used similar broadband fluctuations in the velocity components but superimposed additional pressure and density fluctuations. Little unsymmetries in the profiles of the present simulation may be attributed to the density ratio of 1.14 between oxygen in the upper stream and nitrogen in the lower one.

Most of the rms velocity profiles of the current DNS have a somewhat lower peak than the DNS profiles of Rogers & Moser [152] as well as the ones of Pantano & Sarkar [123]. One reason might be that the size of the present computation domain is more than four times larger in all

directions than the simulation of Rogers & Moser and 1.5 times larger in the streamwise and spanwise directions and 2.25 times larger in transverse direction than the one of Pantano & Sarkar. Therefore, the present simulation probably captures the relaxation towards a self-similar state (see Fig. 2.40) more completely than the ones with the smaller domains. This conclusion is drawn from our simulations in shorter domains (not documented here) which led to higher peak values in the rms velocity profiles.

Figure 2.48 shows the most important terms in the transport equation of TKE k for case inert-0.15,

$$\frac{\partial\left(\langle\rho\rangle k\right)}{\partial t}+\frac{\partial\left(\langle\rho\rangle\langle u_k\rangle_f k\right)}{\partial x_k}=P+\epsilon+T+\Pi+\Sigma \tag{2.27}$$

with the production P, the dissipation rate ϵ, the transport T, the pressure dilatation Π and the mass flux coupling term Σ. The agreement between the present DNS and the simulations of Pantano & Sarkar as well as Rogers & Moser is good taking into account the previously mentioned reasons for discrepancies. Equation (2.27) is obtained from the transport equation for the Reynolds stresses,

$$\frac{\partial\langle\rho\rangle R_{ij}}{\partial t}+\frac{\partial\left(\langle\rho\rangle\langle u_k\rangle_f R_{ij}\right)}{\partial x_k}=P_{ij}+\epsilon_{ij}+T_{ij}+\Pi_{ij}+\Sigma_{ij}, \tag{2.28}$$

by contracting the indices ($k=0.5R_{kk}$). In Eq. (2.28), the production term is

$$P_{ij}=-\langle\rho\rangle\left(R_{ik}\frac{\partial\langle u_j\rangle_f}{\partial x_k}+R_{jk}\frac{\partial\langle u_i\rangle_f}{\partial x_k}\right), \tag{2.29}$$

the dissipation rate,

$$\epsilon_{ij}=-\langle\tau'_{jk}\frac{\partial u''_i}{\partial x_k}+\tau'_{ik}\frac{\partial u''_j}{\partial x_k}\rangle, \tag{2.30}$$

the transport by velocity and pressure fluctuations as well as viscous effects,

$$T_{ij}=-\frac{\partial}{\partial x_k}\langle\rho u''_i u''_j u''_k+p'u'_i\delta_{jk}+p'u'_j\delta_{ik}-\tau'_{jk}u''_i-\tau'_{ik}u''_j\rangle, \tag{2.31}$$

the pressure-strain term,

$$\Pi_{ij}=\langle p'\left(\frac{\partial u''_i}{\partial x_j}+\frac{\partial u''_j}{\partial x_i}\right)\rangle \tag{2.32}$$

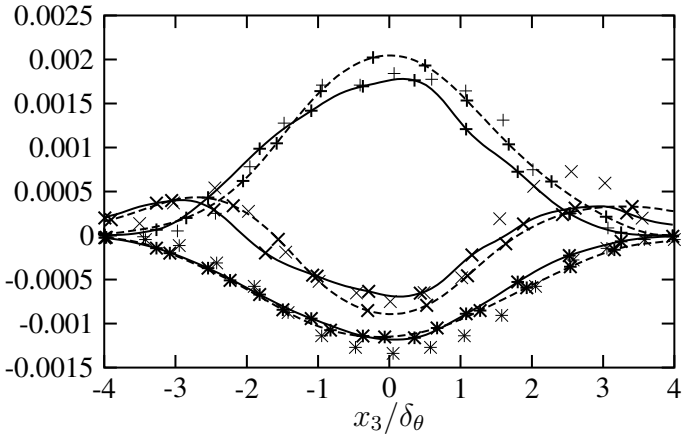

Figure 2.48: Turbulent kinetic energy budget, $+$: production, $\times$: transport, $*$: dissipation, normalized by $\Delta u^3\delta_\theta$, solid lines: inert-0.15, dashed lines: DNS Pantano & Sarkar $M_c=0.3$ [123], dotted line: DNS Rogers & Moser, [152]

and the mass flux coupling term

$$\Sigma_{ij} = \langle u_i'' \rangle \left(\frac{\partial \langle \tau_{jk} \rangle}{\partial x_k} - \frac{\partial \langle p \rangle}{\partial x_j} \right) + \langle u_j'' \rangle \left(\frac{\partial \langle \tau_{ik} \rangle}{\partial x_k} - \frac{\partial \langle p \rangle}{\partial x_i} \right). \tag{2.33}$$

When comparing the temporally and spatially averaged rms velocity profiles of case inert-0.7 with the computations of Pantano & Sarkar [123] and the experiments of Elliott & Samimy [49] in Figs. 2.49 to 2.51, the differences between the peak values are even more pronounced than for the incompressible case. Again, a possible reason could be that the large present domain size allows a more complete relaxation towards a self-similar state than the smaller ones from the previous simulations of Pantano & Sarkar with their domain being three times smaller in streamwise and transverse direction and 1.5 times smaller in the spanwise direction. Similar tendencies can be observed for the major terms in the TKE transport equation (2.27) shown in Fig. 2.52. The suspicion that descrepancies between the self-similar profiles of the present simulation at $M_c = 0.7$ and the ones of the simulation by Pantano & Sarkar [123] is caused by an early break-off of the latter ones due to their smaller domain size is substantiated by the fact that the momentum thickness growth rate of case inert-0.7 has a small plateau between $\tau_\omega = 300$ and $\tau_\omega = 400$ with $\dot{\delta}_\omega \approx 0.007$ before it decreases again to the growth rate that is identified in this work to be the self-similar one ($\delta_\omega \approx 0.0054$ between $\tau_\omega = 626$ and 980) (see Fig. 2.53). As Pantano & Sarkar identified the growth rate of the mixing layer at $M_c = 0.7$ to be 0.0108, it seems as if they took an early, higher plateau in the growth rate as the self-similar state since the limited domain size does not allow the mixing layer to grow further. Equation 2.20 shows that a larger growth rate is related with a larger Reynolds shear stress. Having a larger self-similar growth rate it is clear, that the Reynolds shear stress (and also the other Reynolds stresses) of Pantano & Sarkar must be larger than the ones of the present simulation which is confirmed by Figs. 2.49 to 2.51. A similar argumention is true for the Reynolds stresses of case inert-1.1. The

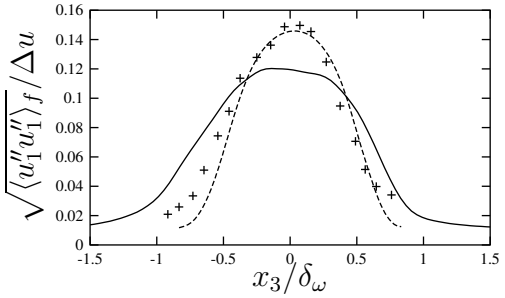

Figure 2.49: Streamwise rms velocity, solid line: inert-0.7, dashed line: DNS Pantano & Sarkar $M_c = 0.7$ [123], $+$: Experiments Elliott & Samimy [49]

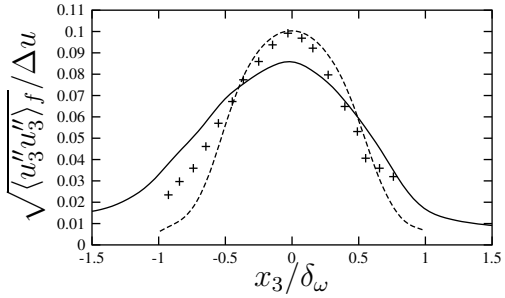

Figure 2.50: Transverse rms velocity, curves as in Fig. 2.44

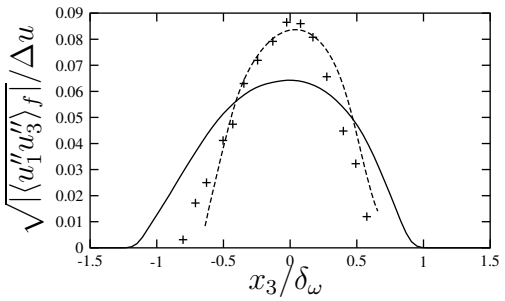

Figure 2.51: Velocity computed from Reynolds shear stress, curves as in Fig. 2.44

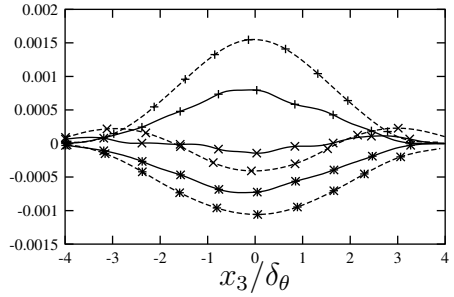

Figure 2.52: Turbulent kinetic energy budget, $+$: production, $\times$: transport, $*$: dissipation, normalized by $\Delta u^3/\delta_\theta$, solid lines: inert-0.7, dashed lines: DNS Pantano & Sarkar $M_c = 0.7$ [123]

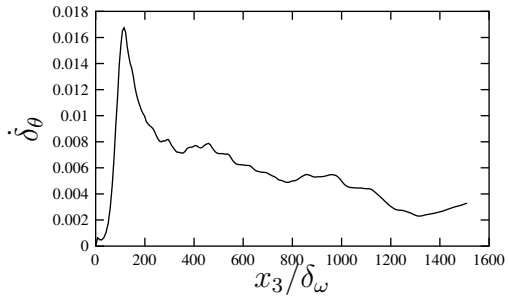

Figure 2.53: Dimensionless momentum thickness growth rate of the inert-0.7 case, computed with Eq. (2.20)

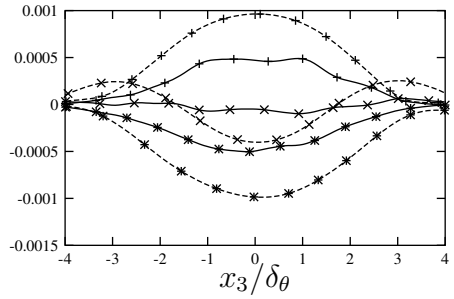

Figure 2.54: Turbulent kinetic energy budget, $+$: production, $\times$: transport, $*$: dissipation, normalized by $\Delta u^3/\delta_\theta$, solid lines: inert-1.1, dashed lines: DNS Pantano & Sarkar $M_c = 1.1$ [123]

most important terms of the TKE budget equation for this test case are shown in Fig. 2.54 in comparison with the results of Pantano & Sarkar [123] which are again larger than the present results.

2.4.3 Check of resolution, domain sizes and filtering

In order to verify the accuracy of the results, resolution and domain sizes are checked. All simulations are well resolved with a minimal Kolmogorov length

$$l_k = \left(\frac{\langle \nu \rangle^3 \langle \rho \rangle}{\epsilon} \right)^{1/4} \tag{2.34}$$

of $0.32\Delta x_3$ for case inert-0.15, $0.44\Delta x_3$ for case inert-0.7 and $0.58\Delta x_3$ for case inert-1.1 during the self-similar state. These resolutions are fine enough to accurately capture most of the dissipation (cf. Sect. 2.4.4.1) and therefore adequate for DNS [117]. As the Schmidt numbers of gases are smaller than 1, no resolution problems concerning the scalar fields are expected, either. Various spectra, which are dealt with in Sections 2.4.4.1 and 2.4.4.2, show no accumulation of energy at the highest wavenumbers as it would be the case for an under-resolved simulation.

The appropriateness of the domain size in the periodic directions is checked by computing two-point correlations of the velocity components and the species mass fraction. The two-point cor-

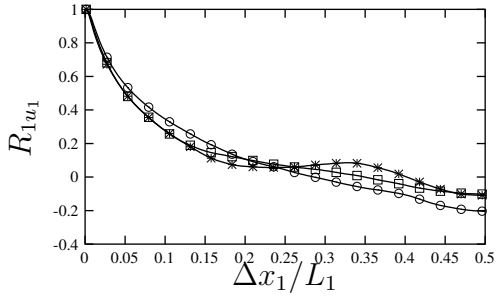

Figure 2.55: Two-point correlation R_1 with $f = u_1$, in the middle of the computational domain, averaged over the self-similar state, $*$: inert-0.15, $\square$: inert-0.7, $\circ$: inert-1.1

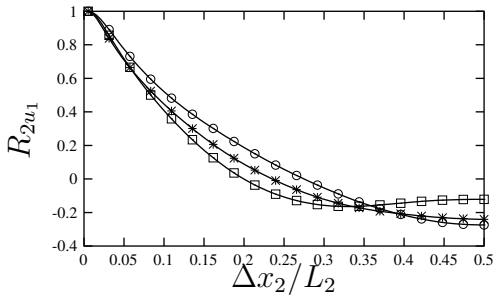

Figure 2.56: Two-point correlation R_2 with $f = u_1$, in the middle of the computational domain, averaged over the self-similar state, symbols as in Fig. 2.55

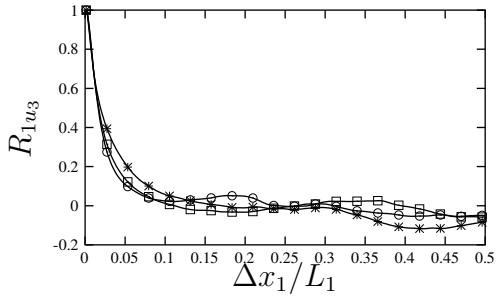

Figure 2.57: Two-point correlation R_1 with $f = u_3$, in the middle of the computational domain, averaged over the self-similar state, symbols as in Fig. 2.55

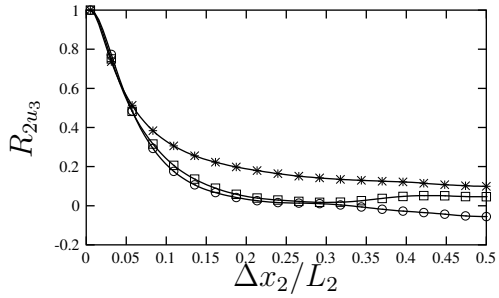

Figure 2.58: Two-point correlation R_2 with $f = u_3$, in the middle of the computational domain, averaged over the self-similar state, symbols as in Fig. 2.55

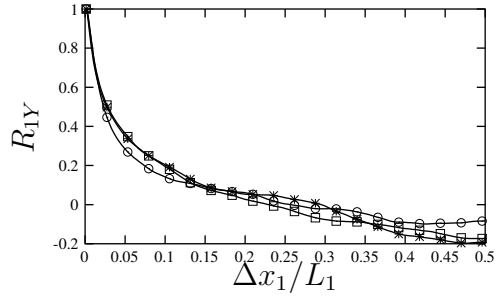

Figure 2.59: Two-point correlation R_1 with $f = Y_{O2}$, in the middle of the computational domain, averaged over the self-similar state, symbols as in Fig. 2.55

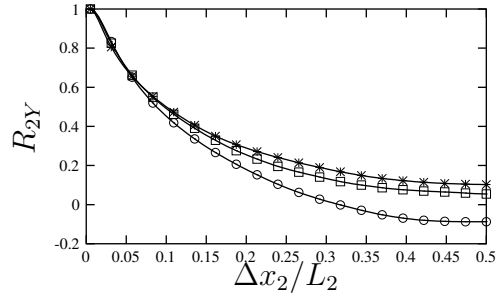

Figure 2.60: Two-point correlation R_2 with $f = Y_{O2}$, in the middle of the computational domain, averaged over the self-similar state, symbols as in Fig. 2.55

relation of a quantity f reads in streamwise direction

$$R_{1f} = \frac{\langle f'(x_1, x_2, x_3, t)\, f'(x_1 + \Delta x_1, x_2, x_3, t)\rangle}{f'^2_{rms}} \tag{2.35}$$

and in spanwise direction

$$R_{2f} = \frac{\langle f'(x_1, x_2, x_3, t)\, f'(x_1, x_2 + \Delta x_2, x_3, t)\rangle}{f'^2_{rms}}. \tag{2.36}$$

In order to eliminate the contamination of the results by finite domain size, the correlation should be small for large x_i, i.e. in the middle of the domain. Figures 2.55 to 2.60, in which half of the domain size is shown, prove that this is the case.

Table 2.3: Integral length scales

	l_1/L_1	l_2/L_2
inert-0.15	0.073	0.046
inert-0.7	0.068	0.044
inert-1.1	0.060	0.069

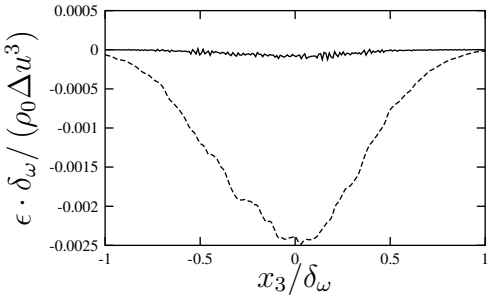

Figure 2.61: Test of compact filter, solid: filter dissipation, dashed: ϵ

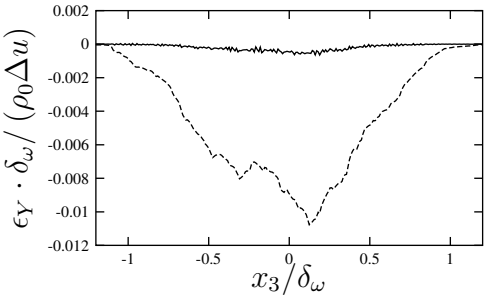

Figure 2.62: Test of compact filter, solid: filter scalar dissipation, dashed: ϵ_Y

Integral length scales in streamwise and spanwise directions are given by

$$l_1 = \int_0^{\Delta x_1 = L_1/2} R_{1u_1} d\,(\Delta x_1) \tag{2.37}$$

and

$$l_2 = \int_0^{\Delta x_2 = L_2/2} R_{2u_1} d\,(\Delta x_2) \tag{2.38}$$

[123]. In order to have good large-scale resolution, these length scales must be small compared to the dimensions of the computational box. Table 2.3 shows that this is the case by giving the spatially and temporally averaged results in the middle of the computational domain in transverse direction.

To prevent accumulation of spurious energy the primitive flow variables are filtered every 20th time step. The filtering has only a weak influence and can be quantified by comparing it to the dissipation rate of the TKE, ϵ [123]. To do so, the profile of the TKE, averaged over the two homogeneous directions, after filtering is subtracted from the one before, and the result is divided by the time between two filterings, (20 time steps). This gives an artificial dissipation rate due to the filtering which can be compared to the dissipation rate of the TKE. The corresponding profiles for one of the test cases (inert-0.15) are shown in Fig. 2.61 and prove that the dissipation rate due to filtering is small compared to the TKE dissipation rate. A similar test can be done by obtaining a filtering dissipation rate from the scalar (mass fraction) variance and by contrasting it with the scalar dissipation rate ϵ_Y which proves to be much bigger (Fig. 2.62).

2.4.4 The effect of compressibility

2.4.4.1 Turbulence characteristics

Mean flow variables The peak in the averaged temperature profile is rising with increasing Mach number (Fig. 2.63) as a consequence of viscous dissipative heating. This leads to a drop in

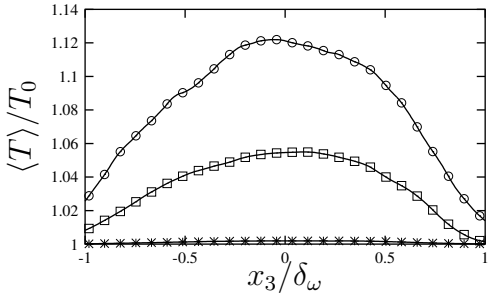

Figure 2.63: Averaged temperature, normalized by $T_0 = 0.5\,(T_1 + T_2)$, $*$: inert-0.15, $\square$: inert-0.7, $\circ$: inert-1.1

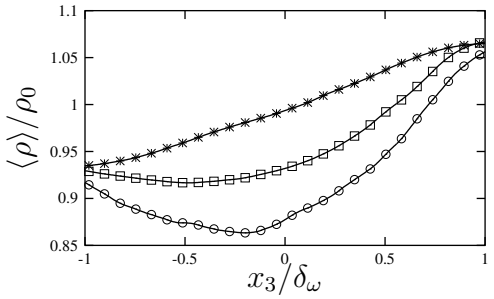

Figure 2.64: Averaged density, normalized by ρ_0, symbols as in Fig. 2.63

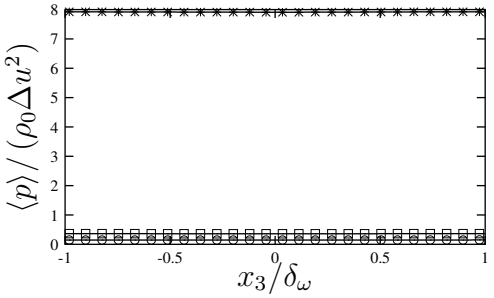

Figure 2.65: Averaged pressure, normalized by $\rho_0 \Delta u^2$, symbols as in Fig. 2.63

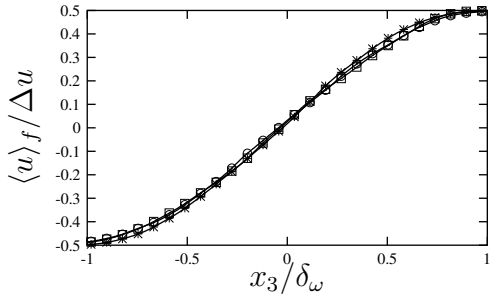

Figure 2.66: Favre averaged streamwise velocity, normalized by Δu, symbols as in Fig. 2.63

the averaged density (Fig. 2.64). The averaged pressure normalized by $\rho_0 \Delta u^2$ is nearly constant across the shear layer (Fig. 2.65) and drops with increasing M_c. Multiplying its value by γM_c^2 respectively, gives the same constant, 0.25, for all M_c which demonstrates that the pressure drop is by γM_c^2. Figure 2.66 shows the Favre averaged streamwise velocity. The differences between the cases with the various convective Mach numbers are small.

Reynolds stresses, turbulent kinetic energy and anisotropies Figures 2.67 to 2.70 show the averaged Reynolds stresses of the three test cases. They are strongly anisotropic with the streamwise stress being the biggest, followed by the spanwise and then the transverse one. The magnitude of the Reynolds shear stress is even smaller. It can be seen that all, the normal stresses and the shear stress, reduce when increasing the convective Mach number. The turbulent kinetic energy in Fig. 2.71 shows the same behaviour. The reduction of R_{22}, R_{33} and R_{13} is in agreement with various experiments [36, 49, 68] and DNS [63, 123]. Concerning the streamwise Reynolds stress R_{11}, different results can be found: While some experiments and DNS [63, 68] find its peak to be independent of the convective Mach number, others [49, 123] notice a decrease which is in agreement with our results.

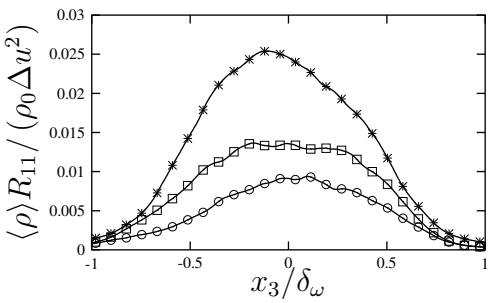

Figure 2.67: Reynolds stress $\langle \rho \rangle R_{11}$, normalized by $\rho_0 \Delta u^2$, curves as in Fig. 2.63

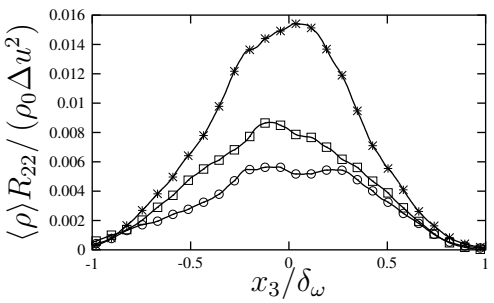

Figure 2.68: Reynolds stress $\langle \rho \rangle R_{22}$, normalized by $\rho_0 \Delta u^2$, curves as in Fig. 2.63

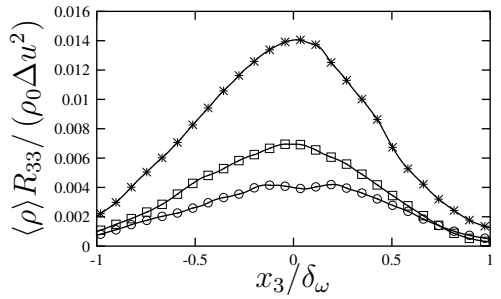

Figure 2.69: Reynolds stress $\langle\rho\rangle R_{33}$, normalized by $\rho_0\Delta u^2$, curves as in Fig. 2.63

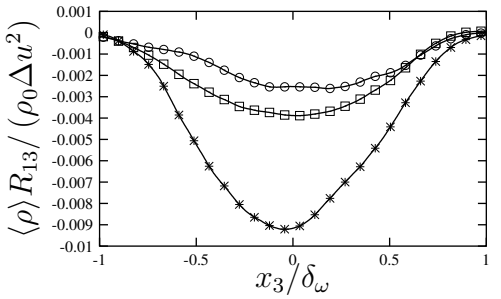

Figure 2.70: Reynolds stress $\langle\rho\rangle R_{13}$, normalized by $\rho_0\Delta u^2$, curves as in Fig. 2.63

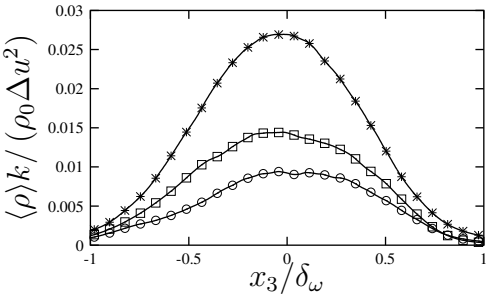

Figure 2.71: Turbulent kinetic energy $\langle\rho\rangle k$, normalized by $\rho_0\Delta u^2$, curves as in Fig. 2.63

The similar behaviour of the normal Reynolds stresses and the shear Reynolds stress with increasing convective Mach number makes the shear stress anisotropy parameter

$$b_{13} = \frac{\langle u_1'' u_3'' \rangle_f}{2k} \tag{2.39}$$

nearly independent of the convective Mach number (Fig. 2.72) which was also noticed by Vreman et al. [183]. The anisotropy parameters of the normal Reynolds stress components,

$$b_{ij} = \frac{\langle u_i'' u_j'' \rangle_f}{2k} - \frac{1}{3}\delta_{ij}, \text{ with } i = j \tag{2.40}$$

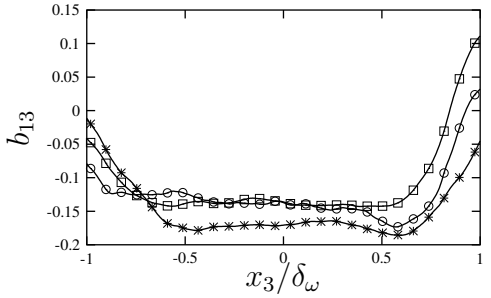

Figure 2.72: Reynolds shear stress anisotropy, b_{13}, curves as in Fig. 2.63

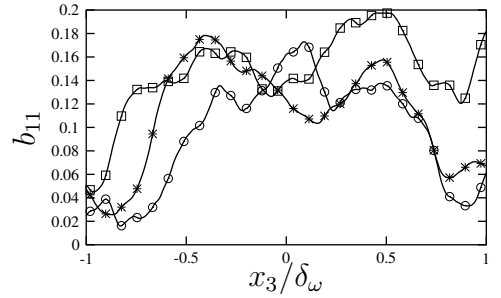

Figure 2.73: Streamwise Reynolds stress anisotropy, b_{11}, curves as in Fig. 2.63

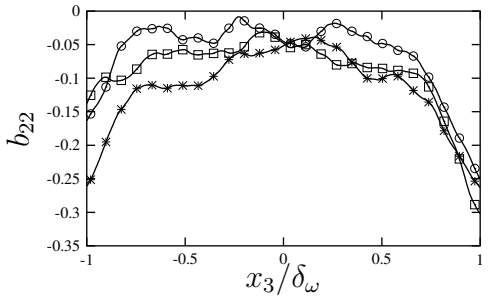

Figure 2.74: Spanwise Reynolds stress anisotropy, b_{22}, curves as in Fig. 2.63

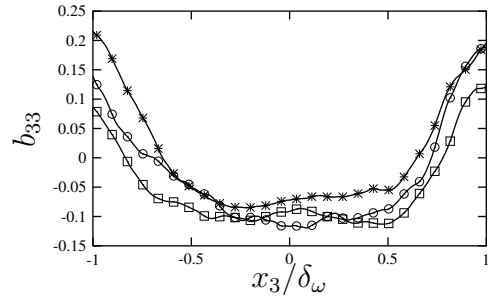

Figure 2.75: Transverse Reynolds stress anisotropy, b_{33}, curves as in Fig. 2.63

are also nearly independent of M_c (Figs. 2.73 to 2.75) which corresponds to the results of [123]. However, there are different statements concerning the consequences of compressibility with respect to the anisotropy of the Reynolds stresses in free shear flows, e.g. [183] (increase of transverse anisotropy, no effect on shear stress anisotropy) or [63] (increase of transverse anisotropy, decrease of shear stress anisotropy). Pantano & Sarkar [123] found in their DNS of turbulent compressible shear layers that all diagonal components of the Reynolds stresses, as well as the Reynolds shear stress decrease with increasing convective Mach number. They also showed in agreement with experiments [6, 155] that compressibility has only a weak influence on the anisotropy of the Reynolds stresses at least in the full turbulent, self-similar state and the Mach number range considered. In addition, Pantano & Sarkar [123] noticed that during the initial transient evolution, the anisotropy tensor is strongly affected by the convective Mach number M_c which could be a possible explanation for the discrepancies of earlier experiments and simulations.

Reynolds stress transport equations Figures 2.76 to 2.83 show the major terms of the transport equation of the Reqnolds stresses (2.28). The biggest source term in the R_{11} equation is the TKE production, the biggest sinks are the dissipation rate and the pressure-strain rate. The latter one acts to redistribute energy from the streamwise component of the Reynolds stresses, R_{11}, to the spanwise and transverse components, R_{22} and R_{33}. The pressure-strain rate is the major source term in the transport equations of these Reynolds stress components. Contrarily to R_{11}, the

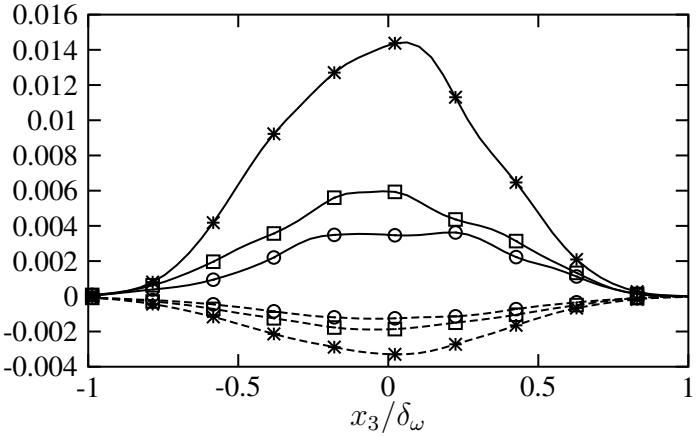

Figure 2.76: Budget of R_{11}, normalized by $\rho_0 \Delta u^3/\delta_\omega$, symbols as in Fig. 2.63, solid: production, dashed: dissipation rate

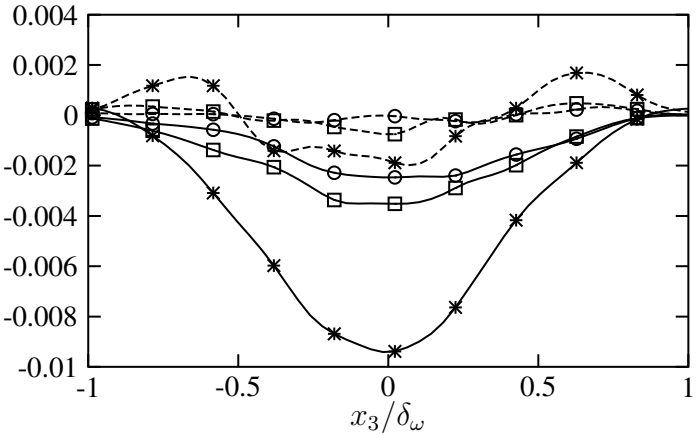

Figure 2.77: Budget of R_{11}, normalized by $\rho_0 \Delta u^3/\delta_\omega$, symbols as in Fig. 2.63, solid: pressure-strain rate, dashed: turbulent transport

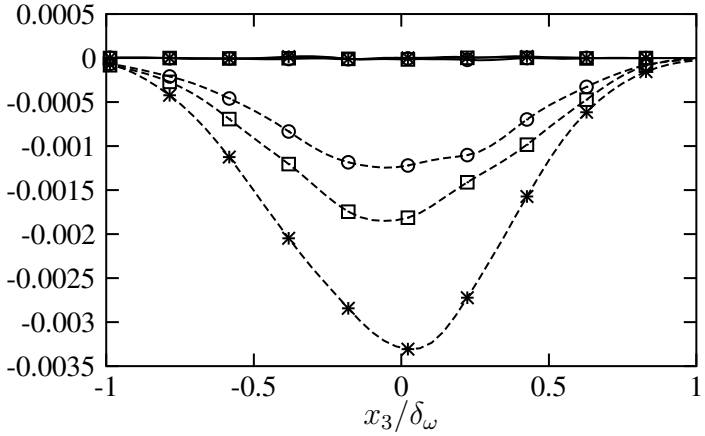

Figure 2.78: Budget of R_{22}, normalized by $\rho_0 \Delta u^3/\delta_\omega$, symbols as in Fig. 2.63, solid: production, dashed: dissipation rate

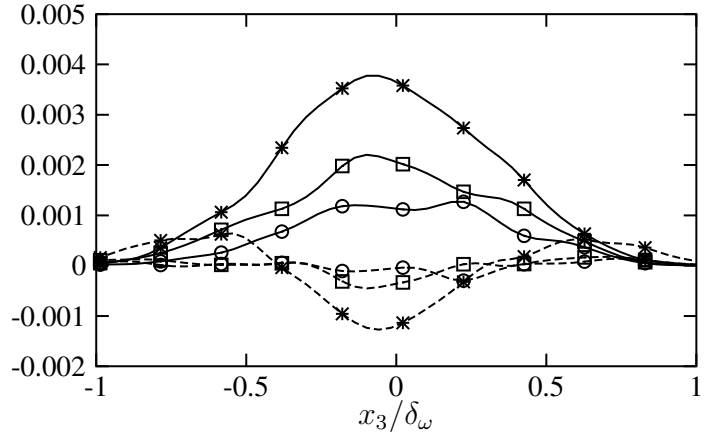

Figure 2.79: Budget of R_{22}, normalized by $\rho_0 \Delta u^3/\delta_\omega$, symbols as in Fig. 2.63, solid: pressure-strain rate, dashed: turbulent transport

production term of R_{22} and R_{33} is zero and no energy is coming directly from the mean flow. The role of the turbulent transport is the same in all diagonal Reynolds stresses: It takes energy away from the central region and transports it to the edges of the shear layer. The dissipation rates have nearly the same magnitudes in all budgets of the diagonal Reynolds stresses at each convective Mach number, respectively, which is supported by the argument that for high Reynolds numbers the turbulence, which is isotropic at small scales, implies isotropic dissipation [183].

One major effect of compressibility is to reduce the production rate of R_{11}. This is a clear consequence of the reduced Reynolds shear stress R_{13} (Fig. 2.70) as it appears as a factor in the production rate

$$P_{11} = -2R_{13}\frac{\partial \langle u_1 \rangle_f}{\partial x_3} \tag{2.41}$$

and the Favre averaged velocity profile hardly changes in particular in the center of the shear layer (Fig. 2.66). Pressure-strain rate and turbulent transport of R_{11} are also decreased with increasing convective Mach number as is the dissipation rate. This is also the case for R_{22} and R_{33}. Pantano & Sarkar [123] found the magnitude of ϵ_{11} rather independent of M_c and noticed a small decrease of ϵ_{33} which is approximately of the size of the decrease found in this study. Even though ϵ_{11} in the present test cases is not constant, it is shown later that its influence on the shear layer growth rate is small compared to the influence of the pressure-strain rate.

The major source of the Reynolds shear stress R_{13} is the production and its only major sink the pressure-strain rate (Figs. 2.82 and 2.83). As R_{13} is negative, the production is negative too and

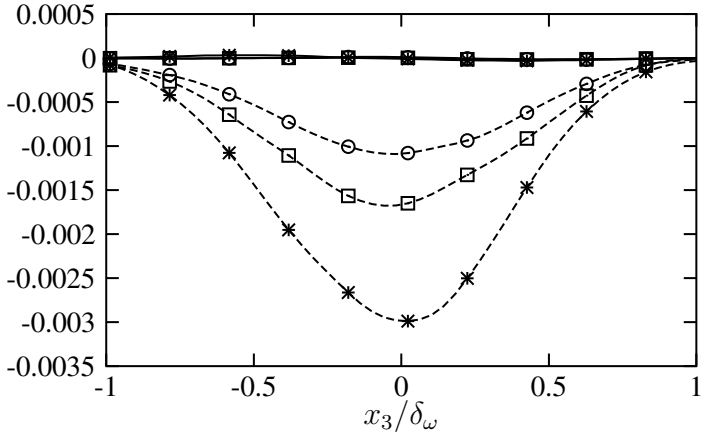

Figure 2.80: Budget of R_{33}, normalized by $\rho_0 \Delta u^3/\delta_\omega$, symbols as in Fig. 2.63, solid: production, dashed: dissipation rate

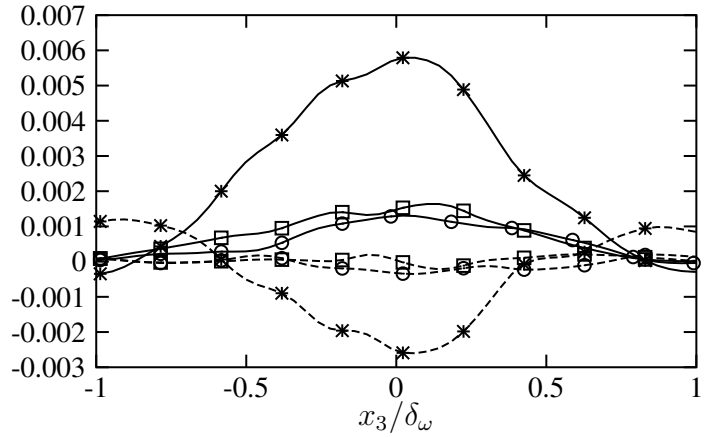

Figure 2.81: Budget of R_{33}, normalized by $\rho_0 \Delta u^3/\delta_\omega$, symbols as in Fig. 2.63, solid: pressure-strain rate, dashed: turbulent transport

the pressure-strain rate is positive. The turbulent transport oscillates around zero (for unknown reasons), and therefore its role is not as clear as for the diagonal Reynolds stresses. The fact that the dissipation rate ϵ_{13} is approximately zero is consistent with the expected isotropic dissipation at sufficiently high Reynolds numbers. The influence of compressibility on the budget terms of the Reynolds shear stress is the same as for the normal Reynolds stresses: In particular the major ones, namely production and pressure-strain rate, are decreased with increasing M_c.

Quantities integrated in the transverse direction are convenient as they are less sensitive to the sample size. They are defined in the following way (using the production P as an example):

$$\breve{P} = \int_{-\infty}^{\infty} P dx_3 \tag{2.42}$$

When integrating all budget terms this way, the following set of ordinary differential equations is obtained:

$$\begin{aligned}
\frac{\partial \langle\rho\rangle \breve{R}_{11}}{\partial t} &= \breve{P}_{11} + \breve{\Pi}_{11} + \breve{\epsilon_{11}} \\
\frac{\partial \langle\rho\rangle \breve{R}_{22}}{\partial t} &= \breve{\Pi}_{22} + \breve{\epsilon}_{22} \\
\frac{\partial \langle\rho\rangle \breve{R}_{33}}{\partial t} &= \breve{\Pi}_{33} + \breve{\epsilon}_{33} \\
\frac{\partial \langle\rho\rangle \breve{R}_{13}}{\partial t} &= \breve{P}_{13} + \breve{\Pi}_{13} + \breve{\epsilon}_{13}
\end{aligned} \tag{2.43}$$

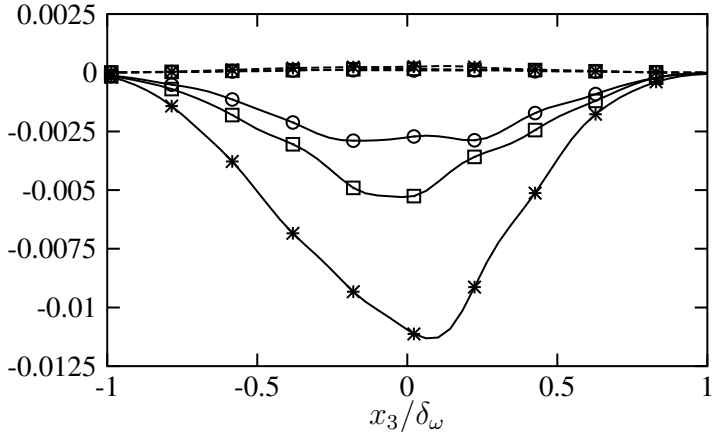

Figure 2.82: Budget of R_{13}, normalized by $\rho_0 \Delta u^3/\delta_\omega$, symbols as in Fig. 2.63, solid: production, dashed: dissipation rate

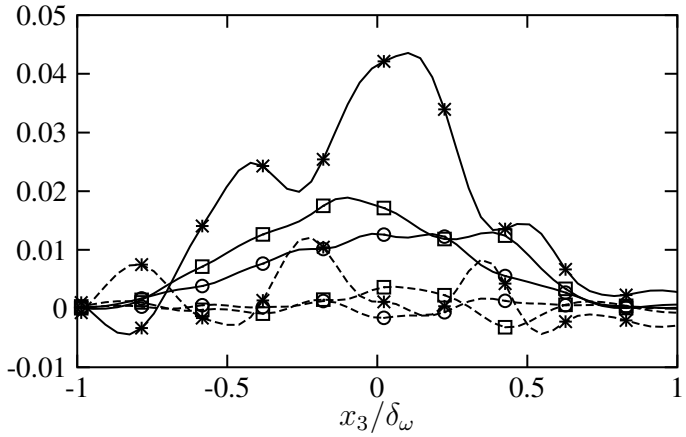

Figure 2.83: Budget of R_{13}, normalized by $\rho_0 \Delta u^3/\delta_\omega$, symbols as in Fig. 2.63, solid: pressure-strain rate, dashed: turbulent transport

as terms in divergence form vanish after integration. These or slightly modified equations where also used by other authors [183, 63, 123] for similar studies. As shown by Fig. 2.82, the shear stress dissipation can be neglected at all M_c ($|\breve{\epsilon}_{13}| < 0.04 \left|\breve{P}_{13}\right|$).

Figures 2.84 to 2.86 show the integrated normalized production, pressure-strain and dissipation rate as functions of the convective Mach number. Certain ratios of these terms are found to be independent of the Mach number and are shown in Fig. 2.87. Freund et al. [63] denoted these constant ratios for their annular mixing layer, too. From Fig. 2.87 it can be seen that a reduced growth rate at high M_c cannot be explained by an increase in the ratios of pressure-strain and production in the budget equation of R_{11} and R_{13} as these ratios are nearly constant. This has also been pointed out by Vreman et al. [183]. The figure also shows that $\breve{P}_{13} \approx 1.28\breve{\Pi}_{11}$ and $\breve{\Pi}_{13} \approx -1.13\breve{\Pi}_{11}$. Neglecting $\breve{\epsilon}_{13}$, the budget equation for $\breve{R}_{13}$ can be simplified to

$$\frac{\partial \langle\rho\rangle \breve{R}_{13}}{\partial t} = 1.28\breve{\Pi}_{11} - 1.13\breve{\Pi}_{11} = 0.15\breve{\Pi}_{11}. \tag{2.44}$$

This demonstrates that the streamwise pressure-strain rate, Π_{11} can be directly linked with the temporal development of the Reynolds shear stress. Any influences of compressibility on Π_{11} are therefore not only influencing R_{11} directly but also via its production rate P_{11} that is linked with R_{13} (Eq. (2.41)).

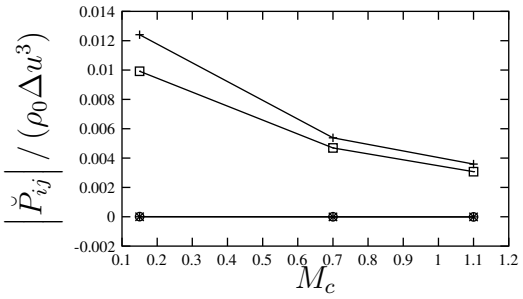

Figure 2.84: Production, integrated in transverse direction, normalized by $\rho_0 \Delta u^3$: $+$: $\breve{P}_{11}$, $\circ$: $\breve{P}_{22}$, $*$: $\breve{P}_{33}$, $\square$: $\breve{P}_{13}$

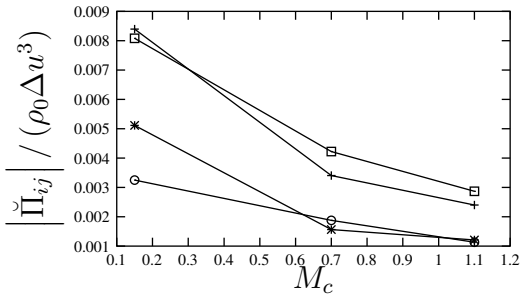

Figure 2.85: Pressure-strain rate, integrated in transverse direction, normalized by $\rho_0 \Delta u^3$: $+$: $\breve{\Pi}_{11}$, $\circ$: $\breve{\Pi}_{22}$, $*$: $\breve{\Pi}_{33}$, $\square$: $\breve{\Pi}_{13}$

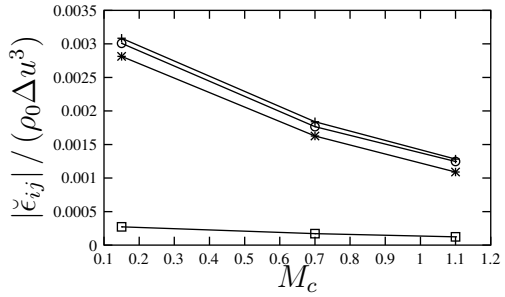

Figure 2.86: Dissipation rate, integrated in transverse direction, normalized by $\rho_0 \Delta u^3$: $+$: $\breve{\epsilon}_{11}$, $\circ$: $\breve{\epsilon}_{22}$, $*$: $\breve{\epsilon}_{33}$, $\square$: $\breve{\epsilon}_{13}$

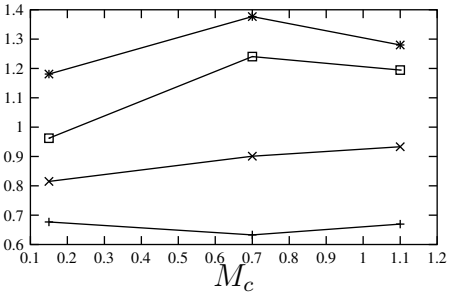

Figure 2.87: Ratios of integrated budget terms: $+$: $-\breve{\Pi}_{11}/\breve{P}_{11}$, $\times$: $-\breve{\Pi}_{13}/\breve{P}_{13}$, $*$: $\breve{P}_{13}/\breve{\Pi}_{11}$, $\square$: $-\breve{\Pi}_{13}/\breve{\Pi}_{11}$

Analysis of the reduced growth rate It is possible to directly explain the growth rate reduction from the streamwise Reynolds stress equation by establishing a relation between the pressure-strain rate and the momentum thickness. This was done in similar ways by Freund et al. [63] and Pantano & Sarkar [123].

The integrated production rate $\breve{P}_{11}$ can be related to the momentum thickness growth rate $\dot{\delta}_\theta$ by using Eq. (2.20):

$$\breve{P}_{11} = \rho_0 \Delta u^3 \dot{\delta}_\theta. \tag{2.45}$$

From Fig. 2.86 it can be seen that the factor K_ϵ in

$$\breve{\epsilon}_{11} = -K_\epsilon \rho_0 \Delta u^3 \tag{2.46}$$

is not constant in our simulation which differs from the results of Freund et al. [63]. However, later we will show that its variation is of little influence on the growth rate. The exact values of K_ϵ for each M_c are given in table 2.4.

By substituting (2.45) and (2.46) into (2.43),

$$\frac{\partial \langle\rho\rangle \breve{R}_{11}}{\partial t} = \rho_0 \Delta u^3 \left(\dot{\delta}_\theta - K_\epsilon \right) + \breve{\Pi}_{11} \tag{2.47}$$

Table 2.4: Values used in the analysis linking momentum thickness growth rate with pressure-strain rate Π_{11} for the inert test cases

M_c	K_ϵ	K_{11}	$\breve{\Pi}_{11} / (\rho_0 \Delta u^3)$
0.15	$3.0845 \cdot 10^{-3}$	$1.0543 \cdot 10^{-1}$	$-8.3972 \cdot 10^{-3}$
0.7	$1.8395 \cdot 10^{-3}$	$6.2236 \cdot 10^{-2}$	$-3.4054 \cdot 10^{-3}$
1.1	$1.2830 \cdot 10^{-3}$	$3.9643 \cdot 10^{-2}$	$-2.4020 \cdot 10^{-3}$

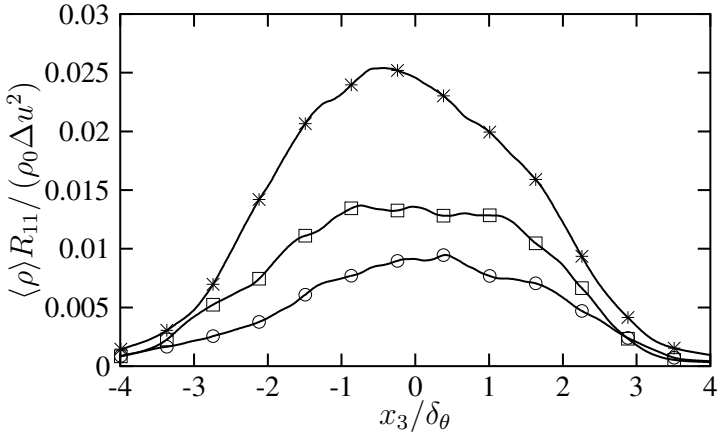

Figure 2.88: Reynolds stress $\langle\rho\rangle R_{11}$, normalized by $\rho_0\Delta u^2$, curves as in Fig. 2.63

is obtained. The integrated streamwise Reynolds stress is defined as:

$$\langle\rho\rangle\breve{R}_{11} = \int_{-\infty}^{\infty}\langle\rho\rangle R_{11}dx_3 = \rho_0\Delta u^2\delta_\theta\int_{-\infty}^{\infty}\frac{\langle\rho\rangle R_{11}}{\rho_0\Delta u^2}\frac{dx_3}{\delta_\theta} \tag{2.48}$$

Since, in our test cases, the profile of $f(\eta) = \langle\rho\rangle R_{11}/(\rho_0\Delta u^2)$ against $\eta = x_3/\delta_\theta$ is not independent of M_c, which can be seen from Fig. 2.88, K_{11} in

$$K_{11} = \frac{\langle\rho\rangle\breve{R}_{11}}{\rho_0\Delta u^2\delta_\theta} \tag{2.49}$$

is not a constant. The values of K_{11} are given in table 2.4 for the various convective Mach numbers. Substituting (2.49) into (2.47), the final expression for the normalized momentum thickness growth rate is

$$\dot{\delta}_\theta = \frac{-\breve{\Pi}_{11}/(\rho_0\Delta u^3) + K_\epsilon}{1 - K_{11}} \tag{2.50}$$

which links it with the integrated pressure-strain rate $\breve{\Pi}_{11}$. The values of the normalized integrated pressure-strain rate $\breve{\Pi}_{11}/(\rho_0\Delta u^3)$ at each M_c are given in table 2.4. Since Eq. (2.50) corresponds to Eq. (2.20), when using the values K_ϵ and K_{11} as well as $\breve{\Pi}_{11}/(\rho_0\Delta u^3)$ from table 2.4, nearly identical growth rates $\dot{\delta}_\theta$ are obtained by Eqs. (2.50) and (2.20) at each M_c, respectively. Minor discrepancies with the values given in Sect. 2.4.2 are due to rounding errors. The growth rates are also repeated in table 2.5. In order to see, whether the reduction of the momentum thickness growth rate with increasing compressibility is provoked by the changes in $\breve{\Pi}_{11}/(\rho_0\Delta u^3)$ or by the ones in K_ϵ and K_{11}, the averaged values of the latter ones, $K_\epsilon = 2.069\cdot10^{-3}$ and $K_{11} = 6.9103\cdot10^{-2}$ are used, along with the exact values of $\breve{\Pi}_{11}/(\rho_0\Delta u^3)$ to compute $\dot{\delta}_{\theta,1}$ which is given together with its relative error (error 1) in table 2.5. In a next step, the exact K_ϵ and K_{11} from 2.4 but the averaged $\breve{\Pi}_{11}/(\rho_0\Delta u^3) = -4.7349\cdot10^{-3}$ is used. This gives $\dot{\delta}_{\theta,2}$ with a relative error

Table 2.5: Actual and approximated momentum thickness growth rates and relative errors for the inert test cases

M_c	$\dot{\delta}_\theta$	$\dot{\delta}_{\theta,1}$	$\dot{\delta}_{\theta,2}$	error 1	error2
0.15	$1.2835\cdot10^{-2}$	$1.1243\cdot10^{-2}$	$8.7409\cdot10^{-3}$	12.4%	31.9%
0.7	$5.5930\cdot10^{-3}$	$5.8808\cdot10^{-3}$	$7.0107\cdot10^{-3}$	5.1%	25.3%
1.1	$3.8371\cdot10^{-3}$	$4.8029\cdot10^{-3}$	$6.2663\cdot10^{-3}$	25.2%	63.3%

(error 2) that is given in table 2.5, too. Comparing the errors, one can see that the influence of the variation of the pressure-strain rate with compressibility has a much greater influence than the variation of K_ϵ and K_{11} which include the influences of dissipation rate and streamwise Reynolds stress. This is particularly true for the highest Mach number.

Pressure-strain terms There are three, maybe simultaneously occuring possibilities, how the pressure-strain rate

$$\Pi_{11} = 2\langle p' \frac{\partial u_1''}{\partial x_1} \rangle \tag{2.51}$$

might be reduced: Either by a reduction of the pressure fluctuations p', by a reduction of the strain rate fluctuations $\partial u_1''/\partial x_1$ or by a reduction of their correlation coefficient. It is demonstrated in the following as an example for the streamwise component of the pressure-strain rate tensor which one of these possibilities is the most plausible one.

Figure 2.89 shows the rms value of the pressure fluctuations, Fig. 2.90, the rms value of strain rate fluctuations and Fig. 2.91, the correlation coefficient of both fluctuations,

$$R\left(p, \partial u_1/\partial x_1\right) = \frac{\langle p' \partial u_1''/\partial x_1 \rangle}{p_{rms}\left(\partial u_1/\partial x_1\right)_{rms}}. \tag{2.52}$$

It is visible that the pressure fluctuations reduce much more with increasing compressibility than the fluctuations of the strain rate and that the correlation coefficient remains small for all M_c, which suggests that the reduction of the pressure fluctuations is primarily responsible for the reduced pressure-strain rates. This is confirmed by Fig. 2.92 which presents the relative reduction of the integrated rms value of p', of the integrated rms value of $\partial u_1''/\partial x_1$ and the integrated

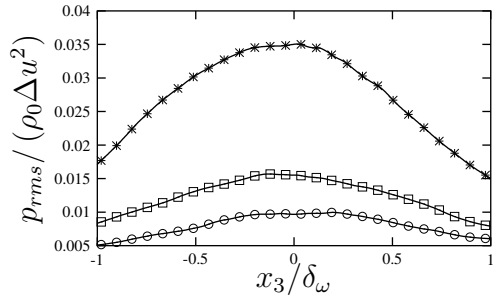

Figure 2.89: Rms value of p', normalized by $\rho_0 \Delta u^2$, curves as in Fig. 2.63

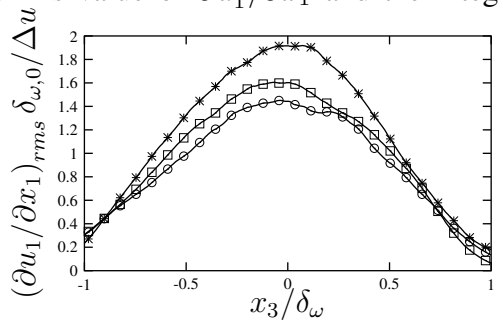

Figure 2.90: Rms value of $\partial u_1''/\partial x_1$, normalized by $\delta_{\omega,0}/\Delta u$, curves as in Fig. 2.63

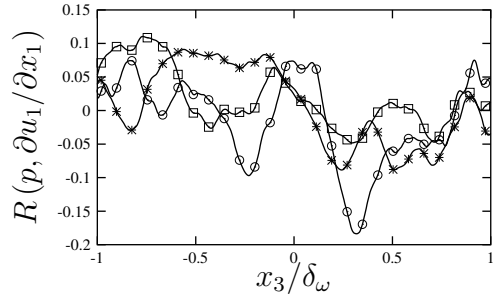

Figure 2.91: Correlation coefficient $R\left(p, \partial u_1/\partial x_1\right)$ between pressure and density fluctuations, curves as in Fig. 2.63

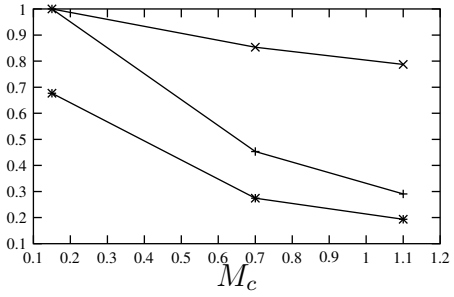

Figure 2.92: Suppression of integrated p_{rms} $(+)$, integrated $\left(\partial u_1''/\partial x_1\right)_{rms}$ $(\times)$ and integrated pressure-strain rate $|\Pi_{11}|$ $(*)$, normalized by the respective incompressible value at $M_c = 0.15$

pressure-strain rate $|\Pi_{11}|$: The pressure fluctuations are the predominant reason for the reduced pressure-strain rate since they are reduced in a similar manner with increasing M_c. The strain rate fluctuations are also reduced for increasing M_c but to a lesser extent. Similar results are obtained for the other components of the pressure-strain rate tensor (not shown). The reduction of the pressure-strain rates with increasing M_c is further investigated in Sect. 2.4.4.1.

TKE transport equation The major terms of the transport equation for the TKE, Eq. (2.27), are shown in Figs. 2.93 and 2.94. The major source term, namely production, is reduced with increasing Mach number. The turbulent transport acts as a sink in the middle of the shear layer and as a source at its edges. It therefore moves kinetic energy away from the region of highest shear, where it is produced, to regions of less production. The pressure dilatation is very small. This means that the pressure-strain tensor is nearly trace free, and that its major role is to redistribute energy from the streamwise component of the Reynolds stress to the spanwise and transverse components the transport equations of which have no production terms. Figure 2.95 shows the ratio of the integrated pressure dilatation term, $\breve{\Pi}$ and the production term $\breve{P}$ against M_c. Its magnitude increases with increasing M_c, which is partially due to the reduced production at high M_c and remains small in total. The dissipation rate, the major sink in the TKE transport equation, is also reduced by compressibility (Fig. 2.94), however not as much as the production rate. This can be seen from Fig. 2.96 which shows that the magnitude of the ratio of the dissipation rate with respect to the production increases with increasing M_c.

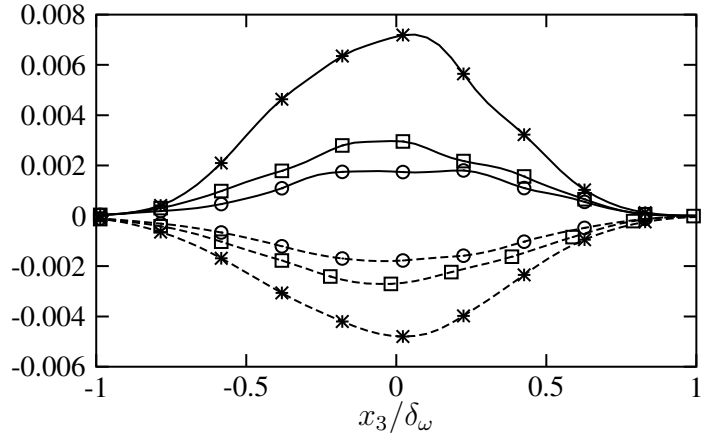

Figure 2.93: Budget of $\langle\rho\rangle k$, normalized by $\rho_0\Delta u^3/\delta_\omega$, symbols as in Fig. 2.63, solid: production, dashed: dissipation rate

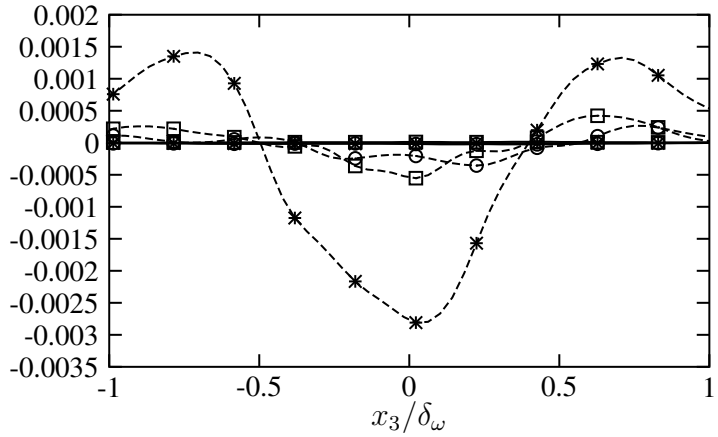

Figure 2.94: Budget of $\langle\rho\rangle k$, normalized by $\rho_0\Delta u^3/\delta_\omega$, symbols as in Fig. 2.63, solid: pressure dilatation, dashed: turbulent transport

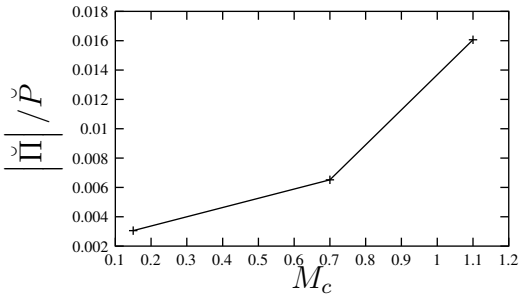

Figure 2.95: Ratio of the integrated pressure dilatation and the TKE production versus M_c

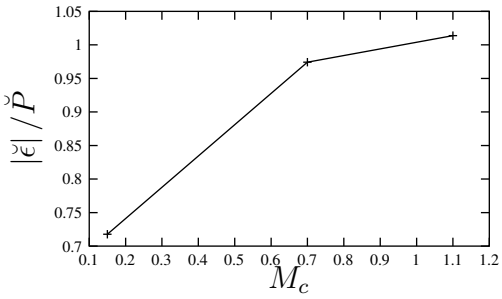

Figure 2.96: Ratio of the integrated dissipation rate and the TKE production versus M_c

To further investigate the influence of compressibility on ϵ, it can be split up into three parts

$$\epsilon = \epsilon_1 + \epsilon_2 + \epsilon_3 \tag{2.53}$$

with

$$\begin{aligned}
\epsilon_1 &= -2\langle\mu\rangle\langle s'_{ij}s'_{ij}\rangle + \frac{2}{3}\langle\mu\rangle\langle s'_{kk}s'_{ll}\rangle, \\
\epsilon_2 &= -2\langle\mu' s'_{ij}s'_{ij}\rangle + \frac{2}{3}\langle\mu' s'_{kk}s'_{ll}\rangle, \\
\epsilon_3 &= -2\langle\mu' s'_{ij}\rangle\langle s_{ij}\rangle + \frac{2}{3}\langle\mu' s'_{kk}\rangle\langle s_{ll}\rangle
\end{aligned} \tag{2.54}$$

where $\langle s_{ij}\rangle$ is the strain rate tensor,

$$\langle s_{ij}\rangle = \frac{1}{2}\left(\frac{\partial\langle u_i\rangle}{\partial x_j} + \frac{\partial\langle u_j\rangle}{\partial x_i}\right) \tag{2.55}$$

and s'_{ij} the fluctuating strain rate tensor

$$s'_{ij} = \frac{1}{2}\left(\frac{\partial u'_i}{\partial x_j} + \frac{\partial u'_j}{\partial x_i}\right). \tag{2.56}$$

The part ϵ_1 can be split up again into three parts, in a quasi-incompressible, 'solenoidal' part ϵ_s, a dilatational part ϵ_d and an inhomogeneous part ϵ_I:

$$\epsilon_1 = \epsilon_s + \epsilon_d + \epsilon_I \tag{2.57}$$

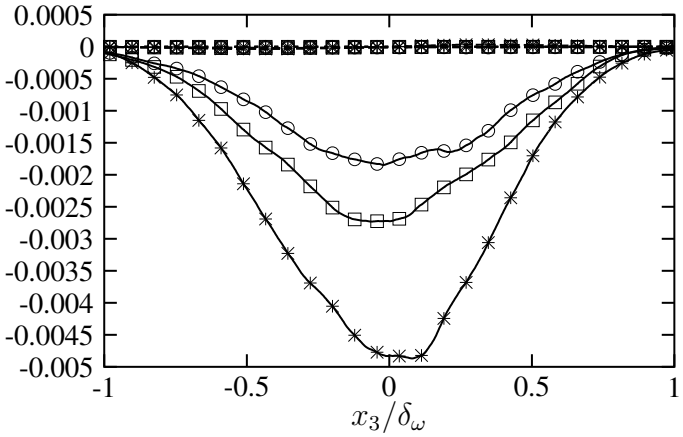

Figure 2.97: Decomposition of TKE dissipation rate, normalized by $\rho_0\Delta u^3/\delta_\omega$, symbols as in Fig. 2.63, solid: ϵ_1, dashed: ϵ_2, dotted: ϵ_3

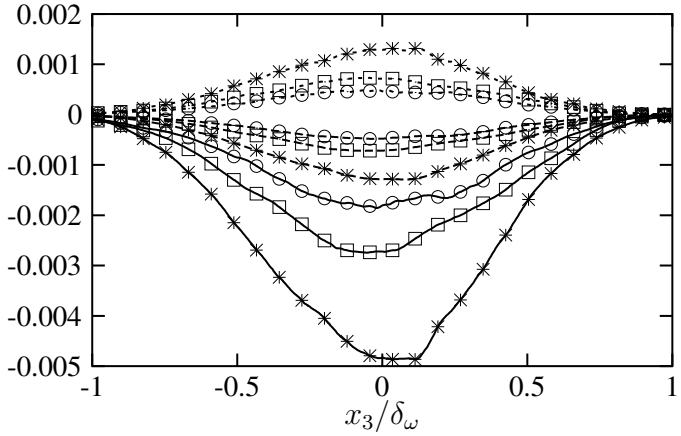

Figure 2.98: Decomposition of ϵ_1, normalized by $\rho_0 \Delta u^3/\delta_\omega$, symbols as in Fig. 2.63, solid: ϵ_s, dashed: ϵ_d, dotted: ϵ_I

with

$$\begin{aligned}
\epsilon_s &= -\langle\mu\rangle\langle\omega_i'\omega_i'\rangle, \\
\epsilon_d &= -\frac{4}{3}\langle\mu\rangle\langle s_{kk}' s_{ll}'\rangle, \\
\epsilon_I &= -2\langle\mu\rangle\left(\frac{\partial^2}{\partial x_i \partial x_j}\langle u_i' u_j'\rangle - 2\frac{\partial}{\partial x_i}\langle u_i'\frac{\partial u_j'}{\partial x_j}\rangle\right).
\end{aligned} \tag{2.58}$$

Here, the fluctuating vorticity is denoted by

$$\omega_i' = \epsilon_{ijk}\frac{\partial u_k'}{\partial x_j}. \tag{2.59}$$

In an incompressible flow only

$$\epsilon = \epsilon_s + \epsilon_I = -\mu\langle\omega_i'\omega_i'\rangle - 2\mu\frac{\partial^2}{\partial x_i \partial x_j}\langle u_i' u_j'\rangle \tag{2.60}$$

would remain as there are no fluctuations of viscosity and dilatation. Figures 2.97 and 2.98 show the terms of this decomposition. It can be seen that for all M_c, the part ϵ_1 is the largest one and ϵ_2 and ϵ_3 are negligible. The biggest contribution to ϵ_1 comes from the solenoidal dissipation rate ϵ_s. However, the other parts are not negligible but have opposite signs and nearly cancel each other out. ϵ_1 as well as all of its parts, ϵ_s, ϵ_d and ϵ_I, are influenced by compressibility and reduced in their magnitude. The ratio of the integrated dilatational dissipation rate and the solenoidal dissipation rate as well as the ratio of the integrated and the total dissipation rate decrease with increasing compressibility (Figs. 2.99 and 2.100) which acts contrarily to the observed stabilizing effect of compressibility. However in total, the changes are very small and therefore of limited influence.

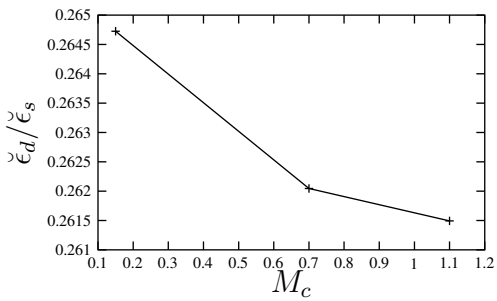

Figure 2.99: Ratio of the integrated compressible and solenoidal dissipation rates versus M_c

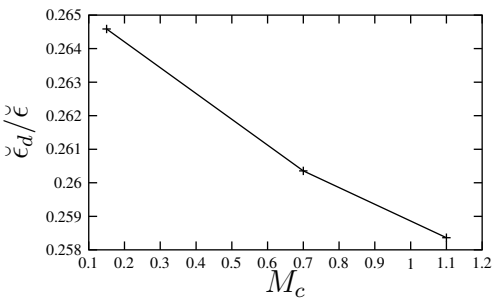

Figure 2.100: Ratio of the integrated dilatational and total dissipation rates versus M_c

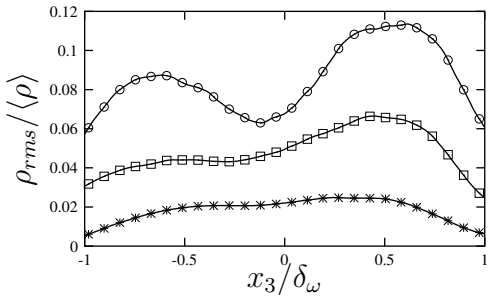

Figure 2.101: Rms value of the density fluctuations, normalized by $\langle\rho\rangle$, symbols as in Fig. 2.63

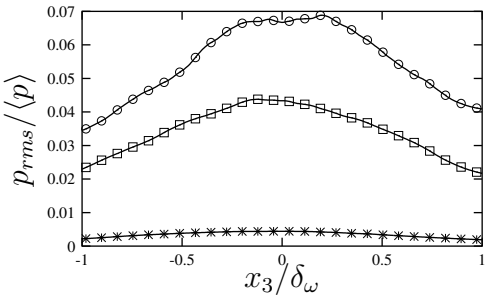

Figure 2.102: Rms value of the pressure fluctuations, normalized by $\langle p\rangle$, symbols as in Fig. 2.63

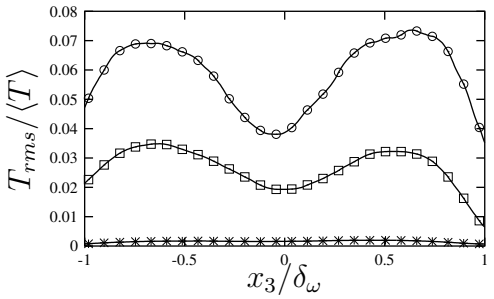

Figure 2.103: Rms value of the temperature fluctuations, normalized by $\langle T\rangle$, symbols as in Fig. 2.63

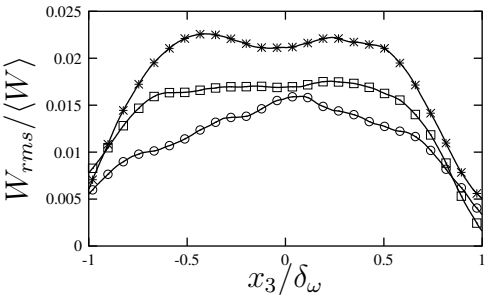

Figure 2.104: Rms value of the molecular weight fluctuations, normalized by $\langle W\rangle$, symbols as in Fig. 2.63

Thermodynamic fluctuations The first order relation

$$\frac{\rho'}{\langle\rho\rangle} = \frac{p'}{\langle p\rangle} - \frac{T'}{\langle T\rangle} + \frac{W'}{\langle W\rangle} \tag{2.61}$$

is derived from the equation of state for gas mixtures (2.5). The corresponding rms values are shown in Figs. 2.101 to 2.104. For the inert compressible flow, case inert-0.7, density fluctuations are of acoustic and entropic nature. The latter comprises fluctuations in temperature and molecular weight. The fluctuations of the molecular weight are reduced by compressibility as a result of reduced mixing and the corresponding rms profiles change shape with increasing compressibility (cf. Sect. 2.4.4.2). Normalizing the pressure rms value with its mean value as done in Fig. 2.102, it is increasing as a consequence of compressibility which is on the contrast to the reduction that can be observed when normalizing by $\rho_0\Delta u^2$ (Fig. 2.89). However, when considering that the normalized averaged pressure $\langle p\rangle/\left(\rho_0\Delta u^2\right)$ decreases with γM_c^2 (Fig. 2.65), it becomes clear that the pressure fluctuations with the same normalization (as in Fig. 2.89) must also decrease in

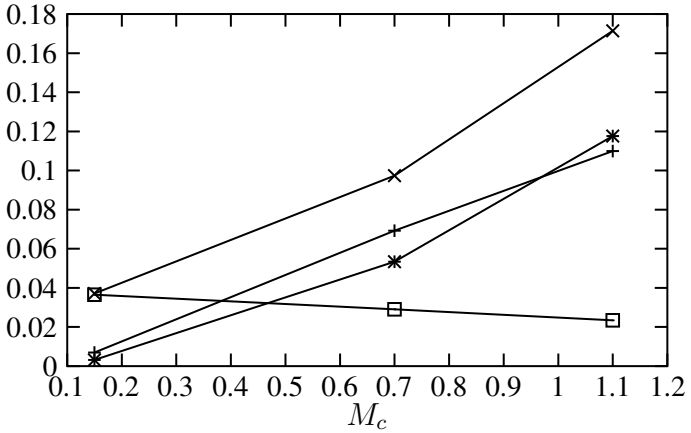

Figure 2.105: Integrated rms values, $+$: $p_{rms}/\langle p\rangle$, $\times$: $\rho_{rms}/\langle\rho\rangle$, $*$: $T_{rms}/\langle T\rangle$, $\square$: $W_{rms}/\langle W\rangle$

order to avoid negative pressure.

Figure 2.105 directly shows the dependence of the thermodynamic fluctations on M_c which is obtained after integrating the profiles in the Figs. 2.101 to 2.104 in the transverse direction. One can see that at all Mach numbers the density fluctuations are the most important ones. Density, pressure and temperature fluctuations increase with increasing compressibility and the temperature fluctuations which are smaller than the pressure fluctuations at $M_c = 0.15$ and $M_c = 0.7$ become bigger than those at $M_c = 1.1$. The rms value of the molecular weight decreases slightly with increasing M_c.

A further quantification of the relation between the pressure and the density fluctuations and the influence of acoustic effects is obtained by a decomposition of the density and temperature fluctuations into acoustic and entropic parts as suggested by Sarkar [163]:

$$\begin{aligned} \rho' &= \rho'^{ac} + \rho'^{en} \\ T' &= T'^{ac} + T'^{en} \\ p' &= p'^{ac} \\ \rho'^{ac} &= \frac{p'^{ac}}{\langle c \rangle^2} \\ T'^{ac} &= \frac{\gamma - 1}{\gamma} \frac{T p'}{p} \end{aligned} \tag{2.62}$$

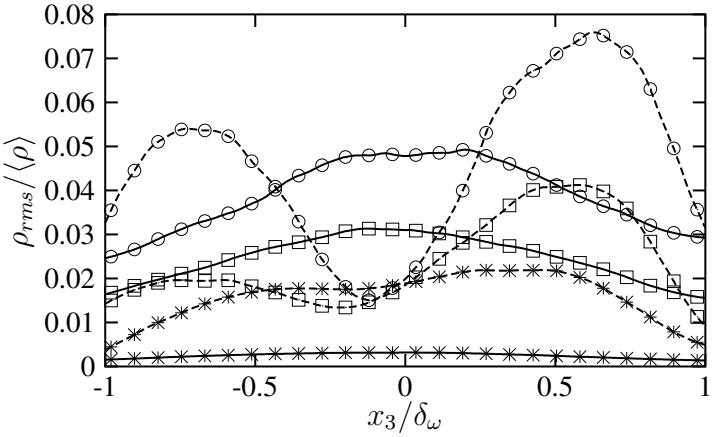

Figure 2.106: Acoustic (solid line) and entropic part (dashed line) of the density fluctuations, normalized by $\langle\rho\rangle$, symbols as in Fig. 2.63

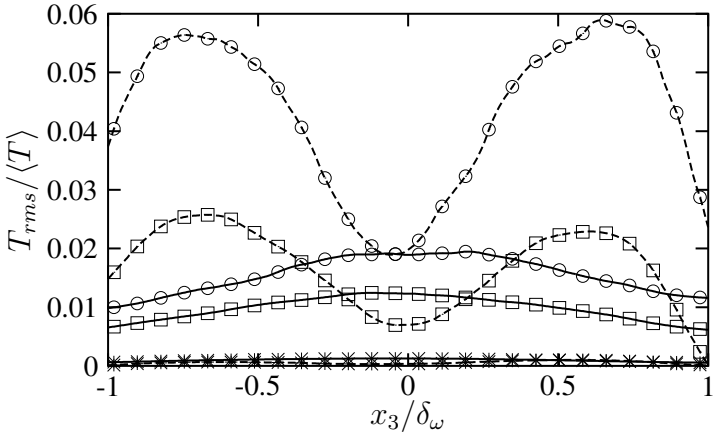

Figure 2.107: Acoustic (solid line) and entropic part (dashed line) of the temperature fluctuations, normalized by $\langle T\rangle$, symbols as in Fig. 2.63

The corresponding rms values for the test cases are shown in Figs. 2.106 and 2.107. While both, acoustic and entropic mode contribute to the density fluctuations in inert shear layers at high Mach numbers, the entropic fluctuations prevail at $M_c = 0.15$. Both, the temperature fluctuations of the acoustic and entropic part are small at $M_c = 0.15$ and increase for higher M_c. While the acoustic fluctuations of density and temperature have their maxima in the center of the shear layer, the maxima of the entropic fluctuations are located at its edges where the free-stream fluid is mixed into the layer. However, it has to be noted that the decomposition in Eqs. (2.62) is not unique and that it is based on the assumption that all pressure fluctuations are of acoustic nature.

Correlations of thermodynamic fluctuations The correlation coefficient of the density and pressure fluctuations

$$R(\rho, p) = \frac{\langle \rho' p' \rangle}{\rho_{rms} p_{rms}}, \tag{2.63}$$

is shown in Fig. 2.108. The coefficient fluctuates around zero for the inert-0.15 case. This is in agreement with the small acoustic part of the density and temperature fluctuations found previously. However, there is a stronger correlation $R(\rho, p) \approx 0.8$ for the simulations inert-0.7 and inert-1.1 which indicates that acoustic effects become more important with the pressure fluctuations traveling at the speed of sound. When neglecting viscous terms, the isentropic relationship

$$\frac{Dp}{Dt} = c^2 \frac{D\rho}{Dt} \tag{2.64}$$

applies. Pantano & Sarkar [123] used this to derive a convective wave equation for the pressure fluctuations. Ananlyzing this equation, they found the reason for the reduction of the pressure-strain terms at high Mach number within the central part of the inert mixing layer: The finite speed of sound in compressible flows introduces a finite time delay in the transmission of pressure-strain signals from one point to an adjacent point, and the resultant increase in decorrelation leads to a reduction in the pressure-strain correlation.

At low M_c, the density fluctuations are correlated with the molecular weight as shows the correlation coefficient

$$R(\rho, W) = \frac{\langle \rho' W' \rangle}{\rho_{rms} W_{rms}} \tag{2.65}$$

in Fig. 2.109. This is in agreement with the entropic density fluctuations being more important than the acoustic ones (Fig. 2.106).

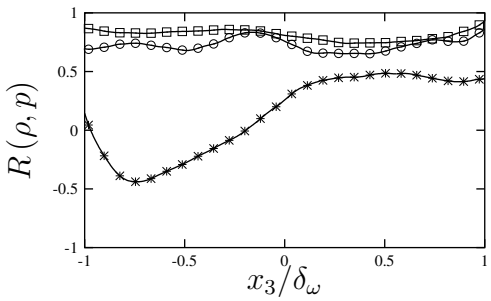

Figure 2.108: Correlation coefficient $R(\rho, p)$ between pressure and density fluctuations, symbols as in Fig. 2.63

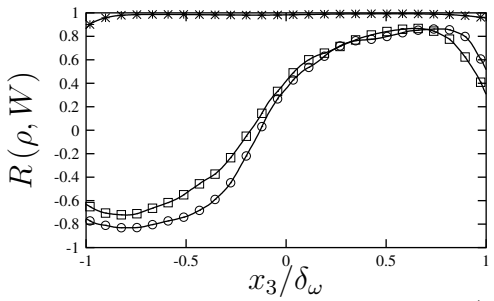

Figure 2.109: Correlation coefficient $R(\rho, W)$ between pressure and molecular weight fluctuations, symbols as in Fig. 2.63

Behaviour of the pressure-strain correlations In the following it is analyzed why compressibility decreases the pressure fluctuations when normalizing by $\rho_0 \Delta u^2$ as done in Fig. 2.89 and why this entails a reduction of the pressure-strain correlations. To do so, an equation determining the pressure fluctuations is derived. It is shown that when acoustic influences on the pressure fluctuations can be neglected, this equation takes the form of a Poisson equation. Then, correlations with the pressure (pressure-strain correlations, pressure scrambling terms) can be computed with the help of a Green function which gives further insight into the various contributions to these terms and reasons for their changes. By a similar procedure, Kim [89] investigated pressure-strain correlations in a channel flow, and Foysi [61] and Foysi et al. [60] showed that mean density effects lead to a reduction of pressure fluctuations in a channel with cooled walls.

Starting point of the derivation is the following equation for the pressure:

$$\frac{\partial^2 p}{\partial x_i \partial x_i} = -\frac{\partial^2 \left(\rho u_i u_j\right)}{\partial x_i \partial x_j} + \frac{\partial^2 \tau_{ij}}{\partial x_i \partial x_j} + 2u_i \frac{\partial^2 \left(\rho u_j\right)}{\partial x_i \partial x_j} - u_i u_j \frac{\partial^2 \rho}{\partial x_i \partial x_j} + \frac{D^2 \rho}{Dt^2} \tag{2.66}$$

This equation is exact for compressible and reacting flows. It is obtained by taking the divergence of the momentum equation and inserting the continuity equation. When taking the statistical average of Eq. (2.66) and subtracting it from Eq. (2.66), one obtains the following equation for

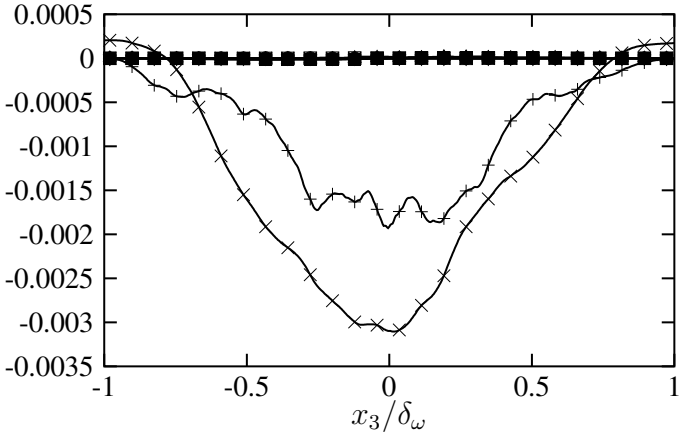

Figure 2.110: Case inert-0.15: Parts of the pressure-strain correlation Π_{11} computed with the Green function, normalized by $\rho_0 \Delta u^3/\delta_\omega$, +: $f = f(A_1)$, ×: $f = f(A_2)$, ∗: $f = f(A_3)$, □: $f = f(A_4)$, ■: $f = f(B_1)$, ○: $f = f(B_2)$, ●: $f = f(B_3)$, △: $f = f(C_1)$, ▲: $f = f(C_2)$, ▽: $f = f(C_3)$, ▼: $f = f(C_4)$, ◇: $f = f(C_5)$

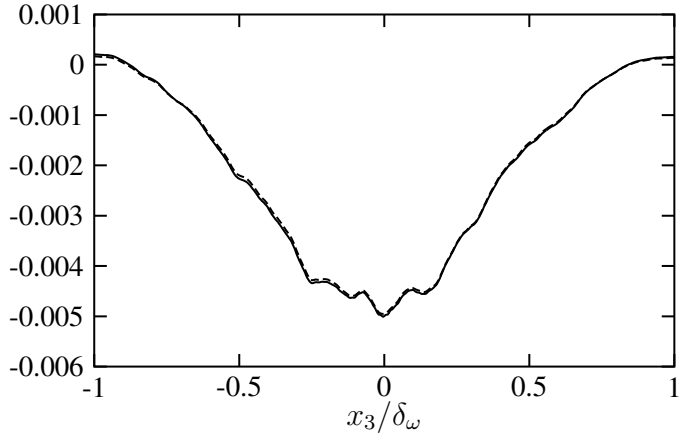

Figure 2.111: Case inert-0.15: Pressure-strain correlation Π_{11}, normalized by $\rho_0 \Delta u^3/\delta_\omega$, solid: computed with the help of the Green function with $f = f\left(\sum_{i=1}^{4} A_i + \sum_{i=1}^{3} B_i + \sum_{i=1}^{5} C_i\right)$, dashed: computed exactly

the pressure fluctuations:

$$\begin{aligned}\frac{\partial^2 p'}{\partial x_j^2} =& -2\frac{\partial\langle u_i\rangle_f}{\partial x_j}\frac{\partial}{\partial x_i}\left(\langle\rho\rangle u_j''\right) - 2\frac{\partial\langle u_i\rangle_f}{\partial x_i}\frac{\partial}{\partial x_j}\left(\langle\rho\rangle u_j''\right) - \frac{\partial^2}{\partial x_i\partial x_j}\left(\langle\rho\rangle u_i''u_j'' - \langle\rho u_i''u_j''\rangle\right)\\ &- 2\langle\rho\rangle u_j''\frac{\partial^2\widetilde{u}_i}{\partial x_i\partial x_j} - \rho'\left(\frac{\partial\langle u_i\rangle_f}{\partial x_i}\right)^2 - \rho'\frac{\partial\langle u_i\rangle_f}{\partial x_j}\frac{\partial\langle u_j\rangle_f}{\partial x_i}\\ &- 2\frac{\partial\langle u_i\rangle_f}{\partial x_j}\frac{\partial}{\partial x_i}\left(\rho' u_j''\right) - 2\frac{\partial\langle u_i\rangle_f}{\partial x_i}\frac{\partial}{\partial x_j}\left(\rho' u_j''\right) - 2\frac{\partial^2\langle u_i\rangle_f}{\partial x_i\partial x_j}\left(\rho' u_j''\right)\\ &- \frac{\partial^2}{\partial x_i\partial x_j}\left(\rho' u_i''u_j''\right) + \frac{\overline{D}^2\rho'}{\overline{D}t^2} + \frac{\partial^2\tau_{ij}'}{\partial x_i\partial x_j}\end{aligned} \tag{2.67}$$

For a fully developed turbulent flow that is periodic in x_1- and x_2-directions this equation simplifies to

$$\begin{aligned}\frac{\partial^2 p'}{\partial x_j^2} =& \underbrace{-\langle\rho\rangle\frac{\partial^2}{\partial x_i x_j}\left(u_i''u_j'' - \langle u_i''u_j''\rangle\right)}_{A_1}\underbrace{-2\langle\rho\rangle\frac{\partial\langle u_1\rangle_f}{\partial x_3}\frac{\partial u_3''}{\partial x_1}}_{A_2}\\ &\underbrace{-2\langle\rho\rangle\frac{\partial\langle u_3\rangle_f}{\partial x_3}\left(\frac{\partial u_1''}{\partial x_1} + \frac{\partial u_2''}{\partial x_2} + 2\frac{\partial u_3''}{\partial x_3}\right)}_{A_3}\underbrace{-2\langle\rho\rangle\frac{\partial^2\langle u_3\rangle_f}{\partial x_3^2}u_3''}_{A_4}\\ &\underbrace{-2\frac{\partial\langle\rho\rangle}{\partial x_3}\frac{\partial}{\partial x_j}\left(u_3''u_j'' - \langle u_3''u_j''\rangle\right)}_{B_1}\underbrace{-\frac{\partial^2\langle\rho\rangle}{\partial x_3^2}\left(u_3''^2 - \langle u_3''^2\rangle\right)}_{B_2}\underbrace{-4u_3''\frac{\partial\langle\rho\rangle}{\partial x_3}\frac{\partial\langle u_3\rangle_f}{\partial x_3}}_{B_3}\\ &\underbrace{-2\frac{\partial\langle u_1\rangle_f}{\partial x_3}\frac{\partial}{\partial x_1}\left(\rho' u_3''\right)}_{C_1}\underbrace{-\frac{\partial^2}{\partial x_i\partial x_j}\left(\rho' u_i''u_j'' - \langle\rho' u_i''u_j''\rangle\right)}_{C_2}\\ &\underbrace{-2\frac{\partial\langle u_3\rangle_f}{\partial x_3}\left(\frac{\partial}{\partial x_1}\left(\rho' u_1''\right) + \frac{\partial}{\partial x_2}\left(\rho' u_2''\right) + 2\frac{\partial}{\partial x_3}\left(\rho' u_3''\right)\right)}_{C_3}\\ &\underbrace{-2\rho'\left(\frac{\partial\langle u_3\rangle_f}{\partial x_3}\right)^2}_{C_4}\underbrace{-2\rho' u_3''\frac{\partial^2\langle u_3\rangle_f}{\partial x_3^2}}_{C_5}\underbrace{+\frac{\overline{D}^2\rho'}{\overline{D}t^2}}_{C_6}\underbrace{+\frac{\partial^2\tau_{ij}'}{\partial x_i\partial x_j}}_{D}.\end{aligned} \tag{2.68}$$

The operator $\overline{D}^2/\overline{D}t^2$ is defined as

$$\frac{\overline{D}^2}{\overline{D}t^2} := \frac{\partial^2}{\partial t^2} + 2\langle u_j\rangle_f\frac{\partial^2}{\partial t\partial x_j} + \langle u_i\rangle_f\langle u_j\rangle_f\frac{\partial^2}{\partial x_i\partial x_j}. \tag{2.69}$$

The terms on the RHS of Eq. (2.68) can be classified into terms that depend explicitly on the mean density (A_1 to A_4), terms that depend on gradients of the mean density (B_1 to B_3), terms that are caused by temporal and spatial variations of the density fluctuations with or without direct coupling to the velocity fluctuations (C_1 to C_6) and a term that is caused by viscous effects (D). The latter one is very small for the flows considered in this work and is neglected in the following. The terms A_1 to A_4 are the only ones that are present in an incompressible case (constant density). If considering the complete term C_6 and assuming the isentropic relation $p' = \langle c\rangle^2\rho'$, a convective wave equation for the pressure fluctuations is obtained [123]. For the inert shear layers studied

here, term C_6 turns out to be small according to DNS data. This makes Eq. (2.68) a Poisson equation for the pressure fluctuations.

The Poisson equation for p' can be studied with the help of a Green function in order to obtain information about the contribution of the individual terms on the RHS. Applying a Fourier transformation in the homogeneous directions, $p\left(x_1, x_2, x_3\right) \rightarrow \hat{p}\left(k_1, k_2, x_3\right)$, and a coordinate transformation in the transverse direction, $x_3' = 2x_3/L_3$, Eq. (2.68) becomes

$$\left(\frac{d^2}{dx_3'^2} - k_1^2 - k_2^2\right) \hat{p}\left(k_1, k_2, x_3'\right) = \hat{f}\left(k_1, k_2, x_3'\right) \tag{2.70}$$

with f denoting the terms on the RHS of Eq. (2.68). It is assumed that the gradients of the pressure fluctuations at the boundary of the computational domain, which is sufficiently far away from the mixing layer, are small. Therefore,

$$\left.\frac{\partial \hat{p}}{\partial x_3'}\right|_{x_3'=\pm 1} = 0. \tag{2.71}$$

The Green function corresponding to Eqs. (2.70) and (2.71) is [89]:

$$\begin{aligned}
\hat{G}\left(k, x_3', x_3''\right) &= -\frac{\cosh\left[k\left(x_3''-1\right)\right]\cosh\left[k\left(x_3'+1\right)\right]}{2k\cosh\left(k\right)\sinh\left(k\right)}, \text{ for } x_3' < x_3'' \\
\hat{G}\left(k, x_3', x_3''\right) &= -\frac{\cosh\left[k\left(x_3''+1\right)\right]\cosh\left[k\left(x_3'-1\right)\right]}{2k\cosh\left(k\right)\sinh\left(k\right)}, \text{ for } x_3' > x_3''
\end{aligned} \tag{2.72}$$

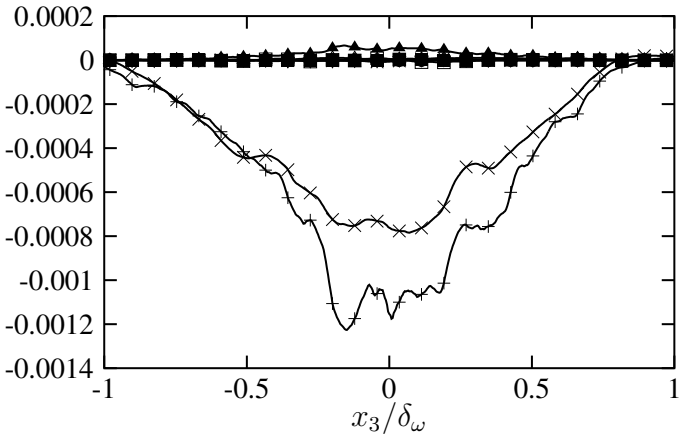

Figure 2.112: Case inert-0.7: Parts of the pressure-strain correlation Π_{11} computed with the Green function, normalized by $\rho_0 \Delta u^3/\delta_\omega$, symbols as in Fig. 2.110

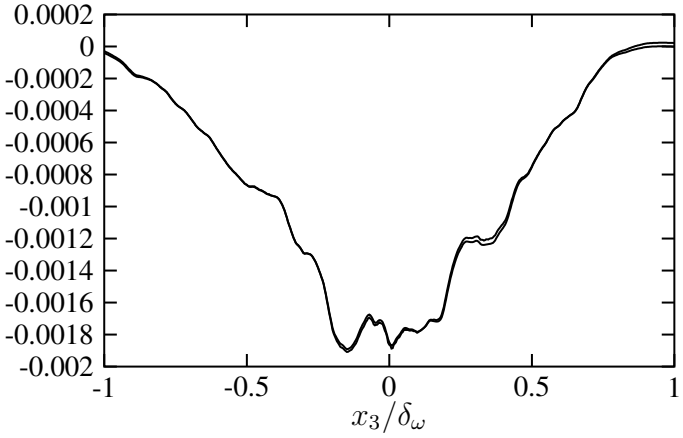

Figure 2.113: Case inert-0.7: Pressure-strain correlation Π_{11}, normalized by $\rho_0 \Delta u^3/\delta_\omega$, solid: computed with the help of the Green function with $f = f\left(\sum_{i=1}^{4} A_i + \sum_{i=1}^{3} B_i + \sum_{i=1}^{5} C_i\right)$, lines as in Fig. 2.111

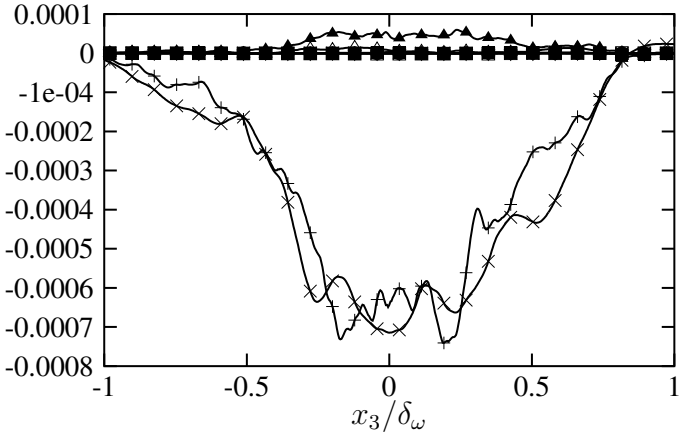

Figure 2.114: Case inert-1.1: Parts of the pressure-strain correlation Π_{11} computed with the Green function, normalized by $\rho_0 \Delta u^3/\delta_\omega$, symbols as in Fig. 2.110

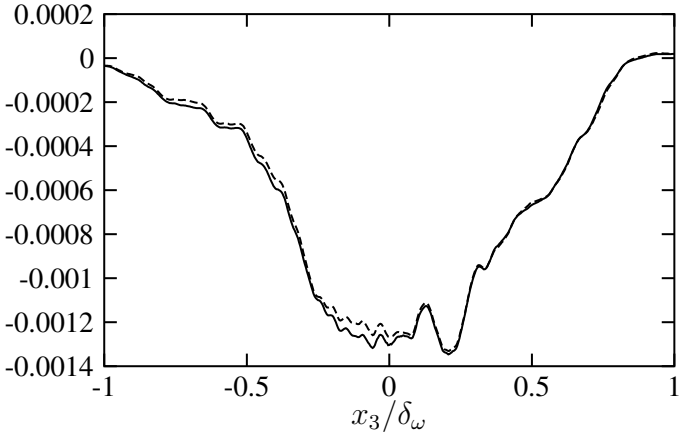

Figure 2.115: Case inert-1.1: Pressure-strain correlation Π_{11}, normalized by $\rho_0 \Delta u^3/\delta_\omega$, solid: computed with the help of the Green function with $f = f\left(\sum_{i=1}^{4} A_i + \sum_{i=1}^{3} B_i + \sum_{i=1}^{5} C_i\right)$, lines as in Fig. 2.111

for $k \neq 0$, where $k = \left(k_1^2 + k_2^2\right)^{1/2}$ and

$$\begin{aligned} \hat{G}\left(0, x_3', x_3''\right) &= 0.5\left(x_3'' - x_3'\right), \text{ for } x_3' < x_3'' \\ \hat{G}\left(0, x_3', x_3''\right) &= 0.5\left(x_3' - x_3''\right), \text{ for } x_3' > x_3'' \end{aligned} \tag{2.73}$$

for $k = 0$. Consequently, the solution of Eq. (2.70) writes

$$p'\left(x_1, x_2, x_3'\right) = \int_{-1}^{1} G * f\left(x_1, x_2, x_3''\right) dx_3'' \tag{2.74}$$

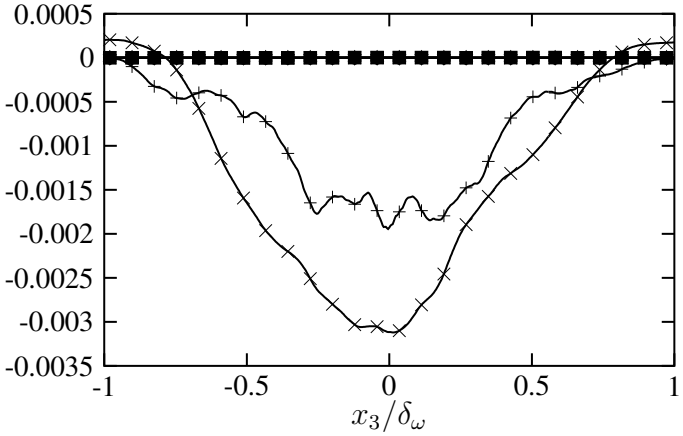

Figure 2.116: Case inert-0.15: Parts of the pressure-strain correlation Π_{11} computed with the Green function and with constant density ρ_0, normalized by $\rho_0 \Delta u^3/\delta_\omega$, symbols as in Fig. 2.110

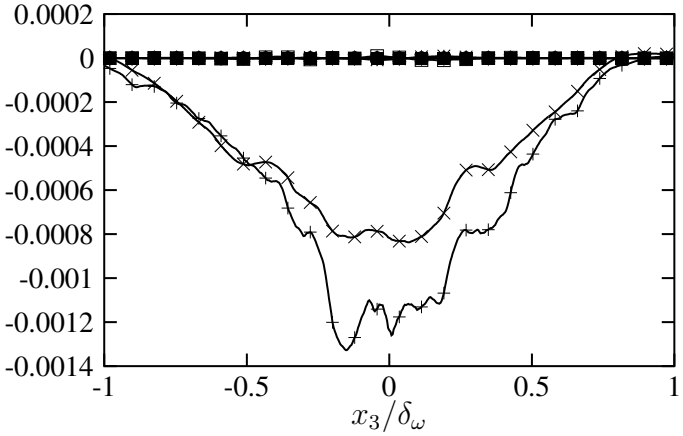

Figure 2.117: Case inert-0.7: Parts of the pressure-strain correlation Π_{11} computed with the Green function and with constant density ρ_0, normalized by $\rho_0 \Delta u^3/\delta_\omega$, symbols as in Fig. 2.110

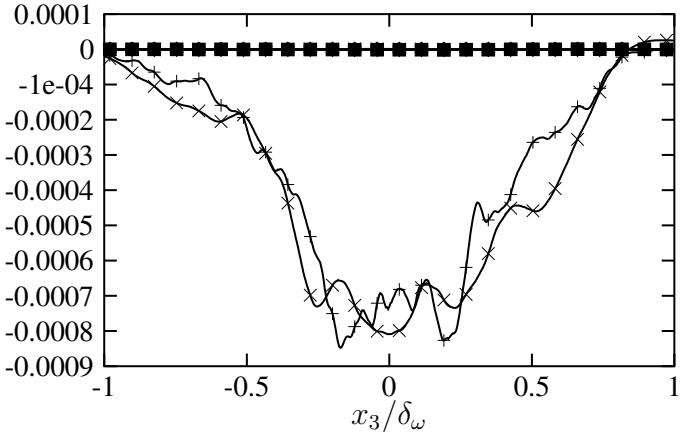

Figure 2.118: Case inert-1.1: Parts of the pressure-strain correlation Π_{11} computed with the Green function and with constant density ρ_0, normalized by $\rho_0 \Delta u^3/\delta_\omega$, symbols as in Fig. 2.110

where the convolution $G * f$ represents the inverse Fourier transform of $\hat{G}\hat{f}$,

$$G*f'\left(x_1,x_2,x_3''\right)=\frac{1}{\left(2\pi\right)^2}\int_{-\infty}^{\infty}dk_1\int_{-\infty}^{\infty}dk_2\exp\left(ik_ix_i\right)\hat{G}\left(k_1,k_2,x_3',x_3''\right)\hat{f}\left(k_1,k_2,x_3''\right). \quad (2.75)$$

Multiplication with s_{ij}'' and averaging, results in the pressure-strain correlations

$$\Pi_{ij}\left(x_3'\right)=\int_{-1}^{1}\langle G*f\left(x_1,x_2,x_3''\right)s_{ij}''\left(x_1,x_2,x_3'\right)\rangle dx_3'' \quad (2.76)$$

Similarly, the pressure-scrambling terms are obtained when multiplying with $\partial Y''/\partial x_i$ instead of s_{ij}''. These terms are further studied in Sect. 2.4.4.2.

When inserting not the complete RHS f into Eq. (2.76), but only a part of it, e.g. term A_1, it is possible to see which of the terms on the RHS contributes most to the pressure fluctuations and to what mechanisms the reduction of the pressure-strain correlations with compressibility are due. Figure 2.110 shows the contributions to the pressure-strain term, Π_{11} of case inert-0.15, computed this way and averaged over the self-similar state. It can be seen that only terms A_1 and A_2 are significant, and all other terms can be neglected. When summing up all terms, the result, shown as a solid line in Fig. 2.111, corresponds well to Π_{11} computed directly as done in the previous sections. This justifies the neglection of terms D and C_6 for this case. When increasing M_c, the contribution from term C_2, which is one of the terms involving density fluctuations starts to grow

somewhat, however, it remains small compared to the contributions from terms A_1 and A_2 (cf. Figs. 2.112 and 2.114). Even though term C_6, which is expected to represent acoustic effects, is neglected, the summation of the rest of the terms provides still a good approximation to Π_{11} as shown in Figs. 2.113 and 2.115. Since the analysis of the other pressure-strain terms gives qualitatively similar results, it can be concluded that acoustic effects do not play a significant role for the pressure-strain correlations of inert mixing layers in the convective Mach number range considered in this study.

A comparison between Figs. 2.110, 2.112 and 2.114 shows, that the contributions from terms A_1 and A_2 decrease with increasing M_c which corresponds to the same behaviour that has been noticed previously for the complete pressure-strain rates. To find out whether this is a consequence of the mean density reduction (cf. Fig. 2.64) by compressibility, the mean density $\langle\rho\rangle$ appearing in terms A_1 to A_4 of Eq. (2.68) is set constant, i.e. ρ_0 is inserted instead. The density fluctuations in the other terms are set to zero. Figures 2.116 to 2.118 show the resulting contributions to Π_{11} when replacing the original terms on the RHS of Eq. (2.68) by these modified terms: The reduction of the contributions from terms A_1 and A_2 with increasing M_c is still visible which excludes mean density effects to be the reason for this behaviour. Consequently, it must be caused by changes in the velocity field.

Turbulent and gradient Mach numbers The turbulent Mach number

$$M_t = \frac{\sqrt{2k}}{\langle c\rangle} \tag{2.77}$$

is an indicator of the level of compressibility of the turbulence and can also be interpreted as the ratio of the eddy-acoustic time scale τ_a to the turbulence time scale τ_t [63]. Fig. 2.119 shows the increase of the turbulent Mach number with increasing M_c. However, Sarkar [161] showed for homogeneously sheared turbulence that it is not the turbulent Mach number but the gradient Mach number

$$M_g = \frac{Sl}{\langle c\rangle}, \tag{2.78}$$

which steers the reduction of the TKE growth rate by a reduced level of turbulent production. In Eq. (2.78), S denotes the mean shear and l a length scale in the direction of the mean shear. Sarkar [161] pointed out that an increase in turbulent Mach number reduced also the growth rate of the TKE, however considerably less than an increase in M_g. The reason for the decrease with M_t was

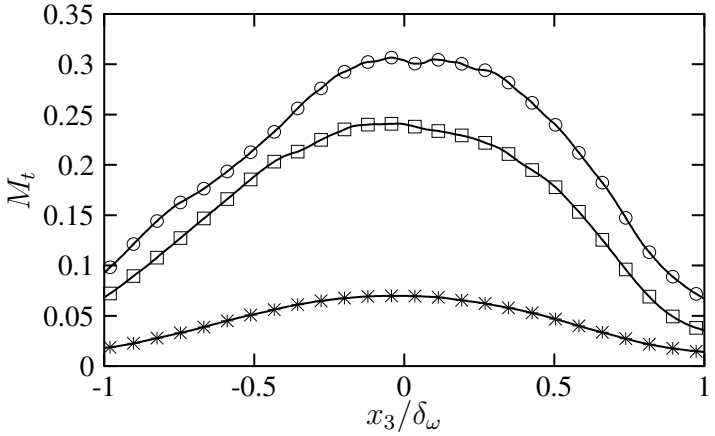

Figure 2.119: Turbulent Mach number M_t, symbols as in Fig. 2.63

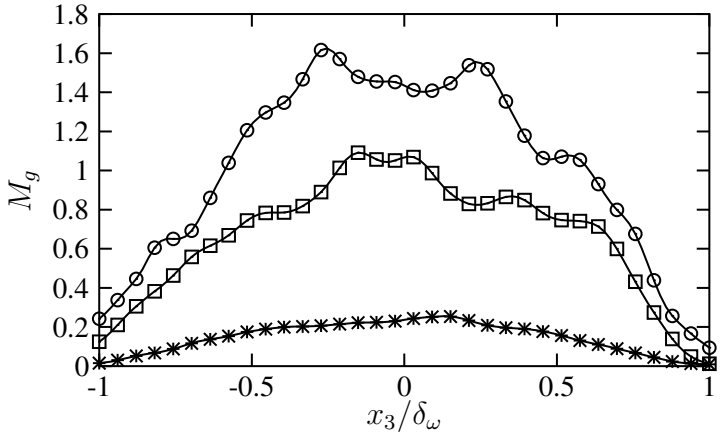

Figure 2.120: Gradient Mach number M_g, symbols as in Fig. 2.63

identified to be due to a contribution from pressure dilatation and dilatational dissipation. These findings can also explain why compressibility effects are strong in shear layers and rather lack in boundary layers: The gradient Mach number in the latter ones is much smaller than in shear layers. Pantano & Sarkar [123] pursued the investigations for the compressible mixing layer and also found the gradient Mach number to be the key quantity that determines the reduction of the pressure-strain term. Figure 2.120 shows the gradient Mach number, computed with $l = \delta_\omega$ for the inert mixing layers. In agreement with the just mentioned studies, it increases with increasing M_c. Since both, M_t and M_g are affected by compressibility it is interesting to see whether both quantities are correlated. Blaisdell et al. indeed found a correlation [12] which can be confirmed by the present results (Fig. 2.121). However, due to different initial conditions and the use of another length scale in the computation of M_g, the slopes of the approximately linear relations do not coincide.

Since the gradient Mach number can also be interpreted as the acoustic time scale τ_a divided by the mean distortion time scale of the flow, τ_d, the ratio of the gradient Mach number to the turbulent Mach number,

$$\frac{M_g}{M_t} = \frac{\tau_a/\tau_d}{\tau_a/\tau_t} = \frac{\tau_t}{\tau_d}, \tag{2.79}$$

is the turbulence time scale, τ_t, divided by the mean distortion time scale and quantifies the degree to which rapid-distortion effects govern the flow [63]. The approximately linear relation between M_g and M_t for the inert mixing layers makes this ratio constant at all convective Mach numbers that have been investigated and leads to the conclusion that such effects do not increase

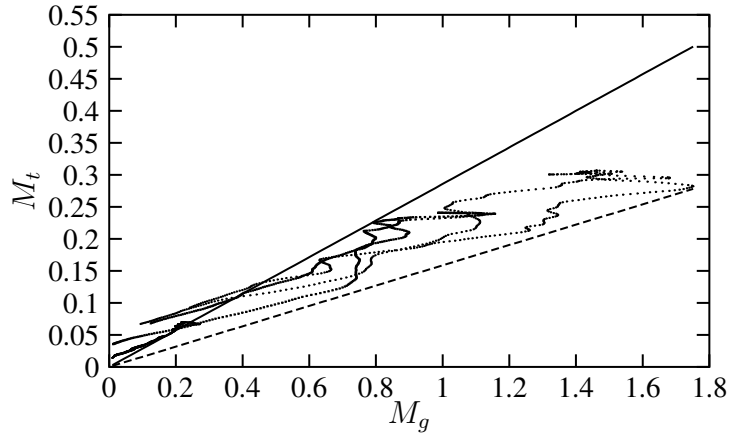

Figure 2.121: Turbulent Mach number M_t plotted as a function of the gradient Mach number M_g. Symbols as in Fig. 2.63, solid line: $M_t = 0.286 M_g$, dashed line: $M_t = 0.159 M_g$

significantly with M_c. This is in agreement with the findings of Freund et al. for the annular inert mixing layer [63].

Spectra Figure 2.122 shows the one-dimensional, streamwise spectra of the velocity u_1 ($\hat{u_1}'\hat{u_1}'^*$ with $\hat{u_1}'$ denoting the velocity component u_1 Fourier transformed in x_1 direction and $\hat{u_1}'^*$ its complex conjugate) after averaging over directions x_2 and x_3. None of the spectra shows signs of under-resolution like accumulation of energy at the highest wavenumbers. Mostly the higher wave numbers are affected by increasing compressibility and a decrease of the energy that is contained in the highest wavenumbers (smallest scales) can be noticed. This is in agreement with the structural changes that were noticed earlier, like the larger-scale ondulations that show the mixing layers at higher convective Mach number in comparison to the simulation inert-0.15 (cf. Sect. 2.4.1). The spectra of the other velocity components evaluated in the streamwise and also in the other homogeneous direction, which is the spanwise one, demonstrate a similar behaviour (not shown). Therefore, it can also be found in the spectra of the TKE in Fig. 2.123. A comparison to the reference line with a slope of $-5/3$, which gives the energy fall-off in the inertial range for high Reynolds number turbulence [153], shows that the energy cascade follows this slope for at least a small part of the spectrum. However, due to the relatively small Reynolds number, a large inertial range cannot be expected. Pantano & Sarkar [123] also present energy spectra that show a decrease in the highest wavenumbers with increasing M_c, but they do not comment on

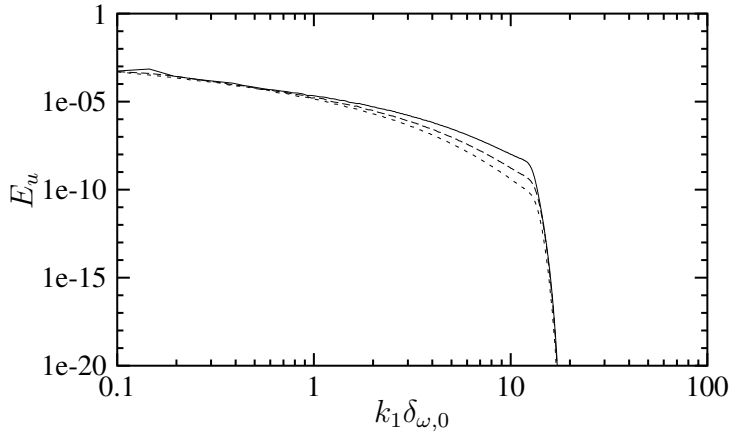

Figure 2.122: One-dimensional, streamwise spectrum of $u_1/\Delta u$ at the beginning of the self-similar state, solid: inert-0.15, dashed: inert-0.7, dotted: inert-1.1

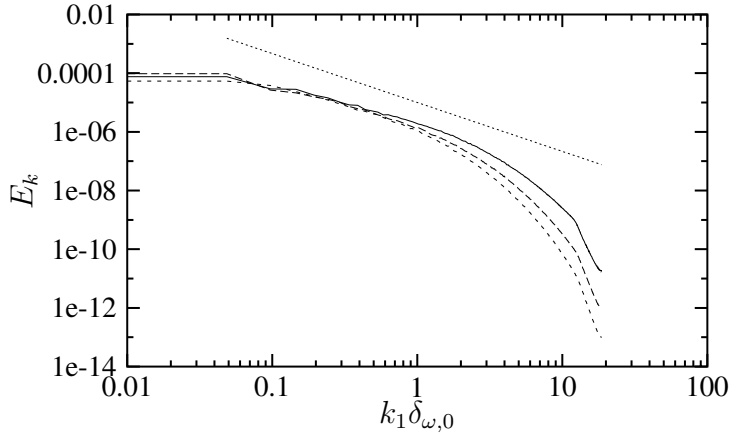

Figure 2.123: One-dimensional, streamwise spectrum of TKE $k/\Delta u^2$ at the beginning of the self-similar state, solid: inert-0.15, dashed: inert-0.7, dotted: inert-1.1, the straight line has $-5/3$ slope

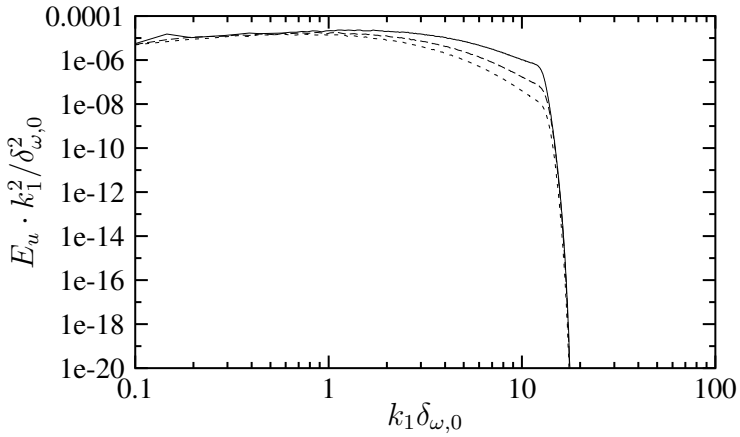

Figure 2.124: One-dimensional, streamwise dissipation spectrum (spectrum of $u_1/\Delta u$ multiplied with $(k_1\delta_{\omega,0})^2$) at the beginning of the self-similar state, solid: inert-0.15, dashed: inert-0.7, dotted: inert-1.1

this feature.

One-dimensional dissipation spectra, evaluated as $k_1^2\hat{u}'\hat{u}'^*$, are shown in Fig. 2.124. Compared to the TKE spectra there is more 'dissipated energy' situated in the higher wave numbers which is to be expected since the dissipation of energy takes mostly place in the smallest scales. Again, increasing compressibility leads to a reduction of the energy content in the highest wavenumbers.

2.4.4.2 Scalar mixing

In the present test cases, the species mass fractions are active, but non-reactive scalars. They are called 'active' as they influence the flow field by their molecular weight through the density and by the transport coefficients that depend among other thermodynamic variables (the temperature and partially the pressure) on their concentration.

The influence of compressibility on molecular mixing has been investigated previously mostly by experimentalists. While some authors report a small increase of mixing efficiency with compressibility [27, 28, 45], others found no apparent dependency on the convective Mach number [78] or even encountered a decrease [70]. However, some of these experiments, e.g. [27] are not fully spatially resolved as pointed out by [114]. Freund et al. [64] found an increase in mixing efficiency for their DNS of annular mixing layers between $M_c = 0.1$ and $M_c = 1.54$ but a decrease for their highest Mach number case $M_c = 1.8$ which they are unable to explain. Many of these studies also deal with the entrainment ratio, which is the average amount of fluid entrained into the mixing layer from the high-speed side divided by the average amount of fluid entrained from the low-speed side, and found it significantly altered by compresssibility. However, due to the symmetry of the temporally evolving mixing layer, corresponding studies can not be performed for the present configuration.

Mean profile and variance The differences between the Favre averaged profiles of the oxygen mass fraction at different M_c (Fig. 2.125) are larger than those of the streamwise velocity profiles (Fig. 2.66). The case inert-0.15 seems to have a flatter and more extended linear region in the center of the shear layer than the shear layers at higher M_c the profiles of which are fuller and closer to the shape of a hyperbolic-tangent or an error function.

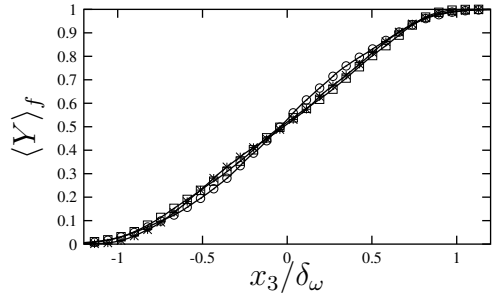

Figure 2.125: Favre averaged oxygen mass fraction, $*$: inert-0.15, $\square$: inert-0.7, $\circ$: inert-1.1

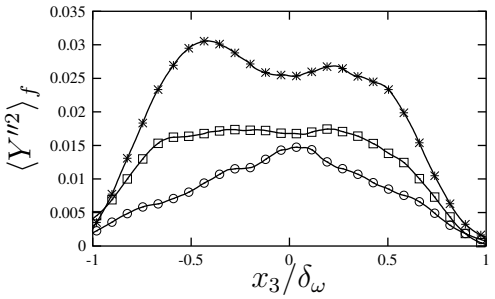

Figure 2.126: Scalar variance, symbols as in Fig. 2.125

The variance of the oxygen mass fraction (Fig. 2.126) and consequently also the variance of the nitrogen mass fraction are reduced by compressibility, which is in agreement with earlier results, e.g. [27, 63]. In addition to a reduction of the peak value, a change of the profile shape can be noticed: At $M_c = 0.15$, it has a local minimum in the center of the shear layer and two maxima at its edges. The same double hump has been observed by other authors, too [58, 115, 124]. It is related with the fact that engulfment is most dominant at the edges of the shear layer and leads to an increased intermittency at these locations. Compressibility first levels the minimum ($M_c = 0.7$) and finally leads to a peak in the center of the shear layer ($M_c = 1.1$). This means that at low convective Mach number strong deviations from the averaged mass fraction are in particular present at the edges of the shear layer while at higher Mach number the strongest deviations can be found in the center of the layer where also the peak value of the TKE is located (Fig. 2.71). A similar change in the shape of the profiles with increasing M_c is observed for the rms value of the molecular weight (Fig. 2.104). The general decrease of the scalar fluctuations at higher convective Mach number can be understood when taking into account that the penetration of free-stream fluid into the mixing layer decreases with increasing compressibility (cf. Sect. 2.4.4.3) resulting in less flucutations about the respective mean.

Scalar pdfs Figures 2.127 to 2.129 show the probability density functions (pdfs) of the oxygen mass fraction for various x_1-x_2-planes corresponding to different $\langle Y \rangle$ whereby the samples were taken from the self-similar state. The pdfs were constructed by dividing the range between the

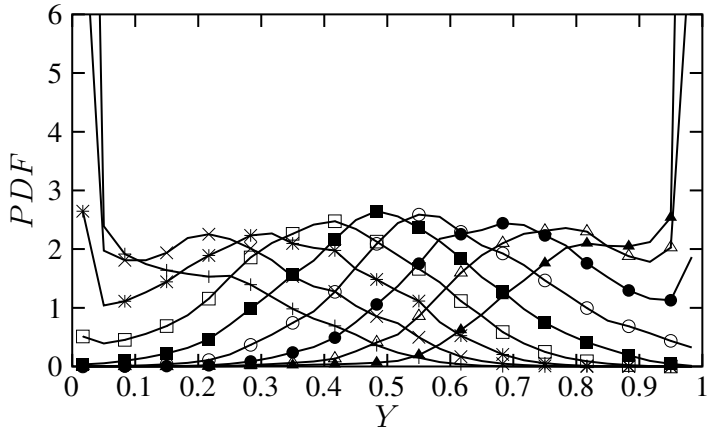

Figure 2.127: Case inert-0.15: pdfs of oxygen mass fraction in planes with various $\langle Y \rangle$, $+$: 0.1, $\times$: 0.2, $*$: 0.3, $\square$: 0.4, $\blacksquare$: 0.5, $\circ$: 0.6, $\bullet$: 0.7, $\triangle$: 0.8, $\blacktriangle$: 0.9

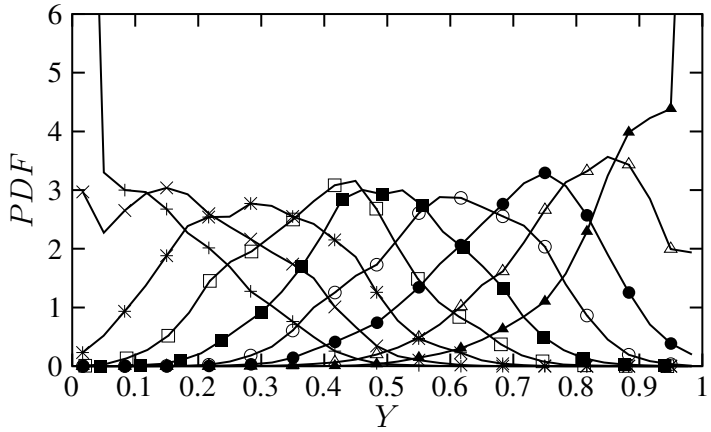

Figure 2.128: Case inert-0.7: pdfs of oxygen mass fraction in planes with various $\langle Y \rangle$, $+$: 0.1, $\times$: 0.2, $*$: 0.3, $\square$: 0.4, $\blacksquare$: 0.5, $\circ$: 0.6, $\bullet$: 0.7, $\triangle$: 0.8, $\blacktriangle$: 0.9

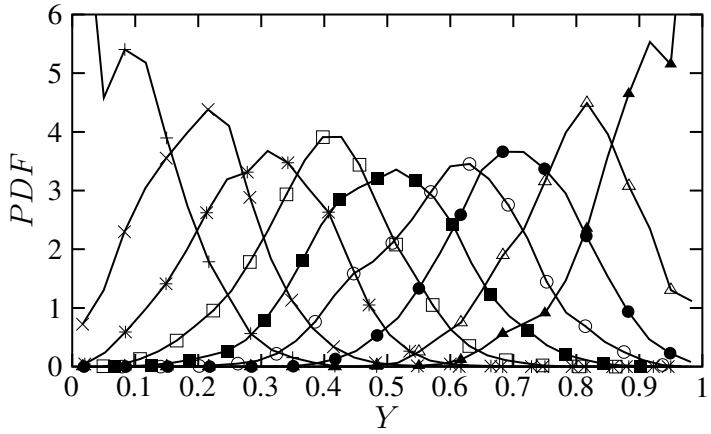

Figure 2.129: Case inert-1.1: pdfs of oxygen mass fraction in planes with various $\langle Y \rangle$, $+$: 0.1, $\times$: 0.2, $*$: 0.3, $\square$: 0.4, $\blacksquare$: 0.5, $\circ$: 0.6, $\bullet$: 0.7, $\triangle$: 0.8, $\blacktriangle$: 0.9

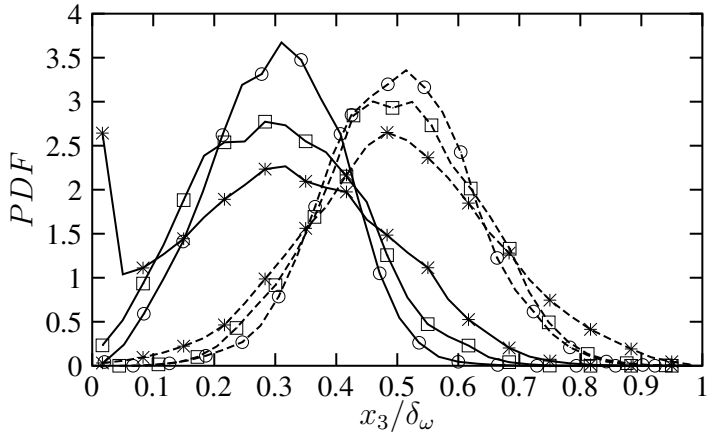

Figure 2.130: Pdfs of oxygen mass fraction in the plane with $\langle Y \rangle = 0.3$ (solid) and $\langle Y \rangle = 0.5$ (dashed), symbols as in Fig. 2.125

maximum value (1.) and the minimum value (0.) in 50 bins and normalizing such that:

$$\int_0^1 PDF\,(Y) = 1. \tag{2.80}$$

Comparing the pdfs for the different convective Mach numbers, one can see that for $M_c = 0.15$ more pure, unmixed fluid is present at $\langle Y \rangle = 0.8$, 0.7, 0.3 and 0.2 than for the other cases. This is in agreement with the stronger engulfment of this shear layer (cf. Sect. 2.4.4.3). Comparing directly the pdfs for certain $\langle Y \rangle$, as it is done in Figs. 2.130, it is visible that the higher the

Mach number the narrower and more pointed the pdfs. This is directly related with the lower fluctuations noticed at higher Mach number.

Figures 2.127 to 2.129 also show that the most probable value of the mass fraction, i.e. the maximum of the pdfs, varies across the layer. At each side of the layer, it is closer to the free-stream value of that side which proofs that the fluid gets mixed into the layer at the edges. Such pdfs are called marching pdfs. The other cathegory that pdfs can fall in are the so-called non-marching pdfs in which the most probable value is independent of the position in the layer. Rogers & Moser [152] found marching and non-marching pdfs in their incompressible mixing layer depending upon the initial conditions. The layer with the largest initial forcing, which developed large roller structures and braid regions, had a non-marching scalar pdf which the authors suggested to be caused by pure fluid which is engulfed by the large structures. As all the pdfs found here are marching, it is expected to find the engulfed fluid volume rather small compared to the mixed one, which is confirmed and further investigated in Sect. 2.4.4.3. Clemens & Mungal [27] also found marching pdfs at both, low and high convective Mach number with the pdfs at low convective Mach number being broader. They elucidated what types of turbulent structures are responsible for the nature of the pdfs: Narrow, marching pdfs are caused by mixing layers the structures of which closely resemble the mean profiles being uniform in the streamwise and sloped in the transverse direction. Broad and non-marching pdfs are the consequence of structures that are sloped in the streamwise direction and uniform in the transverse direction. As the pdfs that are encountered here and also by these authors are relatively broad and marching both kind of turbulent structures must be present in the mixing layer. However, with the high compressibility pdfs being narrower, the structures of this mixing layer resemble more closely the mean profile which is equivalent to having less fluctuations.

Mixing efficiency The mixing efficiency measures the mixing of the fluid in the layer that takes place at the molecular level. Following Freund et al. [64], it is defined in terms of the scalar pdf $P(Y, x_3)$ measured at different transverse positions:

$$\frac{\delta_M}{\delta_Y} = \frac{1}{\delta_Y} \int_{-\infty}^{\infty} dx_3 \int_{\epsilon}^{1-\epsilon} dY P(Y, x_3) \tag{2.81}$$

where δ_Y denotes the 99% scalar thickness. The choice of the small parameter ϵ influences the resulting mixing efficiency. The higher ϵ is chosen, the more fluid is considered unmixed. Figure 2.131 shows the mixing efficiency for different ϵ. Since 50 bins have been used to determine the

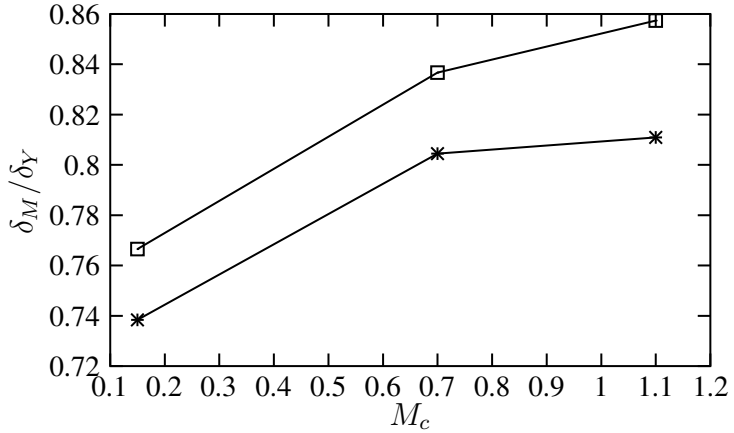

Figure 2.131: Mixing efficiency, □: $\epsilon = 0.02$, ∗: $\epsilon = 0.04$

pdfs, $\epsilon = 0.02$ corresponds to defining the fluid in the extreme bins to be pure and $\epsilon = 0.04$, to defining the fluid in the two outer bins to be pure. In the figure it can be seen that there is an increasing trend in the mixing efficiency from low to high convective Mach number which is in agreement with the results of Freund et al. [64]. In other words, with increasing M_c, there is less free-stream fluid present, i.e. fluid with species mass fractions of $0 \leq Y_\alpha < \epsilon$ or $1 - \epsilon < Y_\alpha \leq 1$. This is consistent with the already observed decrease in mass fraction fluctuations and with reduced engulfment (cf. Sect. 2.4.4.3).

Scalar variance transport equation The transport equation of the scalar variance reads for temporally evolving shear layers:

$$\begin{aligned}\frac{\partial}{\partial t}\langle\frac{1}{2}\rho Y_\alpha''^2\rangle = &-\frac{1}{2}\langle u_3\rangle_f\frac{\partial}{\partial x_3}\langle\rho Y_\alpha''^2\rangle - \frac{1}{2}\frac{\partial}{\partial x_3}\langle\rho u_3'' Y_\alpha''^2\rangle \\ &- \langle\rho Y_\alpha'' u_3''\rangle\frac{\partial\langle Y_\alpha\rangle_f}{\partial x_3} - \frac{1}{2}\langle\rho Y_\alpha''^2\rangle\frac{\partial\langle u_3\rangle_f}{\partial x_3} \\ &- \frac{\partial}{\partial x_3}\langle\rho Y_\alpha Y_\alpha'' V_{\alpha 3}\rangle + \langle\rho Y_\alpha V_{\alpha i}\frac{\partial Y_\alpha''}{\partial x_i}\rangle\end{aligned} \tag{2.82}$$

The first term on the right hand side describes mean convection, the second is called turbulent transport, the third and fourth turbulent production, the fifth molecular diffusion and the last one is

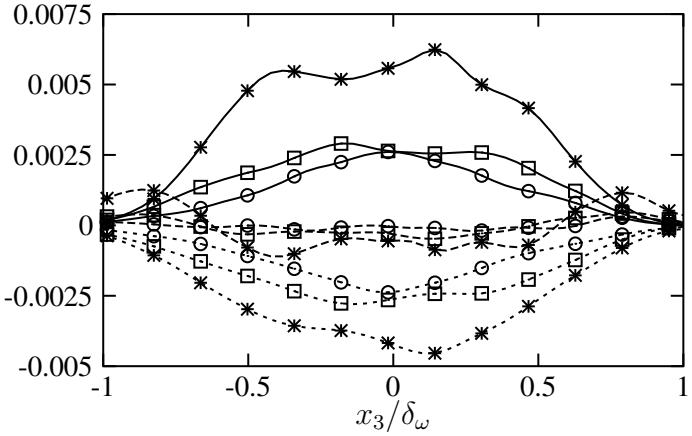

Figure 2.132: Major terms in the scalar variance transport equation, normalized by $\rho_0\Delta u/\delta_\omega$, solid: turbulent production, dashed: turbulent transport, dotted: dissipation rate, symbols as in Fig. 2.125

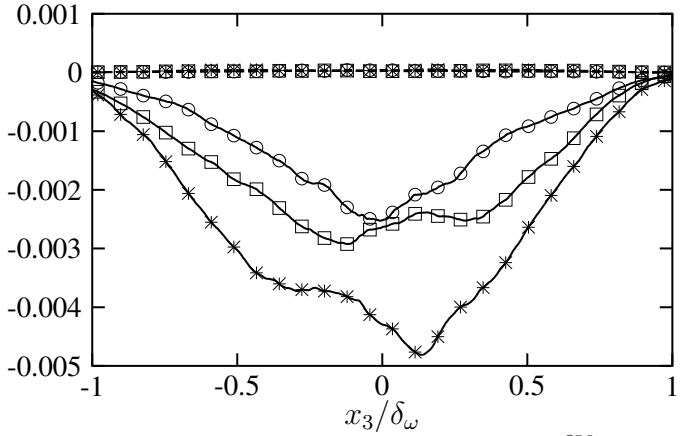

Figure 2.133: Parts of the scalar dissipation rate, solid: $\langle\rho Y_\alpha V_{\alpha i}\frac{\partial Y_\alpha}{\partial x_i}\rangle$, dashed: $\langle\rho Y_\alpha V_{\alpha i}\rangle\frac{\partial\langle Y_\alpha\rangle_f}{\partial x_i}$, normalized by $\rho_0\Delta u/\delta_\omega$, symbols as in Fig. 2.125

the dissipation term. Figure 2.132 shows the most important terms: Positive turbulent production is the major source term, the negative dissipation rate is the major sink and the turbulent transport is negative in the center of the shear layer and positive at its edges at $M_c = 0.15$ and oscillates around zero for higher convective Mach numbers.

The most important change that occurs with increasing M_c is the reduction of the turbulent production. In addition, a decrease in the magnitude of the turbulent transport and of the dissipation rate is noticed. The dissipation rate can be split up into:

$$\epsilon_Y = \langle \rho Y_\alpha V_{\alpha i} \frac{\partial Y_\alpha''}{\partial x_i} \rangle = \langle \rho Y_\alpha V_{\alpha i} \frac{\partial Y_\alpha}{\partial x_i} \rangle - \langle \rho Y_\alpha V_{\alpha i} \rangle \frac{\partial \langle Y_\alpha \rangle_f}{\partial x_i} \tag{2.83}$$

Figure 2.133 shows that the second part on the RHS, which is the product of two mean values, can be neglected with respect to the first part, so that

$$\epsilon_Y \approx \langle \rho Y_\alpha V_{\alpha i} \frac{\partial Y_\alpha}{\partial x_i} \rangle \tag{2.84}$$

is a valid approximation.

Scalar fluxes Figures 2.134 and 2.135 show the most important scalar fluxes, $\langle \rho u_1'' Y_\alpha'' \rangle$ and $\langle \rho u_3'' Y_\alpha'' \rangle$. It can be seen that both, the streamwise scalar flux, $\langle \rho u_1'' Y_\alpha'' \rangle$, as well as the transverse scalar flux, $\langle \rho u_3'' Y_\alpha'' \rangle$, reduce with increasing compressibility. The reduction of the latter one, in particular from $M_c = 0.7$ to $M_c = 1.1$, however, is considerably larger than the reduction of the streamwise flux which has also been noticed by Freund et al. [64]. The spanwise scalar flux (not shown) is one order of magnitude smaller than the other scalar fluxes and not investigated further.

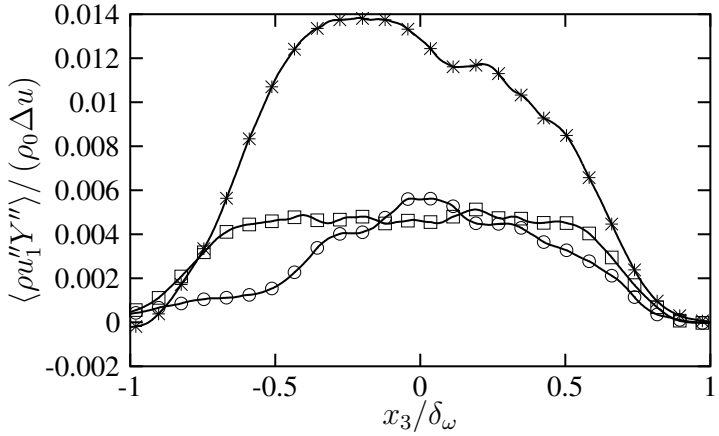

Figure 2.134: Scalar flux $\langle \rho u_1'' Y_\alpha'' \rangle$ of oxygen, normalized by $\rho_0 \Delta u$, symbols as in Fig. 2.125

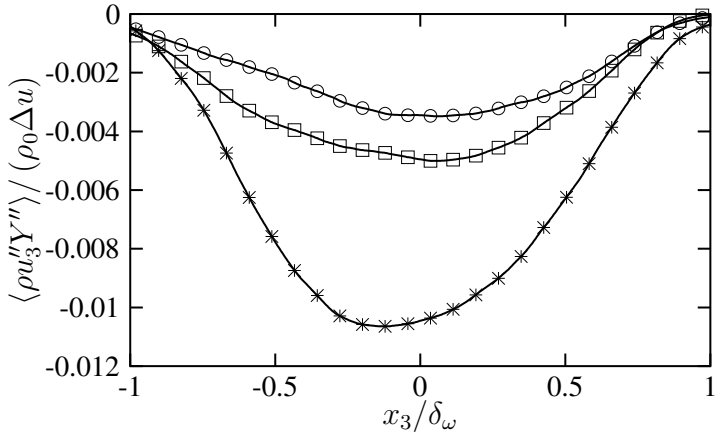

Figure 2.135: Scalar flux $\langle \rho u_3'' Y_\alpha'' \rangle$ of oxygen, normalized by $\rho_0 \Delta u$, symbols as in Fig. 2.125

Transport equations of scalar fluxes The general form of the transport equation for the scalar fluxes in Cartesian coordinates is:

$$\begin{aligned}\frac{\partial}{\partial t}\langle\rho u_i'' Y_\alpha''\rangle = &- \langle u_j\rangle_f \frac{\partial}{\partial x_j}\langle\rho u_i'' Y_\alpha''\rangle - \frac{\partial}{\partial x_j}\langle\rho u_i'' u_j'' Y_\alpha''\rangle \\ &- \langle\rho u_i'' Y_\alpha''\rangle \frac{\partial\langle u_j\rangle_f}{\partial x_j} - \langle\rho u_j'' Y_\alpha''\rangle \frac{\partial\langle u_i\rangle_f}{\partial x_j} - \langle\rho u_i'' u_j''\rangle \frac{\partial\langle Y_\alpha\rangle_f}{\partial x_j} \\ &+ \langle p\frac{\partial Y_\alpha''}{\partial x_i}\rangle \\ &- \frac{\partial}{\partial x_j}\langle pY_\alpha''\rangle\delta_{ij} + \frac{\partial}{\partial x_j}\langle\tau_{ij}Y_\alpha''\rangle - \frac{\partial}{\partial x_j}\langle u_i''\rho Y_\alpha V_{\alpha j}\rangle \\ &- \langle\tau_{ij}\frac{\partial Y_\alpha''}{\partial x_j}\rangle + \langle\rho Y V_{\alpha j}\frac{\partial u_i''}{\partial x_j}\rangle\end{aligned} \tag{2.85}$$

The first term on the RHS denotes convection, the second term is the turbulent transport and the next three terms are production terms. The term in the third line is the pressure scalar-gradient correlation and the terms in the fourth line are diffusion terms. The last two terms describe the dissipation.

For a shear layer which is periodic in x_1- and x_2-directions the transport equation in the x_1-direction can be simplified to

$$\begin{aligned}\frac{\partial}{\partial t}\langle\rho u_1'' Y_\alpha''\rangle = &- \langle u_3\rangle_f \frac{\partial}{\partial x_3}\langle\rho u_1'' Y_\alpha''\rangle - \frac{\partial}{\partial x_3}\langle\rho u_1'' u_3'' Y_\alpha''\rangle \\ &- \langle\rho u_1'' Y_\alpha''\rangle \frac{\partial\langle u_3\rangle_f}{\partial x_3} - \langle\rho u_3'' Y_\alpha''\rangle \frac{\partial\langle u_1\rangle_f}{\partial x_3} - \langle\rho u_1'' u_3''\rangle \frac{\partial\langle Y_\alpha\rangle_f}{\partial x_3} \\ &+ \langle p\frac{\partial Y_\alpha''}{\partial x_1}\rangle \\ &+ \frac{\partial}{\partial x_3}\langle\tau_{13}Y_\alpha''\rangle - \frac{\partial}{\partial x_3}\langle u_1''\rho Y_\alpha V_{\alpha 3}\rangle \\ &- \langle\tau_{1j}\frac{\partial Y_\alpha''}{\partial x_j}\rangle + \langle\rho Y_\alpha V_{\alpha j}\frac{\partial u_1''}{\partial x_j}\rangle.\end{aligned} \tag{2.86}$$

The resulting equation for the flux in the x_3-direction is:

$$\begin{aligned}\frac{\partial}{\partial t}\langle\rho u_3'' Y_\alpha''\rangle = &- \langle u_3\rangle_f \frac{\partial}{\partial x_3}\langle\rho u_3'' Y_\alpha''\rangle - \frac{\partial}{\partial x_3}\langle\rho u_3'' u_3'' Y_\alpha''\rangle \\ &- 2\langle\rho u_3'' Y_\alpha''\rangle \frac{\partial\langle u_3\rangle_f}{\partial x_3} - \langle\rho u_3'' u_3''\rangle \frac{\partial\langle Y_\alpha\rangle_f}{\partial x_3} \\ &+ \langle p\frac{\partial Y_\alpha''}{\partial x_3}\rangle \\ &- \frac{\partial}{\partial x_3}\langle pY_\alpha''\rangle + \frac{\partial}{\partial x_3}\langle\tau_{33}Y_\alpha''\rangle - \frac{\partial}{\partial x_3}\langle u_3''\rho Y_\alpha V_{\alpha 3}\rangle \\ &- \langle\tau_{3j}\frac{\partial Y_\alpha''}{\partial x_j}\rangle + \langle\rho Y_\alpha V_{\alpha j}\frac{\partial u_3''}{\partial x_j}\rangle.\end{aligned} \tag{2.87}$$

The pressure scalar-gradient correlation can also be written as

$$\langle p\frac{\partial Y_\alpha''}{\partial x_i}\rangle = \langle p\rangle\frac{\partial\langle Y_\alpha\rangle}{\partial x_i} - \langle p\rangle\frac{\partial\langle Y_\alpha\rangle_f}{\partial x_i} + \langle p'\frac{\partial Y_\alpha''}{\partial x_i}\rangle. \tag{2.88}$$

For the x_1-direction this becomes

$$\langle p\frac{\partial Y_\alpha''}{\partial x_1}\rangle = \langle p'\frac{\partial Y_\alpha''}{\partial x_1}\rangle, \tag{2.89}$$

and for the x_3-direction:

$$\langle p\frac{\partial Y_\alpha''}{\partial x_3}\rangle = \langle p\rangle\frac{\partial\langle Y_\alpha\rangle}{\partial x_3} - \langle p\rangle\frac{\partial\langle Y_\alpha\rangle_f}{\partial x_3} + \langle p'\frac{\partial Y_\alpha''}{\partial x_3}\rangle \tag{2.90}$$

is obtained.

In the following, the changes due to compressibility of the major terms in these equations are investigated. The major terms are the production, the diffusion, the dissipation rates and the turbulent transport as well as the correlation between the pressure fluctuations and the spatial derivatives of the mass fraction fluctuations (third term on the RHS of Eq. (2.88)).

Figures 2.136 and 2.137 show the two major production terms of the streamwise scalar flux which are the ones involving the mean gradient of the streamwise velocity and the mean gradient of the scalar mass fraction (second and third term in the second line of Eq. (2.86)). For the transverse scalar flux, only the latter one (second term in the second line of Eq. (2.87)), which is shown in Fig. 2.138, is important. It is negative and constitutes a source term since the transverse flux itself is also negative (Fig. 2.135). All production terms are reduced by compressibility. Particularly striking is the reduction between $M_c = 0.15$ and $M_c = 0.7$. The further increase to $M_c = 1.1$ seems to have less effect which could indicate an asymptotic behaviour. The reduction of the

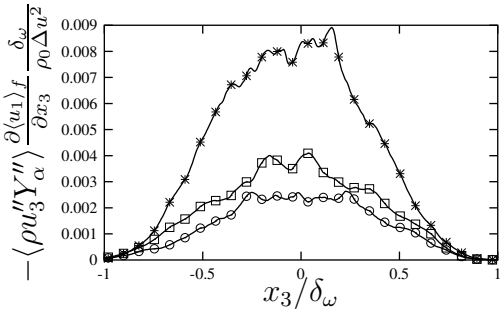

Figure 2.136: Part of the streamwise scalar flux production, normalized by $\rho_0\Delta u^2/\delta_\omega$, symbols as in Fig. 2.125

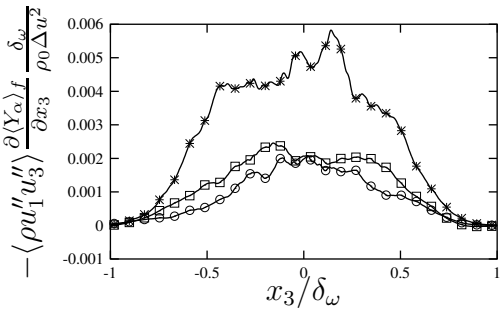

Figure 2.137: Part of the streamwise scalar flux production, normalized by $\rho_0\Delta u^2/\delta_\omega$, symbols as in Fig. 2.125

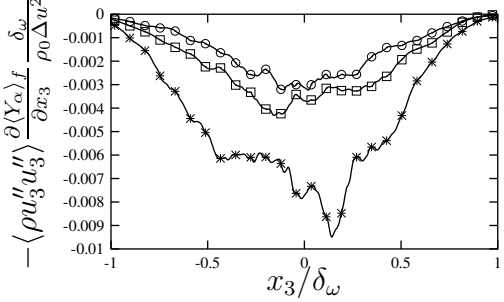

Figure 2.138: Part of the transverse scalar flux production, normalized by $\rho_0\Delta u^2/\delta_\omega$, symbols as in Fig. 2.125

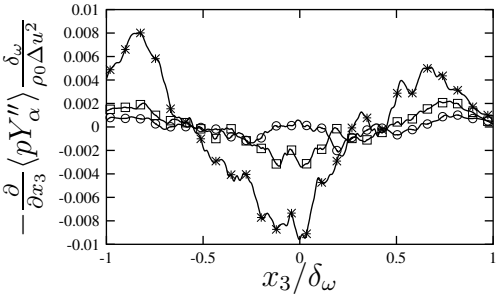

Figure 2.139: Major part of the diffusion of the transverse scalar flux, normalized by $\rho_0\Delta u^2/\delta_\omega$, symbols as in Fig. 2.125

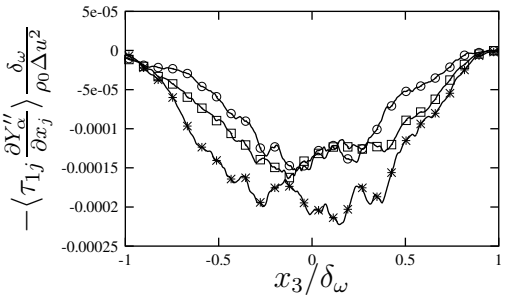

Figure 2.140: Part of the dissipation rate of the streamwise scalar flux, normalized by $\rho_0 \Delta u^2/\delta_\omega$, symbols as in Fig. 2.125

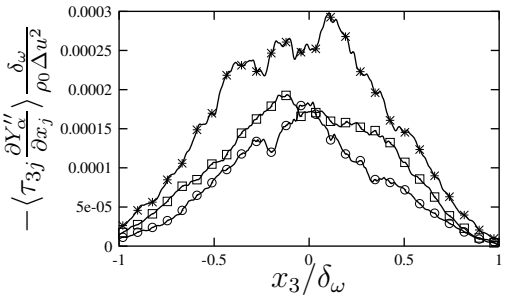

Figure 2.141: Part of the dissipation rate of the transverse scalar flux, normalized by $\rho_0 \Delta u^2/\delta_\omega$, symbols as in Fig. 2.125

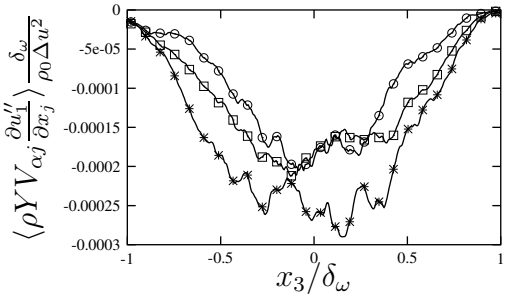

Figure 2.142: Part of the dissipation rate of the streamwise scalar flux, normalized by $\rho_0 \Delta u^2/\delta_\omega$, symbols as in Fig. 2.125

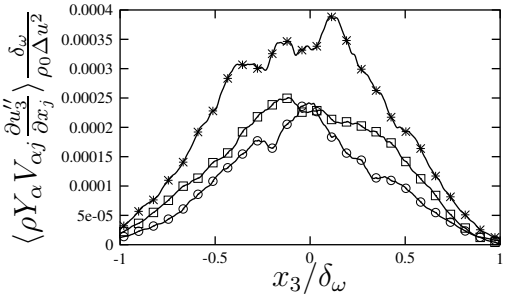

Figure 2.143: Part of the dissipation rate of the transverse scalar flux, normalized by $\rho_0 \Delta u^2/\delta_\omega$, symbols as in Fig. 2.125

scalar flux production is closely related with the reduction of the Reynolds stresses, which appear as factors in the part involving the mean mass fraction gradients, and with the reduction of the scalar fluxes themselves which are factors in the parts with the mean velocity gradients.

From the diffusion terms, only the first term in the third line of Eq. (2.87) plays a major role. It is shown in Fig. 2.139 and decreases with increasing compressibility.

The reduction of the two parts of the dissipation rate of each scalar flux, respectively, (Figs. 2.140 to 2.143) is not as strong as the reduction of the production which is similar to what has been noticed earlier for production and dissipation rate of the Reynolds stresses and the scalar variance.

Figures 2.144 and 2.145 show the turbulent transport of the streamwise and transverse scalar flux. It can be seen that for $M_c = 0.15$, the direction of the turbulent transport for both fluxes is from the center to the edges of the mixing layer. The turbulent transport decreases with increasing compressibility and is strongly damped for the higher convective Mach numbers.

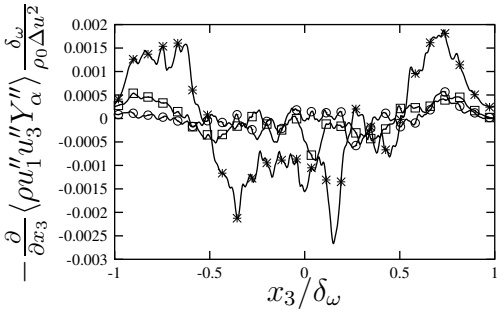

Figure 2.144: Turbulent transport of the streamwise scalar flux, normalized by $\rho_0 \Delta u^2/\delta_\omega$, symbols as in Fig. 2.125

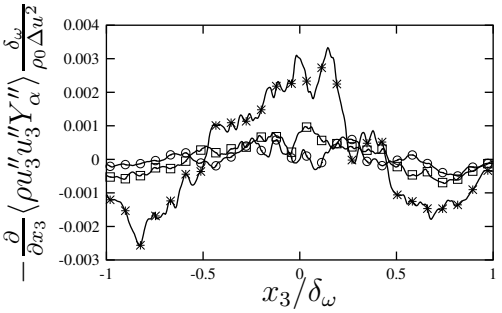

Figure 2.145: Turbulent transport of the transverse scalar flux, normalized by $\rho_0 \Delta u^2/\delta_\omega$, symbols as in Fig. 2.125

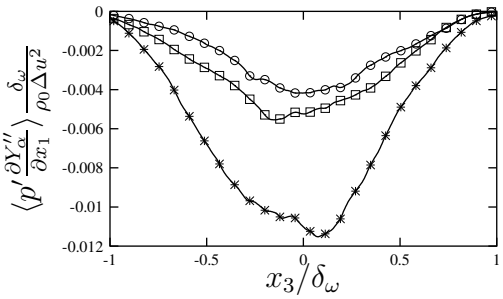

Figure 2.146: Pressure-scrambling term in streamwise direction, Π_{Y1}, normalized by $\rho_0 \Delta u^2/\delta_\omega$, symbols as in Fig. 2.125

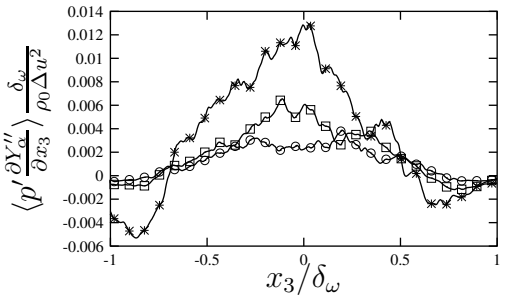

Figure 2.147: Pressure-scrambling term in transverse direction, Π_{Y3}, normalized by $\rho_0 \Delta u^2/\delta_\omega$, symbols as in Fig. 2.125

The reduction of the correlation between the pressure fluctuations and the spatial derivatives of the mass fraction fluctuations (last term in Eq. (2.88)) with compressibility is more pronounced for the streamwise derivative than for the transverse derivative (Figs. 2.146 and 2.147). This term, Π_{Yi}, is also called pressure-scrambling term [100]. While it is purely negative and therefore a sink for the streamwise scalar flux (Fig. 2.146), it changes sign for the transverse flux: It is positive and therefore a sink for the negative transverse scalar flux in the center of the mixing layer and a source at the mixing layer edges (Fig. 2.147). The reduction of the pressure-scrambling terms with increasing M_c is further investigated in the next paragraph.

Behaviour of the pressure-scrambling terms In Section 2.4.4.1, the pressure-strain correlations were computed and analyzed with the help of a Green function for the Poisson equation of the pressure fluctuations, Eq. (2.68). A corresponding procedure permits a closer investigation of the pressure-scrambling terms, $\Pi_{Yi} = \langle p' \frac{\partial Y''_\alpha}{\partial x_i} \rangle$, and of the reason for their reduction with increasing M_c. Similar to the pressure-strain correlations in Eq. (2.76), the pressure scrambling terms can be computed by

$$\Pi_{Yi}\left(x_3'\right) = \int_{-1}^{1} \langle G * f\left(x_1, x_2, x_3''\right) \frac{\partial Y''}{\partial x_i}\left(x_1, x_2, x_3'\right) \rangle dx_3'' \tag{2.91}$$

with the Green function G (cf. Eqs. (2.72) and (2.72)) and the source term f which corresponds to the RHS of Eq. (2.68). When inserting the terms on the RHS of Eq. (2.68) separately, the

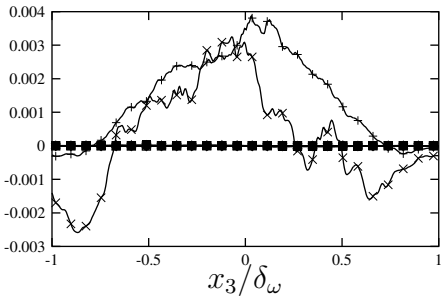

Figure 2.148: Case inert-0.15: Parts of the pressure-scrambling term Π_{Y3} computed with the Green function, normalized by $\rho_0 \Delta u/\delta_\omega$, $+$: $f = f(A_1)$, $\times$: $f = f(A_2)$, $*$: $f = f(A_3)$, $\square$: $f = f(A_4)$, $\blacksquare$: $f = f(B_1)$, $\circ$: $f = f(B_2)$, $\bullet$: $f = f(B_3)$, $\triangle$: $f = f(C_1)$, $\blacktriangle$: $f = f(C_2)$, $\triangledown$: $f = f(C_3)$, $\blacktriangledown$: $f = f(C_4)$, $\Diamond$: $f = f(C_5)$

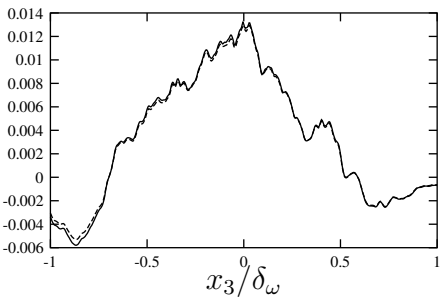

Figure 2.149: Case inert-0.15: Pressure-scrambling term Π_{Y3}, normalized by $\rho_0 \Delta u/\delta_\omega$, solid: computed with the help of the Green function with $f = f\left(\sum_{i=1}^{4} A_i + \sum_{i=1}^{3} B_i + \sum_{i=1}^{5} C_i\right)$, dashed: computed exactly

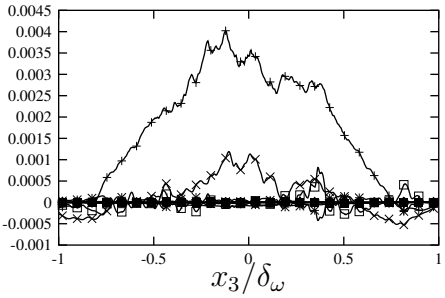

Figure 2.150: Case inert-0.7: Parts of the pressure-scrambling term Π_{Y3} computed with the Green function, normalized by $\rho_0 \Delta u/\delta_\omega$, symbols as in Fig. 2.148

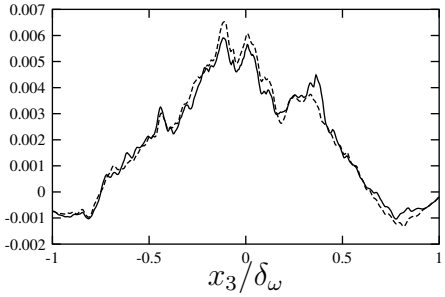

Figure 2.151: Case inert-0.7: Pressure-scrambling term Π_{Y3}, normalized by $\rho_0 \Delta u/\delta_\omega$, solid: computed with the help of the Green function with $f = f\left(\sum_{i=1}^{4} A_i + \sum_{i=1}^{3} B_i + \sum_{i=1}^{5} C_i\right)$, lines as in Fig. 2.149

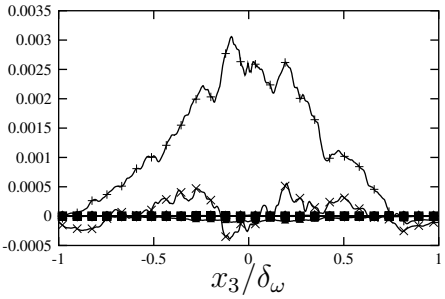

Figure 2.152: Case inert-1.1: Parts of the pressure-scrambling term Π_{Y3} computed with the Green function, normalized by $\rho_0 \Delta u/\delta_\omega$, symbols as in Fig. 2.148

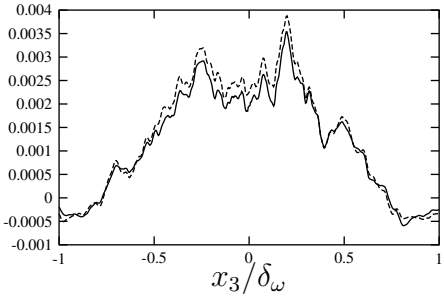

Figure 2.153: Case inert-1.1: Pressure-scrambling term Π_{Y3}, normalized by $\rho_0 \Delta u/\delta_\omega$, solid: computed with the help of the Green function with $f = f\left(\sum_{i=1}^{4} A_i + \sum_{i=1}^{3} B_i + \sum_{i=1}^{5} C_i\right)$, lines as in Fig. 2.149

split-up of Π_{Y3} in Fig. 2.148 is obtained for case inert-0.15. Since the results for the other pressure-scrambling terms are qualitatively the same, just Π_{Y3} is analyzed in the following. As for the pressure-strain correlations, only terms A_1 and A_2 contribute significantly to the complete correlation. The comparison of Π_{Y3} computed without terms C_6 and D with the exact term in Fig. 2.149, shows that the neglection of C_6 and D is justified. The same conclusions apply to the pressure-scrambling terms at higher convective Mach numbers (Figs. 2.150 to 2.153).

To obtain Figs. 2.154 to 2.156 modified source terms with constant density, equal to ρ_0 were

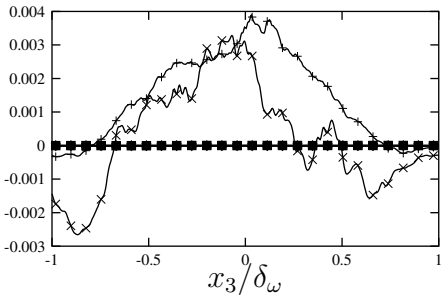

Figure 2.154: Case inert-0.15: Parts of the pressure-scrambling term Π_{Y3} computed with the Green function and with constant density ρ_0, normalized by $\rho_0 \Delta u/\delta_\omega$, symbols as in Fig. 2.148

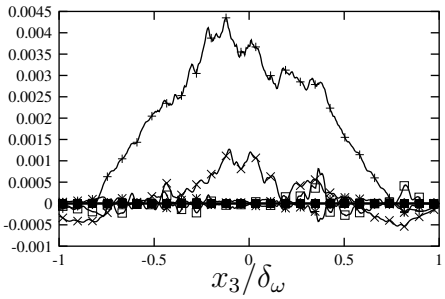

Figure 2.155: Case inert-0.7: Parts of the pressure-scrambling term Π_{Y3} computed with the Green function and with constant density ρ_0, normalized by $\rho_0 \Delta u/\delta_\omega$, symbols as in Fig. 2.148

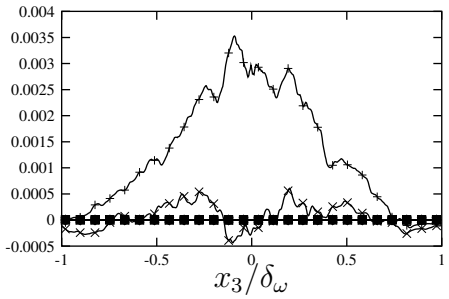

Figure 2.156: Case inert-1.1: Parts of the pressure-scrambling term Π_{Y3} computed with the Green function and with constant density ρ_0, normalized by $\rho_0 \Delta u/\delta_\omega$, symbols as in Fig. 2.148

inserted in Eq. (2.91). The reduction of terms A_1 and A_2 and therefore of the complete Π_{Y3} with increasing M_c is not removed by the modification of the source terms which leads to the conclusion that the reduction of the pressure-scrambling terms with compressibility is not a mean density effect, but caused by changes in the velocity field of the flow.

Spectra Figure 2.157 shows the one-dimensional, streamwise spectrum of the scalar, the oxygen mass fraction Y ($\hat{Y}'\hat{Y}'^*$) after averaging over directions x_2 and x_3. A small inertial range of the energy cascade with an approximate slope of $-5/3$ can be seen. There is no significant

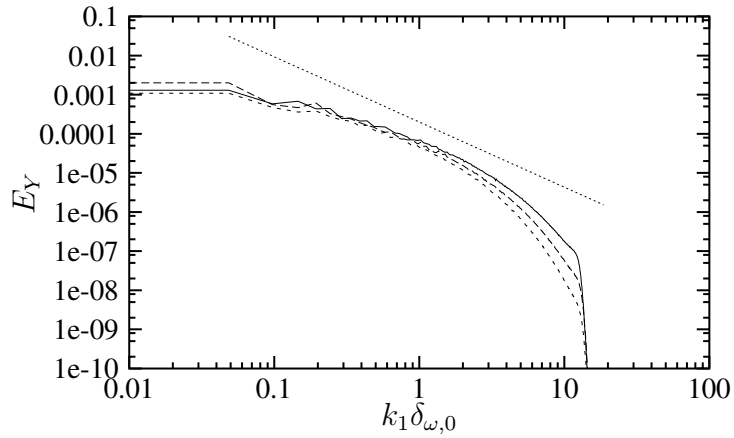

Figure 2.157: One-dimensional, streamwise spectrum of the oxygen mass fraction Y, solid: inert-0.15, dashed: inert-0.7, dotted: inert-1.1, the straight line has $-5/3$ slope

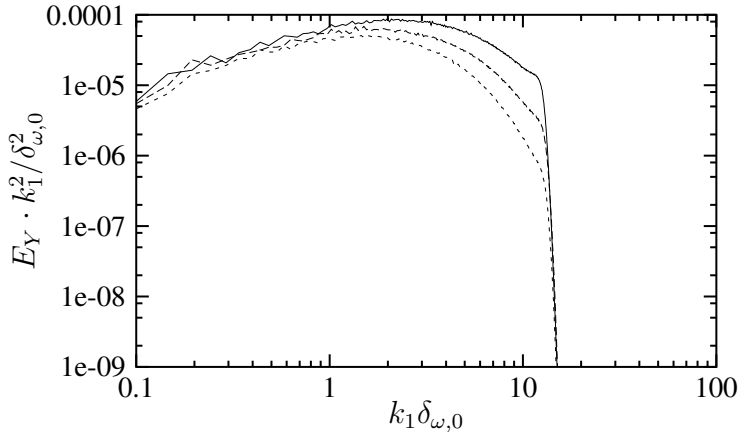

Figure 2.158: One-dimensional dissipation spectrum of the oxygen mass fraction Y (spectrum of Y multiplied with $(k_1\delta_{\omega,0})^2$), solid: inert-0.15, dashed: inert-0.7, dotted: inert-1.1

accumulation of energy in the highest wavenumbers which would be a sign of under-resolution. The behaviour with increasing compressibility corresponds to the one noticed for the spectra of other quantities (cf. Sect. 2.4.4.1), like the TKE: The energy content in the highest wavenumbers decreases when the convective Mach number rises. The scalar dissipation spectrum in Fig. 2.158, evaluated as $k_1^2 \hat{Y}' \hat{Y}'^*$, peaks at a higher wavenumber than the scalar energy spectrum and shows a similar behaviour for the highest wavenumbers with increasing compressibility.

2.4.4.3 Entrainment

In this section, the processes by which surrounding fluid enters the mixing layer and becomes a part of it is investigated. The focus is on the effects that compressibility has on this entrainment mechanism.

While entrainment has often been described as an engulfment of large packets of irrotational fluid from the surrounding non-turbulent region by the action of large-scale coherent structures followed by disintegration and acquisition of vorticity well within the turbulent region, a recent study by Mathew & Basu [105] showed that a circular mixing layer grows by nibbling, a fast, small-scale process occurring very close to the turbulent-nonturbulent interface. The engulfed fluid volume, on the contrary, was revealed to be very small compared to the total volume of the turbulent region. These results have been confirmed by subsequent PIV measurements in a laboratory jet [186].

In this section, studies similar to those found in [105] for a cylindrical, incompressible mixing layer are performed with the DNS data of the inert, plane mixing layers at different convective Mach number.

Measurement of volumes To numerically measure the engulfed fluid, one has to define first a criterion to distinguish between ambient fluid regions and the mixing layer which contains the engulfed fluid. Engulfed fluid lies inside the turbulent region but still has the scalar concentration and the low vorticity levels of the freestream fluid. Here, fixed thresholds are used to distinguish between ambient fluid, engulfed fluid and the rest of the mixing layer, which consists of mixed fluid. One threshold concerns the magnitude of the vorticity and one the scalar value. For the

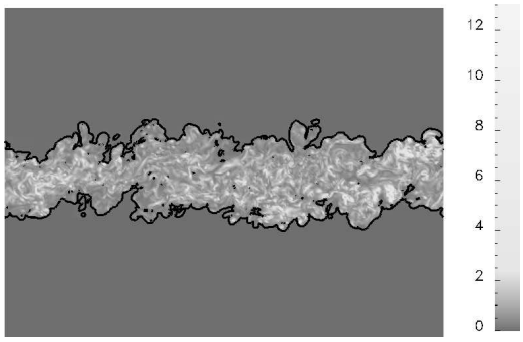

Figure 2.159: Case inert-0.15: Instantaneous vorticity field, normalized by $\langle\omega\rangle_{max}$, x_1-x_3-plane in the middle of the computational domain at $\tau_\omega = 286$, isoline at 0.1 is shown

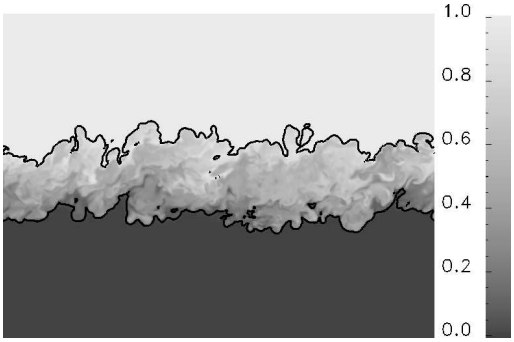

Figure 2.160: Case inert-0.15: Instantaneous mass fraction field of O_2, x_1-x_3-plane in the middle of the computational domain at $\tau_\omega = 286$, isolines $Y_{O2} = 0.05$ and 0.95 are shown

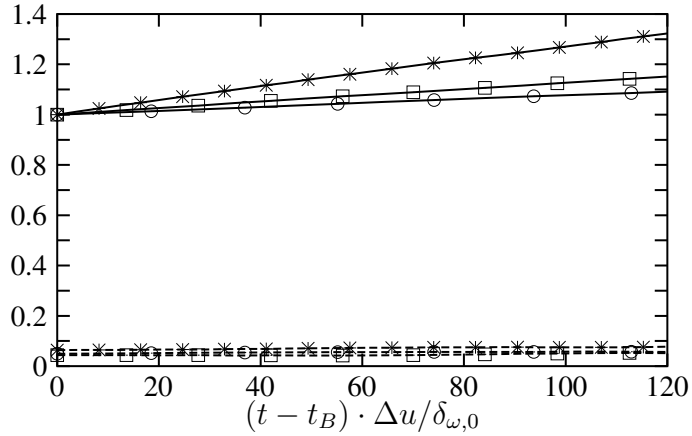

Figure 2.161: Based on vorticity thresholds: Mixing layer volume V_{ml} (solid) and engulfed volume V_{en} (dashed) vs. the normalized time passed since the beginning of the self-similar state at t_B. Volumes are normalized with the mixing layer volume at the beginning of the self-similar state, $V_{ml,B}$, $*$: inert-0.15, $\square$: inert-0.7, $\circ$: inert-1.1

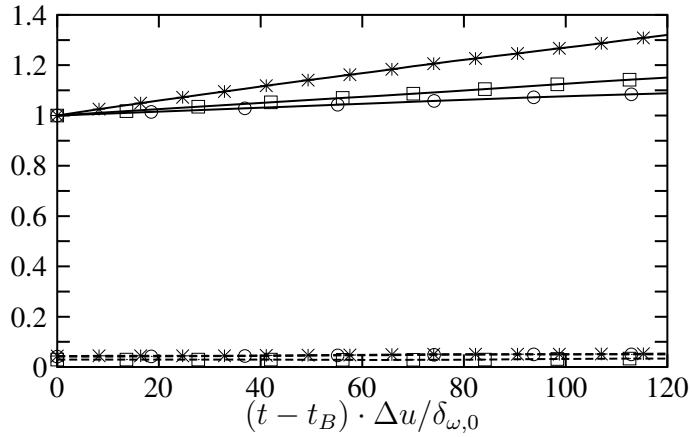

Figure 2.162: Based on mass fraction thresholds: Mixing layer volume V_{ml} (solid) and engulfed volume V_{en} (dashed) vs. the normalized time passed since the beginning of the self-similar state at t_B. Volumes are normalized with the mixing layer volume at the beginning of the self-similar state, $V_{ml,B}$. Symbols as in Fig. 2.161

vorticity, the threshold is set at $0.1\langle\omega\rangle_{max}$ with $\langle\omega\rangle_{max}$ denoting the maximum value of the spatially averaged vorticity at an instant. For the oxygen mass fraction, 0.95 is the threshold close to the oxygen-rich stream and 0.05 the one on the other side. Engulfed fluid has vorticity or scalar levels as in the ambient fluid but lies within the mixing layer. The thresholds used were identified as the most reliable thresholds nearest to the freestream levels by plotting isolines of the vorticity and the mass fraction and examining their sensitivity to small variations of the isoline value. For variations around the thresholds the changes were small, whereas larger variations led to large excursions of the isolines due to numerical noise. The choice of thresholds is also discussed in [105]. Figures 2.159 and 2.160 show such isolines for the vorticity and the oxygen mass fraction at the beginning of the self-similar state of case inert-0.15. When comparing Fig. 2.160 (isolines 0.05 and 0.95) with Fig. 2.3 (isolines 0.1 and 0.9), one can see that there are hardly any differences between the isolines 0.05 and 0.1 as well as 0.95 and 0.9.

Figures 2.161 and 2.162 show the growth of the mixing layer volume and of the engulfed volume from the beginning of the self-similar state. The mixing layer volume is the total volume minus the ambient fluid volume. The latter is computed by comparing grid point values against the thresholds, proceeding at each x_1-x_2-location from both freestream towards the mixing layer

until locations where the thresholds were crossed. All these locations constitute the ambient fluid volume. The engulfed volume consists of the grid points within the mixing layer, the values of which are below the threshold. The rest of the mixing layer can be considered the mixed volume. Figure 2.161 shows the curves based on the vorticity threshold ($0.1\langle\omega\rangle_{max}$) and Fig. 2.162 the ones based on the mass fraction thresholds (0.05 and 0.95). The conclusions from the two figures are the same: Both, mixing layer volume and engulfed volume, grow during the simulations. The growth rate of the mixing layer volume reduces with increasing M_c, and the growth rate of the engulfed volume is smaller than the one of the mixing layer volume at all M_c. Both growth rates are nearly constant throughout the self-similar state. In total, the engulfed volume is just a very small part of the mixing layer volume, around 6% for $M_c = 0.15$. This percentage even reduces with increasing M_c (5% for $M_c = 0.7$ and 4% for $M_c = 1.1$) which indicates that compressibility suppresses engulfment.

Visual thickness The visual thickness δ_{vis} is the distance in transverse direction between the two points where $\langle\omega\rangle = 0.1\langle\omega\rangle_{max}$ or, alternatively, where the spatially averaged mass fraction has the values 0.05 and 0.95. Its temporal development and the temporal development of a thickness computed from the mixing layer volume, $\delta_{vol} = V_{ml}/\left(L_1 \cdot L_2\right)$, is shown in Figs. 2.163 (based on vorticity thresholds) and 2.164 (based on mass fraction thresholds) for the self-similar state. At all convective Mach numbers, the growth rates of both thicknesses are nearly linear and equal. They decrease with increasing Mach number which is in agreement with other measurements of the mixing layer thickness, e.g. the momentum and vorticity thicknesses and with the Langley curve (cf. Sect. 2.4.2).

At all convective Mach numbers, the visual thickness is larger than the thickness derived from the mixing layer volume. This is due to intermittent outward ejections of vortical fluid from the mixing layer and can be understood when taking into account the different ways by which the two thicknesses are computed: In a laminar mixing layer, both thicknesses would coincide and represent the boundary of the mixing layer. In a turbulent flow, when there are a few ejections from the turbulent region to the non-turbulent surrounding, the mean boundary, computed by averaging the mixing layer volume, will move slightly. The shift is not very large as only few ejections are present. However, the ejections consist of core fluid and carry therefore high levels of vorticity and concentration. The consequence is that even though these events are not frequent, the average vorticity and concentration profiles are affected considerably and the visual thickness which is obtained from these profiles is larger than the thickness derived from the mixing layer volume. This intermittency effect is more pronounced when using vorticity thresholds (Fig. 2.163) to determine the mixing layer boundary than when using mass fraction thresholds (Fig. 2.164). Figures 2.163 and 2.164 also show that the higher the Mach number, the closer are the visual thickness and the thickness computed from the mixing layer volume which indicates a decrase of intermittency.

Measurement of densities Figure 2.165 shows the density of the mixing layer, the density of the engulfed volume and the density of the mixed volume which are determined based on the vorticity threshold. It can be seen that the mixing layer density and the density of the mixed volume decrease with increasing compressibility which is due to heating by dissipation. Shocklets, even

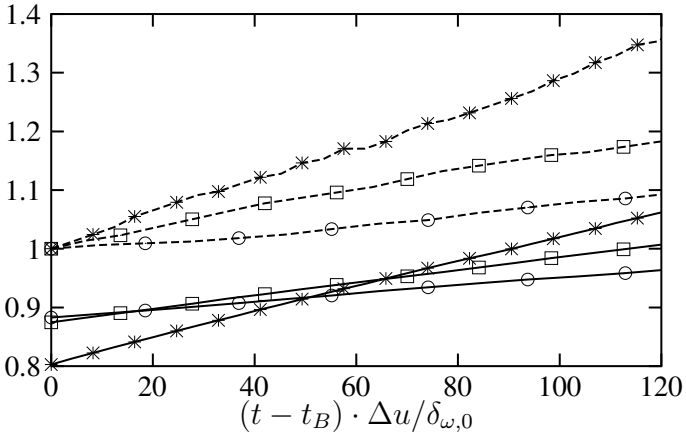

Figure 2.163: Based on vorticity thresholds: Thickness computed from mixing layer volume δ_{vol} (solid) and visual thickness δ_{vis} (dashed). Thicknesses are normalized by the visual thickness at the beginning of the self-similar state, $\delta_{vis,B}$. Symbols as in Fig. 2.161

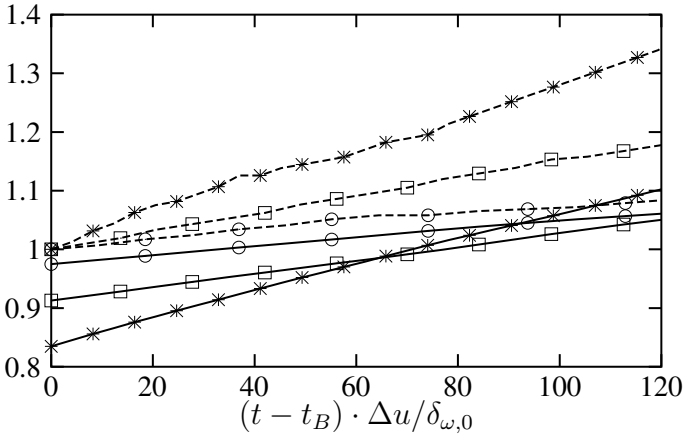

Figure 2.164: Based on mass fraction thresholds: Thickness computed from mixing layer volume δ_{vol} (solid) and visual thickness δ_{vis} (dashed). Thicknesses are normalized by the visual thickness at the beginning of the self-similar state, $\delta_{vis,B}$. Symbols as in Fig. 2.161

though present in the mixing layer at $M_c = 1.1$ (cf. Sect. 2.4.4.4), are not frequent enough to rise the density again.

The density of the engulfed volume is always higher than the density of the mixing layer, since it enters the mixing layer from the non-turbulent region where no heating due to dissipation takes place. However, the fact that the difference between the reference density ρ_0 and the density of the engulfed volume increases with increasing convective Mach number shows that dissipative heating is not completely absent within the engulfed volume.

For all convective Mach numbers, the density of the mixed volume is lower than the density of the complete mixing layer which includes also the engulfed volume. Since the density difference between the engulfed volume and the mixed volume increases with compressibility, the difference between the mixed volume density and the mixing layer density increases also.

Figure 2.166 shows the corresponding density curves whereby the regions are determined with the help of the mass fraction thresholds. It can be seen that the curves of the engulfed volume are all very close to the reference density ρ_0 now. This demonstrates that the two threshold definitions are not fully equivalent and that dissipative heating has less effect on the engulfed volume determined by the mass fraction criteria than on the one determined by the vorticity criteria.

In both figures, the density of the engulfed volume of the mixing layer at $M_c = 1.1$ has a rising

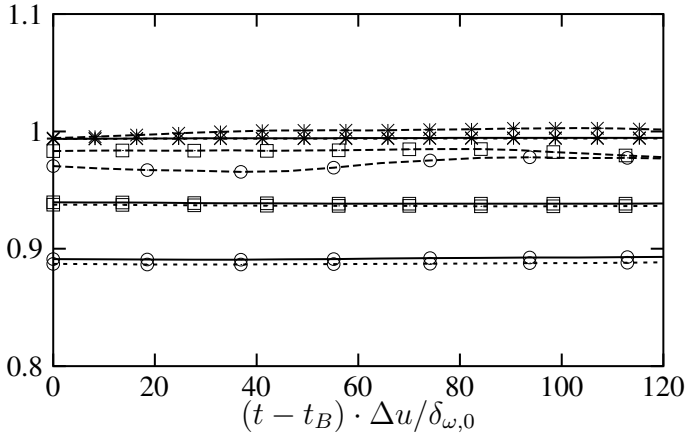

Figure 2.165: Based on vorticity thresholds: Mixing layer density ρ_{ml}/ρ_0 (solid), density of the engulfed volume, ρ_{en}/ρ_0 (dashed), and density of the mixed volume, ρ_{mix}/ρ_0 (dotted), vs. the normalized time passed since the beginning of the self-similar state at t_B. Symbols as in Fig. 2.161

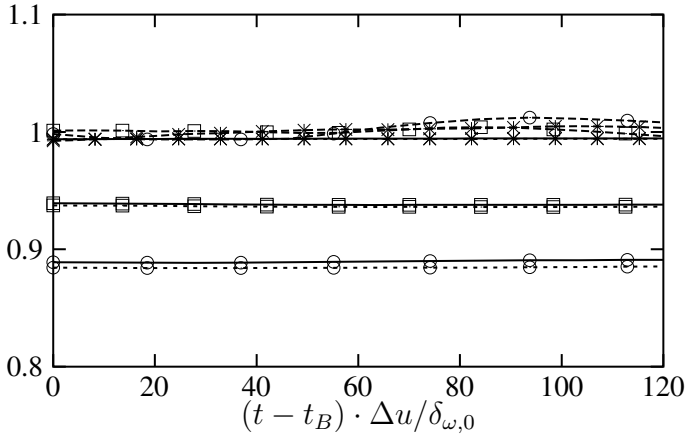

Figure 2.166: Based on mass fraction thresholds: Mixing layer density ρ_{ml}/ρ_0 (solid), density of the engulfed volume, ρ_{en}/ρ_0 (dashed), and density of the mixed volume, ρ_{mix}/ρ_0 (dotted), vs. the normalized time passed since the beginning of the self-similar state at t_B. Symbols as in Fig. 2.161

tendency and even exceeds the reference density in Fig. 2.166. It is assumed that this is due to compression processes like shocklets (cf. Sect. 2.4.4.4) that within the engulfed volume - in contrast to the complete mixing layer - overcome the density decrease by dissipation.

Particle statistics During the self-similar state pathlines of fluid particles were computed. To do so, the velocity components at the locations of the particles were integrated every time step, and the new positions of the particles were determined. The interpolation of the velocity field from the grid points to the locations of the particles was performed with a third order Taylor series 13-point scheme proposed by Yeung & Pope [191]. This scheme requires data at staggered grid points which were obtained by spectral (exact) interpolation in the periodic x_1- and x_2-directions and by sixth-order explicit interpolation in the x_3-direction [99]. In addition to the velocity components, the vorticity and the scalar mass fraction at the locations of the particles were also computed.

The initialization of the particles is done at times when the mixing layers are already turbulent but have not yet reached the self-similar state. Table 2.6 lists the number of the particles, the times at which they are initialized and their initial transverse positions for all test cases. Particles

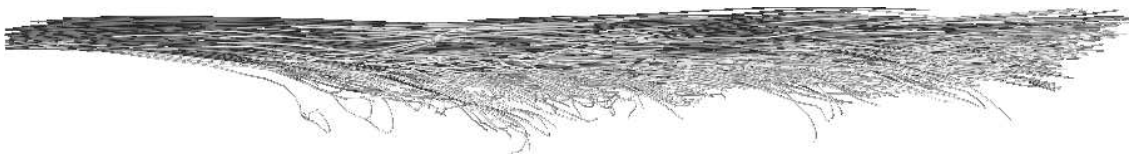

Figure 2.167: Particle tracks in the upper half of the computational domain during the self-similar state of inert-0.7

were placed at every 12th grid point in the x_1- and x_2-directions and at every 8th point in the x_3-intervals that are mentioned in table 2.6. These intervals were chosen such that initially nearly all particles are situated outside the mixing layer (defined by the vorticity criteria) but close to its edges.

In the following, it is investigated how the vorticity and the concentration grow along pathlines, examples of which are shown in Fig. 2.167. It was found by Mathew and Basu [105] that in a circular mixing layer, the growth of vorticity and concentration occurs close to the turbulent boundary, and that they are often relatively fast processes. To determine if a particle has entered the mixing layer, a lower and an upper threshold for the vorticity and the mass fraction are used. This also captures a transition stage between the non-turbulent and turbulent flow which would not be the case when using just one threshold, i.e. a sharp cut-off. The lower threshold for the vorticity is at $0.1\langle\omega\rangle_{\max}$, the upper one at $0.2\langle\omega\rangle_{\max}$. For the scalar value (oxygen mass fraction), the thresholds are 0.95 and 0.9 on the oxygen-rich side and 0.05 and 0.1 on the other.

In Table 2.7, statistical quantities for the particles during the self-similar state are listed. The first two rows are displacements in the direction of the mean shear between the locations when crossing the lower (subscript l) and upper (subscript u) thresholds. The values obtained with the vorticity thresholds have the index ω, while the ones obtained with the mass fraction thresholds have the index Y. For normalization, δ_{vis} at the time t_l at which the lower threshold was crossed has been used. The third and the fourth rows are the elapsed times between the crossing of the lower and the upper thresholds, and the last two rows are the times between the crossing of the vorticity and the mass fraction thresholds. The times are normalized by $t_{vis} = \delta_{vis}\left(t_l\right)/\Delta u$. In the last two rows, a $\delta_{vis}\left(t_l\right)$ has been used, which is the averaged value of the one determined with the vorticity and the one determined with the mass fraction. Only particles that are outside the visual thickness of the shear layer at the beginning of the self-similar period are considered. These are 14970 particles for case inert-0.15, 15764 for case inert-0.7 and 13335 for case inert-1.1. The sample size gives the number of particles which among these have crossed the respective thresholds and are therefore used to compute the respective statistical quantity.

Comparing the mean values in the first four lines of each test case with its considerably larger maximum, one can see that most of the threshold crossings occur quite fast and close to the boundary of the mixing layer. The means in the last two lines of each test case are positive which

Table 2.6: Particle parameters: N_P particles are initialized at $\tau_{\omega,PB}$. They are situated initially between $x_3 = x_{3,P1}$ and $x_{3,P2}$ and between $x_3 = x_{3,P3}$ and $x_{3,P4}$

	N_P	$\tau_{\omega,PB}$	$x_{3,P1}/\delta_{\omega,0}$	$x_{3,P2}/\delta_{\omega,0}$	$x_{3,P3}/\delta_{\omega,0}$	$x_{3,P4}/\delta_{\omega,0}$
inert-0.15	20480	209	-23.81	-11.19	10.68	23.30
inert-0.7	24576	404	-28.52	-13.55	13.21	28.18
inert-1.1	20480	843	-37.27	-24.82	21.96	34.41

is suggesting that the growth of vorticity occurs faster than the growth of mass fraction. This can be explained by the fact that the flow is governed by the velocity field from which the vorticity is computed. In summary, the statistics show that the growth of vorticity and concentration is a relatively fast process which is occuring close to the boundary of the turbulent region. This is consistent with the findings of [105] for the circular mixing layer and leads to the conclusion that nibbling, rather than engulfment is the process by which the mixing layer is growing.

At higher convective Mach number the fluid particles that start entering the mixing layer stay close to its edges for a longer time and are carried along before they penetrate inside. This can be seen from the elapsed times between the crossing of the lower and upper thresholds which are larger for the higher convective Mach numbers. In contrast to the times, the displacements in the first two lines of each test case do not change much with compressibility. While the particles at higher M_c are convected downstream near the edges of the mixing layer they are slowed down to a variable degree. This becomes clear when looking at the pdf of the local Mach number assembled at the time the upper vorticity threshold is crossed (Fig. 2.168) While it is narrow with a mean close to 0.15 when $M_c = 0.15$, the distribution at $M_c = 0.7$ is much broader and extends from slightly above 0.7 down to about 0.2. The whole mechanism can be seen as some kind of resistance that the compressible mixing layer as compared to the incompressible mixing layer offers towards fluid particles before they are penetrating the mixing layer. Entrainment, the process of ambient fluid acquiring vorticity, takes place at the very periphery of the turbulent region. Then, the growth rate is diminished as fluid packets spend a longer period at the turbulence

Table 2.7: Statistics of displacements and elapsed times for growth of vorticity and mixture fraction along particle pathlines

		Sample size	Mean	Max	Min
inert-0.15	$\left\|x_{3,\omega u} - x_{3,\omega l}\right\| / \delta_{vis}\left(t_l\right)$	4220	0.0250	0.5201	0
	$\left\|x_{3,Yu} - x_{3,Yl}\right\| / \delta_{vis}\left(t_l\right)$	3875	0.0337	0.5878	0
	$\left(t_{\omega u} - t_{\omega l}\right) / t_{vis}$	4220	0.4696	9.1722	0
	$\left(t_{Yu} - t_{Yl}\right) / t_{vis}$	3875	0.6144	8.6643	0
	$\left(t_{Yl} - t_{\omega l}\right) / t_{vis}$	4728	0.0301	5.4441	-5.8458
	$\left(t_{Yu} - t_{\omega u}\right) / t_{vis}$	3636	0.1419	6.3473	-9.1722
inert-0.7	$\left\|x_{3,\omega u} - x_{3,\omega l}\right\| / \delta_{vis}\left(t_l\right)$	12760	0.0290	0.6667	0
	$\left\|x_{3,Yu} - x_{3,Yl}\right\| / \delta_{vis}\left(t_l\right)$	11792	0.0423	0.6769	0
	$\left(t_{\omega u} - t_{\omega l}\right) / t_{vis}$	12760	0.8359	17.8751	0
	$\left(t_{Yu} - t_{Yl}\right) / t_{vis}$	11792	1.1986	19.4045	0
	$\left(t_{Yl} - t_{\omega l}\right) / t_{vis}$	13333	0.3018	9.8935	-13.2233
	$\left(t_{Yu} - t_{\omega u}\right) / t_{vis}$	11561	0.6607	17.7959	-17.7959
inert-1.1	$\left\|x_{3,\omega u} - x_{3,\omega l}\right\| / \delta_{vis}\left(t_l\right)$	5364	0.0205	0.3878	0
	$\left\|x_{3,Yu} - x_{3,Yl}\right\| / \delta_{vis}\left(t_l\right)$	2909	0.0362	0.5031	0
	$\left(t_{\omega u} - t_{\omega l}\right) / t_{vis}$	5364	0.7808	9.8476	0
	$\left(t_{Yu} - t_{Yl}\right) / t_{vis}$	2909	1.2193	9.8476	0
	$\left(t_{Yl} - t_{\omega l}\right) / t_{vis}$	5299	0.5850	7.9822	-8.2881
	$\left(t_{Yu} - t_{\omega u}\right) / t_{vis}$	2841	0.9067	9.8476	9.4413

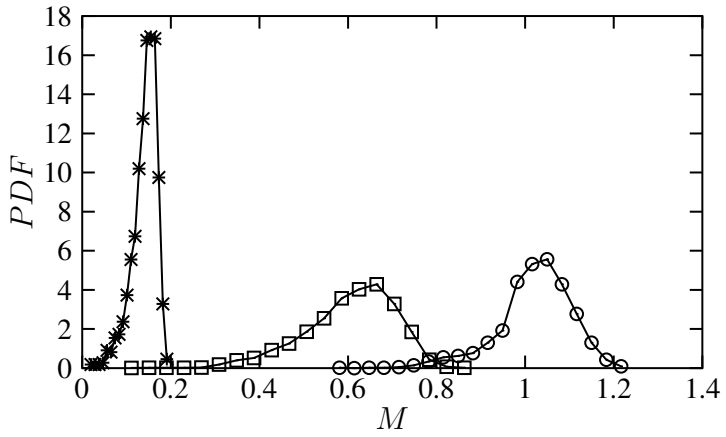

Figure 2.168: Pdfs of the local Mach number magnitude at the time when the particles are crossing the upper vorticity threshold. Symbols as in Fig. 2.161

boundary becoming a part of the turbulence. The lowered entrainment with compressibility goes in hand with the structural changes that are experiencing the turbulence interfaces with increasing M_c, which result in them being smoother than at low M_c (cf. next paragraph).

Fractal nature of the mixing layer interface It is of interest to see how the geometrical properties of the turbulent-nonturbulent interfaces of the mixing layer vary with compressibility and to see whether these changes can be related with the changes noticed concerning the entrainment. One question that arises in this context is whether the interfaces are fractal. Sreenivasan & Meneveau [173] performed measurements in turbulent shear flow and came to the conclusion that several aspects of turbulence, among others this very interface, can be described roughly by fractals. Mathew & Basu [105] argued that, if this were the case, the entrainment flux estimated on large scales could equal that summed from the actual small-scale processes due to the equilibrium across scales that is usually obtained in the self-preserving canonical shear layer.

Figures 2.169 to 2.174 show some of the interfaces that are investigated in the following. It is clearly visible how the dominant scales of the vorticity isosurfaces and the mass fraction isosurfaces increase with increasing M_c (cf. also Sect. 2.4.1). Close examination reveals that the surface has small, evenly distributed protrusions into the non-turbulent region at the lower convective Mach number, while at higher M_c the protrusions are thicker. In total, the observed changes in the dominant interface scales are consistent with the reduced entrainment and mixing layer growth at higher Mach numbers when the process is small-scale and occurs at the interface.

A quantitative characterization of the turbulence interface is obtained by measuring its fractal dimension. The evaluation of the fractal dimensions of the mixing layers is done in the following by finding the dimension D_2 of this interface, determined by vorticity or by mass fraction, within

Table 2.8: Fractal dimensions D of isosurfaces determined from the slopes of the curves in Figs. 2.175 to 2.176 and corresponding ones for $\omega = 0.2\langle\omega\rangle_{max}$ and $Y = 0.9$

	$\omega = 0.2\langle\omega\rangle_{max}$	$\omega = 0.1\langle\omega\rangle_{max}$	$Y = 0.9$	$Y = 0.95$
inert-0.15	2.56	2.41	2.41	2.35
inert-0.7	2.64	2.45	2.40	2.31
inert-1.1	2.68	2.49	2.46	2.37

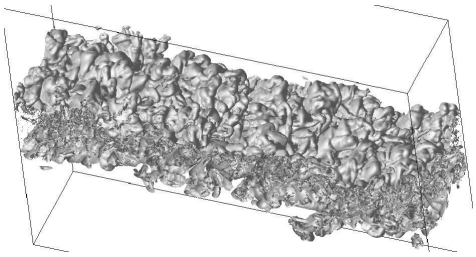

Figure 2.169: Case inert-0.15: Instantaneous isosurface of vorticity $\omega = 0.2\langle\omega\rangle_{max}$ at $\tau_\omega = 286$

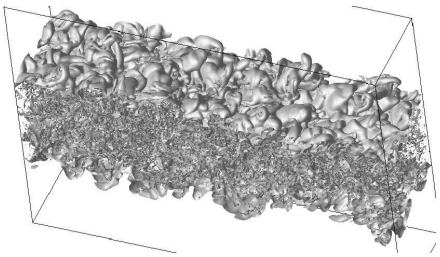

Figure 2.170: Case inert-0.7: Instantaneous isosurface of vorticity $\omega = 0.2\langle\omega\rangle_{max}$ at $\tau_\omega = 697$

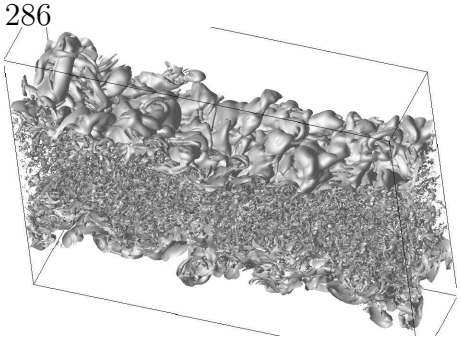

Figure 2.171: Case inert-1.1: Instantaneous isosurface of vorticity $\omega = 0.2\langle\omega\rangle_{max}$ at $\tau_\omega = 1098$

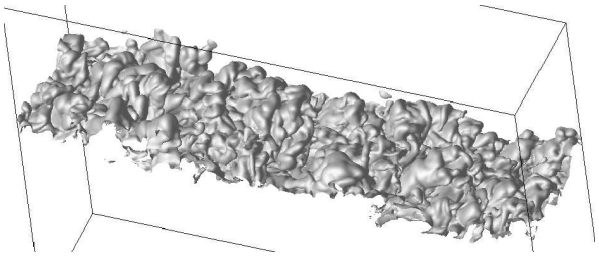

Figure 2.172: Case inert-0.15: Instantaneous isosurface of oxygen mass fraction $Y = 0.9$ at $\tau_\omega = 286$

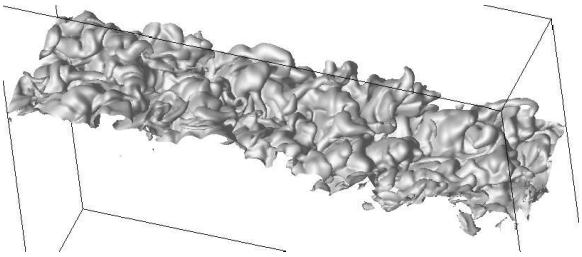

Figure 2.173: Case inert-0.7: Instantaneous isosurface of oxygen mass fraction $Y = 0.9$ at $\tau_\omega = 697$

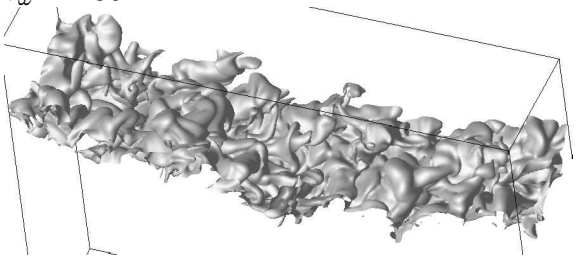

Figure 2.174: Case inert-1.1: Instantaneous isosurface of oxygen mass fraction $Y = 0.9$ at $\tau_\omega = 1098$

plane sections as for example shown in Figs. 2.159 and 2.160. Each section chosen is covered by squares of side $r_j = j\Delta x$ ($j = 1, 2, \ldots$) and the number of squares $N(r)$ which include a segment of the interface contour are counted. The dimension is $D_2 = \log N / \log(1/r)$, and is obtained as the slope of the curve $N(r)$ on log scales (e.g. Figs. 2.175 to 2.176). The dimension of the surface in three dimensions is then $D = D_2 + 1$.

Table 2.8 lists the fractal dimensions for the isosurfaces $\omega = 0.2\langle\omega\rangle_{max}$, $\omega = 0.1\langle\omega\rangle_{max}$, $Y = 0.9$ and $Y = 0.95$. All values are close to the value of 2.37 that Sreenivasan & Meneveau [173] determined for the turbulent-nonturbulent interface of a jet with the help of smoke pictures. However,

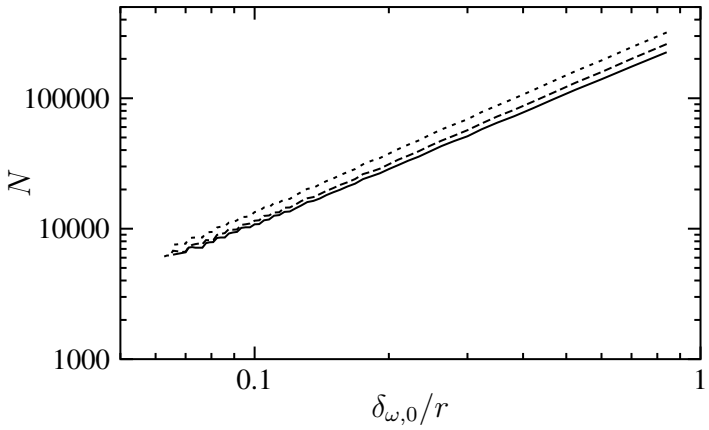

Figure 2.175: Number of squares N covering the interface $\omega = 0.1\langle\omega\rangle_{max}$ vs. $\delta_{\omega,0}/r$, averaged over the self-similar state, solid: inert-0.15, dashed: inert-0.7, dotted: inert-1.1

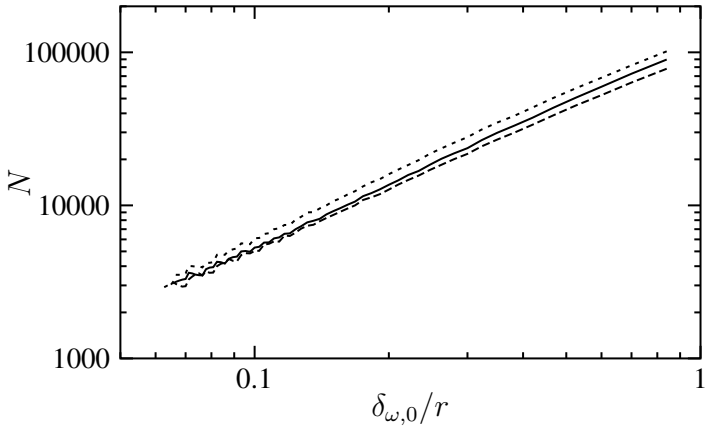

Figure 2.176: Number of squares N covering the interface $Y = 0.95$ vs. $\delta_{\omega,0}/r$, averaged over the self-similar state, solid: inert-0.15, dashed: inert-0.7, dotted: inert-1.1

small differences can be noticed between the different interfaces that are listed in table 2.8 and between the different convective Mach numbers. The fractal dimensions generally decrease when chosing the interface closer to the free-stream value, i.e. chosing $Y = 0.95$ instead of $Y = 0.9$ and $\omega = 0.1\langle\omega\rangle_{max}$ instead of $\omega = 0.2\langle\omega\rangle_{max}$, and the fractal dimensions of the vorticity isosurfaces are higher than the ones of the mass fraction isosurfaces due to less intermittency of the latter one. With increasing compressibility, the fractal dimension of the mixing layer interfaces defined by vorticity increases. For the mixing layer interfaces defined by mass frations, the fractal dimension decreases when rising M_c from 0.15 to 0.7, but increases again for $M_c = 1.1$. The fall between $M_c = 0.15$ and $M_c = 0.7$ is consistent with a decrease in entrainment and shear layer growth rate. The increase at $M_c = 1.1$ may be due to rapid changes in scale in the infrequent indentations, but the generally smoother boundary is nonetheless consistent with the observed further decrease in growth rate and entrainment by processes at the turbulence boundaries. This smoothening of the boundary could also account for the observed tapering off of the fall in growth rate at $M_c \approx 1.1$.

2.4.4.4 Shocklets

When monitoring the temporal development of the normalized, maximum pressure gradient during the simulations with different convective Mach numbers (Fig. 2.177), one notices that it is

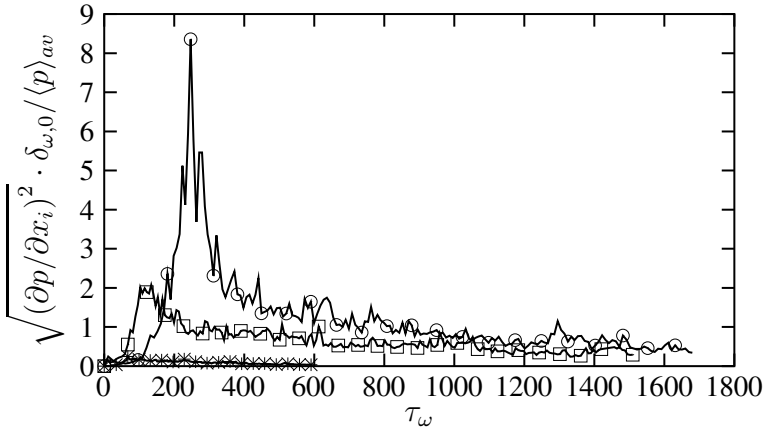

Figure 2.177: Temporal development of the maximum pressure gradient, normalized by $\langle p \rangle_{av}/\delta_{\omega,0}$, $*$: inert-0.15, $\square$: inert-0.7, $\circ$: inert-1.1

much higher for the mixing layer at $M_c = 1.1$ than for the ones at smaller convective Mach number. This is particularly the case during the initial development, but also later during the self-similar state where the peak values of the maximum pressure gradient of case inert-1.1 are about double the values of case inert-0.7. In Figure 2.177, the pressure gradient is normalized by $\langle p \rangle_{av}$, the box-averaged pressure, temporally averaged over the self-similar state. The high pressure gradients of the inert-1.1 case suggest the existence of so-called 'eddy shocklets', which are small shocklets that are associated with turbulent eddies.

Eddy shocklets were first observed in two- and three-dimensional simulations of isotropic turbulence [97, 127]. In two-dimensional simulations of mixing layers, shocklets were found to occur at convective Mach numbers higher than 0.7 [98, 159]. However, in 3D, the flow has another dimension in which it can change direction and thus avoid high pressure regions that are due to vortical motions. Therefore, shocks were only observed at considerably higher convective Mach numbers than in 2D, e.g. $M_c = 1.2$ [182] or 1.25 and larger [115]. Other authors [63], found shocklets only from $M_c = 1.54$, which they attribute on one hand to the influence of different initial conditions or the finite box size and on the other to the lack of a definitive criterion of when a pressure disturbance is really a shock. Experiments have also revealed the presence of shocklets in a counterflowing supersonic shear layer [125].

In order to detect possible shocklets in the simulation inert-1.1, locations with high pressure gradients and strongly negative dilatation are investigated in more detail, and it is checked whether the shock jump (Rankine-Hugeniot) relations apply. However, as Freund et al. [63] point out, they are not expected to hold exactly since they are derived for an ideal gas, and the shocklets in the simulation have a finite thickness and are not steady. However, despite these deficiencies, these and others authors [12], were able to verify the shock jump relations with an accuracy between 3 and 30 %.

The first structure that is investigated in the following occurs at $\tau_\omega = 1023$, which is shortly after the beginning of the self-similar state. The maximum pressure gradient at this instance is found at $x_1 = 0.30L_1$, $x_2 = 0.30L_2$, $x_3 = 0.32L_3$ and has an inclination of 6.4° with respect to the x_1-x_2-plane and an inclination of 10.3° with respect to the x_1-x_3-plane. Since these angles are small, the shock jump relations are verified with the help of the values along a line, parallel to the x_1-axis, through the location of the maximum pressure gradient. Figures 2.178 to 2.179 show the pressure gradient, the pressure, the density and the temperature along this line. In these figures, every fourth grid point is shown which demonstrates that the shock is well resolved by five grid-points.

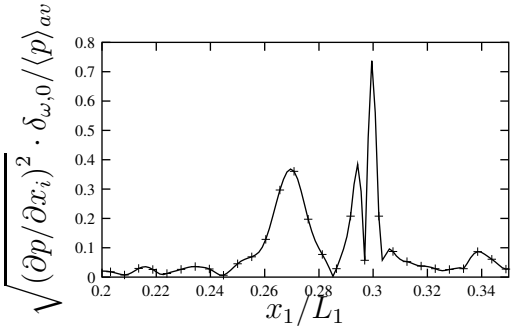

Figure 2.178: Case inert-1.1: Pressure gradient normalized by $\langle p \rangle_{av}/\delta_{\omega,0}$ on a line parallel to the x_1-axis through $x_2 = 0.30L_2$ and $x_3 = 0.32L_3$ at $\tau_\omega = 1023$. Every 4th grid point is shown

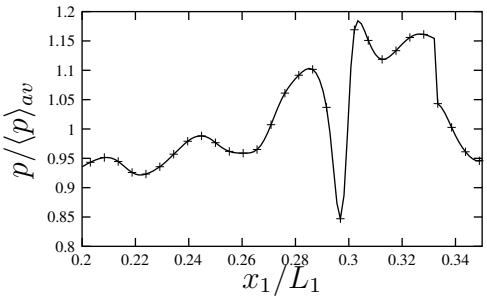

Figure 2.179: Case inert-1.1: Pressure normalized by $\langle p \rangle_{av}$ on a line parallel to the x_1-axis through $x_2 = 0.30L_2$ and $x_3 = 0.32L_3$ at $\tau_\omega = 1023$. Every 4th grid point is shown

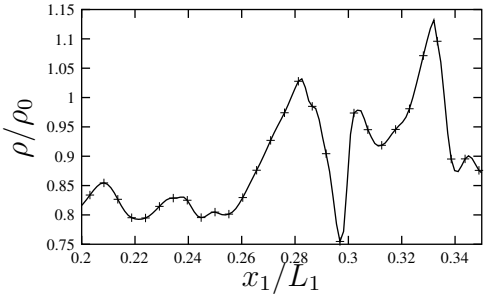

Figure 2.180: Case inert-1.1: Density in x_1-direction normalized by ρ_0 on a line parallel to the x_1-axis through $x_2 = 0.30L_2$ and $x_3 = 0.32L_3$ at $\tau_\omega = 1023$. Every 4th grid point is shown

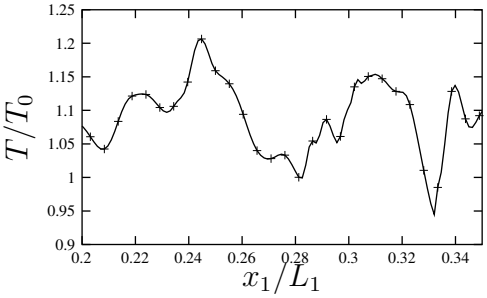

Figure 2.181: Case inert-1.1: Temperature normalized by T_0 on a line parallel to the x_1-axis through $x_2 = 0.30L_2$ and $x_3 = 0.32L_3$ at $\tau_\omega = 1023$. Every 4th grid point is shown

Therefore, no Gibbs-phenomenon due to under-resolution occurs. Computing ratios with the minimum and maximum values to the left and right side of the shock at $x_1 = 0.30L_1$, one obtains: $p_{max}/p_{min} = 1.398$, $\rho_{max}/\rho_{min} = 1.296$ and $T_{max}/T_{min} = 1.089$. With the shock relations for an ideal gas ($\gamma = 1.4$), one would obtain a density ratio of 1.269 and a temperatur ratio of 1.102 for the same pressure ratio which is a difference of less than $2.5\ \%$ from the actual values. The corresponding upstream normal shock number would be 1.158. However, when checking it, one has to take into account that the shock is not necessarily stationary with respect to the grid and that its speed is unknown. According to Blaisdell et al. [12], it can be checked anyway with the help of the velocity jump across the shock, $u_a - u_b$, which is Galilean invariant and consequently independent of the shock velocity. When the shock does not contain any mass, i.e. is very thin, the

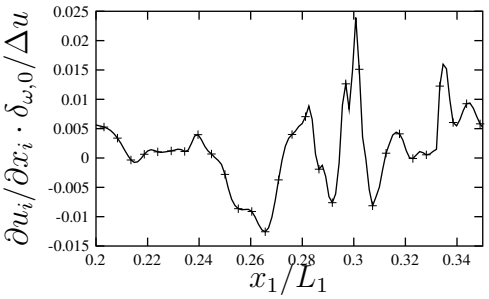

Figure 2.182: Case inert-1.1: Dilatation normalized by $\Delta u/\delta_{\omega,0}$ on a line parallel to the x_1-axis through $x_2 = 0.30L_2$ and $x_3 = 0.32L_3$ at $\tau_\omega = 1023$. Every 4th grid point is shown

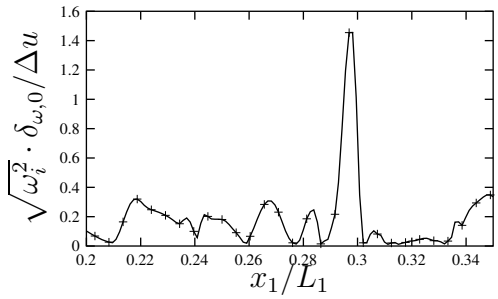

Figure 2.183: Case inert-1.1: Vorticity normalized by $\Delta u/\delta_{\omega,0}$ on a line parallel to the x_1-axis through $x_2 = 0.30L_2$ and $x_3 = 0.32L_3$ at $\tau_\omega = 1023$. Every 4th grid point is shown

velocity jump remains even uninfluenced by a shock acceleration. If v_a and v_b are the velocities relative to the moving shock, it therefore holds that $u_a - u_b = v_a - v_b = c_a M_a^{rel} - c_b M_b^{rel}$ and that M_b^{rel} is a known function of M_a^{rel} (e.g. [51]):

$$\left(M_b^{rel}\right)^2 = \frac{1 + \left[(\gamma - 1)/2\right]\left(M_a^{rel}\right)^2}{\gamma\left(M_a^{rel}\right)^2 - \left[(\gamma - 1)/2\right]} \tag{2.92}$$

With u_a, the velocity in the direction of the maximum pressure gradient (normal to the shock) evaluated at the location of the minimum pressure and u_b, the velocity in the same direction at the location of the maximum pressure, as well as the correspoding speeds of sound, c_a and c_b, a Mach number of 1.147 is obtained which is less than $1\ \%$ difference from the previously obtained value. However, the next example will show that such a high precision is rather incidential and cannot generally be expected since, among other deficiencies, the states on both sides of the shock are not uniform . Nevertheless, shocklets seem to be present in the mixing layer at $M_c = 1.1$. Figure 2.182 shows the dilatation along the line along which the shock jump conditions have been verified. Next the expected minimum in the dilatation at the location where the pressure rises steeply, there is an even more marked dilatation maximum on the right side of the shocklet where the pressure falls. The peak of the vorticity, shown in figure 2.183, is much larger than the magnitude of the dilatation extrema, which has also been noticed by [63].

The other compressible structure, that is further investigated in the following, manifests the highest pressure gradient during the self-similar state. It is found at $x_1 = 0.02L_2$, $x_2 = 0.38$, $x_3 = 0.31L_3$ and $\tau_\omega = 1295$. The maximum pressure gradient has an inclination of $4.93°$ with respect to the x_1-x_2-plane and an inclination of $38.5°$ with respect to the x_1-x_3-plane. Therefore, it is appropriate to verify the shocklet jump conditions on a line in the x_1-x_2-plane which has an inclination of $45°$ with respect to the x_1-x_3-plane. Figures 2.184 to 2.187 show thermodynamic quantities along this line on which the shocklet is situated at $\left(x_1^2 + x_2^2\right)^{0.5} = 0.093\left(L_1^2 + L_2^2\right)^{0.5}$. It is found that $p_{max}/p_{min} = 1.835$, $\rho_{max}/\rho_{min} = 1.874$ and $T_{max}/T_{min} = 1.119$. With the shocklet relations for an ideal gas ($\gamma = 1.4$), one would obtain with the same pressure ratio $\rho_{max}/\rho_{min} = 1.533$, which is a difference of $22\ \%$ to the actual value and $T_{max}/T_{min} = 1.197$, which is $6.5\ \%$ difference. The upstream normal Mach number would be 1.310. Again, this Mach number can be verified with the help of the velocity jump that is the same as in a moving reference frame. With the values u_a, u_b, c_a and c_b inserted in Eq. (2.92), one obtaines $M_{1,rel} = 1.137$,

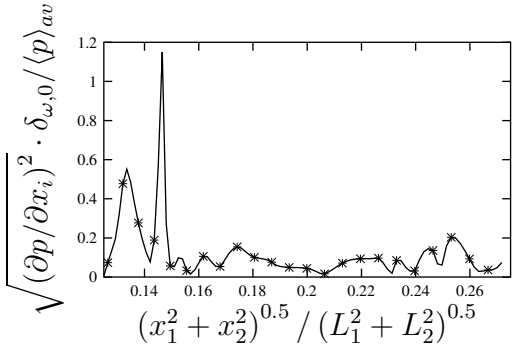

Figure 2.184: Case inert-1.1: Pressure gradient normalized by $\langle p\rangle_{av}/\delta_{\omega,0}$ on a line through $x_1 = 0.02L_2$, $x_2 = 0.38$ and $x_3 = 0.31L_3$ (in x_1-x_2-plane, inclined $45°$ to the x_1-x_3-plane) at $\tau_\omega = 1295$. Every 4th grid point is shown

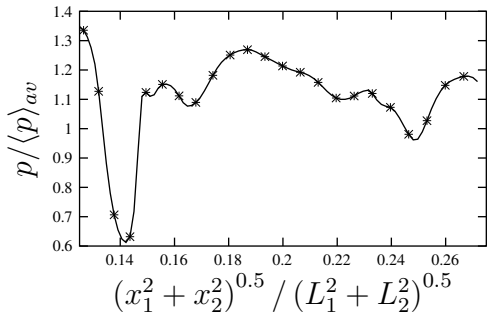

Figure 2.185: Case inert-1.1: Pressure normalized by $\langle p\rangle_{av}$ on a line through $x_1 = 0.02L_2$, $x_2 = 0.38$ and $x_3 = 0.31L_3$ (in x_1-x_2-plane, inclined $45°$ to the x_1-x_3-plane) at $\tau_\omega = 1295$. Every 4th grid point is shown

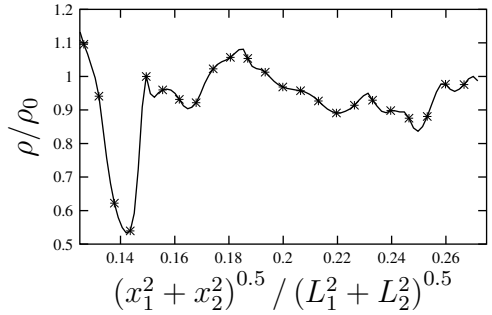

Figure 2.186: Case inert-1.1: Density in x_1-direction normalized by ρ_0 on a line through $x_1 = 0.02L_2$, $x_2 = 0.38$ and $x_3 = 0.31L_3$ (in x_1-x_2-plane, inclined $45°$ to the x_1-x_3-plane) at $\tau_\omega = 1295$. Every 4th grid point is shown

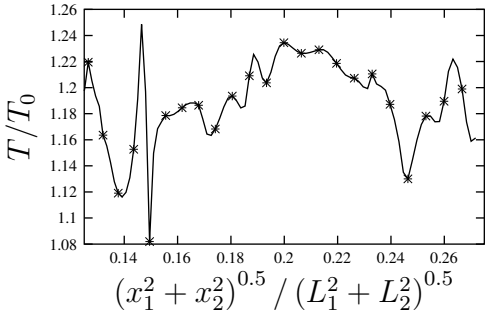

Figure 2.187: Case inert-1.1: Temperature normalized by T_0 on a line through $x_1 = 0.02L_2$, $x_2 = 0.38$ and $x_3 = 0.31L_3$ (in x_1-x_2-plane, inclined $45°$ to the x_1-x_3-plane) at $\tau_\omega = 1295$. Every 4th grid point is shown on

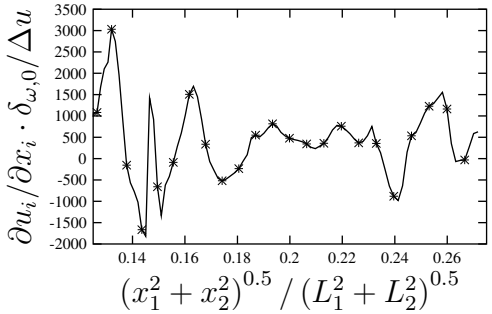

Figure 2.188: Case inert-1.1: Dilatation normalized by $\Delta u/\delta_{\omega,0}$ on a line through $x_1 = 0.02L_2$, $x_2 = 0.38$ and $x_3 = 0.31L_3$ (in x_1-x_2-plane, inclined $45°$ to the x_1-x_3-plane) at $\tau_\omega = 1295$. Every 4th grid point is shown

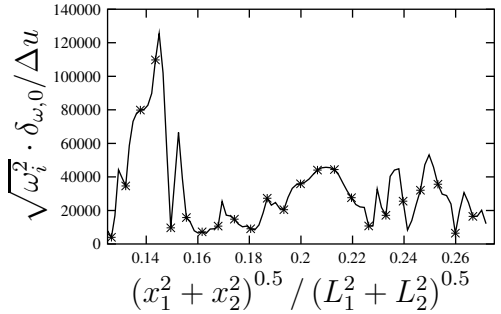

Figure 2.189: Case inert-1.1: Vorticity normalized by $\Delta u/\delta_{\omega,0}$ on a line through $x_1 = 0.02L_2$, $x_2 = 0.38$ and $x_3 = 0.31L_3$ (in x_1-x_2-plane, inclined $45°$ to the x_1-x_3-plane) at $\tau_\omega = 1295$. Every 4th grid point is shown

which is a difference of $13\,\%$ to the previously estimated value. Therefore, the verification of the Rankine-Hugeniot relations can be considered successful and the compressible structure can be called a shocklet. Figures 2.188 and 2.189 show the dilatation and the vorticity and confirm the observations already made: While there is a local minimum of the dilatation at the location of the shocklet, a local maximum is situated right next to it. A vorticity maximum, which is much larger in magnitude than the dilatation extrema, is found close to the shocklet.

Figure 2.190 presents the instantaneous dilatation field together with the pressure isolines in the

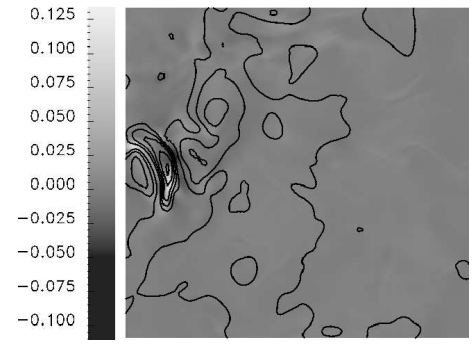

Figure 2.190: Case inert-1.1: Instantaneous dilatation field and pressure isolines, x_1-x_2-plane through $x_3 = 0.49L_3$ at $\tau_\omega = 1295$. Dilatation is normalized by $\delta_{\omega,0}/\Delta u$

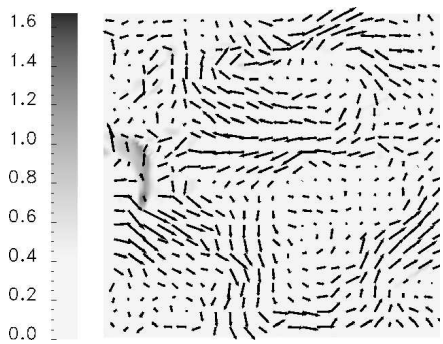

Figure 2.191: Case inert-1.1: Instantaneous magnitude of vorticity and velocity vectors, x_1-x_2-plane through $x_3 = 0.49L_3$ at $\tau_\omega = 1295$. Vorticity is normalized by $\delta_{\omega,0}/\Delta u$

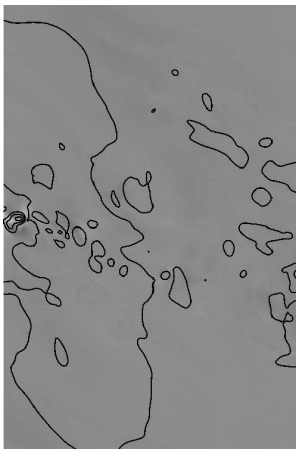

Figure 2.192: Case inert-1.1: Instantaneous dilatation field and pressure isolines, x_1-x_3-plane through $x_2 = 0.59L_2$ at $\tau_\omega = 1295$. Scale as in Fig. 2.190

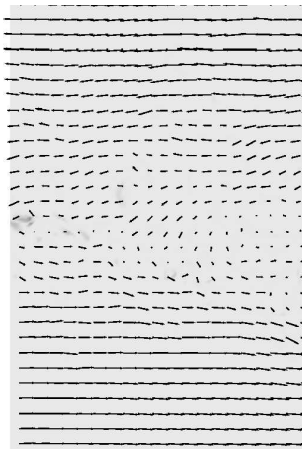

Figure 2.193: Case inert-1.1: Instantaneous magnitude of vorticity and velocity vectors, x_1-x_3-plane through $x_2 = 0.59L_2$ at $\tau_\omega = 1295$. Scale as in Fig. 2.191

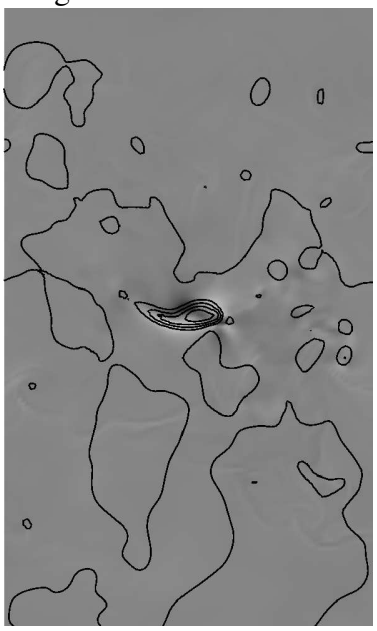

Figure 2.194: Case inert-1.1: Instantaneous dilatation field and pressure isolines, x_2-x_3-plane through $x_1 = 0.03L_1$ at $\tau_\omega = 1295$. Scale as in Fig. 2.190

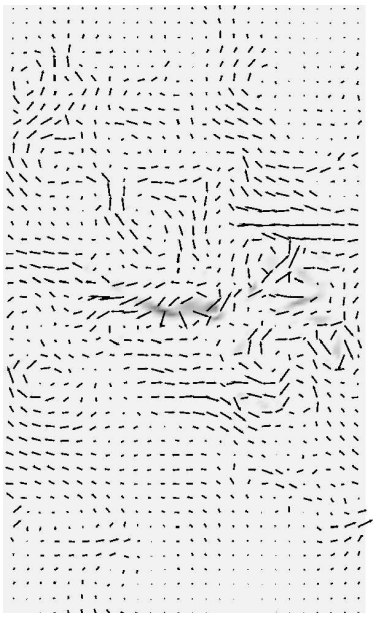

Figure 2.195: Case inert-1.1: Instantaneous magnitude of vorticity and velocity vectors, x_2-x_3-plane through $x_1 = 0.03L_1$ at $\tau_\omega = 1295$. Scale as in Fig. 2.191

x_1-x_2-plane in which the shocklet is situated. The shocklet is on the left side of the section which is shown. It can be seen how close the dilatation minimum at the location of the shocklet and a maximum are situated next to each other. Fig. 2.191 shows the velocity vectors and the vorticity field in the same part of the domain. The change of velocity direction by the shocklet as well as the vortical structures that are causing it are clearly visible. Figures 2.192 and 2.193 show x_1-x_3-cuts through the shocklet. In this view, it is only visible as a kind of point (in the middle on the far left side of the figure) and one could think it had a pencil-like shape. However, the other figures (e.g. Figs. 2.190 and 2.191) reveal its curved nature. Blaisdell et al. [12] suggested a mechanism for the formation of shocklets based on their observation from instantaneous pressure and vorticity fields: Most of the shocklets in their simulations seem to be caused by vortex motions which transport fluid in the direction of the mean shear. This brings together high-speed and low-speed fluid and the collision caused strong compressions and shock waves. In our simulation such

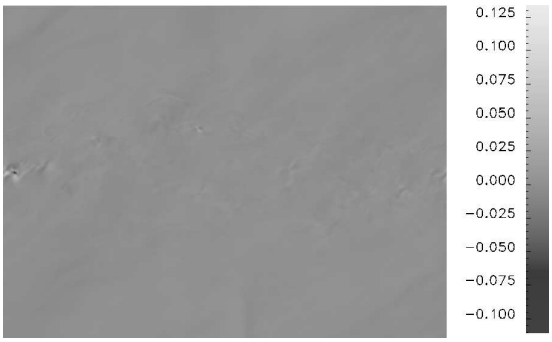

Figure 2.196: Case inert-1.1: Instantaneous dilatation field, x_1-x_3-plane through $x_2 = 0.59L_2$ at $\tau_\omega = 1295$. Dilatation is normalized by $\delta_{\omega,0}/\Delta u$

Figure 2.197: Case inert-1.1: Instantaneous pressure gradient field, x_1-x_3-plane through $x_2 = 0.59L_2$ at $\tau_\omega = 1295$. Pressure gradient is normalized by $\delta_{\omega,0}/\langle p \rangle_{av}$

vortical motions, which are transporting fluid in the direction of the shear, are visible in Fig. 2.193, too. Figs. 2.194 and 2.195, x_2-x_3-cuts, reveal them even more clearly. The superposition of the downwashs of various vortical structures cause sudden changes of the velocity direction and lead to the formation of the shocklet.

Finally, Figs. 2.196 and 2.197 show the complete computational domain. The recently investigated shocklet is visible to the extreme left. The figures demonstrate that neither extremely high pressure gradients nor dilatation minima are very frequent. Therefore, the shocklets in the simulation inert-1.1 do not seem to play a major role for the overall dynamics which is confirmed by the fact that the pressure dilatation is small even at $M_c = 1.1$ and the decreasing tendency of the dilatational dissipation lingers between $M_c = 0.7$ and $M_c = 1.1$ despite the presence of shocklets (cf. Sect. 2.4.4.1).

2.5 Summary and conclusions

In this chapter, DNS of turbulent, temporally evolving, inert mixing layers at different convective Mach numbers ($M_c = 0.15$, 0.7 and 1.1) - equivalent to different levels of compressibility - have been described and analyzed. The particular focus of the study is on the effects that compressibility has on the turbulence in general, on scalar mixing and entrainment. All simulations have been performed over a sufficiently long period of time which allowed the attainment of a self-similar state with constant momentum thickness growth rates. Statistics have been taken over this state during which profiles of adequately normalized flow quantities collapse.

Instantaneous contour plots of the scalar, i.e. species mass fraction, have shown a smoothening of the field by compressibility and an increase in the visible length scales of the turbulence interfaces with increasing M_c. This stabilizing effect of compressibility has manifested itself also in reduced mixing layer growth rates which are a consequence of reduced Reynolds stresses and reduced turbulent kinetic energy. A reduction of all main terms in the Reynolds stress transport equations and the transport equation of the turbulent kinetic energy with increasing M_c has also been noticed, and an analysis of the corresponding transversely integrated terms has shown that the pressure-strain correlation of the streamwise Reynolds stress is directly connected to the momentum thickness growth rate and responsible for its attenuation by compressibility. Changes in

the fluctuating pressure field have been identified to be the reason for the decrease of all pressure-strain correlations with increasing M_c. Since the pressure-strain correlations are responsible for the redistribution of turbulent kinetic energy from the streamwise component to the transverse and spanwise components, this mechanism is also hampered by increasing Mach numbers. Their significant influence on the pressure-strain correlations demonstrates that any attempts of Reynolds stress closure for compressible turbulence must pay particular attention to the modeling of the pressure-strain rate correlations. A further analysis of the Poisson equation, which governs the fluctuating pressure field when acoustic effects can be neglected, has shown with the help of a Green function that the reduction of the pressure-strain correlations and other pressure-related correlations in the investigated Mach number range is predominantly caused by changes in the velocity field itself. Explicit compressibility terms, e.g. the dilatational dissipation rate and the pressure-dilatation correlation, have been found to have negligible influence on the flow field even when shocklets are present as it is the case for the simulation with $M_c = 1.1$.

Concerning the scalar mixing, i.e. the mixing of the inert chemical species oxygen and nitrogen, a general decrease with Mach number and a reduction of scalar fluctuations within the mixing layer have been observed. Pdfs of the oxygen mass fraction at different transverse locations within the mixing layers have confirmed that outside fluid penetrates less deeply into the mixing layer, the higher the convective Mach number is. This implies that there is a higher level of intermittency for the quasi-incompressible mixing layer than for the compressible one.

A closer study of the entrainment mechanism, i.e. the way by which the mixing layer acquires surrounding fluid, has shown that this process happens very close to the mixing layer edge at all convective Mach numbers under investigation. The amount of fluid that is engulfed within the mixing layer before it becomes part of it, i.e. before it adopts the vorticity level and scalar concentrations that are typical for the mixed fluid, is small and reduces further with increasing Mach number. This has been confirmed further by the investigation of pathlines of fluid particles which enter the mixing layer from outside. Changes of the particle properties (vorticity and scalar concentrations) have occured close to the mixing layer edge. At low M_c, the time that elapses between the entering of the mixing layer and the instant at which the vorticity value and the scalar concentration of the particle crosses a certain threshold, which indicates that the fluid particle has become part of the mixing layer, is short. However, this time increases with increasing M_c and confirms the hampering of the entrainment mechanism by compressibility which in total seems to be detrimental for the combustion that depends on a proper mixing of fuel and oxidizer. This suggestion is further investigated and confirmed in Chapter 3.

3 DNS of infinitely fast reacting compressible turbulent shear layers

3.1 Introduction and literature survey

In most practical combustion applications, like aircraft or car engines, the combustion takes place in a turbulent flow. Therefore, it is important to understand the interaction between turbulence and combustion including chemical, thermodynamical and fluid mechanical processes. On one hand, turbulence leads to increased mixing which speeds up the overall reaction rate by stretching and wrinkling of the reaction zone. On the other hand, the density and pressure changes caused by the heat release of the reaction can significantly affect the turbulence. Compressibility further complicates the mixing process.

The emphasis of the present study is on how heat release influences turbulence. The effects of compressibility without combustion and heat release on plane, temporally developing mixing layers were subject of Chapter 2. In the following sections, it is studied how these effects are altered by heat release. It is clear that heat release leads to a density reduction, an increase in kinematic viscosity and therefore a coupling of fluid dynamics with chemical kinetics. However, it is not immediately obvious how heat release would influence the growth and entrainment of the mixing layer. One might expect, for example, that dilatation and consequent displacement effects caused by an increase in temperature in the mixing zone would increase the rate of growth.

As the influence of turbulence and compressibility on the reaction rate is not subject of investigation in this chapter, the chemistry is simplified with the reaction-sheet approximations of Burke & Schumann [22] by assuming a one-step, infinitely fast, irreversible reaction between hydrogen and oxygen. This assumption results in the turbulent mixing and molecular diffusion controlling the reaction rate. Therefore, all changes to these mechanisms, for example by compressibility, directly influence the combustion process and are of interest for practical applications like scramjets.

The investigated reacting mixing layer is a representative of a diffusion flame, where fuel and oxidizer are separated by the flame. Both come into contact in the reaction zone due to molecular diffusion and turbulent motion. An overview over various DNS of diffusion flames can be found in [180].

In the past, extensive experimental work has been dedicated to the objective of understanding the effects of the fluid dynamics on mixing and on reaction rates [18, 96, 118]. In these shear layer studies the density was constant to avoid the reverse effects, namely the influences of the chemistry, in particular the heat release, on the development of the velocity field. This was realized by little heat release. The experiments showed that the reaction products were concentrated in large, spanwise coherent structures. Three-dimensional effects were also found to be important with an increase in product formation coinciding with the development of three-dimensional motions in

the flow [18]. Masutani & Bowman [104] focused on the early stages of mixing layer development and found that the fluid exists in three states: tongues of unmixed free-stream fluid which, occasionally, stretch across the layer, finite-thickness interfacial diffusion zones of mixed fluid which border the parcels of unmixed fluid and regions comprising fluid of nearly homogeneous composition.

Fewer mixing layer experiments were performed with significant heat release. These experiments served to understand how the combustion processes affect the flow field, and, in particular, the layer growth, entrainment, and large-scale structure dynamics. McMurtry & Riley [108] found the density reduction to suppress the turbulent shear stress, the shear layer growth rate and the generation of TKE. Hermanson & Dimotakis [72] confirmed that the heat release resulted in a slower growth rate and noticed a decrease in the mass entrained which they attributed to a reduction in the turbulent shear stress representing a decrease in turbulent momentum transport. They found large-scale structures to persist in the shear layer at all levels of heat release, and large hot structures to be separated by cold tongues of free-stream fluid penetrating deep into the layer.

All these experiments were realized in the incompressible regime. Even fewer investigations took into account both, heat release and compressibility. Erdos et al. [52] investigated compressible reacting mixing layers ($M_c = 0.86$ and 2.5), but reported only measurements of wall static pressure and heat flux. Barlow et al. [4] performed experiments with annular reacting mixing layers in the near field of supersonic jets (from $M_c = 0.1$ to $M_c = 0.4$) and found a lower degree of organization with increasing compressibility, similar to non-reacting flows. However, the authors did not exclude influences of the Reynolds number which was higher for the compressible case. Miller et al. [114] investigated compressible, reacting mixing layers at $M_c = 0.32$, 0.35 and 0.7 and found them to have structural features consistent with those observed in inert mixing layers at similar M_c. They concluded that higher compressibility leads to a more disorganized, three-dimensional structure. Consequences were, for example, a change from non-marching scalar pdfs to marching scalar pdfs and a beneficial effect on combustion due to changes in the entrainment process. However, these authors took into account only moderate heat release.

On the numerical side, three-dimensional DNS of temporally developing reacting mixing layers were performed and analyzed by Riley et al. [151], McMurtry et al. [109], Planché & Reynolds [141], Miller et al. [115], de Bruyn Kops et al. [38] and recently by Pantano et al. [124]. Day et al. [35] simulated spatially developing, compressible reacting mixing layers. Additionally, many two-dimensional investigations can be found in the literature, for example Givi et al. [67] who reported reduced mixing with both compressibility and exothermicity. However, it is known that the 2D approximation excludes vortex stretching and overestimates effects of baroclinicity in variable-density turbulent diffusion flames. No secondary instabilities can develop into streamwise vortices or ribs which might increase mixing and enhance product formation. Therefore, three-dimensional computations are necessary to realistically simulate the turbulent flow behaviour.

Riley et al. [151] computed an incompressible reacting mixing layer with a temperature independent, single-step chemical reaction without heat release. The authors focused on how the turbulent flow field affects the transport of chemical species and validated their results by comparison with analytical and experimental data.

McMurtry et al. [109] investigated the effects of chemical heat release on the large-scale structure in an incompressible mixing layer with a one-step, irreversible reaction having a Damköhler

number (Da, ratio of the turbulent time scale to the chemical time scale) of 2. For simplification, they used temperature-independent transport coefficients. Their results indicated that with moderate heat release ($T_{max}/T_{ref} = 2$), the development of the large-scale structures is slowed down and their wavelengths are shifted to larger scales. The entrainment of reactants as well as the overall chemical product formation rate was reduced due to reduced mixing. The reactant field was much less contorted which the authors attributed to a stabilizing effect of heat release on the 3D structures in the flow. Consequently, the surface area across which the species can diffuse was decreased, resulting in a lower chemical formation rate. The suppression of Reynolds shear stress led to a lower transfer of energy from the mean flow to the turbulence and a smaller growth rate of the mixing layer. Disadvantages of the simulation of McMurtry et al. were their relatively small domain, that did not allow for subsequent pairings of the vortices, and only moderate heat release.

Planché & Reynolds [141] performed both, linear stability analysis and DNS of temporally developing compressible mixing layers and found the mixing behaviour dependent on M_c: Large-scale engulfment of fluid from both sides of a mixing layer did not occur at high Mach numbers.

Miller et al. [115] also took into account compressibility and a one-step, irreversible reaction with varying Da and either a constant or a temperature-dependent (Arrhenius law) reaction rate. Viscosity, diffusivity and conductivity were taken as constants. The authors focused on comparing their results with the Steady Laminar Diffusion Flamelet Model (SLDFM) and the Conditional Moment Closure (CMC) and found improved agreement with increasing Da, decreasing value of the stoichiometric mixture fraction and increasing exothermicity. The major influences of heat release that were noticed at constant rate kinetics were a decrease of the growth rate of the layer, delays in the pairing process and a reduction of the TKE and product formation. However, the domain size in these simulations was also very limited and allowed only for one or two pairings. Influences of compressibility were not assessed, either.

De Bruyn Kops et al. [38] performed DNS of various mixing layers without heat release and studied the consequences of different activation energies and stoichiometric ratios.

Day et al. [35] investigated the instability modes of three-dimensional, compressible, infinitely fast reacting, spatially developing mixing layers. Similar to Planché & Reynolds [141], they identified two so-called outer modes that existed when there were two maxima in the $\rho\partial u_1/\partial x_3$ profile as it was the case for certain levels of compressibility and heat release. These two modes led to a mixing of the reactants on each side of the shear layer and resulted in a two-step reaction process. If the two modes grow at different rates, as in the spatial mixing layer with one slow and one fast outer stream, mixing and combustion were found to be deteriorated compared to the mere presence of a central Kelvin-Helmholtz mode. The latter exists in incompressible, non-reacting mixing layers and leads to the existence of pure reactants in a significant span of cross-stream positions.

Pantano et al. [124] simulated temporally developing compressible mixing layers with high resolution and in a domain that was sufficiently large to extend the simulation until a fully turbulent state was reached. The authors considered infinitely fast, irreversible hydrocarbon combustion with variable levels of heat release (up to $T_{max}/T_{ref} = 7$) and observed, in agreement with previous results at lower heat release [109, 115], a substantial decrease of the overall reaction rate with increasing exothermicity. Even though Pantano et al. [124] used a fully compressible code they

did not investigate the interaction of compressibility and heat release which is the main subject of the present chapter. It is organized as follows: The DNS code used for the simulation of infinitely fast reacting mixing layers is presented in Sect. 3.2 with a particular emphasis on the modeling and implementation of the chemistry and the transport equations solved during the simulation. Section 3.3 gives a description of the three test cases under investigation which differ mainly by their convective Mach number. Since the reacting mixing layer simulations are performed at the same convective Mach numbers as the inert ones in Chapter 2, the isolated effects of compressibility and heat release can be analyzed as it is done in Sect. 3.4: Instantaneous images of the scalar (mixture fraction) fields give a first impression of the effects (Sect. 3.4.1). Then, a self-similar state is identified for each mixing layer, respectively, over which statistics are taken for the subsequent investigations (Sect. 3.4.2). The appropriateness of resolution and domain sizes is verified in Sect. 3.4.3. The rest of the chapter follows the outline of the preceeding one, thereby allowing direct comparisons between the inert and reacting mixing layers: First, statistical quantities refering to the turbulent flow fields are studied in Sect. 3.4.4.2, then a particular emphasis is placed on scalar mixing (Sect. 3.4.4.3) and entrainment (Sect. 3.4.4.4). Some remarks concerning the non-existence of shocklets in the reacting mixing layers under investigation and a summary of results conclude the chapter.

3.2 The DNS code with an infinitely fast chemical reaction

3.2.1 Infinitely fast chemistry

The reaction of hydrogen and oxygen is simplified by assuming just one irreversible global reaction:

$$2H_2 + O_2 \rightarrow 2H_2O \tag{3.1}$$

In addition, diffusion processes are simplified by neglecting thermo- and barodiffusion and by using Fick's law,

$$\rho Y_\alpha V_{\alpha i} = -\rho D_\alpha \frac{\partial Y_\alpha}{\partial x_i} \tag{3.2}$$

with the diffusion coefficient D_α for species α. Introducing a Schmidt number for each species,

$$Sc_\alpha = \frac{\mu}{\rho D_\alpha}, \tag{3.3}$$

and denoting the fuel, in this case hydrogen, with index F and the oxidizer, here oxygen, with index O, the transport equations for the corresponding mass fractions are:

$$\begin{aligned} \rho\frac{DY_F}{Dt} &= \frac{\partial}{\partial x_i}\left(\frac{\mu}{Sc_F}\frac{\partial Y_F}{\partial x_i}\right) + \omega_F \\ \rho\frac{DY_O}{Dt} &= \frac{\partial}{\partial x_i}\left(\frac{\mu}{Sc_O}\frac{\partial Y_O}{\partial x_i}\right) + \omega_O \end{aligned} \tag{3.4}$$

Due to the reaction equation (3.1), there is a particular relation between the mass production rates of oxidizer and fuel,

$$\omega_O = s \cdot \omega_F \tag{3.5}$$

with the stoichiometric ratio

$$s = \frac{\nu_O W_O}{\nu_F W_F}. \tag{3.6}$$

ν_O and ν_F are the stoichiometric coefficients of the reaction. Assuming a common, constant Schmidt number for fuel and oxidizer, $Sc = Sc_F = Sc_O$, and combining Eqs. (3.4), a conservation equation for $Z = sY_F - Y_O$ is obtained:

$$\rho \frac{DZ}{Dt} = \frac{1}{Sc} \cdot \frac{\partial}{\partial x_i} \left(\mu \frac{\partial Z}{\partial x_i} \right) \tag{3.7}$$

In the simulations that are described in this chapter $Sc = 0.7$ is used. Since this equation contains no source term, it is clear that Z is a passive scalar. With an appropriate normalization,

$$z = \frac{Z - Z_o}{Z_f - Z_o} = \frac{sY_F - Y_O + Y_{O,o}}{sY_{F,f} + Y_{O,o}}, \tag{3.8}$$

z is a quantity which is 0 in the oxidizer stream (index o) and 1 in the fuel stream (index f). z is called mixture fraction and follows the transport equation for a passive scalar. With the help of the equivalence ratio,

$$\Phi = s \frac{Y_{F,f}}{Y_{O,o}}, \tag{3.9}$$

the mixture fraction can also be expressed as

$$z = \frac{1}{1 + \Phi} \left(\Phi \frac{Y_F}{Y_{F,f}} - \frac{Y_O}{Y_{O,o}} + 1 \right). \tag{3.10}$$

In the literature, different definitions are used for the mixture fraction [8, 138], but essentially the mixture fraction is a measure of the local equivalence ratio [135] and always a passive scalar. Therefore, the methods using this quantity are part of the so-called conserved scalar methods. They are not necessarily based on infinitely fast chemistry as it is the case here, but can also use equilibrium chemistry [31]. Other examples of conserved scalar methods that take into account finite-rate chemistry effects are the Conditional Moment Closure (CMC) model and flamelet models (see Sect. 4.1 and Chapter 5).

With the assumption that the mass fractions of the species are pure functions of the mixture fraction z, $Y_\alpha = Y_\alpha(z)$, which is called 'steady flamelet assumption', the location of the flame is determined by the temporally and spatially varying z-distribution. It is situated at

$$z_s = \frac{1}{1 + \Phi}, \tag{3.11}$$

which is the stoichiometric value of the mixture fraction. The structure of the flame is then given by the functions $Y_\alpha(z)$. In a multidimensional flow, the steady flamelet assumption implies that the flame is thin compared to characteristic length scales of the flow which is satisfied for hydrogen chemistry [57]. Each element of the flame front can then be seen as a small laminar flame.

The assumption of an infinitely fast, irreversible global reaction, which implies that fuel and oxidizer cannot be present at the same time at the same place, leads to piecewise-linear relations

between the species mass fractions (index P for the product H_2O) and the mixture fraction [187]:

$$\begin{aligned} Y_O(z) &= \begin{cases} Y_{O,o}(1+\Phi)(z_s - z) & \text{, if } z < z_s \\ 0 & \text{, if } z \geq z_s \end{cases} \\ Y_F(z) &= \begin{cases} 0 & \text{, if } z < z_s \\ Y_{F,f}\frac{1+\Phi}{\Phi}(z - z_s) & \text{, if } z \geq z_s \end{cases} \\ Y_P(z) &= \frac{W_P \nu_P Y_{F,f}}{\nu_F W_F}\left(z - \frac{Y_F(z)}{Y_{F,f}}\right) \end{aligned} \tag{3.12}$$

These relations are called 'Burke-Schumann relations' [22] and are shown in Fig. 3.1. Freezing the chemistry would lead to pure mixing, which can be expressed by (Fig. 3.2):

$$\begin{aligned} Y_O(z) &= Y_{O,o} \cdot (1 - z) \\ Y_F(z) &= Y_{F,f} \cdot z \end{aligned} \tag{3.13}$$

The additional assumption of a Lewis number, $Le = \lambda / (\rho D c_p)$ of 1, which implies that the heat conduction proceeds as fast as diffusion of the species, would permit to write the temperature as a function of the mixture fraction, $T = T(z)$, too. However, in order to retain realistic heat conduction and to take into account compressibility effects, this is not used here. Instead, a transport equation for the temperature is solved (see Sect. 3.2.2).

3.2.2 Transport equations for infinitely fast reacting flows

The set of compressible transport equations, which are integrated in the DNS with infinitely fast chemistry, writes:

$$\begin{aligned} \frac{\partial p}{\partial t} &= -u_i \frac{\partial p}{\partial x_i} - p\gamma \frac{\partial u_i}{\partial x_i} + \sum_\alpha \left[-\rho(\gamma - 1) h_\alpha + \rho\gamma \frac{\mathcal{R}}{M_\alpha} T\right] \sigma_\alpha + (\gamma - 1)\left(\phi - \frac{\partial q_i}{\partial x_i}\right) \\ \frac{\partial u_j}{\partial t} &= -u_i \frac{\partial u_j}{\partial x_i} - \frac{1}{\rho}\left(\frac{\partial p}{\partial x_j} - \frac{\partial \tau_{ij}}{\partial x_i}\right) \\ \frac{\partial T}{\partial t} &= -u_i \frac{\partial T}{\partial x_i} + \frac{1}{\rho c_p}\left(\phi - \frac{\partial q_i}{\partial x_i} + \frac{Dp}{Dt}\right) - \frac{1}{c_p}\sum_\alpha h_\alpha \sigma_\alpha \\ \frac{\partial z}{\partial t} &= -u_i \frac{\partial z}{\partial x_i} + \frac{1}{\rho Sc}\frac{\partial}{\partial x_i}\left(\mu \frac{\partial z}{\partial x_i}\right) \end{aligned} \tag{3.14}$$

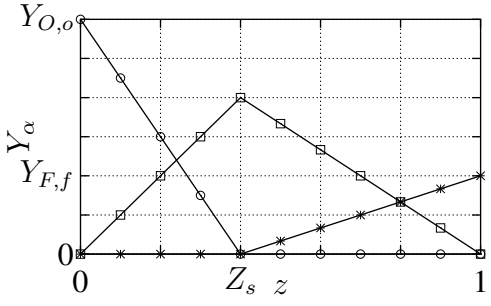

Figure 3.1: Burke-Schumann relations, ○: Y_O, ∗: Y_F, □: Y_P

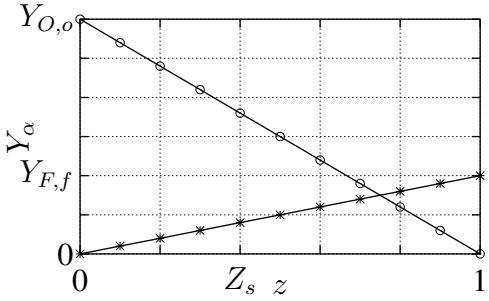

Figure 3.2: Frozen chemistry, ○: Y_O, ∗: Y_F

The density ρ is computed from the ideal gas law, Eq. (2.5). ϕ is the dissipation function $\tau_{ij}\partial u_i \partial x_j$. Using relations of the form $Y_\alpha = Y_\alpha(z)$, the source term σ_α can be computed from

$$\sigma_\alpha = \frac{DY_\alpha}{Dt} = \frac{Dz}{Dt} \cdot \frac{dY_\alpha}{dz} \tag{3.15}$$

and the heat flux vector from

$$q_i = -\sum_\alpha \frac{\mu}{Sc} h_\alpha \frac{\partial Y_\alpha}{\partial x_i} - \lambda \frac{\partial T}{\partial x_i} = -\sum_\alpha \frac{\mu}{Sc} h_\alpha \frac{dY_\alpha}{dz}\frac{\partial z}{\partial x_i} - \lambda \frac{\partial T}{\partial x_i}. \tag{3.16}$$

Neglecting the Dufour effect in the heat flux vector (3.16) is consistent with the assumption of simplified diffusion (3.2) without Soret effect. The specific heat capacities, c_p and c_v, which define the ratio $\gamma = c_p/c_v$, as well as the species enthalpy h_α are computed from polynomial expressions (see Sect. 2.2.1). EGlib (see Sect. 5.3.2) is used to determine the heat conductivity λ and the dynamic viscosity μ. The derivatives dY_α/dz, which appear in Eqs. (3.15) and (3.16), are computed directly from the Burke-Schumann relations, Eqs. (3.12). In order to avoid unsteadiness, a smoothing factor δ is introduced:

$$\frac{dY_\alpha}{dz} = \left.\frac{dY_\alpha}{dz}\right|_o + \frac{1}{2}\left(\left.\frac{dY_\alpha}{dz}\right|_f - \left.\frac{dY_\alpha}{dz}\right|_o\right)\left(1. + \tanh\left(\frac{z - z_s}{\delta}\right)\right) \tag{3.17}$$

As in [124], $\delta = 0.02$ is used.

3.2.3 The numerical method

The discretization, integration and filtering of Eqs. (3.14) is the same as for the transport equations of the inert flow (see Section 2.2.2).

3.3 Test cases

The generic configuration of the test cases corresponds to the one of the inert cases: a temporally evolving, three dimensional shear layer with x_1 and x_2 denoting the homogeneous streamwise and spanwise directions and x_3 denoting the transverse direction. The upper stream (index 1) of the infinitely fast reacting shear layer contains air which is approximated as a mixture of oxygen and nitrogen with $Y_{O2,1} = 0.23$ and the lower stream (index 2) contains a mixture of hydrogen and nitrogen. The hydrogen mass fraction in the free-stream is chosen such that a stoichiometric mixture fraction of 0.3 is obtained (see Eq. (3.11)). This leads to $Y_{H2,2} = 0.0675$. Using pure hydrogen would result in $z_s = 0.028$ making a resolution of the steep temperature gradient on the oxygen side very difficult. The density of the two free streams is identical, which, at initially constant pressure, results in a temperature ratio of $T_1/T_2 = 1.926$.

The same convective Mach numbers as for the inert mixing layers are chosen for the infinitely fast reacting mixing layers, which are $M_c = 0.15$ (test case denoted by inf-0.15), 0.7 (case inf-0.7) and 1.1 (case inf-1.1).

The mixing layer inf-0.15 was initialized with a turbulent velocity field from an inert mixing layer which had been simulated previously. Its configuration and initialization at $Re_{\omega,0} = 640$

corresponds to case inert-0.15, except for the lengths of the domain (L_1, L_2 and L_3) which are smaller by a factor 1.5 for L_1 and L_2 and by a factor 2.25 for L_3. The grid point numbers (N_1, N_2 and N_3) in this pre-simulation were reduced by the same factors to keep the same resolution as in case inert-0.15. The inert mixing layer was computed until the Reynolds number reached the value $Re_\omega = 2300$. Then, the velocity fields were scaled to match the free-stream velocities and domain lengths of case inf-0.15 with a Reynolds number of $Re_\omega = 9200$. Ma_c was kept constant during this scaling. The increase in Reynolds number was necessary to reach a fully turbulent self-similar state with reasonable computational effort inspite of the laminarizing effect of heat release. The mixture fraction profile at initialization is a hyperbolic tangent with a vorticity thickness corresponding to $Re_\omega = 9200$. The pressure is set constant, and the temperature is initialized by the Burke-Schumann relation

$$T(z) = \begin{cases} zT_{F,f} + (1-z)\,T_{O,o} + \frac{Q^0 Y_{F,f}}{c_p} z & \text{, if } z < z_s \\ zT_{F,f} + (1-z)\,T_{O,o} + \frac{Q^0 Y_{F,f}}{c_p} z_s \frac{1-z}{1-z_s} & \text{, if } z \geq z_s \end{cases} \tag{3.18}$$

with the heat release $Q^0 = \sum_\alpha \nu_\alpha W_\alpha \Delta h^0_\alpha / (W_F \nu_F)$, wherein Δh^0_α is the standard enthalpy of formation of species α at $T^0 = 298K$. This results in a peak temperature of $2642K$ at $z = z_s$. Equation (3.18) is obtained with equal c_p and diffusion coefficients D for all species and a Lewis number $Le = \lambda / (\rho D c_p) = 1$. However, this linear relation is only used for initialization. During the DNS, a transport equation for the temperature is integrated without the assumption of $Le = 1$ being used (cf. Eqs. (3.14)).

The initialization fields for case inf-0.7 were taken from inf-0.15 at $Re_\omega = 10000$. They are scaled in a way that increases the convective Mach number to $M_c = 0.7$. Correspondingly, the initialization of case inf-1.1 was done with fields from case inf-0.7 at $Re_\omega = 12800$.

Grid and domain sizes of the infinitely fast reacting test cases are given in Table 3.1 and are the same for all reacting test cases. The grid-spacing is constant in all directions.

To compare the infinitely fast reacting mixing layers with results in the literature, a non-dimensional heat release term

$$\mathcal{Q} = \frac{q_0 Y_{F,f} z_s}{c^0_{p,N2} T^0 \nu_F W_F} \tag{3.19}$$

is computed. The enthalpy of reaction is given by [187]

$$q_0 = \sum_\alpha \nu_\alpha W_\alpha \Delta h^0_\alpha. \tag{3.20}$$

With the stoichiometric coefficients of reaction used in this study, $\nu_{H2} = \nu_F = 2$, $\nu_{O2} = 1$ and $\nu_{H2O} = -2$, as well as $\Delta h^0_{H20} = 13.425 MJ/kg$ and $\Delta h^0_{H2} = \Delta h^0_{O2} = 0 J/kg$, an enthalpy of reaction $q_0 = 483.693 MJ/mol$ is obtained. Together with the specific heat of nitrogen at T^0,

Table 3.1: Geometrical parameters of the simulations inf-0.15, inf-0.7, inf-1.1. The computational domain has the dimensions L_1, L_2 and L_3 with N_1, N_2 and N_3 grid points, respectively. The reference vorticity thickness $\delta_{\omega,0}$ is chosen such that it results in $Re_{\omega,0} = 640$.

$L_1/\delta_{\omega,0}$	$L_2/\delta_{\omega,0}$	$L_3/\delta_{\omega,0}$	N_1	N_2	N_3
345	86	172	768	192	432

$c^0_{p,N2} = 1.038kJ/\,(kgK)$, this results in $\mathcal{Q} = 7.856$ which is close to the value that Pantano et al. [124] had in their mixing layer simulation with the highest heat release rate ($\mathcal{Q} = 7.46$ for hydrocarbon combustion).

3.4 Results and analysis

3.4.1 The structure of the infinitely fast reacting shear layers

In this section, instantaneous images of scalar (mixture fraction) fields of the infinitely fast reacting mixing layers are shown in order to visualize changes that occur when their convective Mach number is increased. Furthermore, comparisons of the figures with those of the inert mixing layers in Sect. 2.4.1 are indicative of some consequences of heat release. Since the differences between the infinitely fast reacting mixing layers are less pronounced than for inert mixing layers and since the characteristic features can already be seen from x_1-x_3-cuts, only such figures are shown in the following. For clarity, the analysis is limited to the self-similar state.

3.4.1.1 Infinitely fast reacting shear layer at $M_c = 0.15$

Figure 3.3 shows the instantaneous mixture fraction field of the mixing layer inf-0.15 at $\tau_\omega = 573$ together with the stoichiometric isoline $z_s = 0.3$ and the isolines, $z = 0.1$ and $z = 0.9$, forming the turbulent boundary of the mixing layer (cf. Sect. 3.4.4.4). The temperature field is shown in Fig. 3.4 at the same instant. At first sight, when comparing the figures with those in Chapter 2, the consequences of heat release seem to be similar to those of compressibility: A smoothening of the mixing layer as well as an increase of the dominant length scales, both within the mixing layer and at its boundaries are visible. Less contorted fields involving heat release were also observed by McMurtry et al. [109]. One obvious reason for this is the laminarizing effect of high temperatures. In Fig. 3.4 no clear distinction between braids and rollers can be made which is in agreement with the observations of Hermanson & Dimotakis [72] who found heat release to render the boundaries between two merging structures invisible.

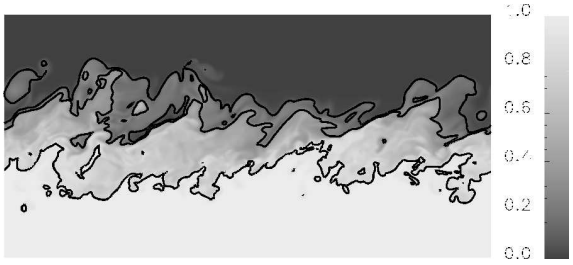

Figure 3.3: Case inf-0.15: Instantaneous mixture fraction field, x_1-x_3-plane in the middle of the computational domain at $\tau_\omega = 573$, isolines $z = 0.1$, $z_s = 0.3$ and $z = 0.9$ are shown

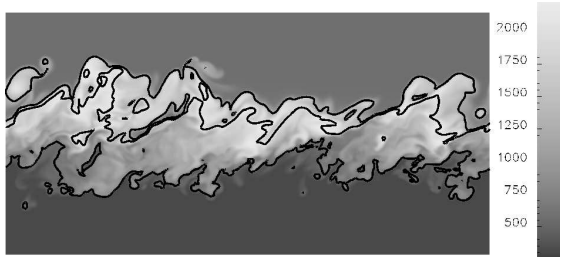

Figure 3.4: Case inf-0.15: Instantaneous temperature field, x_1-x_3-plane in the middle of the computational domain at $\tau_\omega = 573$, isolines $z = 0.1$, $z_s = 0.3$ and $z = 0.9$ are shown

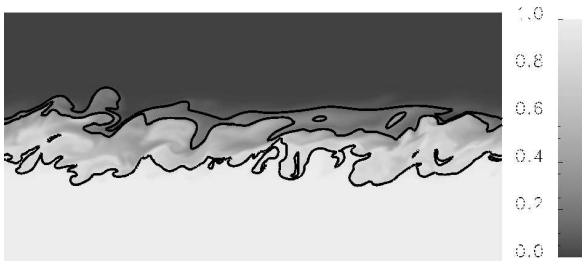

Figure 3.5: Case inf-0.7: Instantaneous mixture fraction field, x_1-x_3-plane in the middle of the computational domain at $\tau_\omega = 761$, isolines $z = 0.1$, $z_s = 0.3$ and $z = 0.9$ are shown

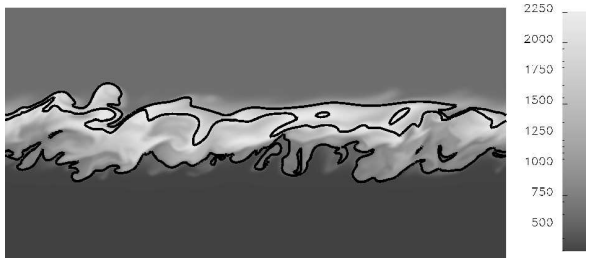

Figure 3.6: Case inf-0.7: Instantaneous temperature field, x_1-x_3-plane in the middle of the computational domain at $\tau_\omega = 761$, isolines $z = 0.1$, $z_s = 0.3$ and $z = 0.9$ are shown

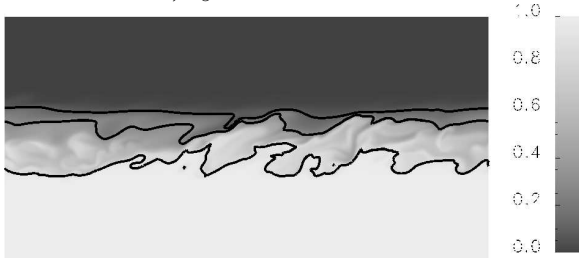

Figure 3.7: Case inf-1.1: Instantaneous mixture fraction field, x_1-x_3-plane in the middle of the computational domain at $\tau_\omega = 803$, isolines $z = 0.1$, $z_s = 0.3$ and $z = 0.9$ are shown

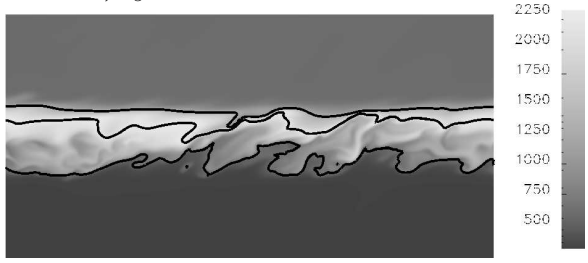

Figure 3.8: Case inf-1.1: Instantaneous temperature field, x_1-x_3-plane in the middle of the computational domain at $\tau_\omega = 803$, isolines $z = 0.1$, $z_s = 0.3$ and $z = 0.9$ are shown

3.4.1.2 Infinitely fast reacting shear layers at $M_c = 0.7$ and $M_c = 1.1$

At higher convective Mach numbers, the mixing layers become even less corrugated with the dominant length scales increasing further (cf. Figs. 3.5 to 3.8), which is in agreement with Planché & Reynolds [141]. A little increase of the maximum temperature compared to Fig. 3.4 (cf. respective scales) due to additional heating by dissipation can be noted. The ondulations of the isolines have a smaller vertical extent than for the incompressible reacting mixing layer which points towards a reduction of intermittency.

3.4.2 The self-similar state

As for the inert mixing layers, the infinitely fast reacting mixing layers reach self-similar states with constant momentum thickness growth rates as shown by Fig. 3.9. With increasing compressibility, the growth rates reduce. The same is true for the product mass thicknesses [72]

$$\delta_P = \int_{-\infty}^{\infty} \frac{\langle\rho\rangle \langle Y_P\rangle_f}{\rho_0 Y_P\left(z_s\right)} dx_3 \tag{3.21}$$

in Fig. 3.10.

Table 3.2 gives the non-dimensional times for the beginning and the end of the self-similar states along with the corresponding Reynolds numbers. The higher the convective Mach number, the longer it takes to reach the self-similar state which is due to the stabilizing effect of compressibility. The same has already been observed for the inert test cases. The Reynolds numbers Re_ω are higher during the self-similar state of the reacting mixing layers than the ones of the inert mixing layers (cf. Table 2.2) which is due to the fact that the initial Reynolds numbers of the reacting

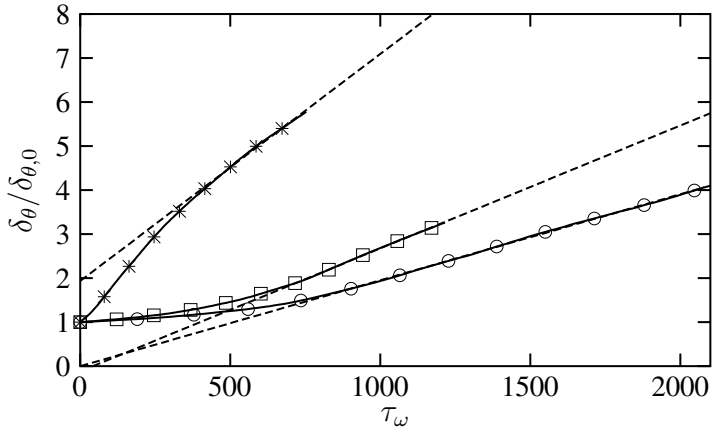

Figure 3.9: Temporal development of the momentum thickness, normalized by the initial momentum thickness $\delta_{\theta,0}$, $*$: inf-0.15, $\square$: inf-0.7, $\circ$: inf-1.1, dashed lines show linear regressions for the self-similar state

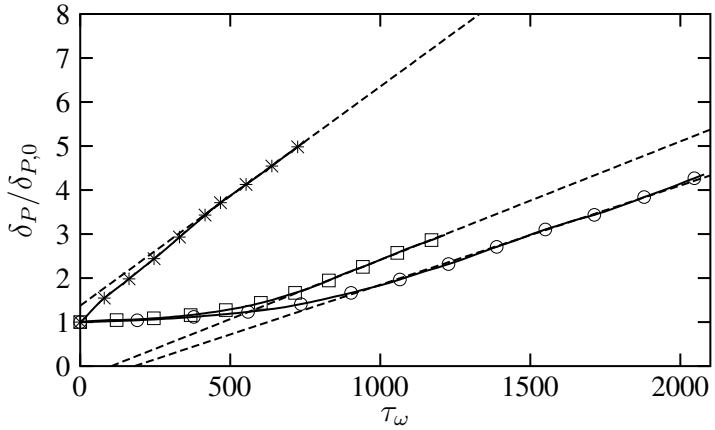

Figure 3.10: Temporal development of the product mass thickness, normalized by the initial product mass thickness $\delta_{\theta,0}$, symbols as in Fig. 3.9, dashed lines show linear regressions for the self-similar state

mixing layers have been increased (see Sect. 3.3). However, since the Reynolds numbers during the self-similar state of all simulations differ by less than a factor of 3 and are therefore within the same order of magnitude, it is reasonable to attribute different behaviours to compressibility and heat release rather than to different Reynolds numbers. The peak micro-scale Reynolds numbers given in Table 3.2 are significantly smaller than the ones in Table 2.2 which is due to the increase of viscosity in the reacting mixing layers. This is in agreement with the laminarizing effect of heat release noticed already in Sect. 3.4.1.

The non-dimensional momentum thickness growth rates δ_θ (according to Eq. (2.19)) are 0.0042 for case inf-0.15, 0.0037 for case inf-0.7 and 0.0030 for case inf-1.1. All these values are significantly smaller than the ones for the inert mixing layers at the respective Reynolds numbers, which

Table 3.2: Dimensionless times and Reynolds numbers at the beginning (index: B) and end (index: E) of the self-similar state

	$\tau_{\omega,B}$	$\tau_{\omega,E}$	$Re_{\omega,B}$	$Re_{\omega,E}$	$Re_{\lambda,B}$	$Re_{\lambda,E}$
inf-0.15	459	803	23810	32450	37	41
inf-0.7	761	1216	22150	33970	34	40
inf-1.1	803	2047	20750	37780	36	46

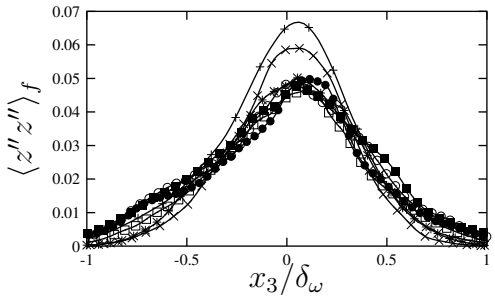

Figure 3.11: Case inf-0.15: Spatially averaged profiles of the mixture fraction variance $\langle z''z'' \rangle_f$ at different times, $+$: $\tau_\omega = 124$, $\times$: $\tau_\omega = 234$, $*$: $\tau_\omega = 346$, $\square$: $\tau_\omega = 459$, $\blacksquare$: $\tau_\omega = 573$, $\circ$: $\tau_\omega = 688$, $\bullet$: $\tau_\omega = 803$

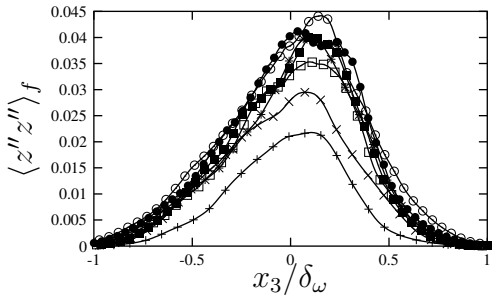

Figure 3.12: Case inf-0.7: Spatially averaged profiles of the mixture fraction variance $\langle z''z'' \rangle_f$ at different times, $+$: $\tau_\omega = 344$, $\times$: $\tau_\omega = 485$, $*$: $\tau_\omega = 625$, $\square$: $\tau_\omega = 761$, $\blacksquare$: $\tau_\omega = 897$, $\circ$: $\tau_\omega = 1034$, $\bullet$: $\tau_\omega = 1170$

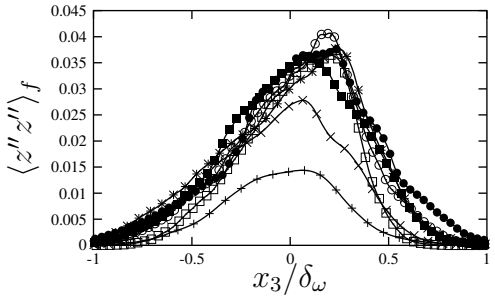

Figure 3.13: Case inf-1.1: Spatially averaged profiles of the mixture fraction variance $\langle z''z'' \rangle_f$ at different times, $+$: $\tau_\omega = 305$, $\times$: $\tau_\omega = 665$, $*$: $\tau_\omega = 999$, $\square$: $\tau_\omega = 1195$, $\blacksquare$: $\tau_\omega = 1388$, $\circ$: $\tau_\omega = 1582$, $\bullet$: $\tau_\omega = 1779$

is in agreement with the results of other authors [72, 109]. The effect of compressibility is not as pronounced for the reacting cases as for the inert ones and consists in a decrease by just a factor of 1.4 between the growth rates of the lowest and the highest M_c (factor 3.4 for the inert cases). Taking into account molecular dissipation effects when computing δ_θ (cf. Eq. (2.18)) results in differences of less than $4\ \%$ compared with the previously given values. Therefore, such effects can be neglected and the use of Eq. (2.19) is justified.

The relaxation towards self-similar states is not only checked by verifying whether the growth rates are approximately constant, but also by examining the normalized spatially averaged profiles of important flow quantities as e.g. the mixture fraction variance $\langle z''z'' \rangle_f$ in Figs. 3.11 to 3.13. The collapse of the profiles onto one 'single' curve during the self-similar state is clearly visible. Therefore, all profiles presented in the following are not only averaged over the two homogeneous directions but also temporally over the self-similar states (if not specified otherwise).

3.4.3 Check of resolution and domain sizes

All simulations are well resolved with a local minimum of the Kolmogorov length l_k (Eq. (2.34)) of $0.77\Delta x_3$ for case inf-0.15, $0.78\Delta x_3$ for case inf-0.7 and $0.9\Delta x_3$ for case inf-1.1 during the self-similar state. In contrast to the inert flows where the minimal Kolmogorov lengths are found in the center of the shear layers, the minimal Kolmogorov lengths in the reacting cases are situated at the edges of the layers and the corresponding profiles present a peak close to the center of

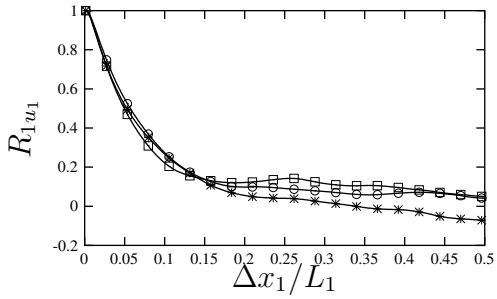

Figure 3.14: Two-point correlation R_1 with $f = u_1$, in the middle of the computational domain, averaged over the self-similar state, $*$: inf-0.15, $\square$: inf-0.7, $\circ$: inf-1.1

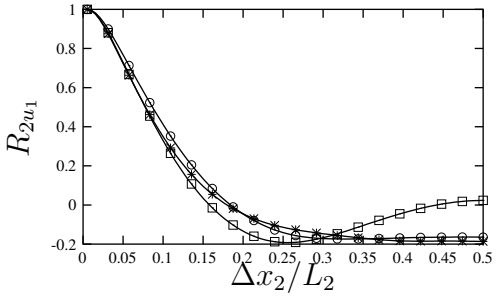

Figure 3.15: Two-point correlation R_2 with $f = u_1$, in the middle of the computational domain, averaged over the self-similar state, symbols as in Fig. 3.14

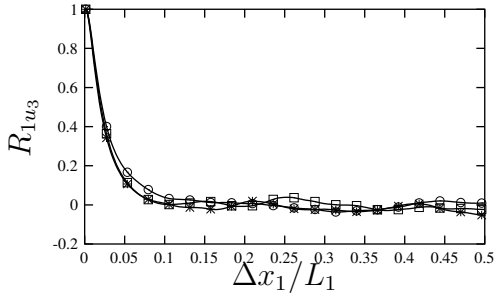

Figure 3.16: Two-point correlation R_1 with $f = u_3$, in the middle of the computational domain, averaged over the self-similar state, symbols as in Fig. 3.14

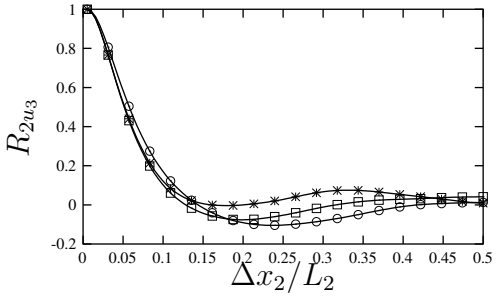

Figure 3.17: Two-point correlation R_2 with $f = u_3$, in the middle of the computational domain, averaged over the self-similar state, symbols as in Fig. 3.14

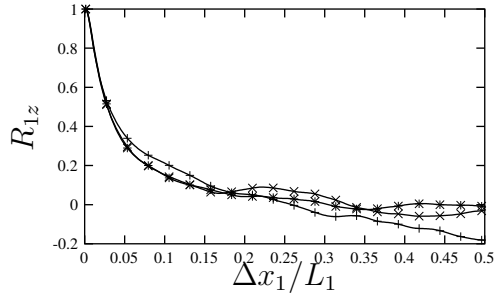

Figure 3.18: Two-point correlation R_1 with $f = z$, in the middle of the computational domain, averaged over the self-similar state, symbols as in Fig. 3.14

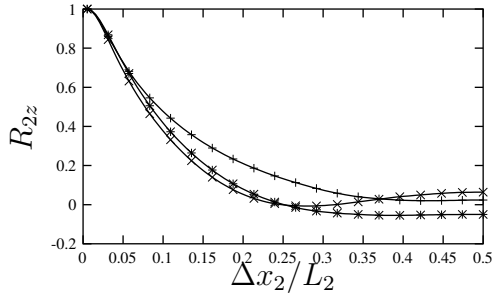

Figure 3.19: Two-point correlation R_2 with $f = z$, in the middle of the computational domain, averaged over the self-similar state, symbols as in Fig. 3.14

the shear layers. This is due to the increased viscosity at the center that goes along with the temperature peak at the location of the flame.

Since a Schmidt number of $Sc = 0.7 < 1$ is used for the mixture fraction and all species, no resolution problems concerning the scalar fields are expected. Spectra that also demonstrate the appropriateness of the resolution and, therefore, show no spurious accumulation of energy in the highest wavenumbers are shown in Sects. 3.4.4.2 and 3.4.4.3.

The domain sizes of the simulations in the periodic directions are large enough which is shown by the two-point correlations of the velocity components and the mixture fraction (Figs. 3.14 to 3.19), computed according to Eqs. (2.35) and (2.36). The two-point correlations are small in the middle of the domain.

The integral length scales, Eqs. (2.37) and (2.38), which are given in Table 3.3, are small com-

Table 3.3: Integral length scales

	l_1/L_1	l_2/L_2
inf-0.15	0.067	0.041
inf-0.7	0.098	0.041
inf-1.1	0.094	0.035

pared to the dimensions of the computational box which confirms the appropriateness of its size.

3.4.4 Effects of compressibility and heat release

3.4.4.1 Mean heat release term

Figure 3.20 shows the term in the pressure equation that describes the heat release effect,

$$Q_p = -(\gamma - 1)\,\rho \sum_{\alpha} h_\alpha \sigma_\alpha \tag{3.22}$$

with σ_α computed according to Eq. (3.15). The reduction of its peak value with compressibility is striking, and the term becomes nearly negligible at $M_c = 1.1$. The peak value of the heat release term is situated to the right of the mixing layer center, which is the side where the stoichiometric surface is located.

The conclusion which can be drawn from Fig. 3.20 and which is confirmed by many of the results in the subsequent sections is that heat release due to infinitely fast chemical reactions has a much larger influence on the mixing layer with $M_c = 0.15$ than on the ones with higher M_c where the differences between the statistics for the inert and reacting mixing layers are small.

3.4.4.2 Turbulence characteristics

Mean flow variables The mean temperature in Fig. 3.21 and the mean density in Fig. 3.22 show the influence of heat release which leads to a temperature maximum and a density minimum.

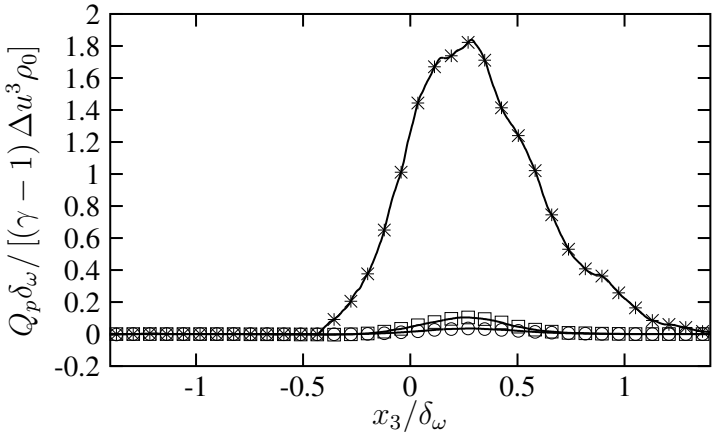

Figure 3.20: Averaged heat release term $Q = Q_p/\left(\gamma - 1\right)$, normalized by $\rho_0 \Delta u^3/\delta_\omega$, $*$: inf-0.15, $\square$: inf-0.7, $\circ$: inf-1.1

The location of these extrema is not in the center of the shear layer, but shifted to the oxygen-rich side of the layer since the stoichiometric mixture fraction is $z_s = 0.3$. The influence of compressibility on the peak value of the temperature is less pronounced for the infinitely fast reacting mixing layers than for the inert ones (cf. Sect. 2.4.4.1): The peak value is only slightly increasing with M_c due to dissipative heating. A larger difference between case inf-0.15 and the other two reacting cases at higher M_c concerns the widths of the temperature and density profiles: The profiles at $M_c = 0.15$ are broader than the others leading to smaller gradients.

As for the inert mixing layers, the averaged pressure of the reacting cases, shown in Fig. 3.23, drops with γM_c^2 and is nearly constant across the layer in each test case, respectively, which leads to the conclusion that temperature and density are mutually dependent.

The influence of compressibility on the Favre averaged velocity profiles in Fig. 3.24 is small. However, there is a difference between the Favre averaged profiles with and without heat release as shown in Fig. 3.25 for the cases with $M_c = 0.7$: On the fuel side, the profile with heat release is above the profile without heat release with the latter being very similar to the Reynolds averaged profile with heat release. On the oxygen side, the Favre averaged profile with heat release is below the Favre averaged profile without heat release and below the Reynolds averaged profile with heat release. Since the relation

$$\langle u_1 \rangle_f - \langle u_1 \rangle = \frac{\langle \rho' u_1' \rangle}{\langle \rho \rangle} \tag{3.23}$$

holds, it can be concluded that the correlation between ρ' and u_1' is positive on the fuel side and negative on the oxygen side of the reacting mixing layer. This is understandable since higher velocity, i.e. positive u_1', is related with colder fluid (positive ρ') on the fuel side and hotter fluid (negative ρ') on the oxygen side.

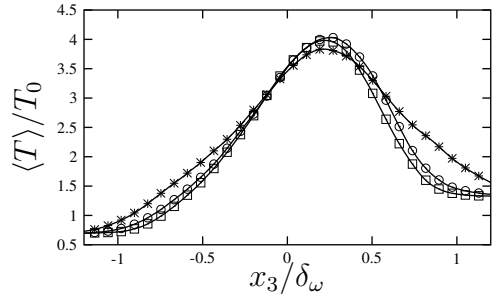

Figure 3.21: Averaged temperature, normalized by $T_0 = 0.5\,(T_1 + T_2)$, $*$: inf-0.15, $\square$: inf-0.7, $\circ$: inf-1.1

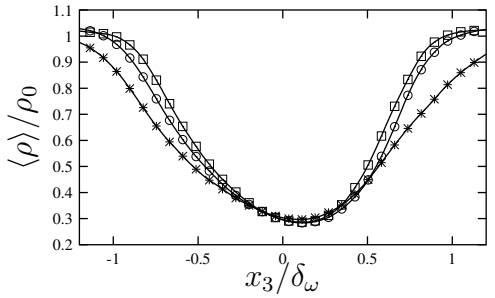

Figure 3.22: Averaged density, normalized by ρ_0, symbols as in Fig. 3.21

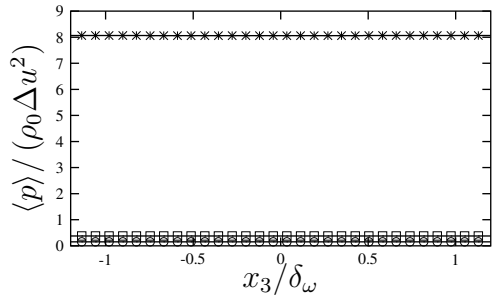

Figure 3.23: Averaged pressure, normalized by $\rho_0 \Delta u^2$, symbols as in Fig. 3.21

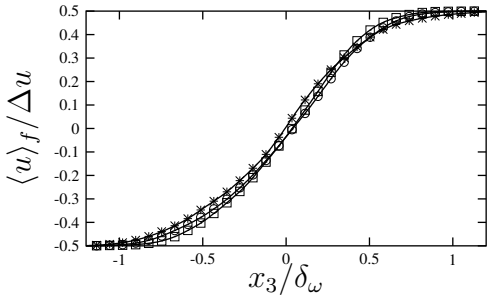

Figure 3.24: Favre averaged streamwise velocity, normalized by Δu, symbols as in Fig. 3.21

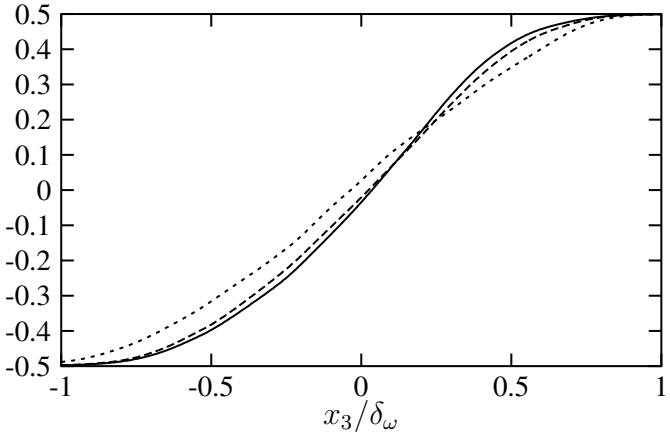

Figure 3.25: Mass-weighted and Reynolds averaged streamwise velocities, cases with $M_c = 0.7$, solid: $\langle u \rangle_f / \Delta u$ of case inf-0.7, dashed: $\langle u \rangle / \Delta u$ of case inf-0.7, dotted: $\langle u \rangle / \Delta u$ of case inert-0.7

Reynolds stresses, turbulent kinetic energy and anisotropies Figures 3.26 to 3.30 show the components of the Reynolds stress tensor and the TKE. As for the inert test cases (cf. Figs. 2.67 to 2.71), the peak values are decreasing with increasing compressibility. However, for the reacting mixing layers the reduction is not as strong as for the inert ones. The higher M_c the smaller the differences between the profiles with and without heat release. This is in agreement with the behaviour of the normalized heat release term which becomes negligible at high M_c (cf. Sect. 3.4.4.1). Particularly striking is the reduction of the magnitude of the low M_c profiles with reaction and heat release with respect to the ones without: reductions of about $69\ \%$ for the peak values of the Reynolds shear stresses and of about $60\ \%$ for the peak value of the TKE for the test cases at $M_c = 0.15$, respectively are observed. The reduction of the Reynolds shear stress is consistent with the reduction of the momentum thickness growth rate by $66\ \%$ (from 0.0124 for case inert-0.15 to 0.0042 for case inf-0.15) caused by heat release, since the latter directly depends on $\langle \rho \rangle R_{13}/\rho_0$ (cf. Eq. (2.19)). A reduction of the Reynolds shear stress by heat release also means

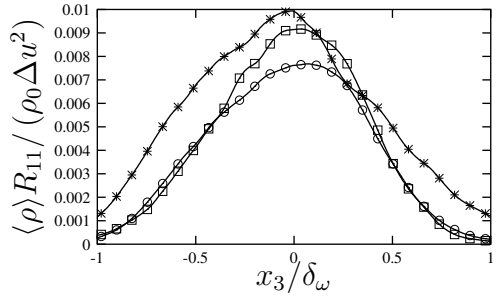

Figure 3.26: Streamwise Reynolds stress $\langle \rho \rangle R_{11}$, normalized by $\rho_0 \Delta u^2$, curves as in Fig. 3.21

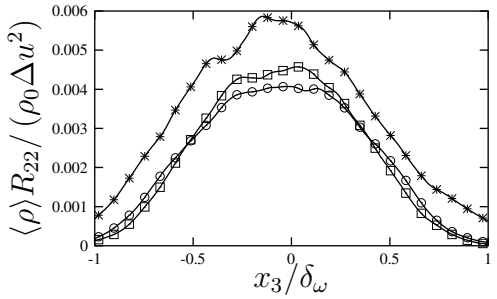

Figure 3.27: Spanwise Reynolds stress $\langle \rho \rangle R_{22}$, normalized by $\rho_0 \Delta u^2$, curves as in Fig. 3.21

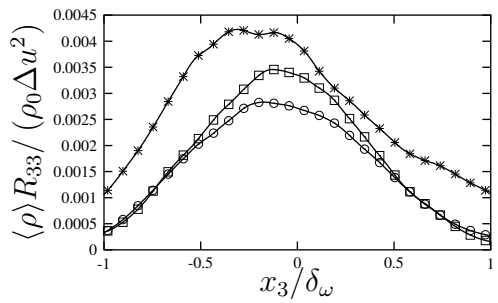

Figure 3.28: Reynolds stress $\langle \rho \rangle R_{33}$, normalized by $\rho_0 \Delta u^2$, curves as in Fig. 3.21

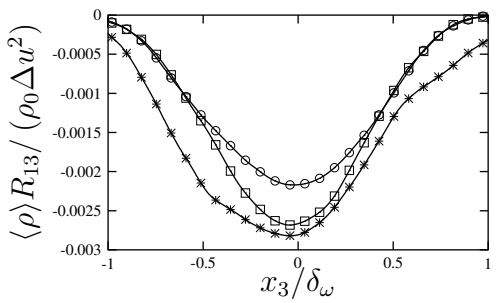

Figure 3.29: Reynolds stress $\langle \rho \rangle R_{13}$, normalized by $\rho_0 \Delta u^2$, curves as in Fig. 3.21

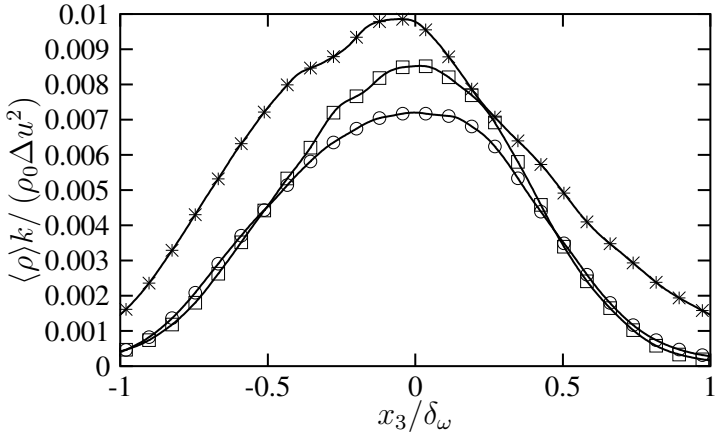

Figure 3.30: Turbulent kinetic energy $\langle\rho\rangle k$, normalized by $\rho_0\Delta u^2$, symbols as in Fig. 3.21

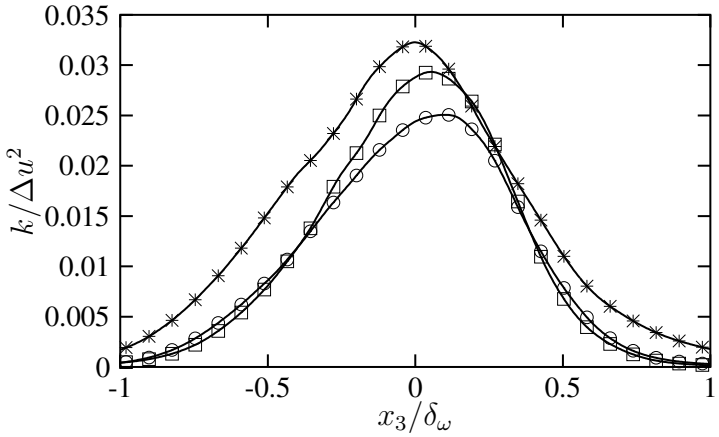

Figure 3.31: Turbulent kinetic energy $\langle\rho\rangle k$, normalized by $\langle\rho\rangle\Delta u^2$, symbols as in Fig. 3.21

a lower transfer of energy from the mean flow to the turbulence, i.e. a lower production rate of the TKE (see below). The reduction of the TKE leads to a lower exchange of mass, momentum and energy among the fluid elements and therefore a reduced mixing with the outer fluid (cf. Sect. 3.4.4.3).

Figure 3.31 shows the TKE with a different normalization, i.e. $\langle\rho\rangle k$ is normalized by $\langle\rho\rangle\Delta u^2$ instead of $\rho_0\Delta u^2$ as it was the case in Fig. 2.71. The reduction of the peak value with increasing M_c is still visible, and a comparison of Fig. 3.31 with Fig. 2.71 reveals that the reduction by heat release has been removed by the change in normalization for the case with $M_c = 0.15$. (Note that Fig. 2.71 does not change significantly when using $\langle\rho\rangle$ instead of ρ_0 since $\langle\rho\rangle/\rho_0 \approx 1$ for the simulation with $M_c = 0.15$.) This suggests that the mechanisms of shear layer stabilization, namely compressibility and heat release act differently: While the first one does not seem to be a mean density effect, the second one seems to be such an effect since it is removed from the profile when using $\langle\rho\rangle$ for normalization instead of ρ_0. Consequently, the reduced transport of the momentum $\langle\rho\rangle R_{ij}$ is rather due to changes in $\langle\rho\rangle$ than in R_{ij}.

Figures 3.32 and 3.33 show direct comparisons between the streamwise Reynolds stress $\langle\rho\rangle R_{11}$ of the inert and reacting test cases with different normalizations. They reveal that while the Reynolds stress is reduced by heat release in the normalization of Fig. 3.32, it is increased in Fig. 3.33. The increase becomes stronger when M_c increases. To explain this difference, two correlation coefficients are investigated: First,

$$R_1 = \frac{\langle\rho u_1'' u_1''\rangle}{\sqrt{\langle\left(\rho u_1''\right)^2\rangle}\sqrt{\langle u_1''^2\rangle}} \tag{3.24}$$

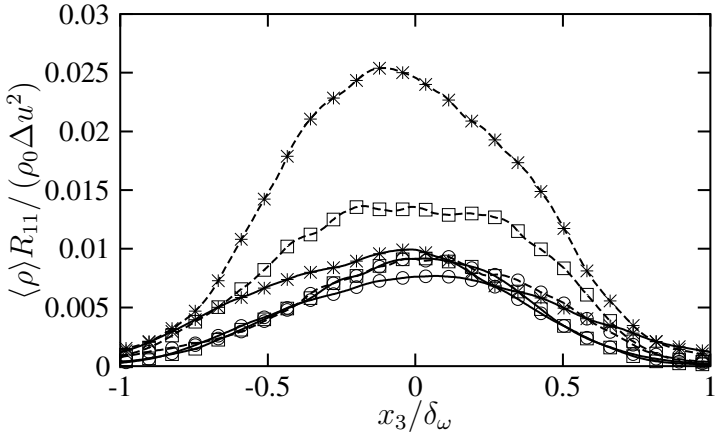

Figure 3.32: Reynolds stress $\langle\rho\rangle R_{11}$, normalized by $\rho_0\Delta u^2$, solid: reacting cases, dashed: inert cases, $*$: $M_c = 0.15$, $\square$: $M_c = 0.7$, $\circ$: $M_c = 1.1$

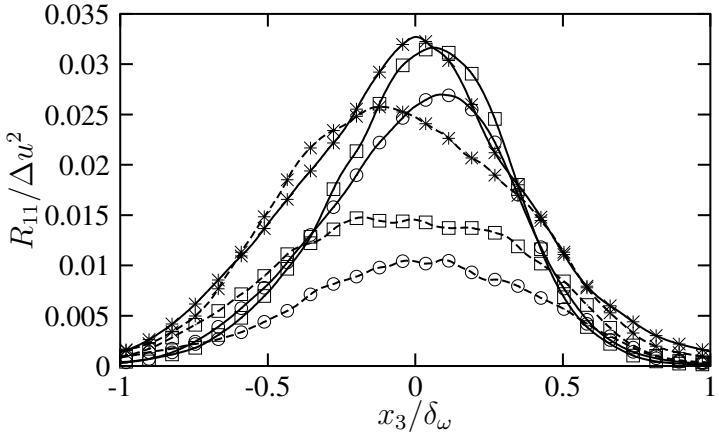

Figure 3.33: Reynolds stress $\langle\rho\rangle R_{11}$, normalized by $\langle\rho\rangle\Delta u^2$, lines and symbols as in Fig. 3.32

which is the correlation coefficient between the mass flux $\rho u_1''$ and the velocity fluctuation u_1''. Second, the correlation coefficient

$$R_2 = \frac{\langle u_1'' u_1'' \rangle_f}{\langle u_1''^2 \rangle}. \tag{3.25}$$

R_1, which is shown in Fig. 3.34 for the various mixing layers, is indicative of the behaviour of $\langle\rho\rangle R_{11}$ in the normalization of Fig. 3.32, i.e. $\langle\rho\rangle R_{11}/(\rho_0\Delta u^2) = \langle\rho u_1'' u_1''\rangle/(\rho_0\Delta u^2)$: Both decrease when heat release sets in. This means that the decrease of $\langle\rho u_1'' u_1''\rangle/(\rho_0\Delta u^2)$ is due to a decrease in the correlation between $\rho u_1''$ and u_1''. Ratio R_2 in Fig. 3.35, on the contrary, increases in the center of the shear layer for the reacting test cases. The difference between the curves of R_2 for two corresponding (inert and reacting) test cases at the same M_c increases with increasing M_c. The same features can be noticed in Fig. 3.33, which confirms that R_2 is indicative of the behaviour of $\langle R_{11}\rangle/\Delta u^2 = \langle u_1'' u_1''\rangle_f/\Delta u^2$.

The reductions of the Reynolds stresses and the TKE by heat release in the normalization of Figs. 3.26 to 3.30 compared to Figs. 2.67 to 2.71 are in agreement with the results of other authors [109, 115, 124]. McMurtry et al. [109] found a decrease of the profiles $\langle\rho\rangle R_{13}$ and $\langle\rho\rangle k$. Using their density decrease of about $\langle\rho\rangle/\rho_0 = 0.5$ and dividing the magnitude of the peak values of $\langle\rho\rangle k$ (from Fig. 12 in [109]) by this ratio, results in peak values for $\rho_0 k$ and therefore also for $k/\Delta u^2$ that are nearly constant despite heat release. This is in agreement with the present findings (Fig. 2.71). Moreover, Hermanson & Demotakis [72] showed by an analysis that the density changes alone suffice to reduce the Reynolds shear stress consistently with the observed decrease in shear layer growth rate.

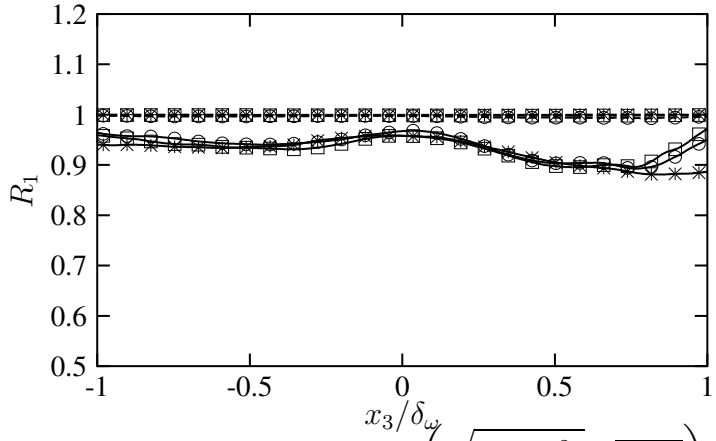

Figure 3.34: Correlation coefficient $R_1 = \langle \rho u_1'' u_1'' \rangle / \left(\sqrt{\langle (\rho u_1'')^2 \rangle} \sqrt{\langle u_1''^2 \rangle} \right)$, lines and symbols as in Fig. 3.32

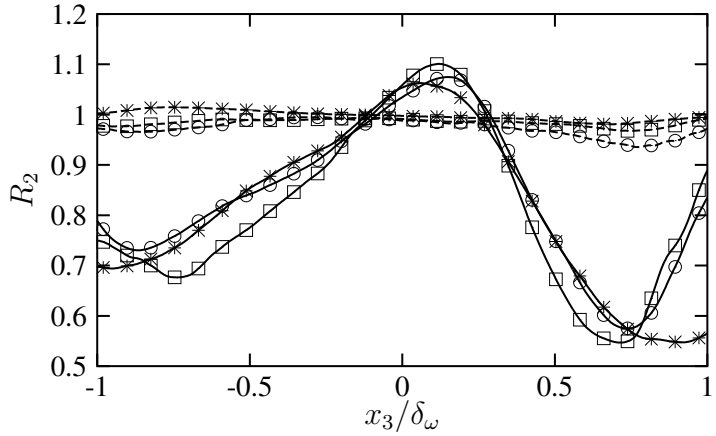

Figure 3.35: Correlation coefficient $R_2 = \langle u_1'' u_1'' \rangle_f / \langle u_1''^2 \rangle$, lines and symbols as in Fig. 3.32

In contrast to this and also to the present results, Pantano et al. [124] noted a reduction of the TKE by heat release by about $30\ \%$ when using the normalization of Fig. 3.31. However, when increasing the heat release to the highest level with which these authors perform a DNS, the corresponding figure in [124] shows once again an increase in the TKE which the authors do not comment on, but which is in agreement with the present results. Two other features that can be seen in Fig. 3.31, namely the pointed shape and the shift of the peak value to the side of the shear layer where the stoichiometric surface is located are also in agreement with what Pantano et al. observe.

What the anisotropy of the Reynolds stresses is concerned, the present results reveal that there is not much influence due to heat release. Plotting the anisotropy parameters from Eqs. (2.39) and (2.40) would result in figures (not shown) that are very similar to the ones presented for the inert mixing layers, i.e. Figs. (2.72) to (2.75). The conclusion that compressibility has little effect on the anisotropy of the Reynolds stresses in the full turbulent, self-similar state and in the Mach number range considered applies therefore also to the present shear layers with heat release.

Reynolds stress transport equations Figures 3.36 to 3.43 show the major terms in the Reynolds stress transport equations (2.28) for the reacting mixing layers. All comments made about the respective role of these terms in Sect. 2.4.4.1 also apply here, one example being the redistributive action of the pressure-strain terms on the fluctuating energy from the streamwise component of the Reynolds stresses to the spanwise and transverse components. Comparing the figures with the

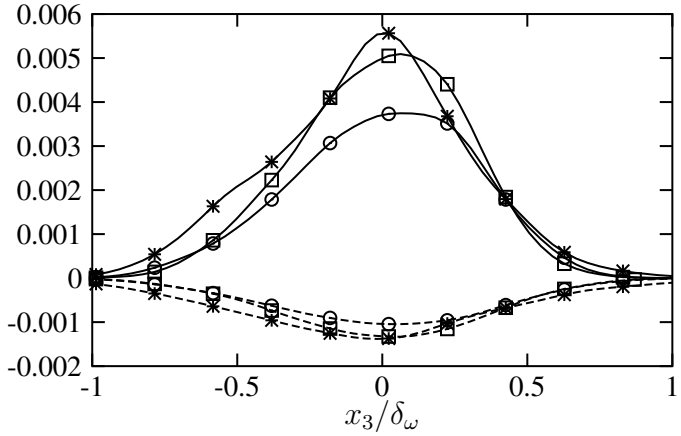

Figure 3.36: Budget of R_{11}, normalized by $\rho_0 \Delta u^3/\delta_\omega$, symbols as in Fig. 3.21, solid: production, dashed: dissipation rate

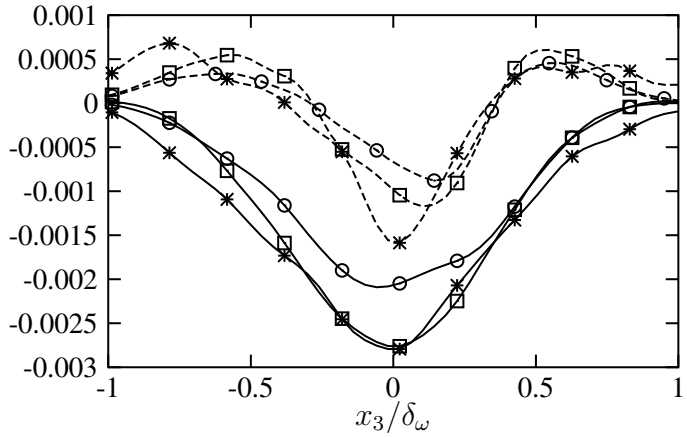

Figure 3.37: Budget of R_{11}, normalized by $\rho_0 \Delta u^3/\delta_\omega$, symbols as in Fig. 3.21, solid: pressure-strain rate, dashed: turbulent transport

corresponding ones for the inert mixing layers (Figs. 2.76 to 2.83), a reduction of all non-zero terms due to heat release is obvious. It is between $60\ \%$ and $70\ \%$ for $M_c = 0.15$ which is comparable to the reduction of other quantities (momentum thickness growth rate, Reynolds stresses, TKE) that have been investigated previously. The reduction is less for higher M_c since the influence of compressibility on the budget terms is less pronounced for the reacting shear layers than for the inert ones; so, heat release has a larger influence at low M_c.

The relatively weak reduction of the production terms, pressure-strain correlations and dissipation

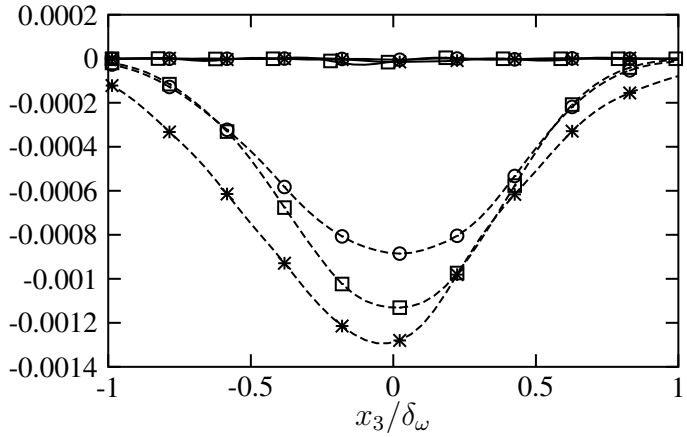

Figure 3.38: Budget of R_{22}, normalized by $\rho_0 \Delta u^3/\delta_\omega$, symbols as in Fig. 3.21, solid: production, dashed: dissipation rate

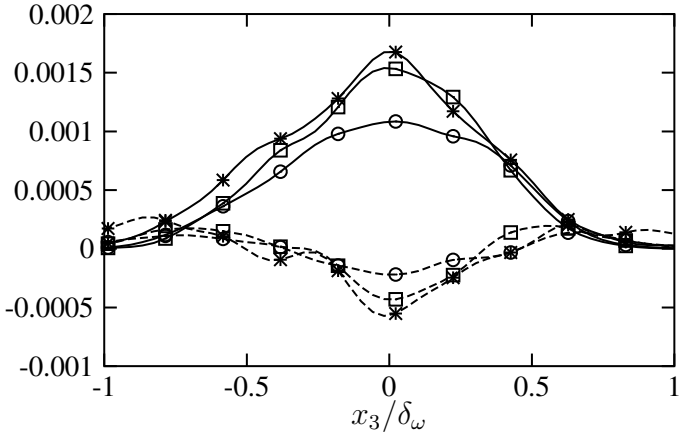

Figure 3.39: Budget of R_{22}, normalized by $\rho_0 \Delta u^3/\delta_\omega$, symbols as in Fig. 3.21, solid: pressure-strain rate, dashed: turbulent transport

rates by compressibility can also be seen when integrating these terms in transverse direction and plotting the results as functions of the convective Mach number as done in Figs. 3.44 to 3.46. The corresponding graphs for the inert mixing layers, Figs. 2.84 to 2.86, have much steeper slopes. The latter observation once more confirms the strong consequences of heat release.

The ratios of certain terms of the transversely integrated Reynolds stress budget equations are nearly independent of the Mach number (Fig. 3.47), which has already been observed for the inert mixing layers (cf. Fig. 2.87). Moreover, the actual values of the constants are close to those

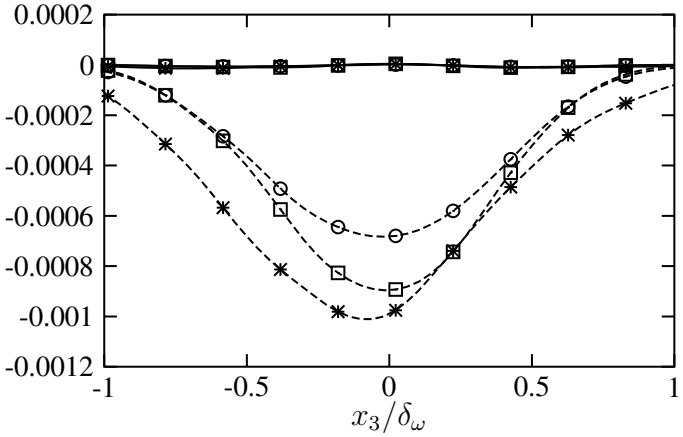

Figure 3.40: Budget of R_{33}, normalized by $\rho_0 \Delta u^3/\delta_\omega$, symbols as in Fig. 3.21, solid: production, dashed: dissipation rate

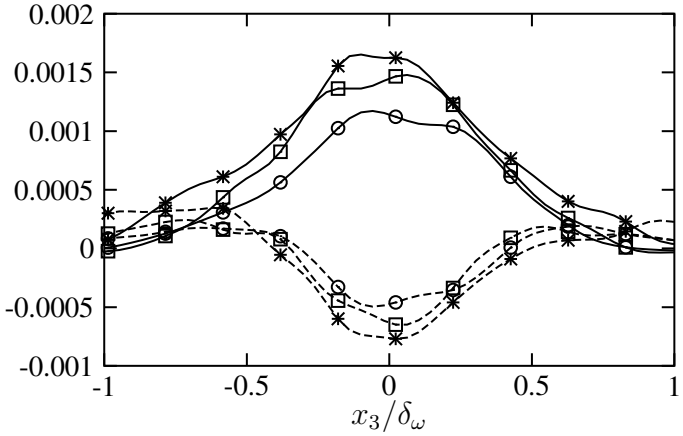

Figure 3.41: Budget of R_{33}, normalized by $\rho_0 \Delta u^3/\delta_\omega$, symbols as in Fig. 3.21, solid: pressure-strain rate, dashed: turbulent transport

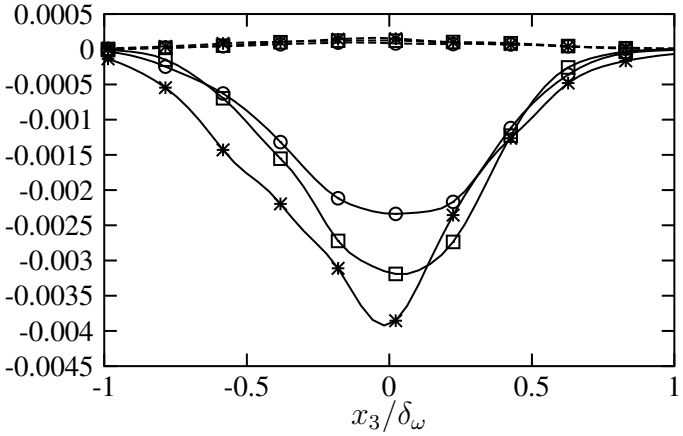

Figure 3.42: Budget of R_{13}, normalized by $\rho_0 \Delta u^3/\delta_\omega$, symbols as in Fig. 3.21, solid: production, dashed: dissipation rate

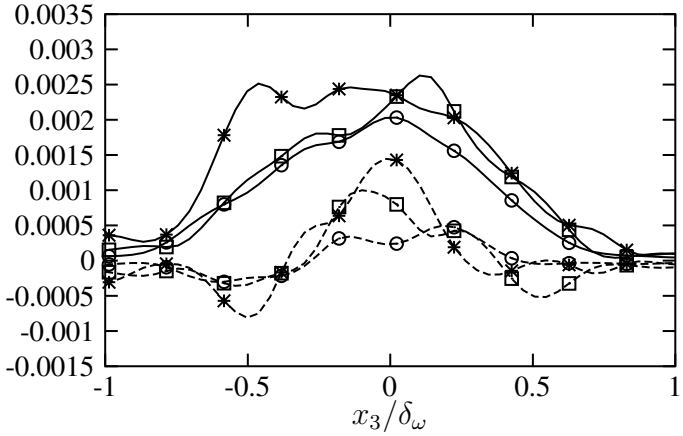

Figure 3.43: Budget of R_{13}, normalized by $\rho_0 \Delta u^3/\delta_\omega$, symbols as in Fig. 3.21, solid: pressure-strain rate, dashed: turbulent transport

without heat release. Figure 3.47 shows that $\breve{P}_{13} \approx 1.13\breve{\Pi}_{11}$ and $\breve{\Pi}_{13} \approx -0.96\breve{\Pi}_{11}$. Neglecting $\breve{\epsilon}_{13}$ ($|\breve{\epsilon}_{13}| \leq 0.05 \left|\breve{P}_{13}\right|$), the budget equation for $\breve{R}_{13}$ from Eqs. (2.43) can be simplified to

$$\frac{\partial \langle\rho\rangle \breve{R}_{13}}{\partial t} = 1.13\breve{\Pi}_{11} - 0.96\breve{\Pi}_{11} = 0.17\breve{\Pi}_{11}. \tag{3.26}$$

A very similar relation has been obtained for the inert mixing layers, $\partial \left(\langle\rho\rangle \breve{R}_{13}\right)/\partial t = 0.15\breve{\Pi}_{11}$. This suggests that the approximate relation (3.26) is not only valid for different M_c but also with and without heat release. As a consequence, the streamwise pressure-strain rate, Π_{11} is not only influencing R_{11} directly but also via its production rate P_{11} that is linked with R_{13} by Eq. (2.41).

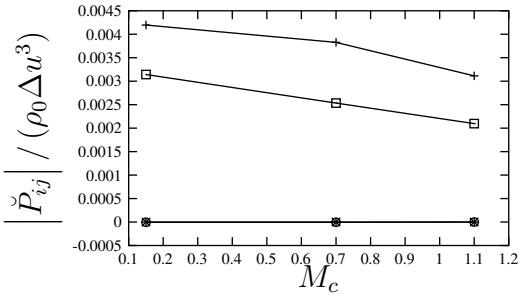

Figure 3.44: Production, integrated in transverse direction, normalized by $\rho_0 \Delta u^3$: $+$: $\breve{P}_{11}$, $\circ$: $\breve{P}_{22}$, $*$: $\breve{P}_{33}$, $\square$: $\breve{P}_{13}$

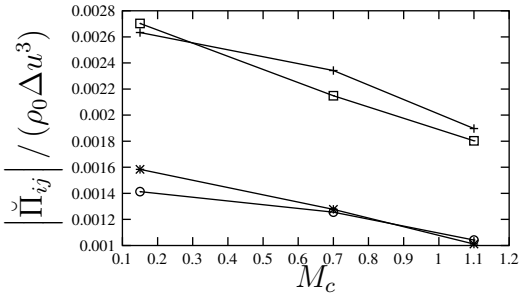

Figure 3.45: Pressure-strain rate, integrated in transverse direction, normalized by $\rho_0 \Delta u^3$: $+$: $\breve{\Pi}_{11}$, $\circ$: $\breve{\Pi}_{22}$, $*$: $\breve{\Pi}_{33}$, $\square$: $\breve{\Pi}_{13}$

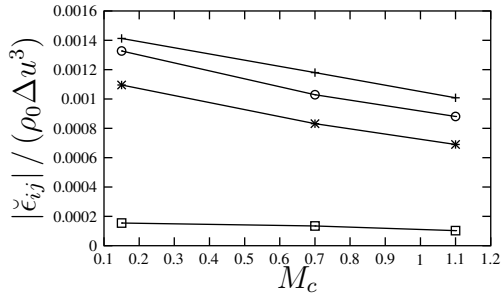

Figure 3.46: Dissipation rate, integrated in transverse direction, normalized by $\rho_0 \Delta u^3$: $+$: $\breve{\epsilon}_{11}$, $\circ$: $\breve{\epsilon}_{22}$, $*$: $\breve{\epsilon}_{33}$, $\square$: $\breve{\epsilon}_{13}$

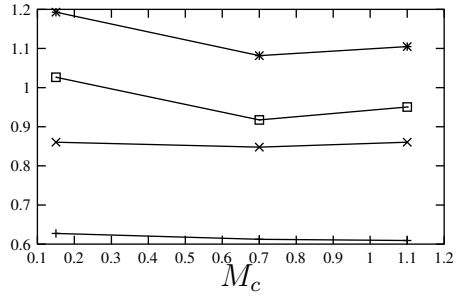

Figure 3.47: Ratios of integrated budget terms versus M_c: $+$: $-\breve{\Pi}_{11}/\breve{P}_{11}$, $\times$: $-\breve{\Pi}_{13}/\breve{P}_{13}$, $*$: $\breve{P}_{13}/\breve{\Pi}_{11}$, $\square$: $-\breve{\Pi}_{13}/\breve{\Pi}_{11}$

Analysis of the reduced growth rate Even though the reduction of the momentum thickness growth rate with increasing M_c is not as pronounced for the reacting mixing layers as for the inert ones, it can be shown that it is predominantly due to the reduced pressure-strain correlation. The procedure to demonstrate this is the same as applied in Sect. 2.4.4.1 to the inert mixing layers. In Sect. 2.4.4.1, an equation linking the normalized momentum thickness growth rate with the pressure-strain rate of the streamwise Reynolds stress component, Eq. (2.50) was derived. It is valid for reacting mixing layers as well and the corresponding values of K_ϵ, K_{11} and $\breve{\Pi}_{11}/(\rho_0 \Delta u^3)$ are given in Table 3.4. Since they are all changing with M_c, it is not immediately obvious which one of them is responsible for the reduction of $\dot{\delta}_\theta$. Using the exact values at each M_c respectively leads to the exact normalized growth rates which are given in the first column of Table 3.5. Discrepancies with the values given in Sect. 3.4.2 are small and only due to rounding errors. The second column in this table, $\dot{\delta}_{\theta,1}$, is obtained when using the averaged (over M_c) values for $K_\epsilon = 1.2004 \cdot 10^{-3}$ and $K_{11} = 6.3003 \cdot 10^{-2}$ along with the exact values for $\breve{\Pi}_{11}/(\rho_0 \Delta u^3)$. The relative error with respect to the exact growth rate is denoted by error 1. Error 2 is the relative error when inserting the averaged value of $\breve{\Pi}_{11}/(\rho_0 \Delta u^3) = -2.2908 \cdot 10^{-3}$, but the exact values of K_ϵ and K_{11}. As for the inert mixing layers, the variation of the pressure-strain term with compressibility has a much greater influence than the variation of the dissipation rate via K_ϵ and the one of the streamwise Reynolds stress via K_{11}. Since the influence of compressibility is smaller

Table 3.4: Values used in the analysis linking momentum thickness growth rate with pressure-strain rate Π_{11} for the infinitely fast reacting test cases

M_c	K_ϵ	K_{11}	$\breve{\Pi}_{11}/(\rho_0 \Delta u^3)$
0.15	$1.4127 \cdot 10^{-3}$	$6.7101 \cdot 10^{-2}$	$-2.6336 \cdot 10^{-3}$
0.7	$1.1804 \cdot 10^{-3}$	$6.6059 \cdot 10^{-2}$	$-2.3423 \cdot 10^{-3}$
1.1	$1.0080 \cdot 10^{-3}$	$5.5849 \cdot 10^{-2}$	$-1.8966 \cdot 10^{-3}$

Table 3.5: Actual and approximated momentum thickness growth rates and relative errors for the infinitely fast reacting test cases

M_c	$\dot{\delta}_\theta$	$\dot{\delta}_{\theta,1}$	$\dot{\delta}_{\theta,2}$	error 1	error 2
0.15	$4.3373 \cdot 10^{-3}$	$4.0918 \cdot 10^{-3}$	$3.9699 \cdot 10^{-3}$	5.7%	8.5%
0.7	$3.7719 \cdot 10^{-3}$	$3.7809 \cdot 10^{-3}$	$3.7167 \cdot 10^{-3}$	0.2%	1.5%
1.1	$3.0764 \cdot 10^{-3}$	$3.3052 \cdot 10^{-3}$	$3.4939 \cdot 10^{-3}$	7.4%	13.8%

Table 3.6: Averaged values (respective inert and reacting cases taken into account) used in the analysis for each convective Mach number

M_c	K_ϵ	K_{11}	$\breve{\Pi}_{11}/\left(\rho_0 \Delta u^3\right)$
0.15	$2.2486 \cdot 10^{-3}$	$8.6266 \cdot 10^{-2}$	$-5.5154 \cdot 10^{-3}$
0.7	$1.5100 \cdot 10^{-3}$	$6.4148 \cdot 10^{-2}$	$-2.8739 \cdot 10^{-3}$
1.1	$1.1455 \cdot 10^{-3}$	$4.7746 \cdot 10^{-2}$	$-2.1493 \cdot 10^{-3}$

Table 3.7: Actual and approximated momentum thickness growth rates and relative errors

Case	$\dot{\delta}_\theta$	$\dot{\delta}_{\theta,3}$	$\dot{\delta}_{\theta,4}$	error 3	error 4
inert-0.15	$1.2835 \cdot 10^{-2}$	$1.1651 \cdot 10^{-2}$	$9.6134 \cdot 10^{-2}$	9.2%	25.1%
inf-0.15	$4.3373 \cdot 10^{-3}$	$5.3431 \cdot 10^{-3}$	$7.4264 \cdot 10^{-3}$	23.2%	71.2%
inert-0.7	$5.5930 \cdot 10^{-3}$	$5.2523 \cdot 10^{-3}$	$5.0262 \cdot 10^{-3}$	6.1%	10.1%
inf-0.7	$3.7719 \cdot 10^{-3}$	$4.1163 \cdot 10^{-3}$	$4.3410 \cdot 10^{-3}$	9.1%	15.1%
inert-1.1	$3.8371 \cdot 10^{-3}$	$3.7254 \cdot 10^{-3}$	$3.5740 \cdot 10^{-3}$	2.9%	6.9%
inf-1.1	$3.0764 \cdot 10^{-3}$	$3.2040 \cdot 10^{-3}$	$3.3441 \cdot 10^{-3}$	4.1%	8.7%

for the reacting cases than for the inert ones, the errors in Table 3.5 are smaller than the ones in Table 2.5.

Similarly to the just described procedure, it can be shown that the pressure-strain correlations are also the reason for the reduction in momentum growth rate with heat release. To do so, averaged values of K_ϵ, K_{11} and $\breve{\Pi}_{11}/\left(\rho_0 \Delta u^3\right)$ for each Mach number computed from the respective inert and reacting test cases are determined and given in Table 3.6. To evaluate $\dot{\delta}_{\theta,3}$, the averaged values of K_ϵ and K_{11} but the exact values of $\breve{\Pi}_{11}/\left(\rho_0 \Delta u^3\right)$ (from Tables 2.4 and 3.4) are taken. For $\dot{\delta}_{\theta,3}$, the averaged $\breve{\Pi}_{11}/\left(\rho_0 \Delta u^3\right)$ are used along with the exact K_ϵ and K_{11}. The values for $\dot{\delta}_{\theta,3}$ and $\dot{\delta}_{\theta,4}$ are given in Table 3.7. Errors 3 and 4 are computed with respect to the exact growth rates $\dot{\delta}_\theta$ which are repeated in the table for clarity. Since error 4 is in all cases larger than error 3, it is the pressure-strain correlation that has the largest influence on the growth rates and their reduction with heat release. Since the influence of heat release is reduced with increasing M_c the errors at $M_c = 1.1$ are considerably smaller than those at lower M_c.

Pressure-strain terms The pressure-strain term Π_{11} in the streamwise Reynolds stress transport equation has been shown in the last paragraph to be responsible for the reduction of the normalized momentum thickness growth rate due to compressibility and heat release. Therefore, it is of interest to see what causes the reduction of $\Pi_{11} = 2\langle p' \frac{\partial u_1''}{\partial x_1} \rangle$. Figures 3.48 to 3.50 suggest that the reduced pressure fluctuations, the rms value of which is shown in Fig. 3.48, are the most probable cause for the reduction of the pressure-strain term Π_{11} with M_c, since the rms value of $\partial u_1''/\partial x_1$ is only slightly influenced by compressibility and the correlation coefficient $R\left(p, \partial u_1/\partial x_1\right)$ oscillates around zero for all convective Mach numbers. Figure 3.51 even reveals that the integrated value of the strain rate fluctuations rises slightly for an increase of M_c from 0.7 to 1.1.

When comparing the figures which contain the rms values of the pressure fluctuations and the

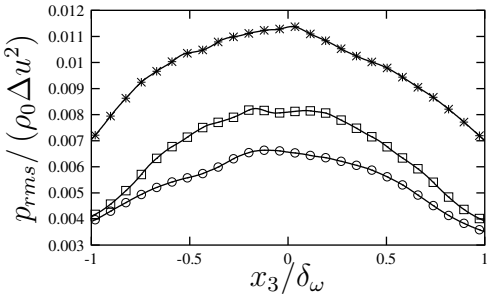

Figure 3.48: Rms value of p', normalized by $\rho_0\Delta u^2$, curves as in Fig. 3.21

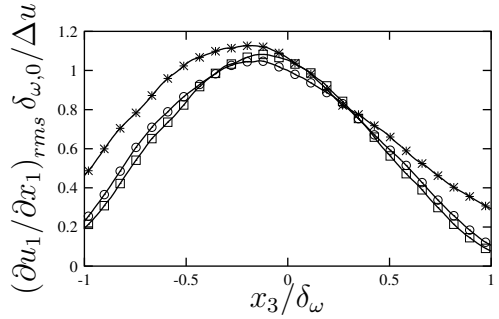

Figure 3.49: Rms value of $\partial u_1''/\partial x_1$, normalized by $\delta_{\omega,0}/\Delta u$, curves as in Fig. 3.21

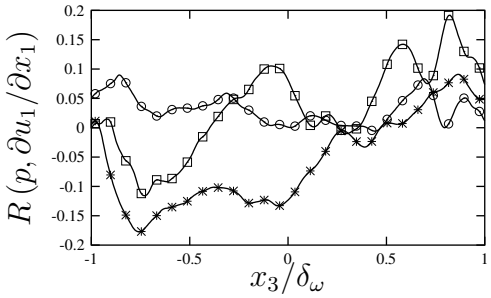

Figure 3.50: Correlation coefficient $R\,(p,\partial u_1/\partial x_1)$ between pressure and density fluctuations, curves as in Fig. 3.21

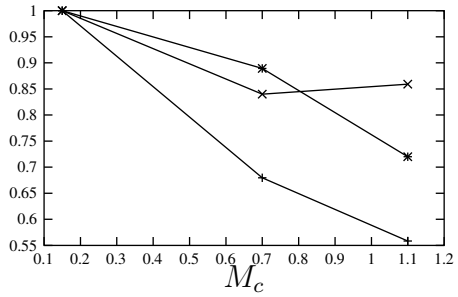

Figure 3.51: Suppression of integrated p_{rms} $(+)$, integrated $(\partial u_1''/\partial x_1)_{rms}$ $(\times)$ and integrated pressure-strain rate $|\Pi_{11}|$ $(*)$, normalized by the respective incompressible value at $M_c = 0.15$

strain rate fluctuations of the reacting mixing layers (Figs. 3.48 and 3.49) to the corresponding ones of the inert mixing layers, a strong reduction of both rms values by the presence of heat release can be observed. Therefore, changes in both, the pressure fluctuations as well as the strain rate fluctuations, seem to contribute to the pressure-strain rate reduction by heat release. However, the influence of heat release on the pressure fluctuations in particular at $M_c = 0.15$ is larger than the influence on the strain rate fluctuations: While the peak magnitude of the normalized rms value of the latter is reduced by a factor of 1.7 only (from approximately 1.9 in Fig. 2.90 to 1.1 in Fig. 3.49), the reduction of the peak value of the rms pressure fluctuation is by more than a factor of 3 (from 0.035 in Fig. 2.89 to 0.0115 in Fig. 3.48).

TKE transport equation Figures 3.52 and 3.53 show the major terms of the TKE transport equation (2.27) for the reacting mixing layers. Compared to the corresponding terms of the inert mixing layers (cf. Figs. 2.93 and 2.94) a decrease of all terms with heat release can be noticed except for the pressure dilatation Π which increases with heat release. A direct comparison between the pressure dilatation profiles of the cases inert-0.15 and inf-0.15 is shown in Fig. 3.54. It can be seen that heat release leads to a positive value of Π, while in non-reacting flow Π is weakly negative as in homogeneous shear turbulence [160]. This completely different behaviour of Π suggests that the underlying mechanisms are different. Dilatation fluctuations in reacting shear layers are certainly not of acoustic nature. An increase of Π in reacting shear layers has also been observed by McMurtry et al. [109]. It means that the pressure dilatation represents a source in the center of the shear when heat release is present. However, due to its small magnitude this source is overshadowed by the production term, the reduction of which leads to a decrease of the TKE with heat release. This result does not support the suggestion of McMurtry et al. [109] that high heat release could lead to such an increase in $\partial u_i''/\partial x_i$ and Π that the TKE increases with

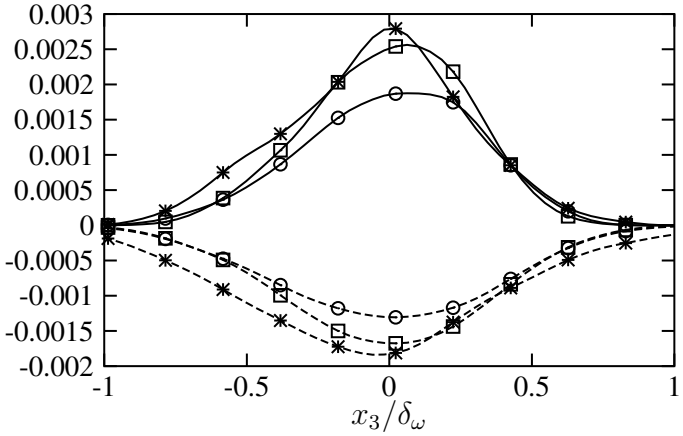

Figure 3.52: Budget of $\langle\rho\rangle k$, normalized by $\rho_0\Delta u^3/\delta_\omega$, symbols as in Fig. 3.21, solid: production, dashed: dissipation rate

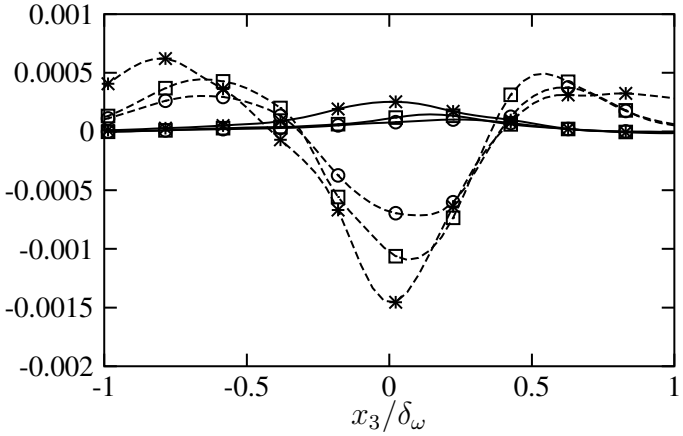

Figure 3.53: Budget of $\langle\rho\rangle k$, normalized by $\rho_0\Delta u^3/\delta_\omega$, symbols as in Fig. 3.21, solid: pressure dilatation, dashed: turbulent transport

heat release. Fig. 3.55 shows the ratio of pressure dilatation and production, both integrated in the transverse direction. The ratio is one order of magnitude larger than for the inert mixing layers (cf. Fig. 2.95) and decreases with increasing compressibility, i.e. the reduction with compressibility is stronger for the pressure dilatation than for the TKE production.

In general, the influence of compressibility on the terms of the TKE transport equation in the absence of heat release is stronger than with heat release (compare Figs. 3.52 and 3.53 with Figs. 2.93 and 2.94), and the effects of heat release are more pronounced for lower M_c than for higher M_c.

The dissipation rate of the TKE is investigated further by decomposing it into three parts, ϵ_1, ϵ_2 and ϵ_3 as shown in Eqs. (2.53) and (2.54). As for the inert mixing layers, the largest part is ϵ_1 (Fig.

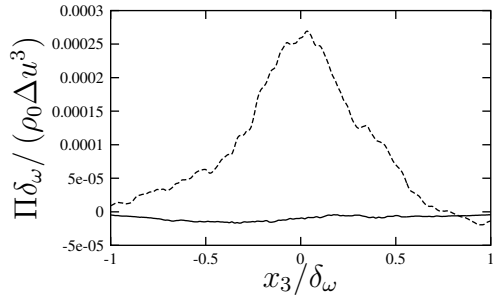

Figure 3.54: Pressure dilatation, normalized by $\rho_0\Delta u^3/\delta_\omega$, solid: inert-0.15, dashed: inf-0.15

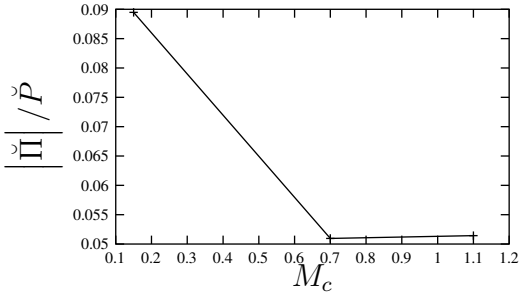

Figure 3.55: Ratio of the integrated pressure dilatation and the TKE production versus M_c

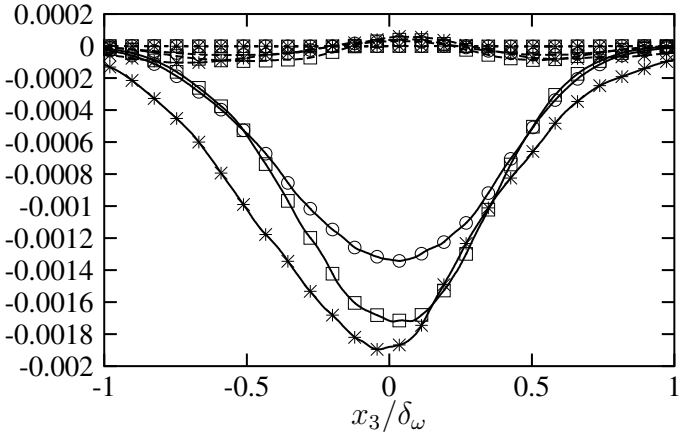

Figure 3.56: Decomposition of TKE dissipation rate, normalized by $\rho_0 \Delta u^3/\delta_\omega$, symbols as in Fig. 3.21, solid: ϵ_1, dashed: ϵ_2, dotted: ϵ_3

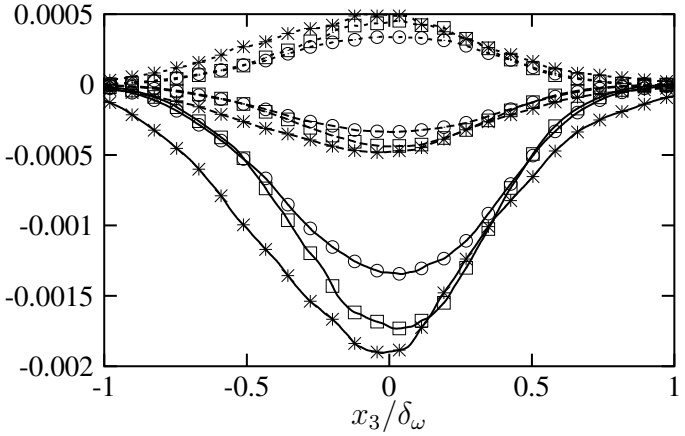

Figure 3.57: Decomposition of ϵ_1, normalized by $\rho_0 \Delta u^3/\delta_\omega$, symbols as in Fig. 3.21, solid: ϵ_s, dashed: ϵ_d, dotted: ϵ_I

3.56), which is computed with the help of the mean viscosity. This means that even though the temperature fluctuations are much stronger than in the inert cases (cf. Figs. 2.103 and 3.61), the dissipation terms ϵ_2 and ϵ_3, in which viscosity fluctuations are contained, remain small. However, Fig. 3.56 reveals that their relative importance compared to ϵ_1 increases somewhat compared to what can be seen from Fig. 2.97.

The further decomposition of ϵ_1 into the solenoidal part ϵ_s, the dilatational part ϵ_d and the inhomogeneous part ϵ_I (cf. Eqs. (2.57) and (2.58)) is shown in Fig. 3.57. As for the inert mixing layers, ϵ_s contributes most to ϵ_1, even at the higher convective Mach numbers. This can also be seen from the fact that the ratio of the transversely integrated ϵ_d and ϵ_s decreases with increasing compressibility (Fig. 3.58). ϵ_d and ϵ_I have nearly the same magnitude but opposite signs and cancel each other out (Fig. 3.57).

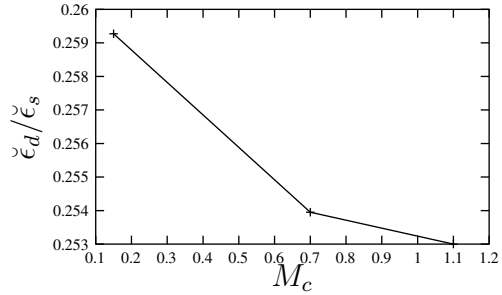

Figure 3.58: Ratio of the integrated dilatational and solenoidal dissipation rates versus M_c

Thermodynamic fluctuations Figures 3.59 to 3.62 show the rms values of the density, pressure, temperature and molecular weight fluctuations which are related via the first order relation (2.61). Temperature and density fluctuations are equally important and strongly correlated as can be seen from the shape of the corresponding curves in Figs. 3.59 and 3.61. The influence of compressibility is mainly on the widths of the profiles and to some extent also on the peak values. As in inert mixing layers, compressibility reduces the turbulence activity and consequently also the thickness of the layer.

Density and temperature fluctuations are much higher for the reacting than for the inert mixing layers (cf. Figs. 2.101 and 2.103) as was to be expected from the presence of heat release. The density and temperature fluctuations are the strongest towards the edges of the shear layer where cold free-stream fluid is entrained, and not at the location of the reaction sheet. This is because there are the strongest mean density and temperature gradients, and they form the main source of density and temperature fluctuations. Another interesting feature is that the peaks of the density and temperature fluctuations on the lean (upper) side of the mixing layer, (which is the side on which the flame is located) are higher than the ones on the fuel-rich side. The pressure fluctuations in Fig. 3.60 are smaller than for the inert cases (Fig. 2.102) and increase with increasing M_c. In contrast to the other thermodynamic fluctuations, the influence of compressibility on the pressure fluctuations is rather strong. The fluctuations of the molecular weight, the rms value of which is shown in Fig. 3.62, are larger than for the inert cases (Fig. 2.104) due to the presence of hydrogen. The pointed shape of the rms value is in contrast to the double-hump shape of the density fluctuations and reveals that molecular weight and density fluctuations are not much correlated. Since the peak height of the molecular weight rms values decreases only little with compressibility, the differences in mixing behaviour are not expected to change much with compressibility when heat release is present (cf. Sect. 3.4.4.3).

A decomposition of the density and temperature fluctuations (cf. Eq. (2.62)) reveals differences

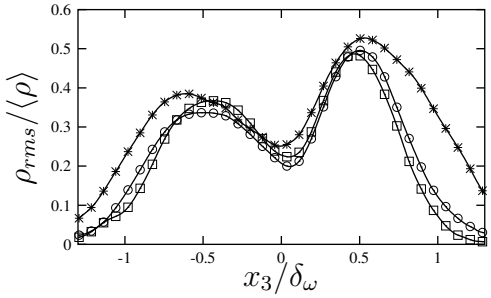

Figure 3.59: Rms value of the density fluctuations, normalized by $\langle\rho\rangle$, symbols as in Fig. 3.21

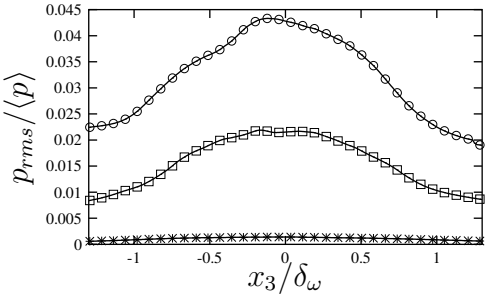

Figure 3.60: Rms value of the pressure fluctuations, normalized by $\langle p\rangle$, symbols as in Fig. 3.21

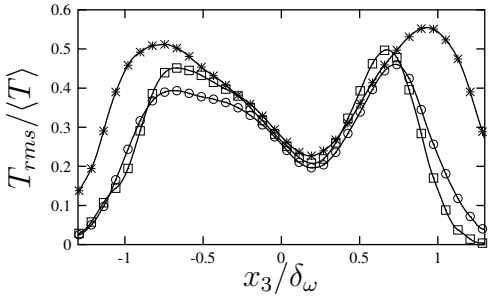

Figure 3.61: Rms value of the temperature fluctuations, normalized by $\langle T\rangle$, symbols as in Fig. 3.21

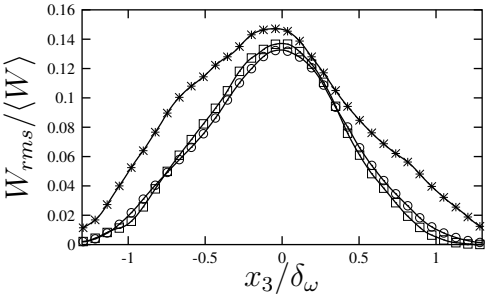

Figure 3.62: Rms value of the molecular weight fluctuations, normalized by $\langle W\rangle$, symbols as in Fig. 3.21

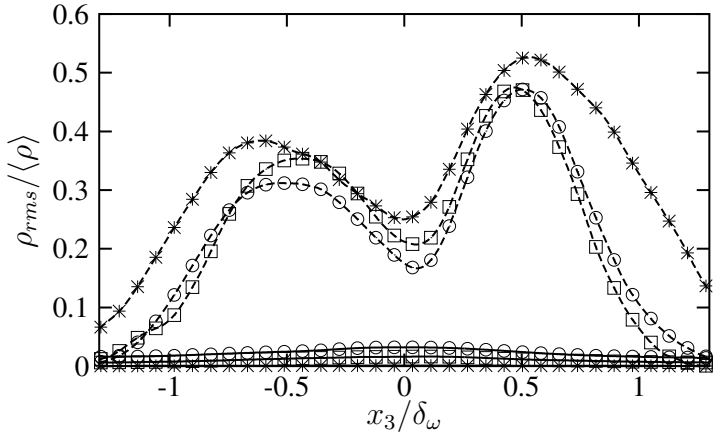

Figure 3.63: Acoustic (solid line) and entropic part (dashed line) of the density fluctuations, normalized by $\langle\rho\rangle$, symbols as in Fig. 3.21

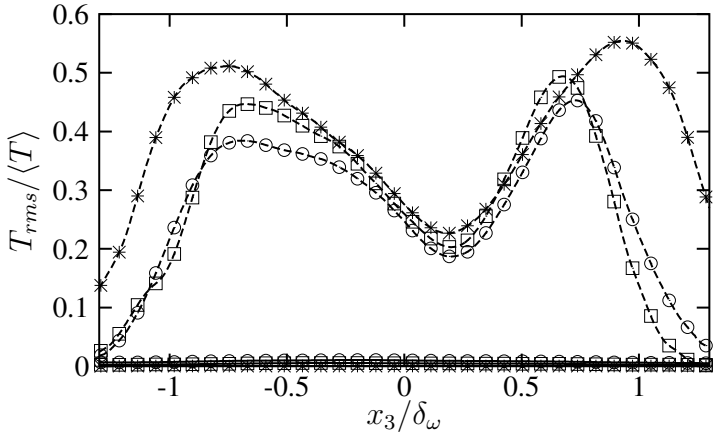

Figure 3.64: Acoustic (solid line) and entropic part (dashed line) of the temperature fluctuations, normalized by $\langle T\rangle$, symbols as in Fig. 3.21

between the inert and the reacting mixing layers: For the latter ones, the entropic parts are much larger than the acoustic ones, even at higher convective Mach numbers (compare Figs. 3.63 and 3.64 with Figs. 2.106 and 2.107).

Correlations of thermodynamic fluctuations A direct investigation of the correlation coefficients $R(\rho,p)$ and $R(\rho,T)$ (Figs. 3.65 and 3.66) confirms what was to be expected from the previous paragraphs: There is only a weak correlation between density and pressure fluctuations, but a strong, inverse correlation of density and temperature fluctuations. Both correlation coefficients are nearly uninfluenced by M_c.

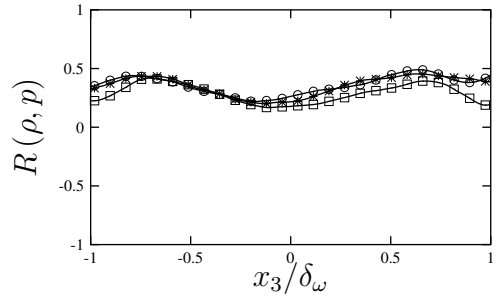

Figure 3.65: Correlation coefficient $R(\rho,p)$ between pressure and density fluctuations, symbols as in Fig. 3.21

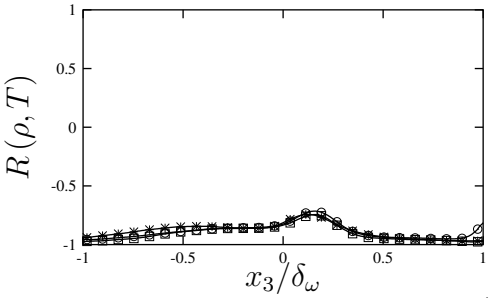

Figure 3.66: Correlation coefficient $R(\rho,T)$ between pressure and temperature fluctuations, symbols as in Fig. 3.21

Behaviour of the pressure-strain correlations In this section, it is analyzed why heat release decreases the pressure fluctuations when normalizing by $\rho_0 \Delta u^2$ as in Fig. 3.48 and why this entails a reduction of the pressure-strain correlations. The procedure is similar to the one in Sect. 2.4.4.1: A Poisson equation for the pressure fluctuations p' is derived which is solved with the help of a Green function. By not considering the complete RHS of the Poisson equation but only single terms it can be seen which of these terms contribute most to the pressure fluctuations, which can be neglected and which are responsible for the reduction of p' due to heat release. The term C_6, $\overline{D}^2 \rho' / \overline{D}t^2$, which was neglected in Eq. (2.68) in Sect. 2.4.4.1 for the inert flows, contains the heat release term explicitly. To show this, the substantial derivative $D\rho/Dt$ is determined first: It is computed as a weighted sum of the substantial derivatives of pressure, entropy and species mass fractions,

$$\frac{D\rho}{Dt} = \mathcal{R}_p \frac{Dp}{Dt} + \mathcal{R}_s \frac{Ds}{Dt} + \sum_\alpha \mathcal{R}_\alpha \frac{DY_\alpha}{Dt}, \tag{3.27}$$

with the partial derivatives as coefficients:

$$\mathcal{R}_p = \left(\frac{\partial \rho}{\partial p}\right)_{s,Y_\alpha} \qquad \mathcal{R}_s = \left(\frac{\partial \rho}{\partial s}\right)_{p,Y_\alpha} \qquad \mathcal{R}_\alpha = \left(\frac{\partial \rho}{\partial Y_\alpha}\right)_{p,s,Y_{\beta\neq\alpha}} \tag{3.28}$$

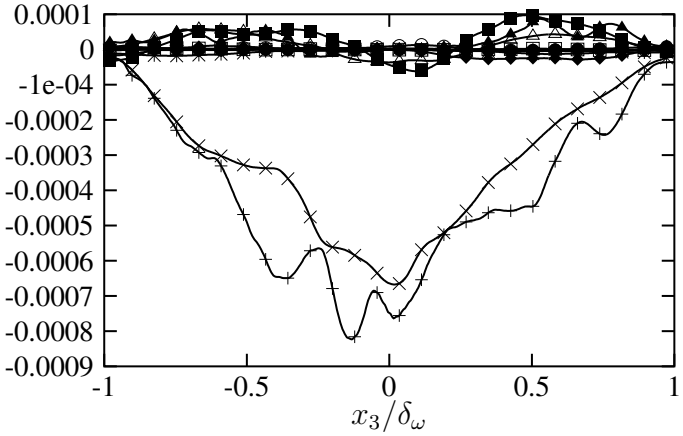

Figure 3.67: Case inf-0.15: Parts of the pressure-strain correlation Π_{11} computed with the Green function, normalized by $\rho_0 \Delta u^3/\delta_\omega$, +: $f = f(A_1)$, ×: $f = f(A_2)$, ∗: $f = f(A_3)$, □: $f = f(A_4)$, ■: $f = f(B_1)$, ○: $f = f(B_2)$, ●: $f = f(B_3)$, △: $f = f(C_1)$, ▲: $f = f(C_2)$, ▽: $f = f(C_3)$, ▼: $f = f(C_4)$, ◊: $f = f(C_5)$, ♦: $f = f(C_5)$

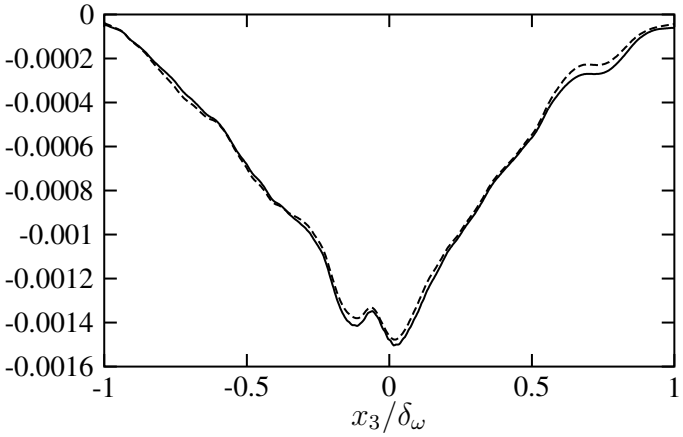

Figure 3.68: Case inf-0.15: Pressure-strain correlation Π_{11}, normalized by $\rho_0 \Delta u^3/\delta_\omega$, solid: computed with the help of the Green function with $f = f\left(\sum_{i=1}^4 A_i + \sum_{i=1}^3 B_i + \sum_{i=1}^6 C_i\right)$, dashed: computed exactly

The partial derivative $\mathcal{R}_s$ is computed from the equation of state for ideal gas mixtures, Eq. (2.5) and the temperature dependence of the specific enthalpy at constant species mass fractions, $dh = c_p dT$:

$$\mathcal{R}_s = \frac{\partial \rho}{\partial s} = \frac{\partial \rho}{\partial T} \cdot \frac{\partial T}{\partial h} \cdot \frac{\partial h}{\partial s} = -\frac{p}{R_G T^2} \cdot \frac{1}{c_p} \cdot \frac{\partial h}{\partial s} \tag{3.29}$$

For the last term, $\partial h/\partial s$, the Gibbs fundamental equation (A.38) is used, which simplifies to $dh = Tds$ for constant pressure and species mass fractions. Therefore $\partial h/\partial s = T$ and

$$\mathcal{R}_s = -\frac{p}{R_G T^2} \cdot \frac{1}{c_p} \cdot T = -\frac{\rho}{c_p}. \tag{3.30}$$

The partial derivative $\mathcal{R}_p$ is

$$\mathcal{R}_p = \frac{\partial \rho}{\partial p} = \frac{1}{\frac{\partial p}{\partial \rho}} = \frac{1}{c^2}, \tag{3.31}$$

whereby Eq. (A.35) is taken into account. To compute $\mathcal{R}_\alpha$, the relation

$$\mathcal{R}_\alpha = \frac{\partial \rho}{\partial Y_\alpha} = \frac{\partial \rho}{\partial T} \cdot \frac{\partial T}{\partial Y_\alpha} \tag{3.32}$$

is useful. When computing $\partial \rho/\partial T$ with the help of the equation of state (2.5), it has to be considered that the gas constant of the mixture, R_G, also depends on the mass fractions of the

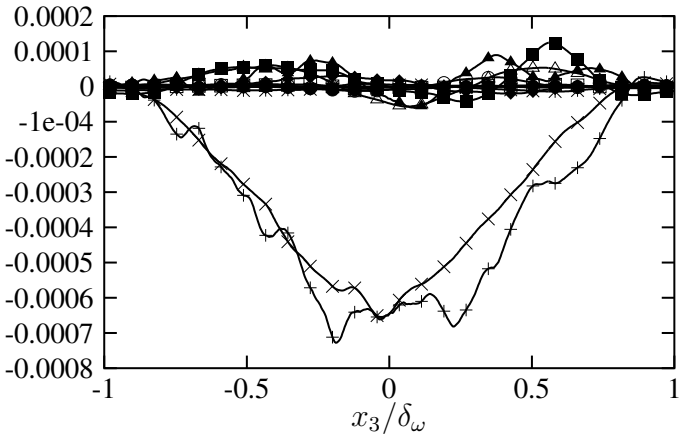

Figure 3.69: Case inf-0.7: Parts of the pressure-strain correlation Π_{11} computed with the Green function, normalized by $\rho_0 \Delta u^3/\delta_\omega$, symbols as in Fig. 3.67

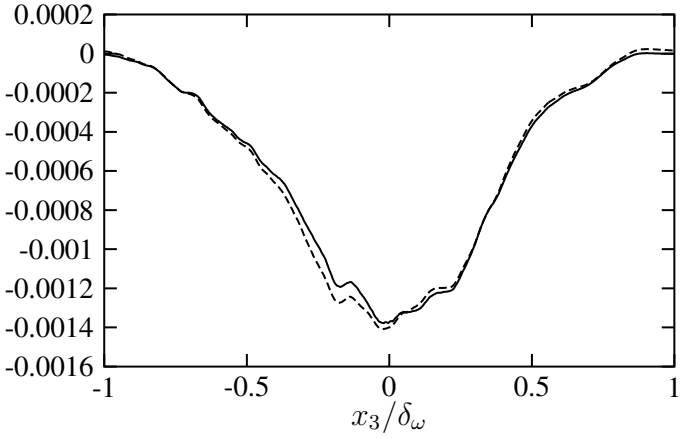

Figure 3.70: Case inf-0.7: Pressure-strain correlation Π_{11}, normalized by $\rho_0 \Delta u^3/\delta_\omega$, solid: computed with the help of the Green function with $f = f\left(\sum_{i=1}^{4} A_i + \sum_{i=1}^{3} B_i + \sum_{i=1}^{6} C_i\right)$, lines as in Fig. 3.68

species which themselves depend on the temperature:

$$\frac{\partial \rho}{\partial T} = -\frac{p}{R_G} T^2 - \frac{p}{R_G^2 T} \cdot \frac{\partial R_G}{\partial Y_\alpha} \cdot \frac{\partial Y_\alpha}{\partial T} = -\frac{p}{R_G T^2} - \frac{p}{R_G^2 T} \cdot \frac{\mathcal{R}}{W_\alpha} \cdot \frac{\partial Y_\alpha}{\partial T} \tag{3.33}$$

Introducing this, as well as Eq. (A.46) into Eq. (3.32),

$$\mathcal{R}_\alpha = -\frac{p}{R_G T} \left(\frac{1}{c_p T} \left(\frac{\mu_\alpha}{W_\alpha} - h_\alpha \right) + \frac{\mathcal{R}}{W_\alpha R_G} \right) \tag{3.34}$$

is obtained. The last term equals zero when the average molecular weight is constant [47]. Using this approximation (which is later justified by the good quality of the results), the final expression for $D\rho/Dt$, after introducing Eqs. (3.30), (3.31) and (3.34), as well as Dp/Dt and Ds/Dt (see Appendix) into Eq. (3.27), is

$$\frac{D\rho}{Dt} = \frac{1}{c^2} \frac{Dp}{Dt} + \frac{1}{c_p T} \left(\rho \sum_\alpha h_\alpha \frac{DY_\alpha}{Dt} + \frac{\partial q_i}{\partial x_i} - \frac{\partial u_i}{\partial x_j} \tau_{ij} \right) \tag{3.35}$$

with $\frac{DY_\alpha}{Dt}$ computed from Eq. (3.15) for infinitely fast reacting flows. When neglecting molecular transport terms, this becomes

$$\frac{D\rho}{Dt} \approx \frac{1}{c^2} \frac{Dp}{Dt} - \frac{1}{c_p T} Q \tag{3.36}$$

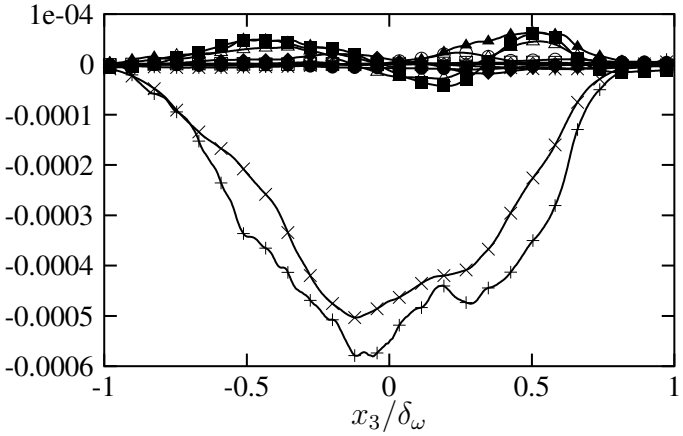

Figure 3.71: Case inf-1.1: Parts of the pressure-strain correlation Π_{11} computed with the Green function, normalized by $\rho_0 \Delta u^3/\delta_\omega$, symbols as in Fig. 3.67

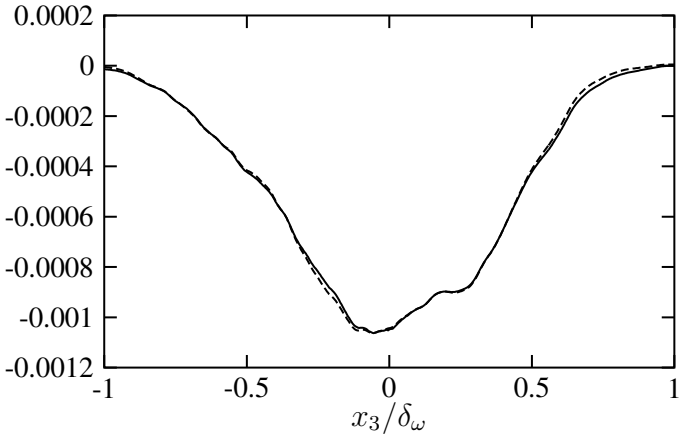

Figure 3.72: Case inf-1.1: Pressure-strain correlation Π_{11}, normalized by $\rho_0 \Delta u^3/\delta_\omega$, solid: computed with the help of the Green function with $f = f\left(\sum_{i=1}^{4} A_i + \sum_{i=1}^{3} B_i + \sum_{i=1}^{6} C_i\right)$, lines as in Fig. 3.68

with the heat release term

$$Q = -\rho \sum_{\alpha} h_{\alpha} \frac{DY_{\alpha}}{Dt} \tag{3.37}$$

which is shown in Fig. 3.20.

When taking into accout the definition of the operator $\overline{D}^2/\overline{D}t^2$, Eq. (2.69), term C_6 can also be written as

$$\frac{\overline{D}^2\rho'}{\overline{D}t^2} = \frac{D^2\rho'}{Dt^2} - 2u_j'' \frac{\partial^2 \rho'}{\partial t \partial x_j} - \left(2\langle u_i \rangle_f u_j'' + u_i'' u_j''\right) \frac{\partial^2 \rho'}{\partial x_i x_j} \tag{3.38}$$

Since the last three terms on the RHS are of higher order, they can be neglected with respect to the first term so that

$$\frac{\overline{D}^2\rho'}{\overline{D}t^2} \approx \frac{D^2\rho'}{Dt^2}. \tag{3.39}$$

Taking into account Eq. (3.36) and neglecting again higher-order terms, term C_6 becomes

$$\frac{\overline{D}^2\rho'}{\overline{D}t^2} = \frac{1}{\langle c \rangle^2} \frac{D^2 p'}{Dt^2} - \frac{1}{\langle c_p T \rangle} \frac{DQ'}{Dt}. \tag{3.40}$$

In Section 2.4.4.1, it was shown that the influence of the complete term C_6 can be neglected for inert mixing layers in the range of convective Mach numbers considered. It is therefore a reasonable assumption that, for the reacting mixing layers, the first term on the RHS of Eq. (3.40) can be neglected with respect to the second term which contains the heat release fluctuations. Therefore,

$$\frac{\overline{D}^2\rho'}{\overline{D}t^2} \approx -\frac{1}{\langle c_p T \rangle} \frac{DQ'}{Dt}. \tag{3.41}$$

Such an assumption makes Eq. (2.68) a Poisson equation for the pressure fluctuations which has the same structure and can therefore be solved with the same Green function, Eqs. (2.72) and (2.73) as the Poisson equation for p' for inert flows. A further approximation of the term C_6 is

$$\frac{\overline{D}^2\rho'}{\overline{D}t^2} \approx -\frac{1}{\langle c_p T \rangle} u_i \frac{\partial Q'}{\partial x_i} \tag{3.42}$$

and consists in only taking into account its convective part. Finally, as for the inert mixing layers, the pressure-strain correlations can be computed by Eq. (2.76). By not inserting the complete RHS of Eq. (2.68), but only single terms it can be seen which ones have the largest influence on the pressure-strain correlations and which are responsible for their decrease due to heat release. Figure 3.67 shows the contributions to the pressure-strain term Π_{11} of case inf-0.15, which are computed this way and averaged over the self-similar state. As for the inert mixing layer (cf. Fig. 2.110), the terms A_1 and A_2 which depend on the mean density are the largest ones. The other terms, even though larger than for the inert case, are small compared to A_1 and A_2. The contribution from term C_6, which contains the heat release term explicitly, is also small. Summing all terms up, as done in Fig. 3.68 gives a good approximation of Π_{11} computed directly from the statistics. This justifies the assumptions involved in the approximation of C_6 in Eq. (3.42) as well as neglecting term D in Eq. (2.68).

At higher Mach numbers, the contributions from terms A_1 and A_2 to Π_{11} decrease, but remain large compared to the contributions from the other terms (Figs. 3.69 and 3.71). The decrease with increasing compressibility is, however, not as significant as for the inert mixing layers in

accordance with what has been observed for the complete pressure-strain rate. The good agreement between the curves in Figs. 3.70 and 3.72, which represent both, Π_{11} computed with the help of the Green function and Π_{11} computed directly from the statistics, shows, that acoustic contributions are not significant for the pressure-strain rate at convective Mach numbers up to $M_c = 1.1$.

Compared to the inert cases, the complete pressure strain rate Π_{11} as well as the contributions from terms A_1 and A_2 are reduced significantly by heat release. To find out, whether this is a consequence of the reduced mean density (cf. Fig. 3.22), which appears as a factor in terms

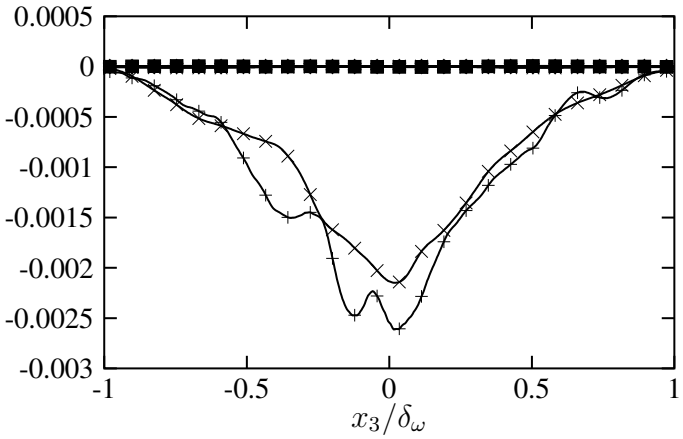

Figure 3.73: Case inf-0.15: Parts of the pressure-strain correlation Π_{11} computed with the Green function and with constant density ρ_0, normalized by $\rho_0 \Delta u^3/\delta_\omega$, symbols as in Fig. 3.67

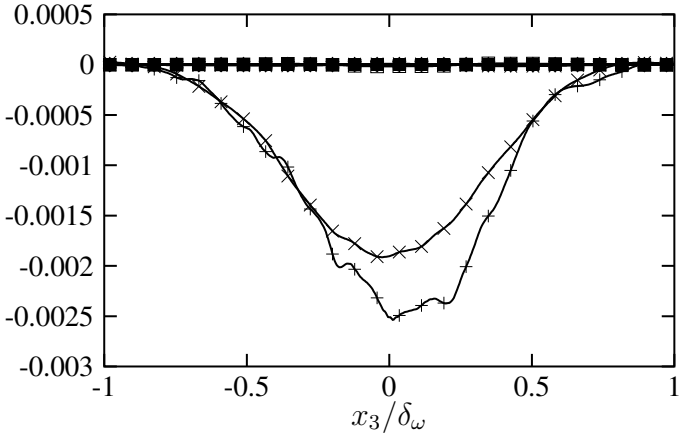

Figure 3.74: Case inf-0.7: Parts of the pressure-strain correlation Π_{11} computed with the Green function and with constant density ρ_0, normalized by $\rho_0 \Delta u^3/\delta_\omega$, symbols as in Fig. 3.67

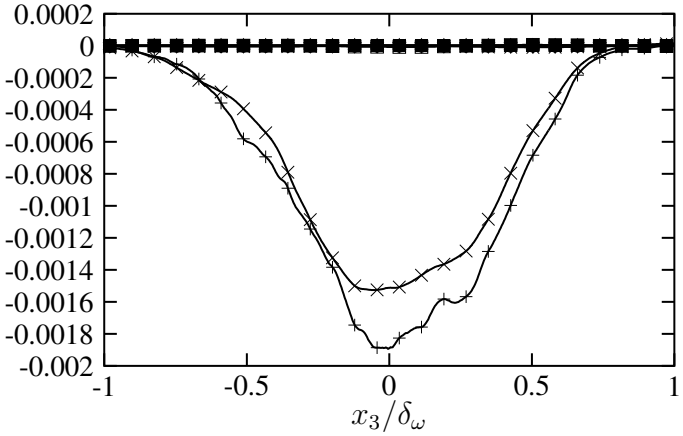

Figure 3.75: Case inf-1.1: Parts of the pressure-strain correlation Π_{11} computed with the Green function and with constant density ρ_0, normalized by $\rho_0 \Delta u^3/\delta_\omega$, symbols as in Fig. 3.67

A_1 and A_2, this quantity is set constant, i.e. instead of $\langle\rho\rangle$, ρ_0 is inserted into the terms on the RHS of Eq. (2.68). Density fluctuations are set to zero. Figures 3.73 to 3.75 show the resulting contributions to Π_{11} when replacing the original terms on the RHS of Eq. (2.68) by these modified terms: In particular for case inf-0.15, this results in the contributions from terms A_1 and A_2 to Π_{11} having approximately the same size as for the mixing layer inert-0.15 (Fig. 2.116). Since the results for the other pressure-strain correlations, as well as the pressure-scrambling terms (cf. Sect. 3.4.4.3) are very similar, the conclusion is that at low convective Mach number, the reduction of the pressure correlations by heat release is predominantly a consequence of the reduction by the mean density. Therefore, it may be called a mean density effect.

Turbulent and gradient Mach numbers A comparison between Figs. 2.119 and 3.76 shows that the turbulent Mach number M_t for cases with the same convective Mach number is reduced by heat release which is mainly due to the increase of $\langle c\rangle/\Delta u$ as can be seen from the fact that the square-root of the TKE, non-dimensionalized as $\sqrt{k}/\Delta u$, increases with heat release, in particular for the higher convective Mach numbers. This is revealed by a comparison between Figs. 3.31 and 2.71 (for the inert mixing layers $k/\Delta u^2 \approx k\langle\rho\rangle/\left(\rho_0\Delta u^2\right)$).

The gradient Mach number, M_g, also decreases slightly with heat release as can be seen from Figs. 2.120 and 3.77. The increase of the gradient Mach number with increasing M_c has been found to be responsible for the reduction of the pressure-strain terms with compressibility [123]. Since M_g is not increased when heat release sets in (at constant M_c, respectively), the mechanisms behind the pressure-strain reduction with heat release must be different from the ones due to compressibility (cf. Sect. 3.4.4.2).

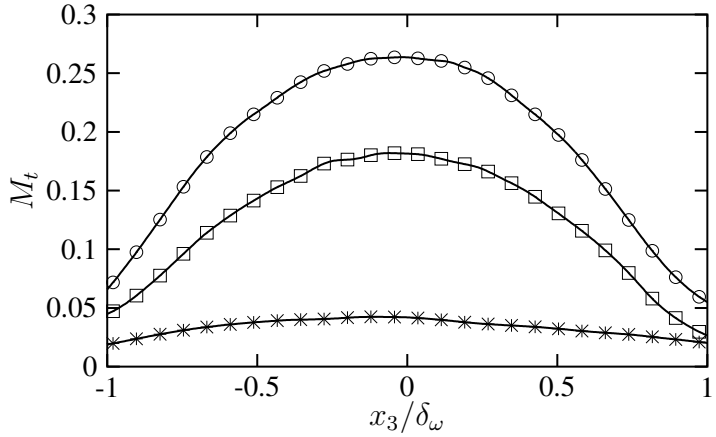

Figure 3.76: Turbulent Mach number M_t, symbols as in Fig. 3.21

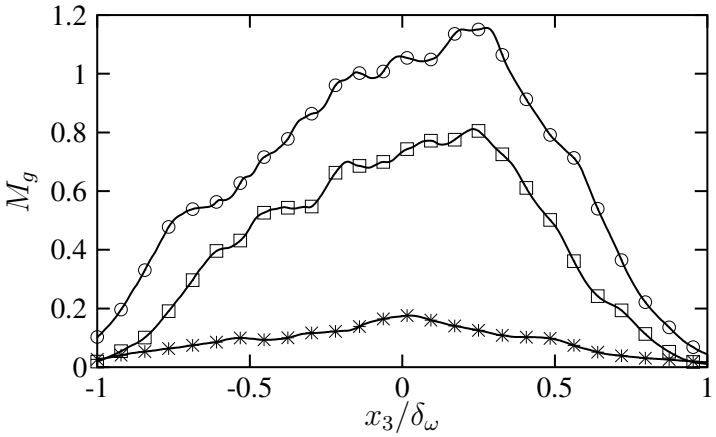

Figure 3.77: Gradient Mach number M_g, symbols as in Fig. 3.21

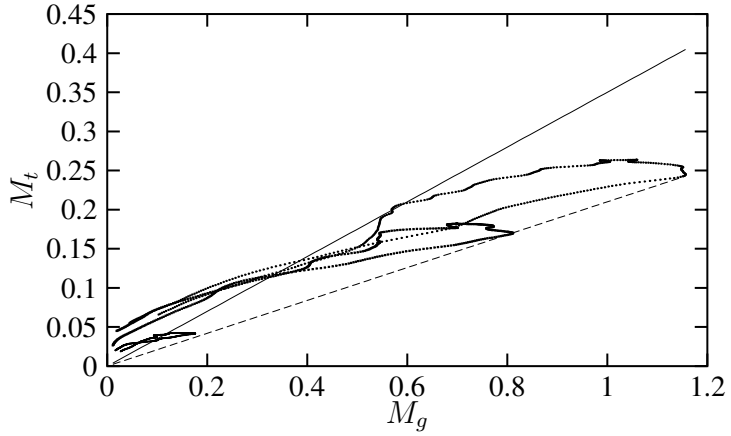

Figure 3.78: Turbulent Mach number M_t plotted as a function of the gradient Mach number M_g. Symbols as in Fig. 3.21, solid line: $M_t = 0.350 M_g$, dashed line: $M_t = 0.210 M_g$

As for the inert mixing layers, there is an approximately linear correlation between M_t and M_g for the reacting mixing layers as the scatter plot in Fig. 3.78 shows. However, the slope of the linear relation is different from that for the inert cases (cf. Fig. 2.121) due to different behaviour of M_t and M_g with heat release.

Spectra Figure 3.79 shows the one-dimensional, streamwise spectrum of the velocity u_1 after averaging over directions x_2 and x_3. Even though the resolution of the reacting cases is lower than for the inert cases (cf. Fig. 2.122), which causes the lower range of wavenumbers on the horizontal axis, no signs of under-resolution are visible, and the energy fall-off in all cases extends smoothly over several orders of magnitude. The higher the wavenumber, the stronger is the effect of heat release which manifests itself in a lower energy content. As for the inert mixing layers, compressibility decreases the energy in the highest wavenumbers resulting in a visible increase of the dominant length scales (cf. Sect. 3.4.1). While the changes from $M_c = 0.15$ to $M_c = 0.7$ are quite strong, an asymptotic behaviour sets in when increasing M_c further.

All scales of the TKE are affected by increasing M_c when heat release is present (Fig. 3.80). Less energy in large and intermediate scales is observed and means that there is less transport of momentum and scalar quantities by the turbulence. Consequences are smaller growth rates and less entrainment of outside fluid due to compressibility (cf. Sect. 3.4.4.4).

In the one-dimensional dissipation spectra in Fig. 3.81, the peak position is rather uninfluenced by

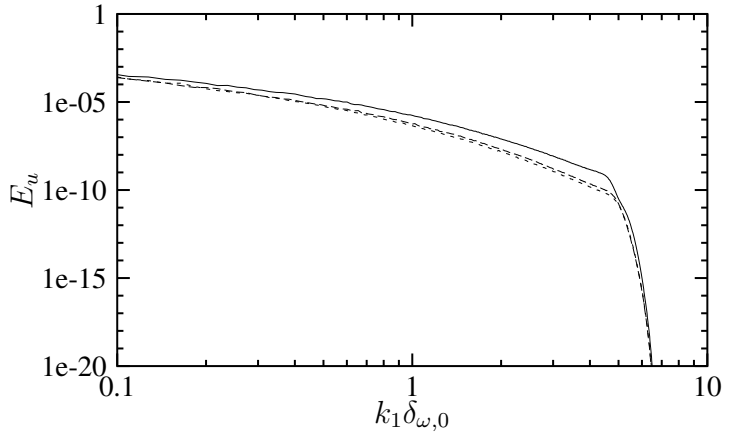

Figure 3.79: One-dimensional, streamwise spectrum of $u_1/\Delta u$ at the beginning of the self-similar state, solid: inf-0.15, dashed: inf-0.7, dotted: inf-1.1

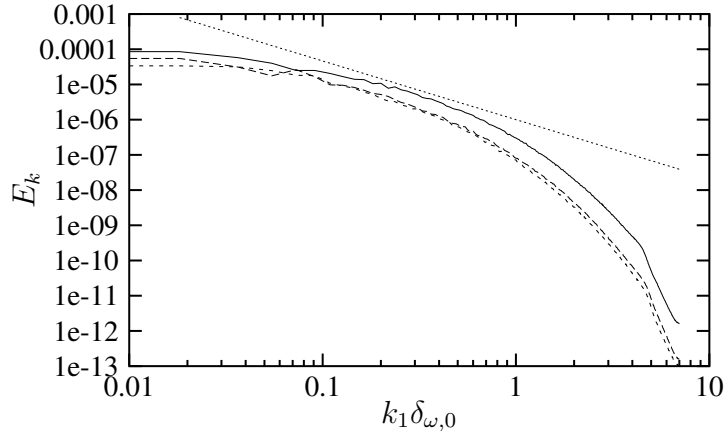

Figure 3.80: One-dimensional, streamwise spectrum of TKE $k/\Delta u^2$ at the beginning of the self-similar state, solid: inf-0.15, dashed: inf-0.7, dotted: inf-1.1, the straight line has $-5/3$ slope

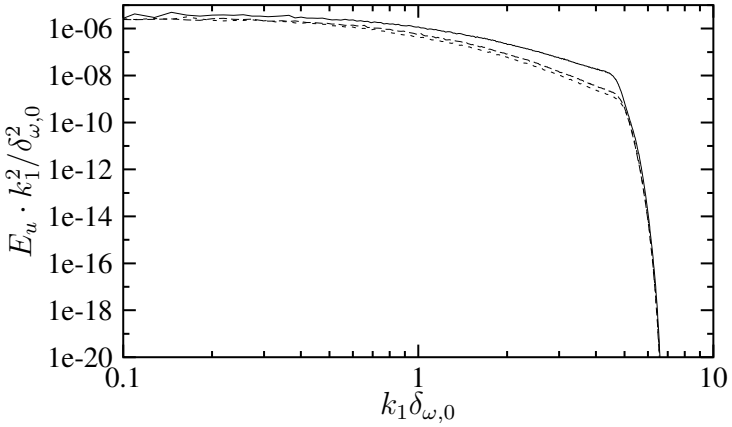

Figure 3.81: One-dimensional, streamwise dissipation spectrum (spectrum of $u_1/\Delta u$ multiplied with $(k_1\delta_{\omega,0})^2$) at the beginning of the self-similar state, solid: inf-0.15, dashed: inf-0.7, dotted: inf-1.1

compressibility but shifted to lower wavenumbers in comparison with the inert spectra (Fig. 3.81). The 'dissipated energy' content decreases in all wavenumbers except for the very small ones with heat release. Compressibility also leads to a decrease but mainly in the largest wavenumbers, i.e. the smallest scales.

3.4.4.3 Scalar mixing

Since chemical reactions can only occur when the reactants become molecularly mixed, a thorough understanding of the mixing process is vital for combustion. Contributing to this is the aim of the following section. There, the mixing characteristics of the reacting shear layers are investigated with the help of statistical quantities of the mixture fraction z. Since z and the species mass fractions are linked by linear relations, the conclusions drawn would be the same when analyzing the corresponding statistical quantities of any of the mass fractions. This would be different if detailed diffusion effects were taken into account. For the inert mixing layers analyzed in Chapter 2, detailed diffusion effects play a minor role only: nitrogen and oxygen have similar diffusion coefficients and no large temperature gradients, which could lead to thermal diffusion, are present. Therefore, even though detailed diffusion effects are taken into account for the mass fractions of the inert mixing layers in Sect. 2.4.4.2, but are excluded in this chapter, direct comparisons are possible and any major differences that are encountered are due to heat release and

compressibility and not to diffusion effects.

Mean profile and variance Figure 3.82 shows the Favre averaged profiles of the mixture fraction. The profiles at the various convective Mach numbers are close to each other, and it is hard to tell whether the differences are larger than those for the velocity profiles of the inert mixing layers. Due to the larger density fluctuations, the differences between the Favre and the Reynolds quantities are larger for the reacting mixing layers than for the inert ones. Figure 3.83 demonstrates this for the mixture fraction of the inert-0.15 case. It can be seen that the Favre averaged profile is above the Reynolds averaged one on the fuel side of the mixing layer and that the opposite is true on the oxidizer side. This is in agreement with the observations of Pantano et al. [124] and can be explained when considering that

$$\langle z \rangle_f - \langle z \rangle = \frac{\langle \rho' z' \rangle}{\langle \rho \rangle}. \tag{3.43}$$

The correlation between the density and the mixture fraction fluctuations is positive on the fuel side since higher ρ (colder fluid) is associated there with higher z (more fuel). On the oxidizer side, the correlation is negative since higher ρ corresponds to more oxygen and therefore lower z. A similar relation has been observed for the Favre and Reynolds averaged velocity profiles in Sect. 3.4.4.2.

Figure 3.84 shows the mixture fraction variance for the reacting mixing layers. Comparing this figure with the corresponding one for the inert mixing layers, Fig. 2.126, it is obvious that the influence of different M_c is less pronounced for the reacting mixing layers than for the inert ones -

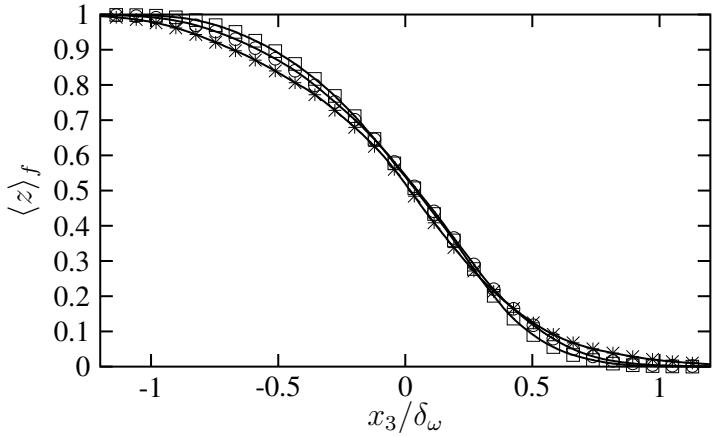

Figure 3.82: Favre averaged mixture fraction, $*$: inf-0.15, $\square$: inf-0.7, $\circ$: inf-1.1

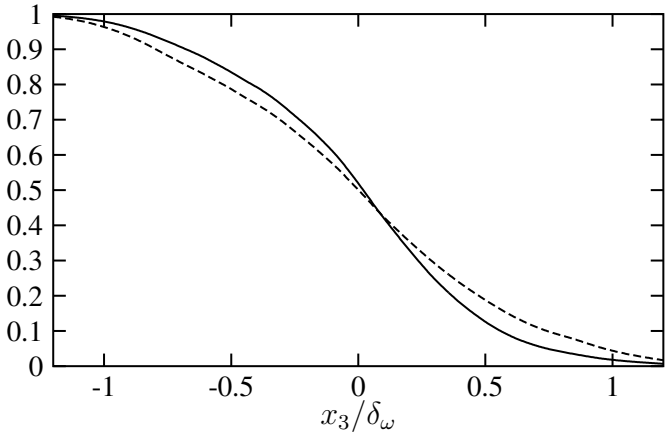

Figure 3.83: Case inert-0.15, solid: $\langle z \rangle_f$, dashed: $\langle z \rangle$

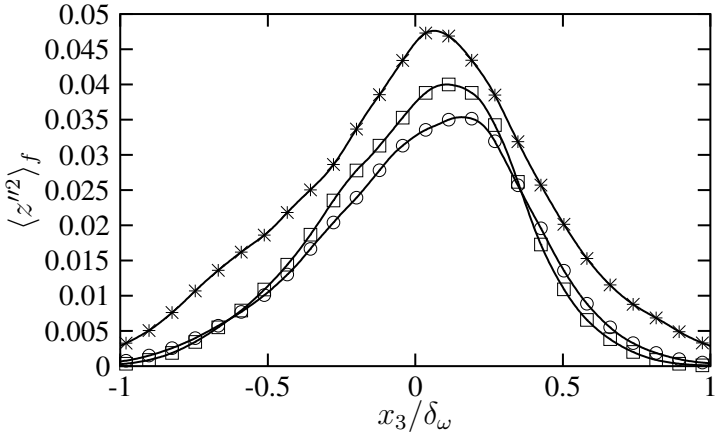

Figure 3.84: Variance of the mixture fraction, symbols as in Fig. 3.82

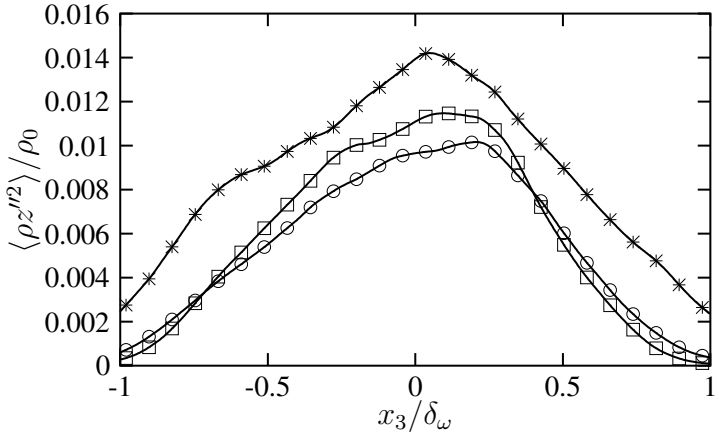

Figure 3.85: Variance of the mixture fraction, normalized by $\rho_0/\langle\rho\rangle$, symbols as in Fig. 3.82

a feature that has already been observed for various other statistical quantities in Sect. 3.4.4.2. In particular, the decrease of the peak value with increasing M_c is relatively small and no significant change in shape is visible. None of the variance profiles of the reacting mixing layers has a double hump as was observed for case inert-0.15. Since the double hump in this case is due to engulfment at the edges of the mixing layer, weak engulfment is expected for the reacting layers. This is confirmed by the results in Sect. 3.4.4.4. The variance profiles are more pointed for the reacting cases than for the inert ones (cf. Fig. 2.126), and the peak value is shifted towards the side of the mixing layer where the stoichiometric surface is located.

When comparing the level of the scalar fluctuations, it is useful to take into account the reduction of the density which is done by a different normalization, applied in Fig. 3.85. A corresponding normalization has been used for the Reynolds stresses and the TKE in Sect. 3.4.4.2 and has revealed that their reduction by heat release is predominantly a mean density effect. This is also the case for the scalar variance, since with the normalization in Fig. 3.85 the scalar fluctuations are reduced by heat release (compare with Fig. 2.126), contrarily to what is observed from comparing Figs. 3.84 and 2.126. Note that a change in normalization would not alter the profiles of the scalar variance of the inert mixing layers much since $\langle\rho\rangle/\rho_0 \approx 1$ in these cases. Therefore, both, Figs. 3.84 and 3.85, can be compared to Fig. 2.126.

Comparing the effects that heat release has on the scalar variance with its effects on the TKE (Figs. 2.71, 3.30 and 3.31), it can be concluded that the influence of heat release on the shape of the profiles is larger for the scalar variance than for the TKE while the peak value of the TKE is stronger influenced than that of the scalar variance (appropriate normalization provided). Pantano et al. [124] made similar observations and concluded that the effect of heat release on scalar and

velocity quantities is approximately the same when integrated across the shear layer.

Scalar pdfs The mixture fraction pdfs of the three reacting test cases in Figs. 3.86 to 3.88 taken in planes with different $\langle z \rangle$ show a marching behaviour with the most probable value varying across the mixing layer. This behaviour is even more pronounced than for the inert mixing layers (cf. Figs. 2.127 to 2.129) since the so-called mixed-fluid peak of the extreme pdfs is situated closer to $\langle z \rangle$ of that plane out of which the respective pdf is taken. From the marching behaviour of the pdfs and the fact that only the two extreme pdfs on each side are bi-modal, i.e. have an intermittency peak in addition to the mixed-fluid peak, it is expected that the fluid gets mixed into the layer at the edges rather than engulfed (cf. Sect. 3.4.4.4). In particular at low M_c, the bi-modal shape is encountered for fewer pdfs than it is the case for the inert mixing layers which shows that the external intermittency decreases with heat release. This observation is in agreement with the results of Pantano et al. [124] and with those in Sect. 3.4.4.4.

The probability to encounter free-stream fluid in the reacting mixing layer in the planes with $\langle z \rangle = 0.2$ and $\langle z \rangle = 0.8$ decreases with increasing compressibility. However, in contrast to the inert mixing layers, the probability to encounter such fluid in the planes with $\langle z \rangle = 0.3$ and $\langle z \rangle = 0.7$ is nearly independent of the Mach number. It can be concluded that for the entrainment, as for other features that have already been investigated in the previous sections, the influence of compressibility on inert mixing layers is larger than on reacting mixing layers.

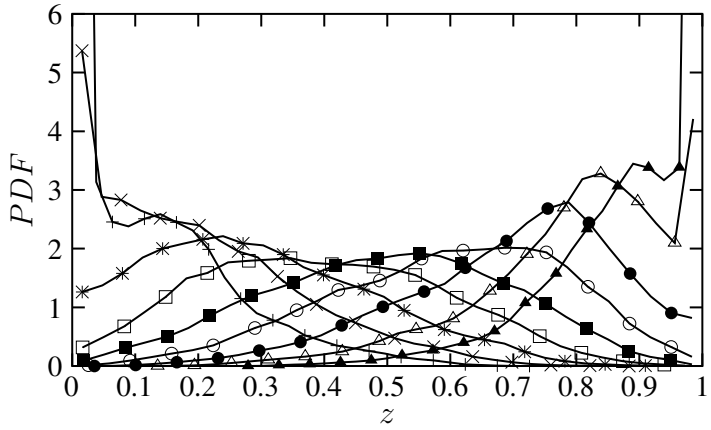

Figure 3.86: Case inf-0.15: pdfs of mixture fraction in planes with various $\langle z \rangle$, $+$: 0.1, $\times$: 0.2, $*$: 0.3, $\square$: 0.4, $\blacksquare$: 0.5, $\circ$: 0.6, $\bullet$: 0.7, $\triangle$: 0.8, $\blacktriangle$: 0.9

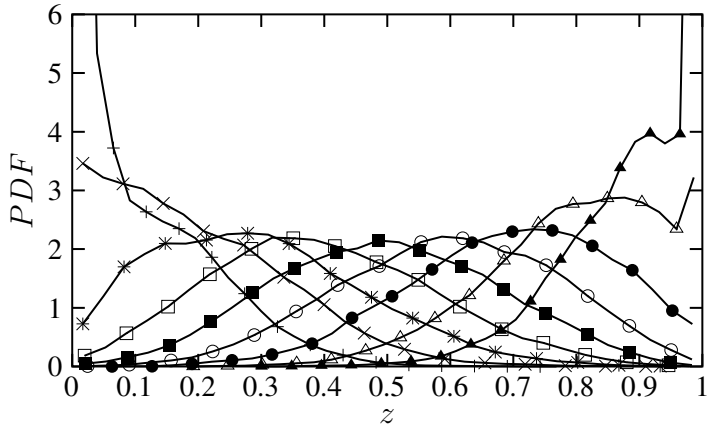

Figure 3.87: Case inf-0.7: pdfs of mixture fraction in planes with various $\langle z \rangle$, $+$: 0.1, $\times$: 0.2, $*$: 0.3, $\square$: 0.4, $\blacksquare$: 0.5, $\circ$: 0.6, $\bullet$: 0.7, $\triangle$: 0.8, $\blacktriangle$: 0.9

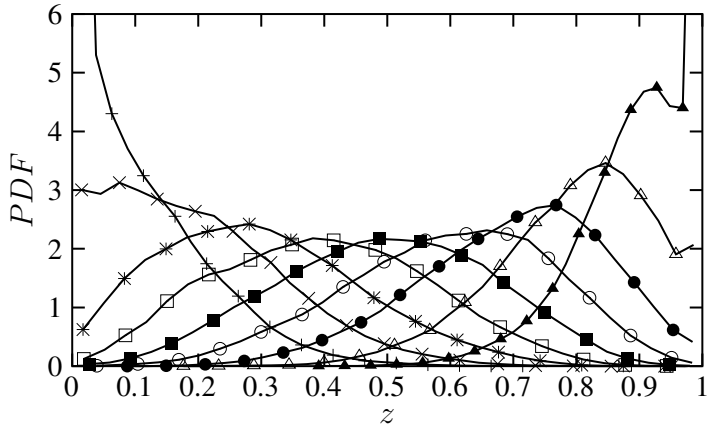

Figure 3.88: Case inf-1.1: pdfs of mixture fraction in planes with various $\langle z \rangle$, $+$: 0.1, $\times$: 0.2, $*$: 0.3, $\square$: 0.4, $\blacksquare$: 0.5, $\circ$: 0.6, $\bullet$: 0.7, $\triangle$: 0.8, $\blacktriangle$: 0.9

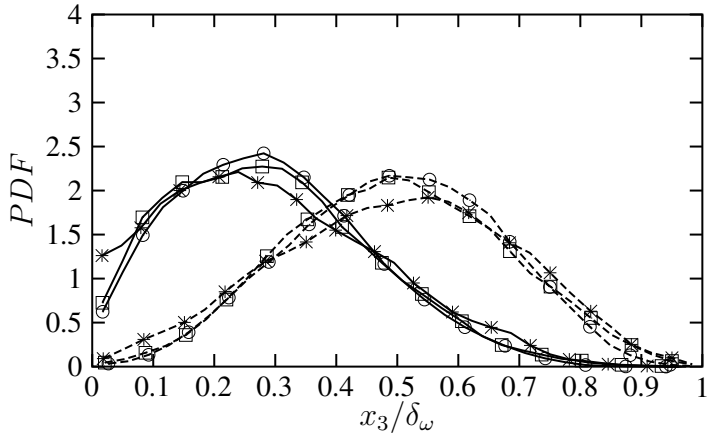

Figure 3.89: Pdfs of mixture fraction in the plane with $\langle z \rangle = 0.3$ (solid) and $\langle z \rangle = 0.5$ (dashed), symbols as in Fig. 3.82

The pointed shape of the scalar variance in Fig. 3.84 and the shift of its peak away from the center of the mixing layer can be related with the different shapes that the mixture fraction pdfs have at the various locations across the mixing layer, as e.g. displayed in Fig. 3.86: The pdfs that are taken from the lower, oxygen side of the mixing layer are broader, i.e. have a higher variance than the ones taken from the upper, fuel side. This is consistent with the maximum of the scalar variance being shifted towards the oxygen side, i.e. towards the plane with the stoichiometric value $\langle z \rangle = 0.3$.

In Fig. 3.89, the scalar pdfs taken in the planes with $\langle z \rangle = 0.3$ and $\langle z \rangle = 0.5$ are plotted for different convective Mach numbers. Again, the relatively weak influence of compressibility is visible.

Mixing efficiency The mixing efficiency, which measures the mixing of the fluid in the layer at the molecular level and reveals how much free-stream fluid is present, is computed for the mixture fraction by

$$\frac{\delta_M}{\delta_z} = \frac{1}{\delta_z} \int_0^\infty dx_3 \int_\epsilon^{1-\epsilon} dz P\left(z, x_3\right) \tag{3.44}$$

where δ_z denotes the 99% scalar thickness. This definition has been suggested by Freund et al. [64]. Fig. 3.90 shows the mixing efficiency as a function of M_c for the reacting mixing layers. The curves for two different values of the small parameter ϵ, which determines what kind of fluid is considered to be pure, are shown. It can be seen that the mixing efficiency increases with

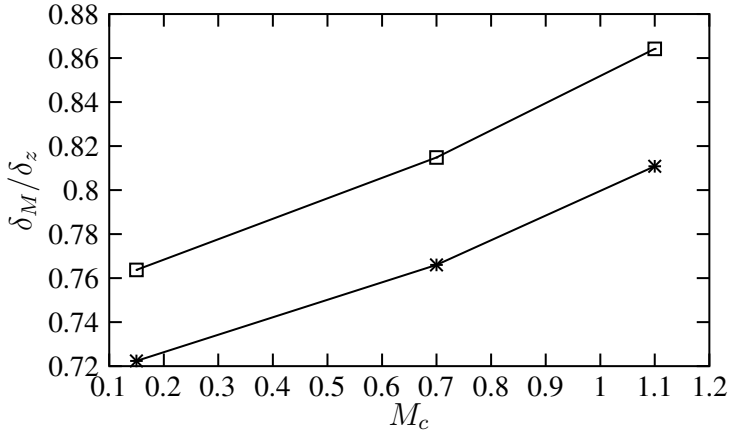

Figure 3.90: Mixing efficiency, □: $\epsilon = 0.02$, ∗: $\epsilon = 0.04$

increasing compressibility. This does not necessarily mean that the fluid is better mixed but can also be related with less free-stream fluid being engulfed when M_c increases (cf. Sect. 3.4.4.4). Whether the mixing efficiency in the reacting mixing layers is higher or lower than the one of the inert mixing layers (cf. Fig. 2.131) depends on the choice of the exact value for ϵ and on M_c. The reacting mixing layer at $M_c = 1.1$ has the highest mixing efficiency (for $\epsilon = 0.02$) of all test cases. For the inert test cases (Fig. 2.131), the increase in mixing efficiency between $M_c = 0.15$ and $M_c = 0.7$ is higher than the one between $M_c = 0.7$ and $M_c = 1.1$. For the reacting mixing layers, the contrary is true. An explanation for this behaviour is not available yet.

Scalar variance transport equation The transport equation of the mixture fraction variance reads for temporally evolving shear layers:

$$\begin{aligned}\frac{\partial}{\partial t}\langle\frac{1}{2}\rho z''^2\rangle = &-\frac{1}{2}\langle u_3\rangle_f\frac{\partial}{\partial x_3}\langle\rho z''^2\rangle - \frac{1}{2}\frac{\partial}{\partial x_3}\langle\rho u_3'' z''^2\rangle \\ &-\langle\rho z'' u_3''\rangle\frac{\partial\langle z\rangle_f}{\partial x_3} - \frac{1}{2}\langle\rho z''^2\rangle\frac{\partial\langle u_3\rangle_f}{\partial x_3} \\ &+\frac{\partial}{\partial x_3}\langle\frac{\mu}{Sc}\frac{\partial z}{\partial x_3}z''\rangle - \langle\frac{\mu}{Sc}\frac{\partial z}{\partial x_i}\frac{\partial z''}{\partial x_i}\rangle\end{aligned} \tag{3.45}$$

The terms on the RHS describe mean convection, turbulent transport, turbulent production (two terms), molecular diffusion and dissipation. The diffusion and the convective transport are small

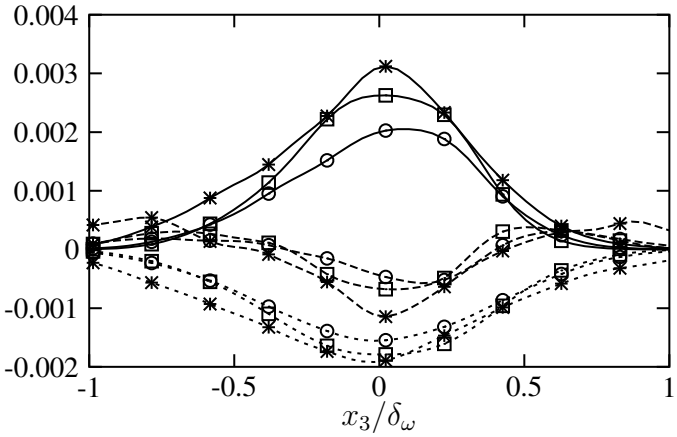

Figure 3.91: Major terms in the scalar variance transport equation, normalized by $\rho_0\Delta u/\delta_\omega$, solid: turbulent production, dashed: turbulent transport, dotted: dissipation rate, symbols as in Fig. 3.82

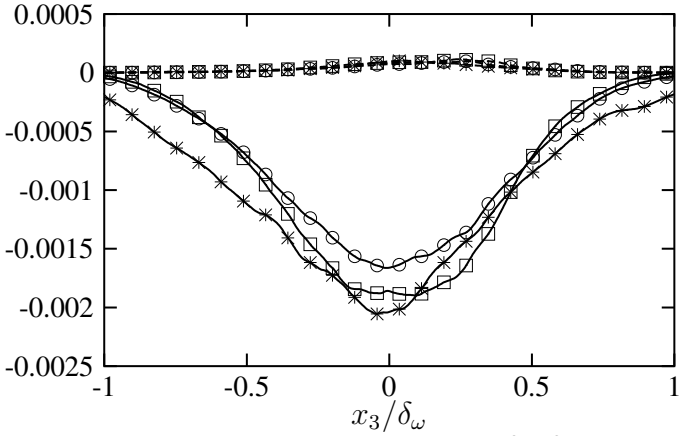

Figure 3.92: Parts of the scalar dissipation rate, solid: $-\langle \frac{\mu}{Sc}\frac{\partial z}{\partial x_j}\frac{\partial z}{\partial x_j}\rangle$, dashed: $\langle \frac{\mu}{Sc}\frac{\partial z}{\partial x_j}\rangle \frac{\partial \langle z\rangle_f}{\partial x_j}$, normalized by $\rho_0 \Delta u/\delta_\omega$, symbols as in Fig. 3.82

compared to the other terms which are shown in Fig. 3.91. They are all reduced by compressibility and heat release (cf. Fig. 2.132) with the reduction due to compressibility being weaker when heat release is present.

The dissipation rate can also be written as

$$\epsilon_z = -\langle \frac{\mu}{Sc}\frac{\partial z}{\partial x_i}\frac{\partial z''}{\partial x_i}\rangle = -\langle \frac{\mu}{Sc}\frac{\partial z}{\partial x_j}\frac{\partial z}{\partial x_j}\rangle + \langle \frac{\mu}{Sc}\frac{\partial z}{\partial x_j}\rangle \frac{\partial \langle z\rangle_f}{\partial x_j} \tag{3.46}$$

with the second term being negligible compared to the first one (Fig. 3.92). Therefore, ϵ_z can be approximated as:

$$\epsilon_z \approx -\langle \frac{\mu}{Sc}\frac{\partial z}{\partial x_j}\frac{\partial z}{\partial x_j}\rangle \tag{3.47}$$

Scalar fluxes The streamwise scalar flux, $\langle \rho u_1'' z''\rangle$, and the transverse scalar flux, $\langle \rho u_3'' z''\rangle$, are shown in Figs. 3.93 and 3.94. They are considerably smaller than for the inert cases (cf. Figs. 2.134 and 2.135). The fact that the fluxes in the inert and reacting cases have different signs results from the different signs of the mean scalar gradient. The spanwise scalar flux is negligible compared to the other fluxes and therefore not shown. As for the inert mixing layers, the transverse scalar flux is more sensitive to an increase in M_c and reduces more strongly than the streamwise scalar flux.

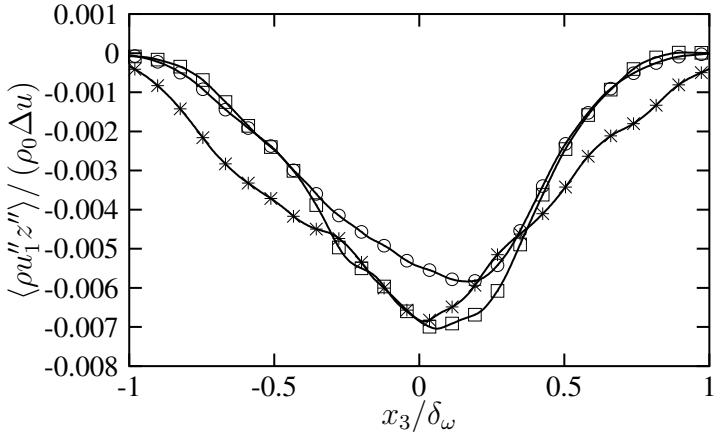

Figure 3.93: Scalar flux $\langle \rho u_1'' z''\rangle$, normalized by $\rho_0 \Delta u$, symbols as in Fig. 3.82

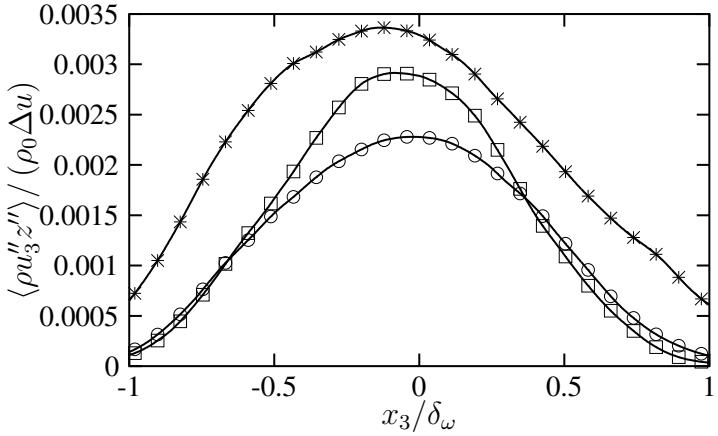

Figure 3.94: Scalar flux $\langle \rho u_3'' z'' \rangle$, normalized by $\rho_0 \Delta u$, symbols as in Fig. 3.82

Transport equations of scalar fluxes The transport equation for the scalar (mass fraction) flux in x_1-direction for the temporally evolving shear layer reads:

$$\begin{aligned}
\frac{\partial}{\partial t}\langle \rho u_1'' z'' \rangle = & - \langle u_3 \rangle_f \frac{\partial}{\partial x_3}\langle \rho u_1'' z'' \rangle - \frac{\partial}{\partial x_3}\langle \rho u_1'' u_3'' z'' \rangle \\
& - \langle \rho u_1'' z'' \rangle \frac{\partial \langle u_3 \rangle_f}{\partial x_3} - \langle \rho u_3'' z'' \rangle \frac{\partial \langle u_1 \rangle_f}{\partial x_3} - \langle \rho u_1'' u_3'' \rangle \frac{\partial \langle z \rangle_f}{\partial x_3} \\
& + \langle p \frac{\partial z''}{\partial x_1} \rangle \\
& + \frac{\partial}{\partial x_3}\langle \tau_{13} z'' \rangle + \frac{\partial}{\partial x_3}\langle u_1'' \frac{\mu}{Sc} \frac{\partial z}{\partial x_3} \rangle \\
& - \langle \tau_{1j} \frac{\partial z''}{\partial x_j} \rangle - \langle \frac{\mu}{Sc} \frac{\partial z}{\partial x_j} \frac{\partial u_1''}{\partial x_j} \rangle .
\end{aligned} \tag{3.48}$$

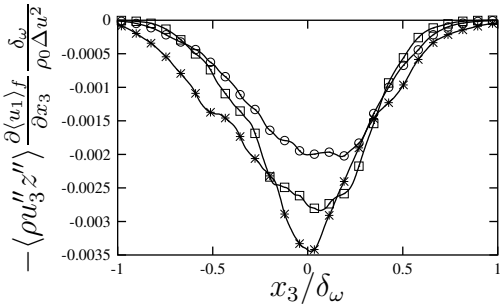

Figure 3.95: Part of the streamwise scalar flux production, normalized by $\rho_0 \Delta u^2/\delta_\omega$, symbols as in Fig. 3.82

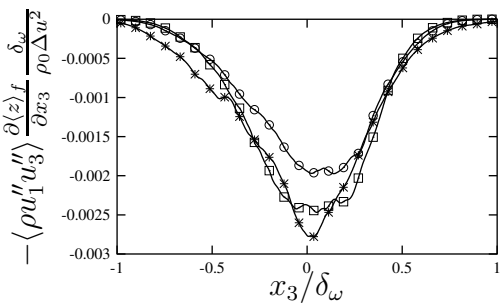

Figure 3.96: Part of the streamwise scalar flux production, normalized by $\rho_0 \Delta u^2/\delta_\omega$, symbols as in Fig. 3.82

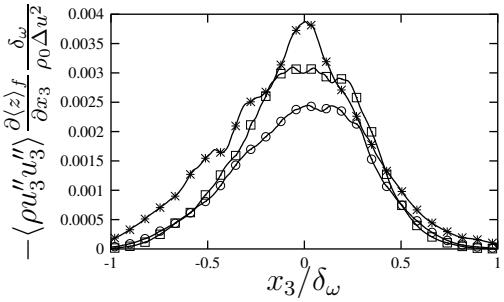

Figure 3.97: Part of the transverse scalar flux production, normalized by $\rho_0 \Delta u^2/\delta_\omega$, symbols as in Fig. 3.82

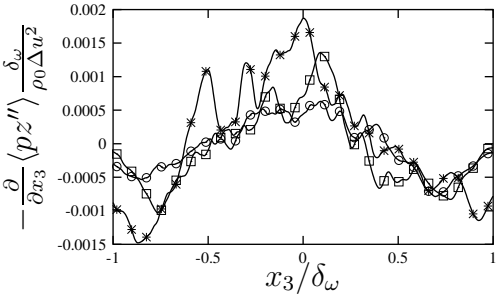

Figure 3.98: Major part of the diffusion of the transverse scalar flux, normalized by $\rho_0 \Delta u^2/\delta_\omega$, symbols as in Fig. 3.82

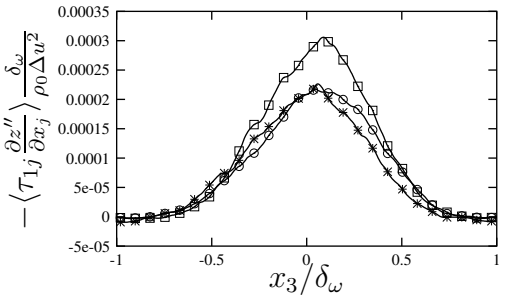

Figure 3.99: Part of the dissipation rate of the streamwise scalar flux, normalized by $\rho_0\Delta u^2/\delta_\omega$, symbols as in Fig. 3.82

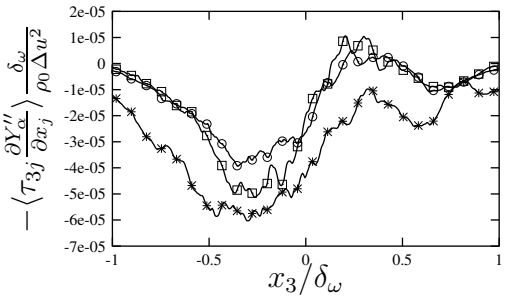

Figure 3.100: Part of the dissipation rate of the transverse scalar flux, normalized by $\rho_0\Delta u^2/\delta_\omega$, symbols as in Fig. 3.82

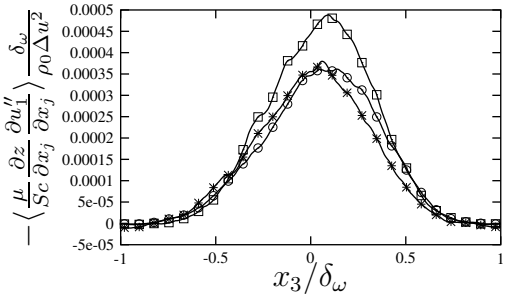

Figure 3.101: Part of the dissipation rate of the streamwise scalar flux, normalized by $\rho_0\Delta u^2/\delta_\omega$, symbols as in Fig. 3.82

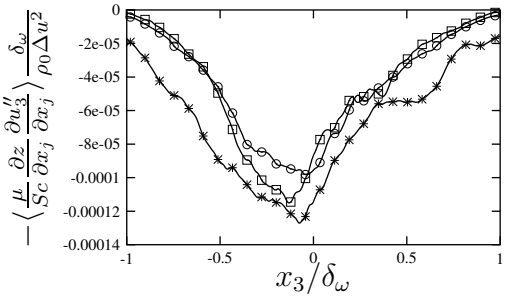

Figure 3.102: Part of the dissipation rate of the transverse scalar flux, normalized by $\rho_0\Delta u^2/\delta_\omega$, symbols as in Fig. 3.82

The corresponding equation for the flux in x_3-direction is:

$$\begin{aligned}\frac{\partial}{\partial t}\langle\rho u_3''z''\rangle =& -\langle u_3\rangle_f\frac{\partial}{\partial x_3}\langle\rho u_3''z''\rangle - \frac{\partial}{\partial x_3}\langle\rho u_3''u_3''z''\rangle\\ &- 2\langle\rho u_3''z''\rangle\frac{\partial\langle u_3\rangle_f}{\partial x_3} - \langle\rho u_3''u_3''\rangle\frac{\partial\langle z\rangle_f}{\partial x_3}\\ &+ \langle p\frac{\partial z''}{\partial x_3}\rangle\\ &- \frac{\partial}{\partial x_3}\langle pz''\rangle + \frac{\partial}{\partial x_3}\langle\tau_{33}z''\rangle + \frac{\partial}{\partial x_3}\langle u_3''\frac{\mu}{Sc}\frac{\partial z}{\partial x_3}\rangle\\ &- \langle\tau_{3j}\frac{\partial z''}{\partial x_j}\rangle - \langle\frac{\mu}{Sc}\frac{\partial z}{\partial x_j}\frac{\partial u_3''}{\partial x_j}\rangle.\end{aligned} \tag{3.49}$$

The terms on the RHS in the first line denote convection and turbulent transport. The ones in the second line are production terms and the term in the third line is the pressure scalar-gradient correlation. The last two lines contain diffusion and dissipation terms.

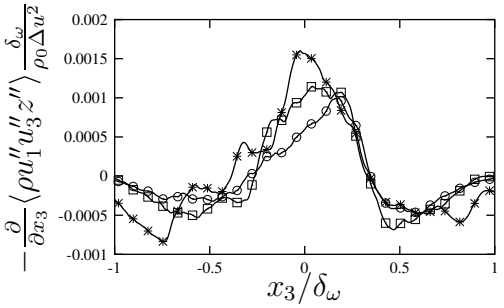

Figure 3.103: Turbulent transport of the streamwise scalar flux, normalized by $\rho_0\Delta u^2/\delta_\omega$, symbols as in Fig. 3.82

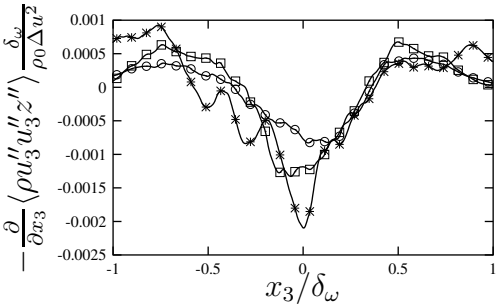

Figure 3.104: Turbulent transport of the transverse scalar flux, normalized by $\rho_0\Delta u^2/\delta_\omega$, symbols as in Fig. 3.82

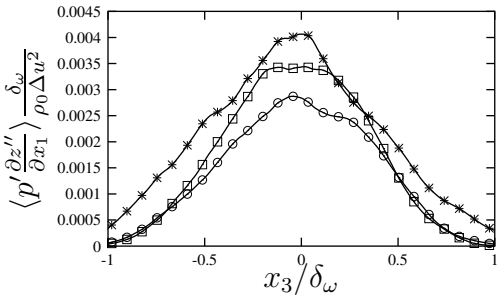

Figure 3.105: Pressure-scrambling term in streamwise direction, normalized by $\rho_0 \Delta u^2/\delta_\omega$, symbols as in Fig. 3.82

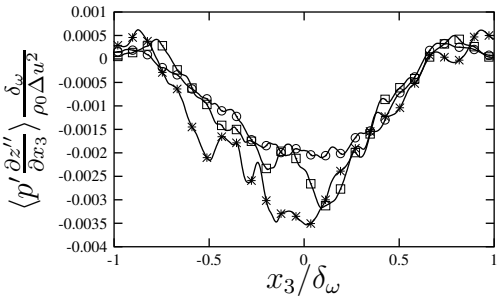

Figure 3.106: Pressure-scrambling term in transverse direction, normalized by $\rho_0 \Delta u^2/\delta_\omega$, symbols as in Fig. 3.82

The pressure scalar gradient correlation can also be written as

$$\langle p \frac{\partial z''}{\partial x_1} \rangle = \langle p' \frac{\partial z''}{\partial x_1} \rangle, \tag{3.50}$$

in x_1-direction and in x_3 direction,

$$\langle p \frac{\partial z''}{\partial x_3} \rangle = \langle p \rangle \frac{\partial \langle z \rangle}{\partial x_3} - \langle p \rangle \frac{\partial \langle z \rangle_f}{\partial x_3} + \langle p' \frac{\partial z''}{\partial x_3} \rangle \tag{3.51}$$

with the last term in each expression being the pressure-scrambling term Π_{zi}.

The major terms in these equations are the production, the diffusion, the dissipation rates and the turbulent transport as well as the pressure-scrambling term. They are shown in Figs. 3.95 to 3.106 and are smaller than for the inert cases. While the production rates, the dissipation rate, the diffusion and the turbulent transport are more pointed in the center than the corresponding terms for the inert cases, the pressure-scrambling term has a similar shape. All terms in the reacting cases show the already expected behaviour of being less sensitive to changes in M_c than without heat release which makes the influence of heat release stronger at low M_c. Moreover, most of the terms are damped by compressibility, except for the two parts of the dissipation rate of the streamwise scalar flux shown in Figs. 3.99 and 3.101.

Spectra The scalar energy spectra in Fig. 3.107 and the scalar dissipation spectra in Fig. 3.108 of the reacting test cases are similar to the inert ones (cf. Figs. 2.157 and 2.158) in the large scales but contain less energy in the small scales. This is in agreement with the smoother scalar

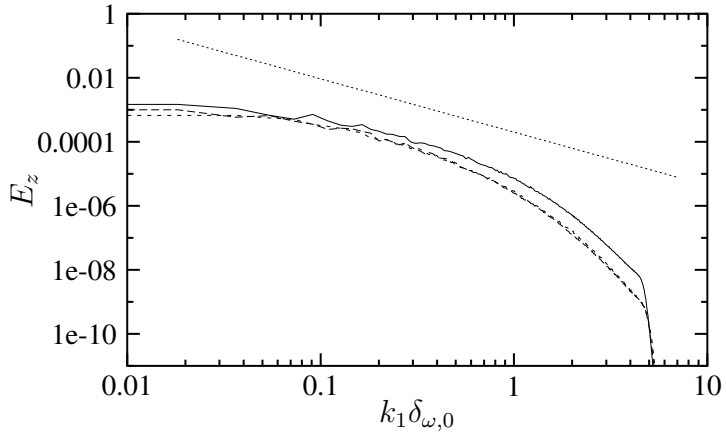

Figure 3.107: One-dimensional, streamwise spectrum of the mixture fraction z, solid: inert-0.15, dashed: inert-0.7, dotted: inert-1.1, the straight line has $-5/3$ slope

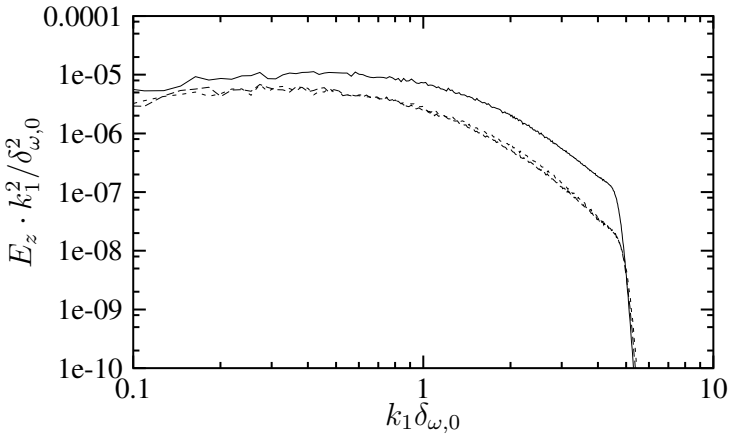

Figure 3.108: One-dimensional dissipation spectrum of the mixture fraction z (spectrum of z multiplied with $(k_1\delta_{\omega,0})^2$), solid: inert-0.15, dashed: inert-0.7, dotted: inert-1.1

fields that have been noticed in Sect. 3.4.1. Additionally, the peaks of the dissipation spectra for the reacting cases are situated at higher wavenumbers than for the inert cases. Due to the coarser resolution of the reacting test cases, the range of wavenumbers on the horizontal axes in Figs. 3.107 and 3.108 do not extend to such high wavenumbers as in Fig. 2.157 and 2.158. Nevertheless, the energy fall-off is smooth over several orders of magnitudes and no signs of spurious energy accumulation in the highest wavenumbers are visible. In contrast to what has been observed from the inert test cases, changes with M_c are only observed between $M_c = 0.15$ and $M_c = 0.7$ and not when rising M_c further. The peak of the dissipation spectrum is rather uninfluenced by compressibility.

3.4.4.4 Entrainment

Knowledge of the entrainment mechanisms and their changes with heat release and combustion is particularly important for reacting flows since the amount of chemical product formed as a result of mixing is limited by the amount of reactant species entrained into the layer [72]. A hint that the entrainment of outside fluid is reduced by heat release is given by the fact that the mixing layer growth rate decreases when heat release is present inspite of a possible increase by displacement effects due to thermal expansion. Hermanson and Dimotakis [72] used different methods, e.g. integral and geometrical formulae, to compute the entrainment into mixing layers with different density reductions by heat release and confirmed this suggestion.

One feature concerning the entrainment that cannot be investigated with the present, temporally evolving mixing layer configuration is the entrainment ratio, i.e. the average amount of fluid entrained into a spatially evolving mixing layer from the high-speed side divided by the average amount of fluid entrained from the low-speed side. Hermanson and Dimotakis [72] showed its reduction with heat release, and Miller et al. [114] found it to be reduced further with compressibility, which is in agreement with the results of Hall et al. [70] for the inert mixing layer. This means that the overall stoichiometry of the mixing layer is affected by both, compressibility and heat release, which can also have feedback effects on the heat release characteristics.

Measurement of volumes The distinction between the mixing layer and its surroundings as well as between the mixed volume and the engulfed volume within the mixing layer is made

here again with the help of vorticity and scalar thresholds. The determination of the different volumes (mixing layer, mixed and engulfed volume) is the same as described previously for the inert mixing layers (cf. Sect. 2.4.4.3). The threshold values used for the reacting mixing layer do not differ from those used for the inert test cases: $z = 0.05$ and 0.95 for the scalar (here the mixture fraction) and $\omega = 0.1\langle\omega_{max}\rangle$ for the vorticity.

Figures 3.109 and 3.110 show the mixing layer volume and the engulfed volume for the reacting flow cases through a part of the self-similar state. To facilitate comparison with the corresponding figures for the inert mixing layers (Figs. 2.161 and 2.162) only part of the self-similar state is shown. However, the growth of mixing layer and engulfed volume that is visible during the time period shown continues throughout the self-similar state, and the growth rates nearly remain constant. The growth of the mixing layer decreases with increasing M_c, but the decrease, in particular between $M_c = 0.15$ and $M_c = 0.7$, is not as pronounced as without combustion. In total, the growth rates for the reacting mixing layers are smaller than for the inert ones, which is most obvious for the test cases at $M_c = 0.15$ and which is in agreement with other authors who found the entrainment being reduced with heat release [72].

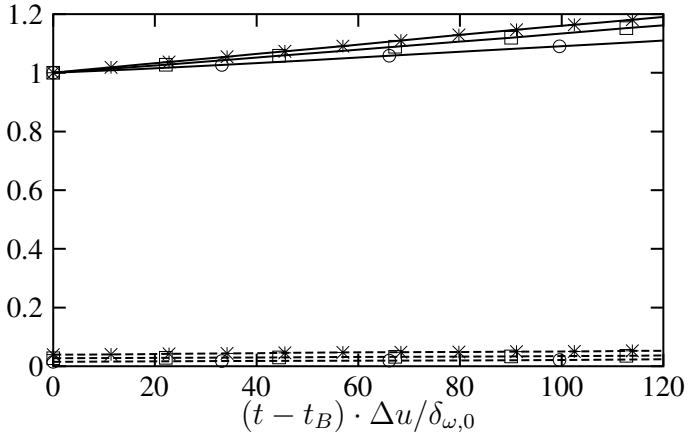

Figure 3.109: Based on vorticity thresholds: Mixing layer volume V_{ml} (solid) and engulfed volume V_{en} (dashed) vs. the normalized time passed since the beginning of the self-similar state at t_B. Volumes are normalized with the mixing layer volume at the beginning of the self-similar state, $V_{ml,B}$, $*$: inf-0.15, $\square$: inf-0.7, $\circ$: inf-1.1

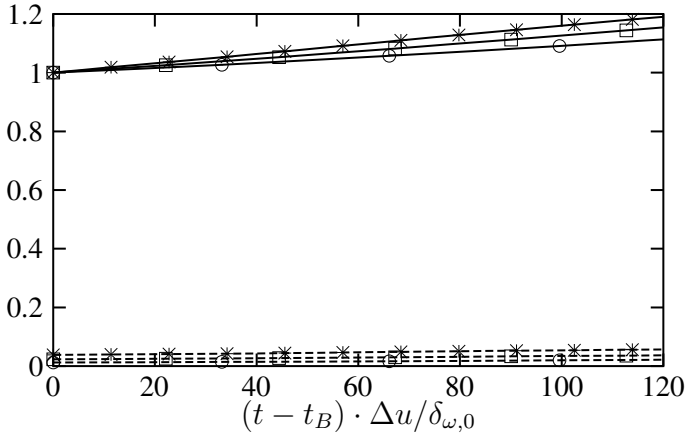

Figure 3.110: Based on mixture fraction thresholds: Mixing layer volume V_{ml} (solid) and engulfed volume V_{en} (dashed) vs. the normalized time passed since the beginning of the self-similar state at t_B. Volumes are normalized with the mixing layer volume at the beginning of the self-similar state, $V_{ml,B}$. Symbols as in Fig. 3.109

The engulfed volume constitutes only a small part of the mixing layer: about $4\ \%$ for case inf-0.15, $2.5\ \%$ for case inf-0.7 and $1.5\ \%$ for case inf-1.1, which is smaller than for the inert cases at the same convective Mach number, a tendency which is in agreement with the results of Planché & Reynolds [141].

A comparison between Fig. 3.109 and Fig. 3.110 shows that it is not of much importance for the volumes and their growth rates whether mixture fraction thresholds are used instead of vorticity thresholds.

Visual thickness Figure 3.111 shows the visual thicknesses δ_{vis} and thicknesses derived from the mixing layer volume, δ_{vol} (cf. Sect. 2.4.4.3), for the reacting mixing layers. Even though a reduction of the respective growth rates with M_c can be observed it is not as strong as for the inert mixing layers (Fig. 2.163), the growth of which is also faster. As explained in the corresponding section about the visual thickness of the inert mixing layers, the distance between the curves of the visual thickness and the ones of the thickness derived from the mixing layer volume is affected by intermittency. As in inert mixing layers, the intermittency decreases with compressibility in reacting ones, i.e. δ_{vis} and δ_{vol} in Fig. 3.111 become closer.

In Fig. 3.112, the mixture fraction thresholds are used to determine δ_{vis} and δ_{vol} which leads to

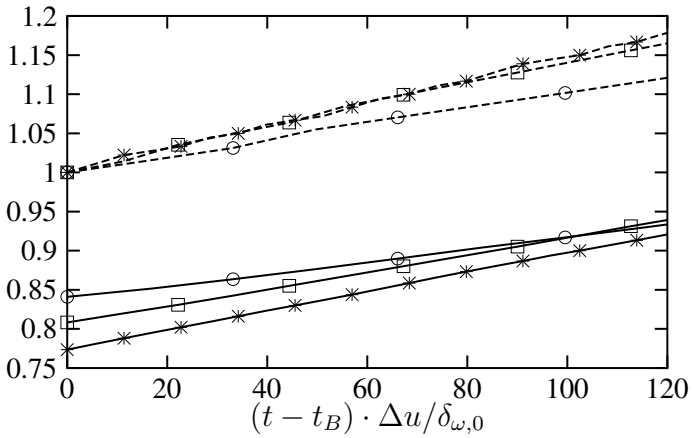

Figure 3.111: Based on vorticity thresholds: Thickness computed from mixing layer volume δ_{vol} (solid) and visual thickness δ_{vis} (dashed). Thicknesses are normalized by the visual thickness at the beginning of the self-similar state, $\delta_{vis,B}$. Symbols as in Fig. 3.109

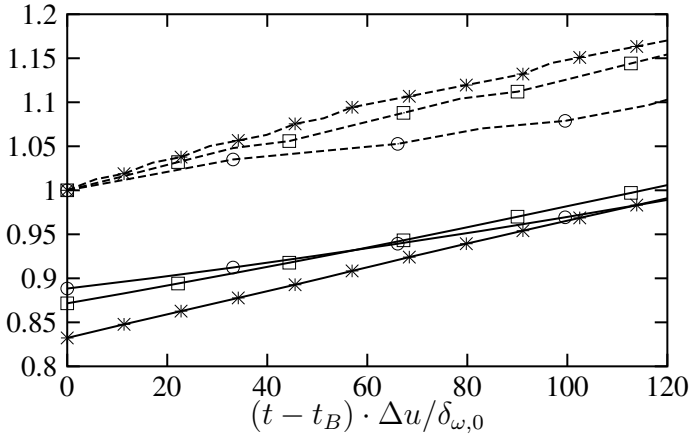

Figure 3.112: Based on mixture fraction thresholds: Thickness computed from mixing layer volume δ_{vol} (solid) and visual thickness δ_{vis} (dashed). Thicknesses are normalized by the visual thickness at the beginning of the self-similar state, $\delta_{vis,B}$. Symbols as in Fig. 3.109

a lower intermittency than when the vorticity thresholds are used (Fig. 3.111). Compared to the inert mixing layers, the intermittency in Fig. 3.111 (reacting, thresholds based on vorticity) is larger than the one in the corresponding Fig. 2.163 (inert, thresholds based on vorticity), but it is slightly smaller in Fig. 3.112 (reacting, thresholds based on scalar) than in Fig. 2.164 (inert, thresholds based on scalar).

Measurement of densities Figure 3.113 shows the densities of the mixing layers, the densities of the engulfed volumes and the densities of the mixed volumes which are determined based on the vorticity threshold. Due to the heat release, the mixing layer density is only $40\ \%$ of the free-stream density. In contrast to the inert mixing layers (cf. Fig. 2.165), only little influence of dissipative heating on the mixing layer density can be noticed, i.e. the curves at high M_c are close to the one at $M_c = 0.15$. The density of the engulfed fluid is higher than the density of the mixing layer, because it enters the mixing layer from the cold, outside region. However, the fact that its density is also smaller than ρ_0 shows that it has already been partially heated by conduction.

The density of the mixed volume is below the density of the mixing layer since the latter includes the engulfed fluid. However, since the amount of engulfed fluid is small at all M_c (cf. previous

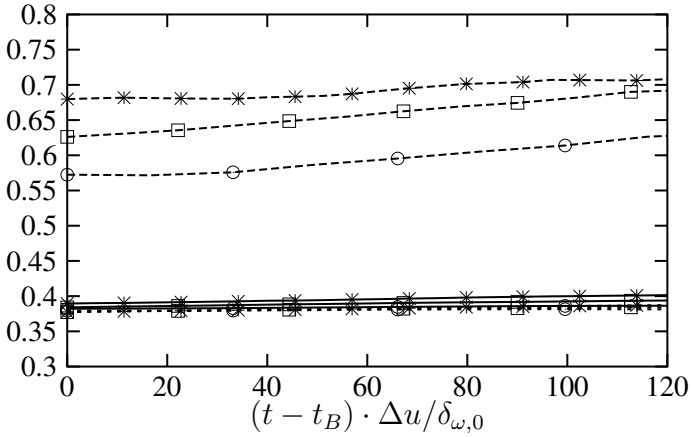

Figure 3.113: Based on vorticity thresholds: Mixing layer density ρ_{ml}/ρ_0 (solid), density of the engulfed volume, ρ_{en}/ρ_0 (dashed), and density of the mixed volume, ρ_{mix}/ρ_0 (dotted), vs. the normalized time passed since the beginning of the self-similar state at t_B. Symbols as in Fig. 3.109

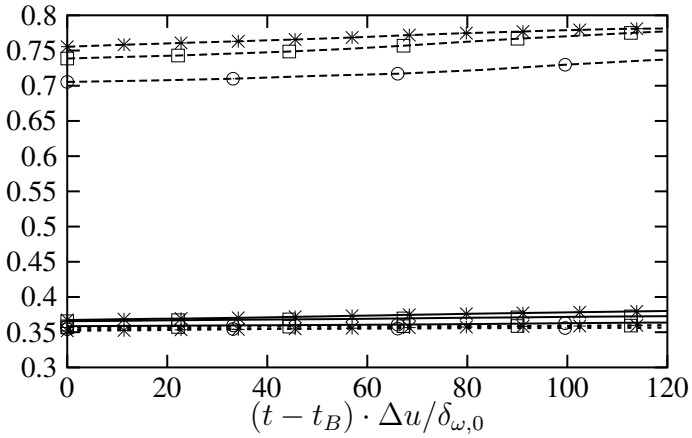

Figure 3.114: Based on mixture fraction thresholds: Mixing layer density ρ_{ml}/ρ_0 (solid), density of the engulfed volume, ρ_{en}/ρ_0 (dashed), and density of the mixed volume, ρ_{mix}/ρ_0 (dotted), vs. the normalized time passed since the beginning of the self-similar state at t_B. Symbols as in Fig. 3.109

sections), the difference between mixing layer density and density of the mixed volume is also small. Using the mixture fraction definition for the thresholds, as done in Fig. 3.114, leads to higher densities of the engulfed fluid. This behaviour has already been observed for the inert mixing layers (cf. Fig. 2.166).

Particle statistics As for the inert mixing layers, paths of fluid particles were also computed for the infinitely fast reacting ones. The procedure is exactly the same as described in the corresponding paragraph in Sect. 2.4.4.3. Numbers of particles and initial parameters are given in Table 3.8. The particles are initially located at every 12th grid point in the x_1- and x_2-direction and at every 8th grid point in the x_3-direction, except for the simulation inf-1.1 where they are initialized at every 12th grid point in all directions.

The growths of vorticity and concentration along pathlines are studied, and statistical quantities are given in Table 3.9. The notations are the same as in the corresponding discussion about the inert mixing layers. Since the mean values of the displacement between the crossings of lower and upper thresholds (first and second lines in table 3.9) as well as those of the time between the crossings of these thresholds (third and fourth lines) are small compared to the maxima, the process of acquiring vorticity and concentration after the entering of the mixing layer occurs quite fast and close to the mixing layer boundaries at all M_c. This can rather be described as nibbling than as engulfment. The same has been noticed for the inert mixing layers and is in agreement with the fact that the engulfed volume is small at all M_c with and without heat release. The means of the values in the last two lines of Table 3.9 are positive. Therefore, as for the inert mixing layers, the acquisition of vorticity occurs faster than the one of scalar concentration. There are also differences between the inert and reacting mixing layers. In particular, what the non-dimensional times between the crossings of the lower and upper thresholds are concerned (third and fourth lines of tables 2.7 and 3.9): A significant increase is noticed when heat release is present. On the contrary, the average displacements between the threshold crossings (first and second lines) do not change much compared to the displacements without heat release. The same tendencies, but with an increase of the times to a smaller extent, were observed with increasing compressibility for the inert mixing layers and can also be found with increasing M_c for the reacting ones. This means that as heat release and compressibility increase, the particles, after having entered the mixing layer, are convected longer right along its edges while acquiring vorticity and concentration. Therefore, at higher convective Mach number, the range of Mach number magnitudes at the time the upper threshold is crossed is much larger than for the quasi-incompressible mixing layer as shown by the pdfs in Fig. 3.115.

Table 3.8: Particle parameters: N_P particles are initialized at $\tau_{\omega,PB}$. They are situated initially between $x_3 = x_{3,P1}$ and $x_{3,P2}$ and between $x_3 = x_{3,P3}$ and $x_{3,P4}$

	N_P	$\tau_{\omega,PB}$	$x_{3,P1}/\delta_{\omega,0}$	$x_{3,P2}/\delta_{\omega,0}$	$x_{3,P3}/\delta_{\omega,0}$	$x_{3,P4}/\delta_{\omega,0}$
inf-0.15	20480	190	-55.67	-24.14	22.55	54.07
inf-0.7	20480	295	-49.29	-17.76	16.56	48.09
inf-1.1	20480	228	-65.65	-18.16	17.36	64.85

Table 3.9: Statistics of displacements and elapsed times for growth of vorticity and mixture fraction along particle pathlines

		Sample size	Mean	Max	Min
inf-0.15	$\lvert x_{3,\omega u} - x_{3,\omega l}\rvert / \delta_{vis}(t_l)$	2229	0.0188	0.5410	0
	$\lvert x_{3,zu} - x_{3,zl}\rvert / \delta_{vis}(t_l)$	859	0.0398	0.5766	0
	$(t_{\omega u} - t_{\omega l}) / t_{vis}$	2229	0.6437	9.6366	0
	$(t_{zu} - t_{zl}) / t_{vis}$	859	0.9912	11.5919	0
	$(t_{zl} - t_{\omega l}) / t_{vis}$	1646	0.9502	6.2618	-5.7861
	$(t_{zu} - t_{\omega u}) / t_{vis}$	853	1.2797	11.3474	-9.6366
inf-0.7	$\lvert x_{3,\omega u} - x_{3,\omega l}\rvert / \delta_{vis}(t_l)$	4288	0.0253	0.8277	0
	$\lvert x_{3,zu} - x_{3,zl}\rvert / \delta_{vis}(t_l)$	2482	0.0513	0.8277	0
	$(t_{\omega u} - t_{\omega l}) / t_{vis}$	4288	1.1730	25.8824	0
	$(t_{zu} - t_{zl}) / t_{vis}$	2482	1.8754	26.5387	0
	$(t_{zl} - t_{\omega l}) / t_{vis}$	3721	1.1978	13.9185	-14.2523
	$(t_{zu} - t_{\omega u}) / t_{vis}$	2466	1.7592	26.5387	-22.5871
inf-1.1	$\lvert x_{3,\omega u} - x_{3,\omega l}\rvert / \delta_{vis}(t_l)$	6265	0.0224	0.5050	0
	$\lvert x_{3,zu} - x_{3,zl}\rvert / \delta_{vis}(t_l)$	4134	0.0045	0.6849	0
	$(t_{\omega u} - t_{\omega l}) / t_{vis}$	6265	1.0353	34.9646	0
	$(t_{zu} - t_{zl}) / t_{vis}$	4134	1.6721	47.8477	0
	$(t_{zl} - t_{\omega l}) / t_{vis}$	5517	1.4929	18.1162	-20.5031
	$(t_{zu} - t_{\omega u}) / t_{vis}$	4131	2.1170	35.8840	-24.8244

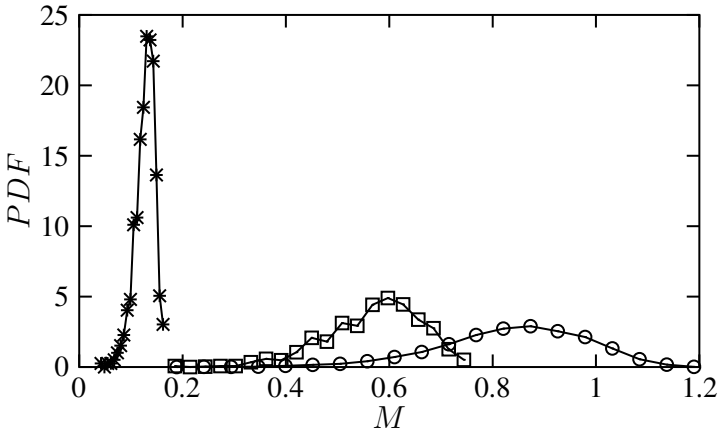

Figure 3.115: Pdfs of the local Mach number magnitude at the time when the particles are crossing the upper vorticity threshold. Symbols as in Fig. 3.109

Fractal nature of the mixing layer interface The fractal dimensions of the mixing layer interfaces, computed as described in the corresponding paragraph of Sect. 2.4.4.3, are given in Table 3.10. In comparison with Table 2.8, a decrease of the fractal dimensions with heat release is visible. The behaviour of the fractal dimensions with increasing M_c, i.e. a decrease between $M_c = 0.15$ and $M_c = 0.7$ followed by an increase between $M_c = 0.7$ and $M_c = 1.1$ is as observed for the scalar isosurfaces of the inert shear layers.

Lower fractal dimensions with heat release (and also with increasing compressibility) are in agreement with less intermittency and smoother vorticity and scalar fields as shown in Figs. 3.116 to 3.121. The increase in dominant length scale with heat release and compressibility is clearly

Table 3.10: Fractal dimensions D of isosurfaces

	$\omega = 0.2\langle\omega\rangle_{max}$	$\omega = 0.1\langle\omega\rangle_{max}$	$z = 0.9$	$z = 0.95$
inf-0.15	2.55	2.39	2.35	2.30
inf-0.7	2.50	2.33	2.28	2.20
inf-1.1	2.54	2.37	2.30	2.26

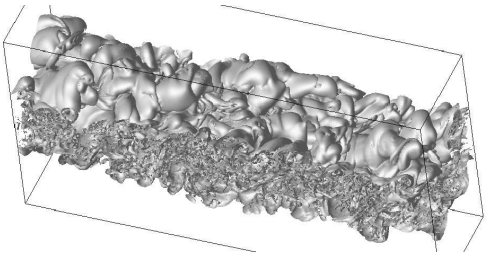

Figure 3.116: Case inf-0.15: Instantaneous isosurface of vorticity $\omega = 0.2\langle\omega\rangle_{max}$ at $\tau_\omega = 573$

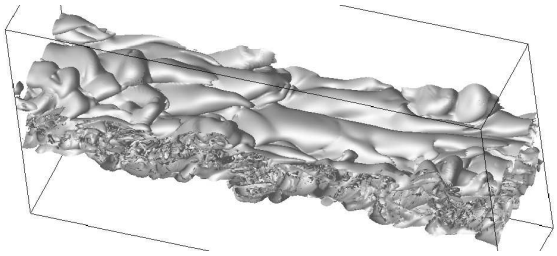

Figure 3.117: Case inf-0.7: Instantaneous isosurface of vorticity $\omega = 0.2\langle\omega\rangle_{max}$ at $\tau_\omega = 761$

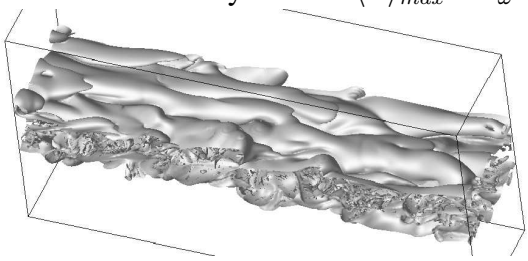

Figure 3.118: Case inf-1.1: Instantaneous isosurface of vorticity $\omega = 0.2\langle\omega\rangle_{max}$ at $\tau_\omega = 803$

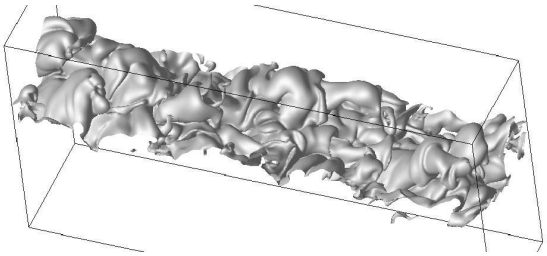

Figure 3.119: Case inf-0.15: Instantaneous isosurface of mixture fraction $z = 0.1$ at $\tau_\omega = 573$

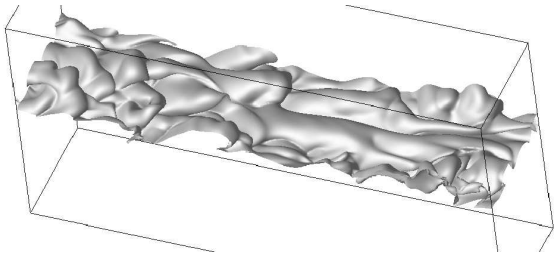

Figure 3.120: Case inf-0.7: Instantaneous isosurface of mixture fraction $z = 0.1$ at $\tau_\omega = 761$

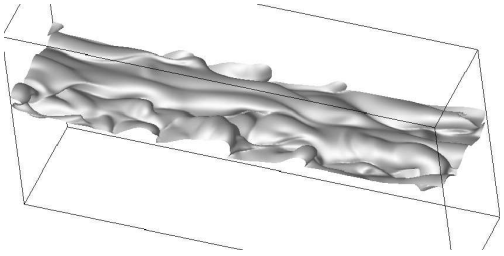

Figure 3.121: Case inf-1.1: Instantaneous isosurface of mixture fraction $z = 0.1$ at $\tau_\omega = 803$

visible from these figures and when comparing them with the corresponding ones for the inert mixing layers, Figs. 2.169 to 2.174. Moreover, it can be stated that the scalar fields are in general smoother, i.e. less intermittent than the vorticity fields, which leads to lower fractal dimensions for the scalar in Table 3.10. This difference is related with the fact that the vorticity is calculated from gradients.

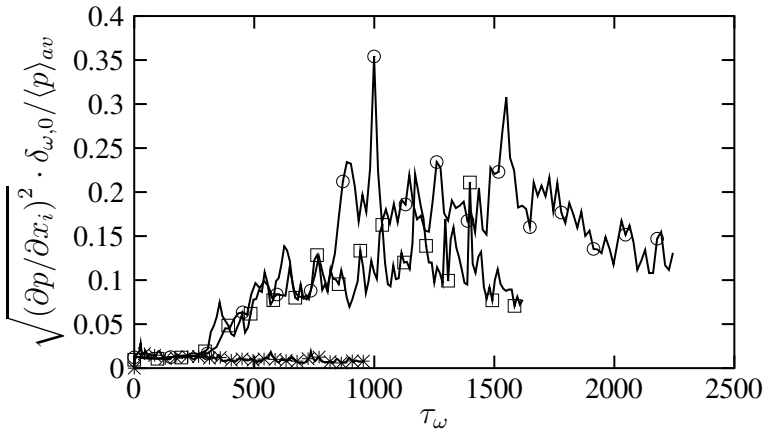

Figure 3.122: Temporal development of the maximum pressure gradient, normalized by $\langle p \rangle_{av}/\delta_{\omega,0}$, $*$: inf-0.15, $\square$: inf-0.7, $\circ$: inf-1.1

3.4.5 Shocklets

In order to investigate the possible appearance of shocklets, the normalized maximum pressure gradient is monitored. Its temporal development for the reacting mixing layers at all M_c is shown in Fig. 3.122. An increase between $M_c = 0.15$ and $M_c = 0.7$ is clearly visible but less prominent than for the inert mixing layers (cf. Fig. 2.177). Since no further increase of the normalized pressure gradient between $M_c = 0.7$ and $M_c = 1.1$, eddy shocklets are less probable and, if present weaker, for case inf-1.1 than for the case inert-1.1.

3.5 Summary and conclusions

The subject of this chapter has been DNS of turbulent, temporal evolving, infinitely fast reacting mixing layers with heat release. The reaction, that has been taken into account, is a one-step, infinitely fast reaction of oxygen and hydrogen which, together with simplifications concerning molecular diffusion mechanisms, has allowed to link the mass fractions of the chemical species with the mixture fraction, using the linear Burke-Schumann relations. Therefore, only the transport equation of one scalar, namely the mixture fraction z, had to be solved, which contained no source term. From the resulting distribution, the species mass fractions have been computed. No additional transport equations for the mass fractions were needed. In order to retain realistic heat conduction and a compressible formulation of the Navier-Stokes equations, an energy equation, in the form of a pressure or temperature equation, has also been integrated in time.

The results obtained have been analyzed with a particular focus on the changes that have occurred compared to the inert mixing layers in Chapter 2. Since the simulations have been performed at three different convective Mach numbers, $M_c = 0.15$, 0.7 and 1.1, which have been the same as in Chapter 2, compressibility effects could also be worked out and compared to those encountered for the inert mixing layers. Contrarily to the inert mixing layers, no shocklets have been found in the reacting mixing layers at any of the convective Mach numbers under investigation.

All simulations have reached a self-similar state with constant growth rates of momentum thickness and product mass thickness. In comparison to the inert mixing layers, the momentum thickness growth rates are lower for the reacting mixing layers. As for the inert mixing layers a further decrease with increasing Mach number has been noticed. However, the effects of compressibility

on the momentum thickness growth rate and on most other statistical quantities are not as strong as for the inert mixing layers, and they are often masked by the much stronger consequences of heat release. It was also observed that heat release has stronger influences at lower than at higher M_c, which is directly visible when regarding the non-dimensionalized heat release terms in the pressure and temperature equations. These terms become very small at the highest convective Mach number under investigation.

The effect of heat release on instantaneous scalar (mixture fraction) fields and isosurfaces is similar to the effect of compressibility that has been noticed in Chapter 2: When heat release is present, the fields are smoother and dominant length scales, which are for example visible from structures at the boundaries of the mixing layers, are larger than for the inert simulations. A corroboration of these observations has been given by the computation of the fractal dimensions of the scalar and vorticity isosurfaces, separating the mixing layer from its non-turbulent surroundings: The dimensions decrease when heat release is present, which is equivalent to the surface becoming smoother.

The temporally and spatially averaged profile shows the strong decrease of the mean density as a consequence of the high temperatures around the flame surface. In general, most profiles of statistical quantities are - in particular at $M_c = 0.15$ - broader for the reacting mixing layers than for the inert ones, which is a consequence of thermal expansion. When using a constant reference density, ρ_0, for non-dimensionalization, a significant decrease of the Reynolds stresses and the turbulent kinetic energy (TKE) is visible. Comparisons with another normalization using the mean density, $\langle\rho\rangle$, have shown that the decrease is mainly a consequence of the drop in mean density and therefore a so-called 'mean density effect'. However, in particular at high M_c, mean density effects are not the only ones responsible for the changes occuring in the presence of heat release: Changes of the fluctuating velocity field itself and its correlation with the massflux field have also been shown to play a role.

When using the normalization with ρ_0, the most important terms in the Reynolds stress and TKE transport equations decrease in the presence of heat release. Even though the pressure-dilatations in the latter equation are one order of magnitude larger than for the inert mixing layers, they are still negligible compared to other terms, and the pressure-strain correlation tensor is consequently nearly trace-free. The pressure-strain correlation in the streamwise Reynolds stress equation, Π_{11}, has been shown to be responsible for the decrease in the momentum thickness growth rate with heat release. Since it is also a decrease in Π_{11} that leads to the reduction of the momentum thickness growth rate by compressibility, this effect once more demonstrates how important a proper capturing and modeling of this key quantity and of the remaining pressure-strain correlations in general is. The decrease of the pressure-strain correlations by heat release has been shown to be due to a decrease in pressure fluctuations. Density and temperature fluctuations (normalized by their mean values), on the contrary, increase in comparison with the inert mixing layers. They are strongly correlated with each other and are shown to be mostly of entropic and not of acoustic nature. This is further confirmed by a low correlation coefficient between pressure and density fluctuations.

Since the pressure fluctuations are shown to be responsible for the reduction of pressure correlations, like the pressure-strain correlations, by heat release, an equation for these fluctuations, has been derived. When neglecting acoustic effects, this equation takes the form of a Poisson equation, similar to the corresponding equation for the inert mixing layers. However, for reacting

flow, the Poisson equation includes one additional term reflecting heat release effects. By solving the Poisson equation with the help of a Green function, the influence of this heat release term has been shown to be small. The terms which provide the largest contributions to the pressure fluctuations, are the same as for inert mixing layers, namely two terms containing the mean density as a factor. However, the amplitudes of these terms and of the pressure-strain correlations as a whole decrease when heat release is present. By evaluating modified pressure-strain correlations with a constant density, ρ_0, instead of the mean density, it could be demonstrated, in particular for low M_c, that the decrease of Π_{ij} is mainly due to the drop in mean density and is therefore called a 'mean density effect'.

Further emphasis of the chapter has been on scalar mixing and on entrainment. In agreement with the observations from the instantaneous scalar (mixture fraction) fields, the scalar variance is smaller with heat release than without. Contrarily to the inert mixing layer at $M_c = 0.15$, no double hump in the scalar variance caused by engulfment is shown by the corresponding profile for the reacting mixing layers. This is already indicative of the fact that engulfment events, which have already been observed to be rather rare for the inert mixing layers, loose further importance in reacting flow. Confirmation of this suggestion has been given by a direct investigation of the engulfed fluid volume. Since less engulfed fluid, i.e. fluid that is situated within the mixing layer but has scalar concentrations or low vorticity values that are typical of free stream fluid, are found within the reacting mixing layers, the degree of intermittency is reduced compared to the inert mixing layers. This is in agreement with the behaviour of pdfs of the mixture fraction taken at different transverse locations: Their marching behaviour is more pronounced for the reacting mixing layers, and pdfs with bi-modal peaks can only be found at the very edges of these mixing layers.

Further studies of entrainment, i.e. the way the mixing layers acquire free stream fluid, have been made by investigating the pathlines of fluid particles, which have initially been situated outside the mixing layers but have become part of them in the course of the simulations. It has been shown that changes in their vorticity and scalar values to values away from values typical for free stream fluid occur very close to the mixing layer edges. This has already been observed for mixing layers without heat release. However, in contrast to the particles in these mixing layers, the changes for the fluid particles of the reacting mixing layers take place after a longer time, i.e. the fluid particles are carried along for a longer time at the edges of the mixing layer before they become part of it.

To sum up the investigations of the reacting mixing layers, it can be said that heat release is not beneficial for mixing. On the contrary, due to its damping effect, it reduces the turbulent fluctuations and hampers the acquisition of outside fluid, i.e. the entrainment and the growth of the mixing layers. Since the amount of entrained fluid determines how much product is generated by the chemical reaction, an isothermal reaction is consequently more efficient in product formation than an exothermal reaction. However, when heat release is present, the detrimental consequences of a further increase in M_c for the mixing process are not as pronounced as without heat release.

4 LES of inert and infinitely fast reacting mixing layers

4.1 Introduction and literature survey

The LES method used in this work is a particular version of the Approximate Deconvolution Method (ADM) [1, 175]. This method aims at reconstructing turbulent flow fields from filtered fields as they are obtained when performing an LES on a coarse grid. Subgrid terms are no longer modeled, but reconstructed using an ad-hoc mathematical procedure [46]. The presently used version of the ADM consists in solving the Navier-Stokes equations (A.22) on a coarse grid and explicitly filtering the solution afterwards in order to account for an energy transfer between resolved and unresolved scales. For brevity we use the initials EFM (Explicit Filtering Method) to denote the method in this thesis.

According to Sagaut [154], ADM and consequently also EFM belong to the family of structural LES models which are independent of any prior knowledge of the nature of the interactions between the subgrid and the resolved scales. Within this family, there are several groups of models: First, models derived by formal series expansions for which even no prior knowledge of flow physics is required. Besides the deconvolution procedures, non-linear models and homogenization-technique-based models also belong to this group. Other structural models are e.g. scale similarity models and mixed models. Explanations of and examples for all these kinds of LES models can be found in [154].

Actually, the idea of filtering, as done explicitly here, is part of any LES as the numerical approximation of a derivative always implies a filtering: Finite difference formulae are equivalent to exact differentiation followed by a filtering which falls off smoothly at high wavenumbers. Spectral differentiation implies a sharp cut-off filter. However, the method presented here involves an additional explicit filter and avoids implicit filtering of a numerical scheme over a broad range of resolved scales, by using highly accurate compact finite differences. ADM and EFM are especially suitable for compressible flows which contain several nonlinear terms. Finding physical or heuristical models for all LES subgrid terms is a difficult task which can be avoided when using ADM or EFM. Here, a mathematically consistent approximation of unresolved terms is used, which applies to any type of nonlinearity unlike other models.

ADM has been used for various types of inert flows: decaying, compressible isotropic turbulence [175], incompressible channel flow [176] and a compression ramp flow [177]. A comprehensive discussion of the method can be found in [2]. So far, EFM has been applied to a compressible channel flow with a passive scalar [106, 107]. In the present work, it is used for the first time to predict flows with different chemical species, namely inert and reacting, temporally evolving, compressible, turbulent shear layers.

Even though LES of combustion is not much older than a decade, much progress in this field has already been made, and it has started to become a tool for the investigation of real combustion devices [42, 90, 103, 116]. Janicka & Sadiki [82] as well as Pitsch [135] recently gave overviews over ongoing work on modeling approaches for combustion LES. However, many questions still remain to be addressed and improvements of currently used models need to be made to realize the full potential of LES with combustion and to meet future demands. The most striking advantage of combustion LES compared with RANS is that large-scale, time-dependant motions are resolved, and the modeling is confined to just the smallest scales. Since the large-scale motions contain most of the turbulent kinetic energy and control the dynamic of the flow, it can be expected that predictions by LES are more 'accurate' than those by RANS. Resolution of the spatial-temporal evolution and not just the mean values makes it possible to capture and investigate unsteady phenomena such as flashback, blow-off [171, 178] and combustion instabilities [3, 169, 185].

However, while turbulent mixing increases the scalar variance, it is the molecular diffusion that forms a mixture which enables chemical reactions to take place. Molecular mixing and chemical reactions occur essentially on the smallest turbulent scales which are entirely unresolved in both, RANS and LES. Therefore, as in RANS, the chemical source terms in LES need to be modeled completely, and LES combustion models are similar to and often derived from corresponding RANS models. The latter are discussed and reviewed for example by [94, 128, 129, 143, 181]. If combustion is controlled by mixing, it is in particular one quantity, the scalar dissipation rate, which quantifies and steers molecular mixing and combustion. High values of the scalar dissipation rate can have important consequences such as local or global flame extinction. Mixing controlled combustion is typical for non-premixed systems with relatively fast combustion. The mixing layers with hydrogen chemistry that are dealt with in this work belong to this class. In the case of infinitely fast, non-premixed combustion, the turbulent reaction rate is even directly proportional to the scalar dissipation rate [8]. Like the chemical source term, the scalar dissipation rate is a small-scale quantity. Nevertheless, even though only the resolved fluctuations of the filtered scalar dissipation rate can be taken into account in an LES, the results promise to be more accurate than those obtained by simple use of the Reynolds-averaged dissipation rate [134].

In the following, a short overview over the most common LES combustion models for non-premixed combustion and a classification of the ones used in this work is given.

The main role of an LES combustion model is to account for the effect of subgrid fluctuations of species and temperature on the filtered chemical source term. Since the direct closure of this term is hardly possible due to its non-linearity, the so-called conserved scalar models, a large group among combustion models, avoid the direct closure entirely. Moreover, the conserved scalar models have the desirable property to reduce the number of thermo-chemical variables. For non-premixed combustion, the conserved scalar is the mixture fraction (cf. Sect. 3.2.1). Under certain conditions (fast reaction etc.) the species mass fractions and the temperature are directly related to it. However, in contrast to DNS using the mixture fraction (see Chapter 3), the effect of subgrid-scale (SGS) turbulence must be accounted for, which is predominantly achieved by integration of filtered density functions (see below).

The most simple conserved scalar models assume the species mass fractions to be functions of the mixture fraction alone, which is essentially the case for an infinitely-fast, irreversible, global reaction [85, 130] or equilibrium chemistry [17, 31, 59], both with simplified diffusion. The

assumption, however, that mixing is equivalent to burning is not always correct, and finite rate chemistry effects have to be taken into account to obtain more precise combustion models. This is for example the case when the strain rate becomes large. Then, the key chemical reactions cannot keep up with the large mixing rate and local or global extinction occurs.

Within the framework of the conserved scalar methods there are several possibilities to account for finite-rate chemistry effects: Frankel et al. [62] treated non-equilibrium chemistry (single-step reaction) by employing a joint beta-pdf distribution (see below) for the fuel and oxidizer. The difficulty with this concept, however, was its dependency on the SGS species covariance that had to be assumed somehow. Other methods of treating finite-rate chemistry are the Conditional Moment Closure (CMC, see below) and flamelet approximations. In the framework of the latter, it is assumed that the chemical timescales are short enough so that the reactions occur in a thin, one-dimensional layer around the stoichiometric mixture fraction. This layer is smaller than the smallest scales of the turbulence. Such an assumption is equivalent to a large Damköhler number (ratio of flow to chemical time scales). As argued by Peters [128], the reaction zone then has as a laminar structure, and the diffusive transport is predominantly normal to the surface of the stoichiometric mixture fraction. Under these assumptions, the scalar transport equations can be transformed into mixture fraction space. A subsequent asymptotic approximation leads to the so-called flamelet equations (see also Chapter 5) [128, 129] describing the flamelets as diffusive-reactive layers around the reaction zone that are embedded in an otherwise non-reacting turbulent flow. Assuming the flamelets to be in steady state, leads to the steady flamelet models, which result in the species mass fractions being functions of the mixture fraction and one further parameter only, which is often the scalar dissipation rate. As a consequence, the chemical kinetics are decoupled from the flow field. For given boundary conditions, the flamelets can be pre-computed and tabulated in a flamelet library, which is accessed during the actual RANS or LES simulation. The dependence of the flamelets on mixture fraction and scalar dissipation rate makes it clear why conserved scalar models with infinitely-fast chemistry are also sometimes classified as flamelet models: They form the limit of the flamelet domain for a one-step global reaction with infinitely high Damköhler number [100]. Within the actual flamelet models, departures from this limit are described by the scalar dissipation rate.

When using conserved scalar methods with or without infinitely fast chemistry, Reynolds averaged or filtered quantities (mass fractions and sometimes temperature) are obtained with the help of pdfs or fdfs (filtered density functions). The latter were introduced for the first time by Pope [144] and are also known under the name large-eddy probability density functions (LEPDF) [65].

Most often fdfs are assumed to have a certain shape, for example a beta-function for the mixture fraction fdf. This assumption benefits from the fact that errors in assumed pdfs are greatly reduced upon integration [9, 101]. Various examples for the use of a beta-fdf can be found: A priori tests were performed for isotropic turbulence with equilibrium chemistry and no heat release [31], isotropic turbulence with a flamelet model and no heat release [33], isotropic turbulence with a flamelet model and heat release [32], a shear layer with infinitely fast chemistry and no heat release [85] and a round jet with finite-rate chemistry and heat release [184]. Examples for actual LES (a posteriori studies) are the simulations of incompressible, isotropic turbulence [37], a turbulent hydrogen jet diffusion flame [59], a turbulent round jet of methane-air with a pilot flame [139], a turbulent round jet of nonpremixed hydrogen-air [17], an incompressible mixing layer [39] and a non-premixed bluff-body flame [87].

Since the beta-function depends on two moments, the filtered mixture fraction value, $\widetilde{z}$, and its SGS variance, $\left(z^2\right)_{sg}$, have to be computed as part of the LES. The first quantity, $\widetilde{z}$ is readily available as a solution of the corresponding transport equation. The SGS scalar variance, $\left(z^2\right)_{sg} = \widetilde{z^2} - \widetilde{z}^2$, however, has to be modeled. This is a crucial step since the above cited a priori and a posteriori investigations have revealed that the beta-pdf gives good predictions only if the SGS scalar variance is predicted very well or available from DNS. Here and in the following, $\widetilde{\bullet}$ denotes a mass-weighted low-pass filtered quantity and $\overline{\bullet}$ a low-pass filtered quantity. There are various possibilities to model $\left(z^2\right)_{sg}$: First, it can be obtained from a transport equation as done in [166, 84]. One difficulty in this context is to find a reasonable initialization. Second, $\left(z^2\right)_{sg}$, can be computed with a gradient model based on small-scale equilibrium assumptions [17], possibly with a dynamically determined coefficient [130]. Furthermore, the SGS scalar variance can be estimated with the help of a scale-similarity assumption which was proposed by [31] and further investigated and applied by [37, 39, 41, 85, 149]. The necessary coefficient can be computed by using an assumed scalar spectrum [30]. Other possibilities to obtain $\left(z^2\right)_{sg}$ are via the Linear Eddy Model (see below) or via the Approximate Reconstruction using Moments (ARM) method [111]. The latter model also provides an entire alternative to the computation of filtered non-linear functions by integration with fdfs [111, 122]. To obtain them, the ARM uses information from the filtered field itself and from spectra, assumed or known from DNS or experiments.

Beside the SGS variance of the scalar, most flamelet approaches in LES require the knowledge of the filtered scalar dissipation rate, $\widetilde{\chi}$. The advantage in modeling this quantity in an LES is that (reasoning with the help of the energy cascade) it is in principle established by the large-scale motions that are resolved in an LES even though it is a small-scale quantity. Most models for $\widetilde{\chi}$ are based on the eddy viscosity approach proposed by Girimaji & Zhou [69]. Variants with dynamically determined coefficients can be found for example in [37, 130].

The quasi-steady flamelet model, which is employed by most studies cited so far, has proven to be inaccurate if slow chemistry or physical processes like the formation of pollutants (NO formation) and radiative heat transfer have to be taken into account [136]. Improvements can be achieved by the use of unsteady flamelet models like the Lagrangian flamelet model as in [136, 133, 139, 140]. Easier to apply, and considering also scalar dissipation rate fluctuations, is the Eulerian flamelet model [134]. An alternative to the unsteady flamelet models, which is also able to capture phenomena like local extinction, re-ignition and flame lift-off, is given by the flamelet progress variable (FPV) by Pierce & Moin [131, 132]. Here, instead of the scalar dissipation rate, a reaction progress variable serves to parameterize the steady state flamelet library. However, further a priori tests [76, 174] have revealed that the critical point within the concept is the modeling of the fdf of the reaction progress variable. The model was further improved by Ihme & Pitsch [77], and an extension to unsteady flamelets was made in [137]

As already mentioned, the Conditional Moment Closure (CMC) is another method within the framework of the conserved scalar concept, that allows to capture finite-rate chemistry effects. It has been proposed by Klimenko [92] and Bilger [10] for RANS and used in an LES by Kim & Pitsch [91]. A variant of it, the conditional source estimation, has been proposed by Bushe & Steiner [23]. The CMC is based upon averaging of the transport equations conditioned on some variable that the chemical source term is known to depend on, for example the mixture fraction in non-premixed combustion. Certain terms within these equations require closure which benefits from the experimental observation that conditioned statistics based on the mixture fraction

exhibit significantly less turbulent fluctuations than their unconditional counterparts [100]. Unconditional quantities are obtained from the conditional filtered variables by using a presumed fdf approach. Investigations about similarities and differences with the flamelet concept can be found in [129, 93].

Other categories of combustion models, besides the conserved scalar models, are direct models of the filtered source term, models related to the Linear Eddy Model (LEM) and transported pdf or fdf models.

Direct models of the filtered source term based on scale similarity assumptions were tested in [41] which imply the smallest resolved scales to be statistically similar to the largest unresolved scales. However, the chemical reactions take place in the very small dissipative scales rather than in the largest unresolved ones. Therefore, it is questionable whether scale similarity models are able to capture them sufficiently.

The LEM, proposed by Kerstein [88] and formulated for LES by McMurtry et al. [110] considers scalar fields to be comprised of many one-dimensional structures, the so-called linear eddies, which are convected by the turbulent velocity field. Within such a structure all relevant length scales are resolved by performing a kind of one-dimensional DNS and solving the species and temperature diffusion equations. While molecular transport as well as combustion are taken into account in this DNS, the convective transport of the linear eddies is modeled by a stochastic rearrangement of adjacent linear eddies based on the resolved velocity field (splicing events). Applications to diffusion flames can be found in [24] and to a gas turbine combustor flow in [90]. One major difficulty within the LES lies in the fact that the simulation of the subgrid stirring process is particularly expensive for 3D simulations with many grid points.

Like the CMC and the LEM, the so-called transported pdf (fdf) models are not only applicable to non-premixed, but also to premixed combustion. The principle to solve transport equations for pdfs was first established for RANS [26, 143, 165, 190] and later extended to LES [29, 65, 80, 144, 150, 168]. Advantages of this concept are the wide variety of possible shapes of the pdfs and the closed form of the chemical source term within the transport equations. However, turbulent diffusion and mixing require modeling, and computationally expensive Monte-Carlo simulation techniques are most often used in the implementation of pdf methods.

The combustion models used within the present work fall entirely in the category of the conserved scalar methods. However, even though the recent overview has shown that such methods are widely used, some particularities and novelties are presented. Above all, the EFM is for the first time combined with different combustion models taking into account heat release effects. The combustion models differ in accuracy: First, the filtered chemical source term is modeled under the assumption of a one-step, irreversible, infinitely fast chemical reaction. This simplification allows to concentrate on the effect of heat release on the EFM and to compare the results directly with corresponding DNS data (Chapters 2 and 3). Later on, a more advanced flamelet model is used to take into account finite-rate chemistry and also detailed diffusion effects. This is described and analyzed in Chapter 5.

The present chapter is organized as follows: In Section 4.2, the LES method is described: First, ADM and EFM are explained and the close relation between them is pointed out (Sect. 4.2.1). Details about filters applied in the simulations are also provided (Sect. 4.2.2). Then, the transport equations, that are integrated and filtered, are given for the inert as well as the reacting LES (Sect.

4.2.3), and the modeling of the heat release term is described in detail (Sect. 4.2.4). The main part of the chapter, Sect. 4.4, concerns the LES results and their comparison with DNS data from Chapters 2 and 3. It is divided into two parts, the inert mixing layers (Sect. 4.4.1) and the reacting ones (Sect. 4.4.2). Instantaneous fields as well as spatially averaged profiles and spectra are taken into account. Finally, a summary of the results is given and conclusions are drawn (Sect. 4.5).

4.2 Description of the LES method

4.2.1 Implicit Modeling Approach

The Approximate Deconvolution Method (ADM), first presented in [175], aims at reconstructing turbulent flow fields from low-pass filtered ones in order to close the LES equations. Subgrid-scale effects are no longer modeled explicitly, but treated by an ad-hoc mathematical procedure [46]. The slightly modified version of ADM [175], which is used in the present LES, is based on the observation that spatial low-pass filtering and deconvolution steps can be combined into a single filtering step [106]. The relation between the presently used explicit filtering method and ADM is explained in the following with the help of a simple example: A one-dimensional transport equation of a flow variable u has the form

$$\frac{\partial u}{\partial t} + \frac{\partial f(u)}{\partial x} = 0 \tag{4.1}$$

with a nonlinear function $f(u)$. The application of a low-pass filter G to this equation results in

$$\frac{\partial \overline{u}}{\partial t} + G * \frac{\partial f(u)}{\partial x} = 0. \tag{4.2}$$

As any LES implies such a kind of filtering, Eq. (4.2) can be regarded as a generic LES equation. The filtered flow field $\overline{u}$ is then the low-wavenumber LES solution. $\overline{u}$ is a continuous function of the independent variables x (space) and t (time) and is defined by the convolution integral

$$\overline{u} = G * u = \int G(x - x', \Delta)\, u(x')\, dx', \tag{4.3}$$

where $G(x - x', \Delta)$ is the low-pass filter kernel with the filter width Δ. Equation (4.2) can be re-arranged in a way that there are only known, namely filtered quantities on the LHS:

$$\frac{\partial \overline{u}}{\partial t} + \frac{\partial f(\overline{u})}{\partial x} = \underbrace{\frac{\partial f(\overline{u})}{\partial x} - G * \frac{\partial f(u)}{\partial x}}_{\mathcal{U}} \tag{4.4}$$

On the RHS, there is the unknown remainder $\mathcal{U}$. Most 'classical' approaches model this term with the help of the known filtered flow field $\overline{u}$, so that $\mathcal{U}$ is replaced by $\mathcal{U}_m(\overline{u})$, a model of $\mathcal{U}$. ADM as presented in [175] computes $\mathcal{U}$ by replacing the original field u by a suitable approximation u^*, viz:

$$\mathcal{U} = \frac{\partial f(\overline{u})}{\partial x} - G * \frac{\partial f(u^*)}{\partial x}. \tag{4.5}$$

Substituting Eq. (4.5) into Eq. (4.4), one obtains

$$\frac{\partial \overline{u}}{\partial t} + G * \frac{\partial f(u^*)}{\partial x} = 0 \tag{4.6}$$

or

$$G * \left[\frac{\partial u^*}{\partial t} + \frac{\partial f(u^*)}{\partial x} \right] = G * \frac{\partial u^*}{\partial t} - \frac{\partial \overline{u}}{\partial t}. \tag{4.7}$$

The relation $G*u^* \approx G*u$ is expected to hold for a broad range of the resolved scales. Therefore, the RHS of Eq. (4.7) may be set to zero:

$$G * \left[\frac{\partial u^*}{\partial t} + \frac{\partial f(u^*)}{\partial x} \right] = 0 \tag{4.8}$$

Now, u^* cannot be more than an approximation to u because the filtering operation has a cut-off, and u^* has to be projected onto a coarse grid on which not all scales of u can be resolved (or represented). From a numerical point of view, Eq. (4.8) can be solved by an integration step followed by a filtering step. The main final task, and that is the essence of ADM [175], is to reconstruct u^* from the filtered field $\overline{u}$. To this end, a filter Q is used, which is the approximate inverse of G:

$$Q \approx G^{-1}. \tag{4.9}$$

The deconvolution (reconstruction) step is then

$$u^* = Q * \overline{u} \approx G^{-1} * \overline{u}. \tag{4.10}$$

In summary, ADM consists in principle of the following steps which constitute an implicit approach as defined by Eq. (4.8):

- Deconvolution: $u^{*(n)} = Q * \overline{u}^{(n)}$
- Integration: $u^{*(n+1)} = u^{*(n)} + \Delta t \cdot \frac{\partial u^*}{\partial t} + O(\Delta t)^2$
- Filtering: $\overline{u}^{(n+1)} = G * u^{*(n+1)}$

The simple time-integration step is just used for demonstration and not typical of ADM. The fact that the above 'ADM-steps' are executed sequentially, led to the idea to execute filtering and deconvolution steps together as a single filtering step, $Q * G * u^{*(n+1)}$, which removes the high wavenumber content. This was proposed by Mathew et al. [106].

4.2.2 Applied filters

A suitable choice of filters for G which are based on five points was proposed by Lele [99]:

$$\beta\overline{u}_{j-2}+\alpha\overline{u}_{j-1}+\hat{u}_j+\alpha\overline{u}_{j+1}+\beta\overline{u}_{j+2} = au_j+\frac{b}{2}(u_{j-1}+u_{j+1})+\frac{c}{2}(u_{j-2}+u_{j+2})+\frac{d}{2}(u_{j-3}+u_{j+3}) \tag{4.11}$$

Here, u_j and $\overline{u}_j$ are values on an equispaced grid. If considering periodic functions, convolution $\overline{u} = G * u$ in Fourier space is equivalent to the product of the corresponding Fourier coefficients, $\hat{\overline{u}}(\xi) = \hat{G}(\xi)\,\hat{u}(\xi)$. The filter response function is then obtained by substituting Fourier series for u and $\overline{u}$ into Eq. (4.11):

$$\hat{G}(\xi) = \frac{\hat{\overline{u}}(\xi)}{\hat{u}(\xi)} = \frac{a + b\cos\xi + c\cos 2\xi + d\cos 3\xi}{1 + 2\alpha\cos\xi + 2\beta\cos 2\xi} \tag{4.12}$$

$\xi(k) = 2\pi k/M \quad (k = 0, \quad \pm 1, ..., \quad \pm M)$ are scaled wavenumbers represented on the grid of M intervals per period. There are six coefficients (a, b, c, d, α and β) which must be specified for the filter. If considering the essential requirements, $\hat{G}(0) = 1$ and $\hat{G}(\pi) = 0$, sixth-order accuracy as well as the additional constraint $d^2\hat{G}/d\xi^2(\pi) = 0$, a one-parameter family

$$\beta = \frac{3 - 2\alpha}{10}, \quad a = \frac{2 + 3\alpha}{4}, \quad b = \frac{6 + 7\alpha}{8}, \quad c = \frac{6 + \alpha}{20}, \quad d = \frac{2 - 3\alpha}{40} \tag{4.13}$$

is obtained [99]. The parameter α controls the filter cut-off. Larger values move the cut-off closer to the high wavenumber end and imply less filtering.

Following Adams & Leonard [1], the fact that $0 < |\hat{G}(\xi)| < 1$ allows to write its inverse as a von Cittert series [99]

$$\hat{Q}(\xi) = \sum_{m=0}^{\infty} \left(1 - \hat{G}(\xi)\right)^m, \tag{4.14}$$

which converges everywhere, except at $\xi = \pi$. It is sufficient to take into account N terms of this series to obtain an excellent inverse over a broad range of wavenumbers. This range increases with N. In former applications [106], $N = 6$ has been proven a value that gives a sufficiently accurate approximation of $\hat{Q}$. Figure 4.1 shows the filter response functions $\hat{G}(\xi)$, $\hat{Q}_N(\xi)$ and $\hat{G}_2 = \hat{Q}_N\hat{G}$ for $N = 6$ and $\alpha = 0.5$. The filter $\hat{G}_2$ is a perfect low-pass filter for $\xi < 0.6\pi$ and then falls off smoothly. With $\alpha = 0.5$, the cut-off is chosen to be in the undistorted range where the numerical scheme is exact. This behaviour is required for the deconvolution operator in order to guarantee that $u^* \approx u$ for most of the resolved wavenumbers. Therefore, in the present study $\alpha = 0.5$ and $N = 6$ are chosen.

A regularization term introduced in [1] and subsequent studies, improves the energy transfer from the resolved to the unresolved fluctuating scales and ensures that errors, which would magnify during the LES, are damped. In [106] and here, this part is taken over by a second filtering step: It is not the filter $Q * G$ that is used, but $(Q * G)^2$, the response function of which is also shown in Fig. 4.1. For periodic directions, this composite filter response function is determined at the start of the computation and the filtering in Fourier space is done after each time integration step by multiplication with the two-dimensional Fourier transform of the primary variable fields. Since the computational costs of Fast Fourier Transformations (FFTs) are of the order $O(M \ln M)$ for

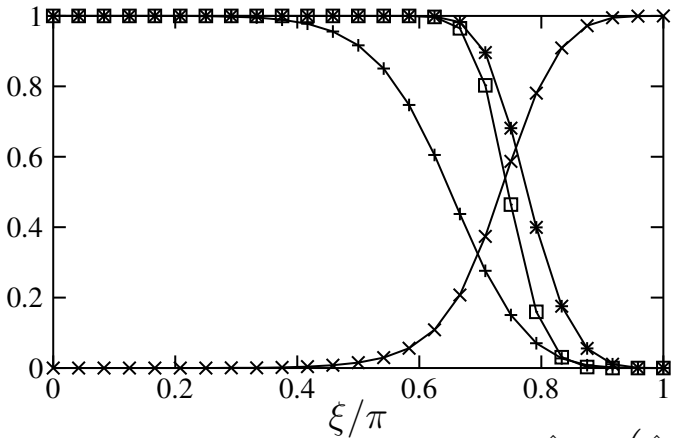

Figure 4.1: Filter response functions for $\alpha = 0.5$ and $N = 6$, $+$: $\hat{G}$, $\times$: $\left(\hat{Q}_N - 1\right)/N$, $*$: $\hat{Q}_N\hat{G}$, $\square$: $\left(\hat{Q}_N\hat{G}\right)^2$

M modes, this is an inexpensive operation, equivalent to the cost of a single derivative calculation. For the non-periodic direction, which is the direction of the shear in this work, the filter recommended by Stolz et al. [176] (see their Appendices A 1 and A 2) is used.

4.2.3 Filtered equations

LES of inert mixing layers uses the same equations as DNS, namely the Navier-Stokes equations written in a characteristic pressure-velocity-entropy formulation (see Appendix A). The only difference between both techniques is the filtering that is performed after each time integration step.

The equations that are integrated and filtered during LES of infinitely fast reacting mixing layers are in principle also the same transport equations as computed in the DNS, Eqs. (3.14). However, σ_α from Eq. (A.34) is inserted with diffusion fluxes being simplified to

$$\rho Y_\alpha V_{\alpha i} = -\frac{\mu}{Sc}\frac{\partial z}{\partial x_i}\frac{dY_\alpha}{dz}. \tag{4.15}$$

Neglecting the Dufour effect in the heat flux vector, the transport equations for LES with infinitely fast chemistry (written without the filtering for clarity) become:

$$\begin{aligned}
\frac{\partial p}{\partial t} =& -u_i\frac{\partial p}{\partial x_i} - p\gamma\frac{\partial u_i}{\partial x_i} + \rho\gamma\mathcal{R}T\sum_\alpha \frac{1}{M_\alpha}\frac{Dz}{Dt}\frac{dY_\alpha}{dz} \\
&+ (\gamma-1)\left[\phi + \frac{\partial}{\partial x_i}\left(\lambda\frac{\partial T}{\partial x_i}\right) + \frac{\mu}{Sc}\frac{\partial z}{\partial x_i}\sum_\alpha \frac{dY_\alpha}{dz}\frac{\partial h_\alpha}{\partial x_i} - \sum_\alpha h_\alpha\omega_\alpha\right] \\
\frac{\partial u_j}{\partial t} =& -u_i\frac{\partial u_j}{\partial x_i} - \frac{1}{\rho}\left(\frac{\partial p}{\partial x_j} - \frac{\partial \tau_{ij}}{\partial x_i}\right) \\
\frac{\partial T}{\partial t} =& -u_i\frac{\partial T}{\partial x_i} + \frac{1}{\rho c_p}\left[\phi + \frac{\partial}{\partial x_i}\left(\lambda\frac{\partial T}{\partial x_i}\right) + \frac{\mu}{Sc}\frac{\partial z}{\partial x_i}\sum_\alpha \frac{dY_\alpha}{dz}\frac{\partial h_\alpha}{\partial x_i} + \frac{Dp}{Dt} - \sum_\alpha h_\alpha\omega_\alpha\right] \\
\frac{\partial z}{\partial t} =& -u_i\frac{\partial z}{\partial x_i} + \frac{1}{\rho Sc}\frac{\partial}{\partial x_i}\left(\mu\frac{\partial z}{\partial x_i}\right)
\end{aligned} \tag{4.16}$$

where ω_α denotes the chemical production rate of species α.

4.2.4 Modeling of the filtered heat release term

The explicit filtering with $(Q * G)^2$ accounts for the quadratic nonlinearities arising from the convection terms of Eqs. (4.16). Assuming subgrid contributions to the other terms, e.g. to the heat flux vector and to the pressure dilatation, to be small, there is just one important term in the pressure and temperature equations that requires additional modeling. This term is the filtered heat release term:

$$\overline{\omega} = -\sum_\alpha \overline{h_\alpha\omega_\alpha} \approx -\sum_\alpha \overline{h_\alpha^0\omega_\alpha} \tag{4.17}$$

with

$$h_\alpha^0 = h_\alpha - \int_{T^0}^{T} c_{p\alpha}(\tau)\, d\tau. \tag{4.18}$$

The last part of Eq. (4.17) would be exact if assuming equal specific heat capacities among the species. The subgrid contribution to the pre-factors of the heat release term in the pressure and temperature equations is neglected in the present work.

In order to bring the filtered heat release term in a form which is appropriate for modeling, the definition of the heat release term is needed:

$$q^0 = -\sum_\alpha h_\alpha^0 W_\alpha \left(\nu_\alpha'' - \nu_\alpha'\right) \tag{4.19}$$

with the stoichiometric coefficients ν_α' and ν_α'' of reactants and products, respectively. For a global reaction, the heat release per unit volume and unit time is then

$$-\sum_\alpha h_\alpha^0 \omega_\alpha = q^0 \omega_G \tag{4.20}$$

with the reaction rate of the global step

$$\omega_G = \frac{\omega_\alpha}{W_\alpha \left(\nu_\alpha'' - \nu_\alpha'\right)} \tag{4.21}$$

being the same for all species. If the species mass fractions are functions of the mixture fraction only, $Y_\alpha = Y_\alpha(z)$, the species and mixture fraction transport equations allow us to write [128]

$$\omega_\alpha = -\chi \frac{d^2 Y_\alpha}{dz^2} \tag{4.22}$$

with the scalar dissipation rate $\chi = -\epsilon_z = \rho D \left(\partial z / \partial x_i\right)^2$ and thus,

$$\omega_G = -\chi \frac{1}{W_\alpha \left(\nu_\alpha'' - \nu_\alpha'\right)} \frac{d^2 Y_\alpha}{dz^2}. \tag{4.23}$$

Choosing for example the fuel as species α, the expression

$$\omega_G = \frac{Y_{F,f}}{W_f \nu_F \left(1 - z_s\right)} \chi \delta \left(z - z_s\right) \tag{4.24}$$

is obtained for the Burke-Schumann case. The filtered source term (4.17) is therefore

$$\overline{\omega} = 2 Q_e \widetilde{\chi}_s \widetilde{F}_z \left(z_s\right) \tag{4.25}$$

with the heat release parameter

$$Q_e = \frac{q^0 Y_{F,f}}{2 W_F \nu_F \left(1 - z_s\right)}. \tag{4.26}$$

$\widetilde{\chi}_s = \widetilde{\chi_z}\left(z_s\right)$ is the conditionally filtered scalar dissipation rate

$$\widetilde{\chi}_z\left(z'\right) = \int_0^\infty \chi' \widetilde{F}_{\chi|z}\left(\chi' | z = z'\right) d\chi' \tag{4.27}$$

at the stoichiometric mixture fraction value, $z = z_s$. The tilde denotes a mass-weighted filtering and $\widetilde{F}_z$ the filtered density function (fdf) of the mixture fraction. In other words, $\widetilde{\chi}_s$ is the average of $\rho\chi$ on the portion of the filter volume for which $z(x,t) = z_s$ divided by the average of ρ on the same portion.

In Eq. (4.25), the conditionally filtered scalar dissipation rate at the stoichiometric value, $\widetilde{\chi}_s$, and the fdf at the stoichiometric value, $\widetilde{F}\left(z_s\right)$, are unknown and have to be modeled. Equation (4.25) emphasizes the particular role of the scalar dissipation rate which characterizes the molecular mixing: In the case of infinitely fast, irreversible combustion, the source term is proportional to it. Therefore, its exact modeling is crucial for realistic LES.

4.2.4.1 The filtered density function

The fdf of the mixture fraction is modeled by a beta-function,

$$\widetilde{F}_z^m(z) = \beta = \frac{z^{a-1}(1-z)^{b-1}}{B(a,b)}, \tag{4.28}$$

with $B(a,b) = \Gamma(a)\Gamma(b)/\Gamma(a+b)$ and $a/\widetilde{z} = b/(1-\widetilde{z}) = \widetilde{z}(1-\widetilde{z})/(z^2)_{sg} - 1$. $\Gamma(z)$ is the gamma function. The beta-function can assume a wide variety of shapes like double-deltas and Gaussian distributions. Such shapes of scalar pdfs have also been observed in experiments and simulations of scalar mixing and chemical reactions [100]. One reason why the use of the beta-function is particularly suited for LES is that intermittency, which is a main source of error when using it as a probability density function (pdf) in RANS, occurs mostly on the resolved scales [135] and the subgrid modeling does not have to account for it.

In the present LES, the filtered mixture fraction $\widetilde{z}$ that is needed in evaluating Eq. (4.28) is known from solving the transport equation for z on the coarse grid followed by the explicit filtering. However for the subgrid variance of the mixture fraction,

$$\left(z^2\right)_{sg} = \widetilde{z^2} - \widetilde{z}^2, \tag{4.29}$$

a model is needed. Here, a gradient model (GR) for $(z^2)_{sg}$ is used:

$$\left(z^2\right)_{sg}^{GR} = C_z^{GR}\Delta^2\left(\frac{\partial\widetilde{z}}{\partial x_i}\right)^2 \tag{4.30}$$

with a filter width Δ that is set equal to an averaged grid spacing,

$$\Delta = \sqrt[3]{\Delta x_1 \Delta x_2 \Delta x_3}, \tag{4.31}$$

computed with the grid spacing Δx_i in x_i-direction. The constant C_z^{GR} is adapted during a priori tests (see Sect. 4.4.2.3).

Figure 4.2 shows the contours of the beta-function at the stoichiometric value $\beta_s = \widetilde{F}_z^m(z_s)$ with $z_s = 0.3$. It is zero at the upper limit, $(z^2)_{sg} = \widetilde{z}(1-\widetilde{z})$, and at the lower one, $(z^2)_{sg} = 0$, except for $\widetilde{z} = z_s$ where it diverges.

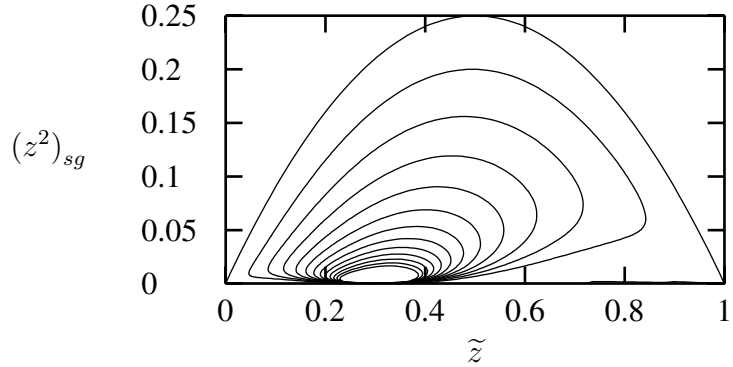

Figure 4.2: Contour lines of β_s from 0 to 3 every 0.25

The fdf in form of a beta-function is not only used in Eq. (4.25), but also to determine the filtered species mass fractions

$$\widetilde{Y}_\alpha = \int_0^1 \widetilde{F}\left(z'\right) Y_\alpha\left(z'\right) dz' \tag{4.32}$$

with $Y_\alpha\left(z\right)$ from the Burke-Schumann relations (3.12). It has proven to be advantageous to pre-calculate and tabulate the filtered species mass fractions in dependence of the filtered mixture fraction and the subgrid variance of the mixture fraction.

4.2.4.2 The conditionally filtered scalar dissipation rate

The conditionally filtered scalar dissipation rate is modeled by assuming an instantaneous relation between the mixture fraction and its dissipation rate [33, 37] which has the form

$$\chi' = \chi_l\left(z', x, t\right) = C\left(x, t\right) f_l\left(z'\right). \tag{4.33}$$

C is constant inside each filter volume, but varies from one to another and with time. The shape function $f_l\left(z'\right)$ is derived from laminar diffusion flames (one-dimensional counterflow problems), with the usual choice [128, 129] being

$$f_l\left(z'\right) = \exp\left(-2\left(\mathrm{erf}^{-1}\left(1-2z'\right)\right)^2\right). \tag{4.34}$$

Relation (4.33) then implies for the conditionally filtered scalar dissipation rate,

$$\widetilde{\chi}_z\left(z'\right) = C\left(x, t\right) f_l\left(z'\right), \tag{4.35}$$

which follows from Eq. (4.27) for $\widetilde{F}_{\chi|z}\left(\chi' \left| z = z'\right.\right) = \delta\left(\chi' - \chi_l\left(z'\right)\right)$. As the filtered scalar dissipation rate is related to the conditionally filtered one by

$$\widetilde{\chi} = \int_0^1 \widetilde{\chi}_z\left(z'\right) \widetilde{F}_z\left(z'\right) dz', \tag{4.36}$$

the scaling factor $C\left(x, t\right)$ can be determined, and the final expression for the modeled conditionally filtered scalar dissipation rate is

$$\widetilde{\chi}_z^m\left(z\right) = f_l\left(z\right) \frac{\widetilde{\chi}}{\int_0^1 f_l\left(z'\right) \widetilde{F}_z\left(z'\right) dz'}. \tag{4.37}$$

Assuming a beta-distribution for the fdf, the quantity in the denominator is a function of $\widetilde{z}$ and $\left(z^2\right)_{sg}$. For $\left(z^2\right)_{sg} = 0$ it is equal to $f_l\left(\widetilde{z}\right)$. Here, the use of a pre-tabulated function has been proven advantageous, too. The expression, for which a table with the coordinates $\widetilde{z}$ and $\left(z^2\right)_{sg}$ is assembled before the start of the LES, is

$$\widetilde{I} = \frac{\widetilde{F}_z\left(z_s\right)}{\int_0^1 f_l\left(z'\right) \widetilde{F}_z\left(z'\right) dz'}. \tag{4.38}$$

It can be extracted as a factor from Eq. (4.25) after inserting Eq. (4.37).

4.2.4.3 The filtered scalar dissipation rate

In Eq. (4.37), a model for the unknown filtered scalar dissipation rate

$$\widetilde{\chi} = \frac{\mu}{Sc}\widetilde{\left(\frac{\partial z}{\partial x_i}\right)^2} \tag{4.39}$$

is needed. To this end, a Smagorinsky-type gradient model (GR) is used in this work, and the filtered scalar dissipation rate $\widetilde{\chi}$ is split up into a large scale part

$$\chi_{ls} = \frac{\overline{\mu}}{Sc}\left(\frac{\partial \widetilde{z}}{\partial x_i}\right)^2, \tag{4.40}$$

which is computed directly from the LES flow fields, and into a subgrid part

$$\chi_{sg} = \widetilde{\chi} - \chi_{ls}, \tag{4.41}$$

which is unknown and has to be modeled. With the gradient model, the subgrid part is expressed as

$$\chi_{sg}^{GR} = \frac{\mu_t}{Sc_t}\left(\frac{\partial \widetilde{z}}{\partial x_i}\right)^2. \tag{4.42}$$

The turbulent viscosity is

$$\mu_t = C_{SM}\Delta^2\overline{\rho}\,|\widetilde{s}_{ij}| \tag{4.43}$$

where $|\widetilde{s}_{ij}| = 2\sqrt{\widetilde{s}_{ij}\widetilde{s}_{ij}}$ uses the strain rate tensor computed with the filtered velocities, $\widetilde{s}_{ij} = 0.5\,(\partial\widetilde{u}_i/\partial x_j + \partial\widetilde{u}_j/\partial x_i)$. The Smagorinsky constant C_{SM} and the turbulent Schmidt number Sc_t are summarized into a single constant C_χ^{GR} that is adapted in a priori tests (see Sect. 4.4.2.3) for the present simulations. With this constant, the complete model expression for the filtered scalar dissipation rate is

$$\widetilde{\chi} = \left(\frac{\overline{\mu}}{Sc} + C_\chi^{GR}\Delta^2\overline{\rho}\,|\widetilde{s}_{ij}|\right)\left(\frac{\partial \widetilde{z}}{\partial x_i}\right)^2 \tag{4.44}$$

4.3 Test cases

The LES that are performed and described in the following correspond to the DNS inert-0.15 and inf-0.15. In order to distinguish between the LES and the DNS, the latter are now denoted by DNS-inert-0.15 and DNS-inf-0.15. Two different resolutions are used for each LES case, one time with a coarsening factor of 4 in each direction and one time with a factor 2. The latter simulations are used to verify whether the LES results approach the DNS results when diminishing the subgrid contributions. The filter parameter α (cf. Sect. 4.2.2) is chosen as $\alpha = 0.5$. Various other values were tested, but for clarity only results with this α are shown, since it has been proven to be the most suitable value.

In the reacting LES cases, the gradient model (GR) described in Sect. 4.2.4 is used to model the subgrid variance $(z^2)_{sg}$. The filtered scalar dissipation rate is modeled with the Smagorinsky-type gradient model (GR) described in the same section.

All LES are summarized in Table 4.1 which gives the denomination, the number of grid points and the model constants that are adapted during a priori tests (cf. Sect. 4.4.2.3).

Table 4.1: LES simulations

Case	$N_1 \times N_2 \times N_3$	C_z^{GR}	C_χ^{GR}
LES-inert-0.15-4	$192 \times 48 \times 144$	–	–
LES-inert-0.15-2	$384 \times 96 \times 288$	–	–
LES-inf-0.15-4	$192 \times 48 \times 108$	0.26	0.06
LES-inf-0.15-2	$384 \times 96 \times 216$	0.23	0.05

The LES are initialized from corresponding DNS flow fields, which are interpolated with splines of fifth order accuracy onto the coarser LES grid and filtered with a tophat filter, the filter width of which is the LES grid spacing. The non-dimensional times at which the LES are started are $\tau_\omega = 139$ for the inert LES and $\tau_\omega = 290$ for the reacting LES. Both instants are well before the beginning of the self-similar states (cf. Scts. 2.4.2 and 3.4.2).

4.4 Results and analysis

In this section, the LES data are compared with the DNS results in two ways: First, the original DNS profiles from Chapters 2 and 3 are used to show the subgrid contents of various quantities. These subgrid contributions make up the essential difference between the LES and the DNS profiles. Since the LES is not able to reproduce them due to the coarse grid, comparisons that allow to judge the quality of the LES results must be made between them and DNS data that are interpolated onto the LES grid and filtered. These data are denoted by i-f-DNS (interpolated and filtered DNS) in the following. Subsequent averaging in the homogeneous directions and over the self-similar state gives profiles of the i-f-DNS data which should ideally be on top of the corresponding LES profiles.

Most results shown in the following are from the LES cases LES-inert-0.15-4 and LES-inf-0.15-4 that use a grid which is coarsened by factor 4 in each direction compared to the DNS grid. Only at the end of the sections on the inert and reacting mixing layers, some results for the cases LES-inert-0.15-2 and LES-inf-0.15-2 are shown for comparison. The grids of these simulations are only by factor 2 coarser than the DNS grids.

4.4.1 Inert mixing layers

4.4.1.1 Instantaneous fields

Figures 4.3 and 4.4 show the instantaneous mass fraction fields at the beginning of the self-similar state of the DNS and LES, respectively. The mixing layers in both simulations present similar structures and have nearly the same thickness. However, a closer look at the inner structure of the mixing layer reveals that the LES is more blurred due to the coarser grid and does not contain as finely resolved features as the DNS. More obvious are the differences between the DNS and the LES when looking at quantities that are more dominated by small scales like the gradient of the oxygen mass fraction, which is shown in Figs. 4.5 and 4.6. Since the strongest scalar gradients

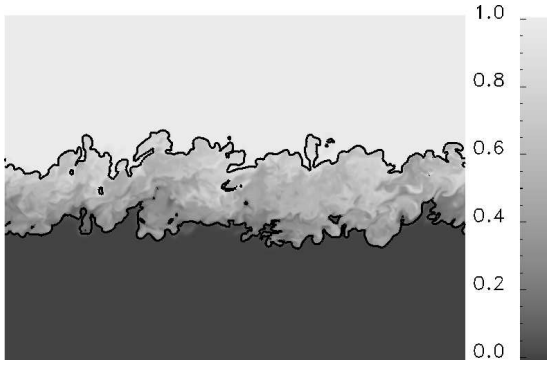

Figure 4.3: DNS-inert-0.15: Instantaneous mass fraction field of O_2, x_1-x_3-plane in the middle of the computational domain at $\tau_\omega = 286$, isolines $Y_{O2} = 0.1$ and 0.9 are shown

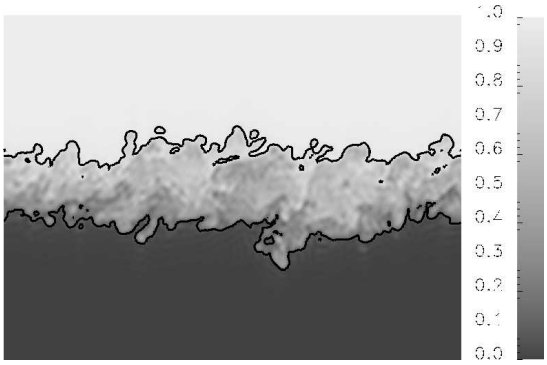

Figure 4.4: LES-inert-0.15-4: Instantaneous mass fraction field of O_2, x_1-x_3-plane in the middle of the computational domain at $\tau_\omega = 286$, isolines $Y_{O2} = 0.1$ and 0.9 are shown

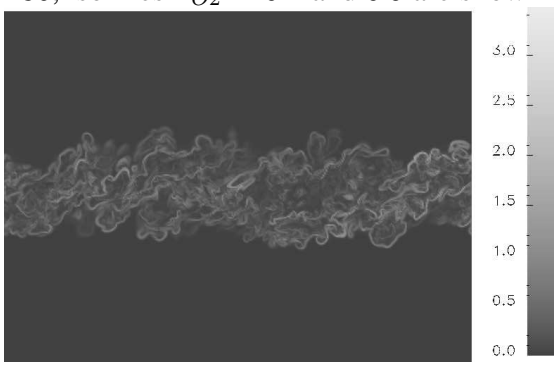

Figure 4.5: DNS-inert-0.15: Instantaneous gradient of oxygen mass fraction, normalized by $\delta_{\omega,0}$, x_1-x_3-plane in the middle of the computational domain at $\tau_\omega = 286$

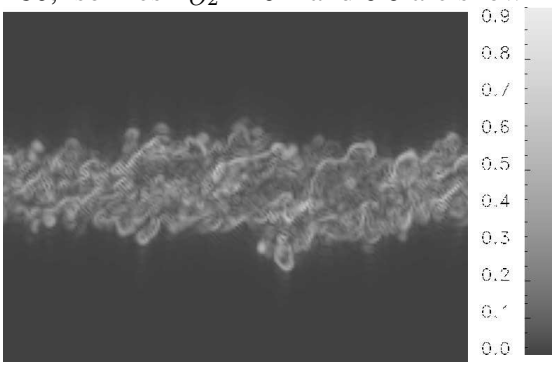

Figure 4.6: LES-inert-0.15-4: Instantaneous gradient of oxygen mass fraction, normalized by $\delta_{\omega,0}$, x_1-x_3-plane in the middle of the computational domain at $\tau_\omega = 286$

are situated in the range of scales which the LES does not resolve, the highest values that are visible in Fig. 4.5 are 3.5 and only 0.9 in Fig. 4.6 (compare the two scales to the right of the respective images).

4.4.1.2 Profiles of averaged flow variables

As far as the mean streamwise velocity in Fig. 4.7 is concerned, the comparison between LES and DNS results is excellent. The oxygen mass fraction profile of the LES (solid line) has a slightly smaller gradient than that of the DNS and the i-f-DNS (Fig. 4.8). The agreement between the TKE of the LES and the interpolated and filtered DNS is also very good (Fig. 4.9) with the LES resulting in a slightly broader profile. In the center of the shear layer, both LES and i-f-DNS have smaller TKE values than the DNS itself which is understandable since the DNS results contain also those scales that are not resolved in the LES. A comparison between the scalar (oxygen mass fraction) variance profiles is shown in Fig. 4.10. While DNS and i-f-DNS are very close, which also shows that the scalar variance is mostly dominated by larger scales, the LES underpredicts the actual value by approximately 20 %. The corresponding profile, however, has the typical shape and shows the two characteristic peaks which give evidence of the entrainment of fresh fluid at the edges of the mixing layer (cf. Sect. 2.4.4.2).

The good agreement between the TKE profiles of LES and i-f-DNS is reflected in an also good

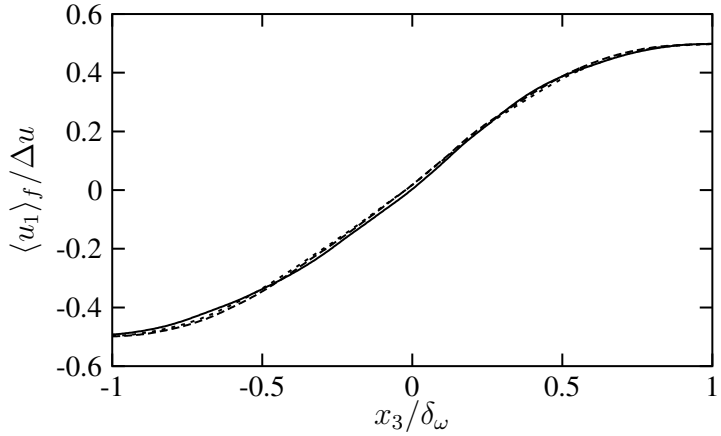

Figure 4.7: Favre averaged streamwise velocity, normalized by Δu, solid: LES-inert-0.15-4, dashed: DNS-inert-0.15 interpolated to LES grid and filtered, dotted: DNS-inert-0.15

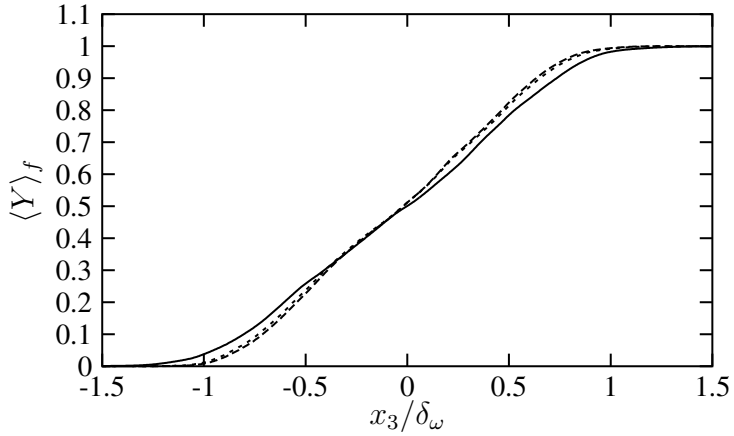

Figure 4.8: Favre averaged oxygen mass fraction, solid: LES-inert-0.15-4, dashed: DNS-inert-0.15 interpolated to LES grid and filtered, dotted: DNS-inert-0.15

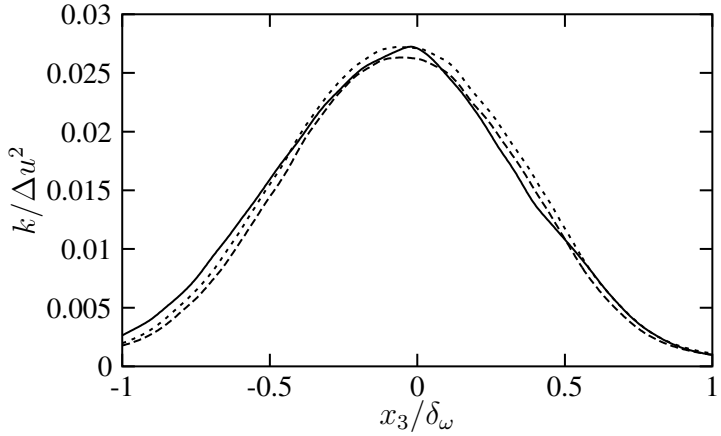

Figure 4.9: Turbulent kinetic energy, normalized by Δu^2, lines as in Fig. 4.7

capturing of the terms in the TKE transport equation by the LES, e.g. the production and dissipation rate in Figs. 4.11 and 4.12 . While TKE production is mostly dominated by large scales (LES and i-f-DNS profiles are therefore close to the DNS profile), the dissipation rate is a predominantly small-scale quantity since it is computed with the help of scalar gradients. This can be seen from the fact, that the magnitude of the DNS value is much larger than that of the LES and i-f-DNS: Nearly 50 % of the dissipation rate are suppressed on the coarser grid. In order to ensure a correct flow development, nevertheless, the transfer of energy from the resolved to the unresolved scales must be modeled. This is accounted for in the present LES by explicitly filtering the flow variables (see Sect. 4.4.1.4).

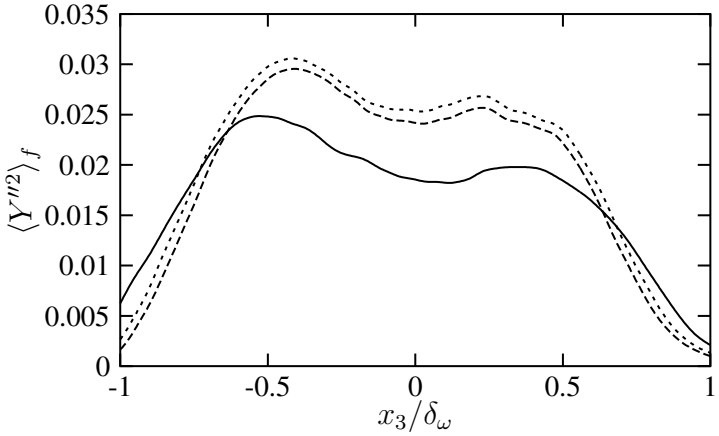

Figure 4.10: Variance of oxygen mass fraction, lines as in Fig. 4.7

In the first two chapters of this work, the importance of the pressure-strain correlations was emphasized: Their role is to distribute the turbulent kinetic energy from the streamwise component of the Reynolds stresses to the spanwise and transverse components. Figures 4.13 to 4.15 show the good prediction of the pressure-strain correlations by the LES which only slightly underestimates their peak values in the center of the mixing layer.

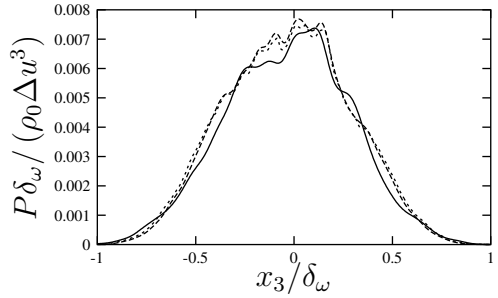

Figure 4.11: Production of TKE, normalized by $\delta_\omega/(\rho_0\Delta u^3)$, lines as in Fig. 4.7

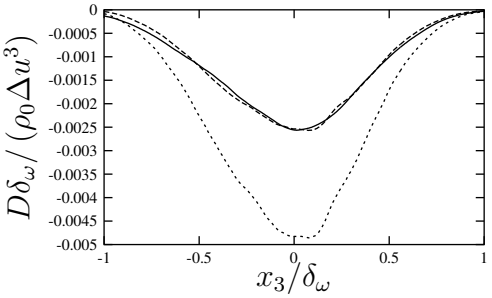

Figure 4.12: Dissipation rate of TKE, normalized by $\delta_\omega/(\rho_0\Delta u^3)$, lines as in Fig. 4.7

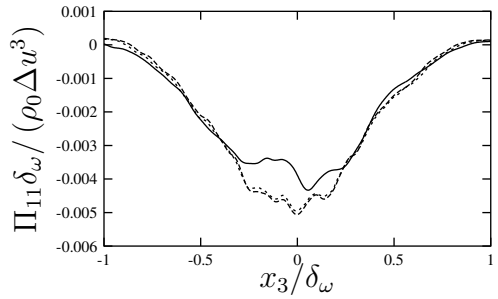

Figure 4.13: Pressure-strain correlation Π_{11}, normalized by $\delta_\omega/(\rho_0\Delta u^3)$, lines as in Fig. 4.7

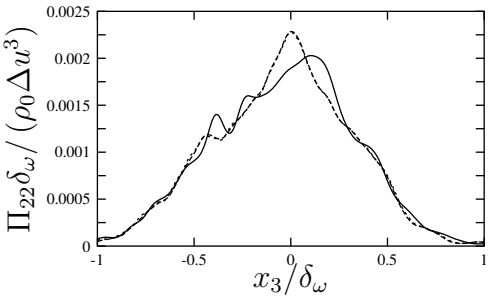

Figure 4.14: Pressure-strain correlation Π_{22}, normalized by $\delta_\omega/(\rho_0\Delta u^3)$, lines as in Fig. 4.7

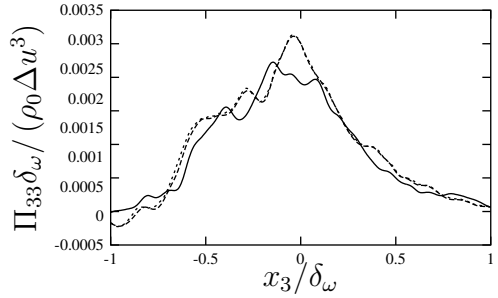

Figure 4.15: Pressure-strain correlation Π_{33}, normalized by $\delta_\omega/(\rho_0\Delta u^3)$, lines as in Fig. 4.7

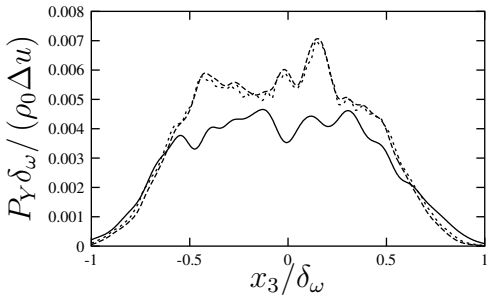

Figure 4.16: Production terms of the scalar variance transport equation, $P_Y = -\langle\rho Y''_\alpha u''_3\rangle\frac{\partial\langle Y_\alpha\rangle_f}{\partial x_3} - \frac{1}{2}\langle\rho Y''^2_\alpha\rangle\frac{\partial\langle u_3\rangle_f}{\partial x_3}$, normalized by $\delta_\omega/(\rho_0\Delta u)$, lines as in Fig. 4.7

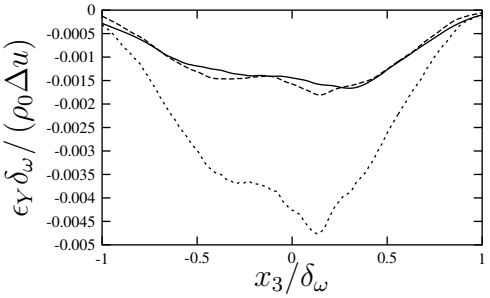

Figure 4.17: Scalar dissipation rate, $\epsilon_Y = \langle\rho Y_\alpha V_{\alpha i}\frac{\partial Y_\alpha}{\partial x_i}\rangle$, normalized by $\delta_\omega/(\rho_0\Delta u)$, lines as in Fig. 4.7

One reason why the scalar variance is not as well predicted in the LES as the TKE, is shown in Fig. 4.16: The most dominant source terms in the scalar variance transport equation, namely the production terms, are underestimated by the LES. The dissipation rate, on the contrary, is very well predicted (Fig. 4.17) which can be seen by the good agreement of LES and i-f-DNS profiles. The fact that the production terms are underestimated underlines that the scalar field depends more strongly on the small scales than the velocity field. This complicates the modeling of the scalar with respect to other turbulent quantities and explains why not the same quality of results can be expected for scalar and velocity related quantities, for example for the scalar variance and the TKE. Section 4.4.1.5 shows that a refinement of the grid leads to better results concerning scalar quantities, demanding therefore a compromise between quality and computational costs.

4.4.1.3 Spectra

In an ideal LES, the spectra of the LES with EFM should follow the DNS spectra up to the cut-off wavenumber. That this is the case for the one-dimensional spectra of the streamwise velocity and the TKE, both averaged over directions x_2 and x_3, is shown in Figs. 4.18 and 4.19. Also the one-dimensional dissipation spectrum, evaluated as $k_1^2\hat{u}'\hat{u}'^*$, in Fig. 4.20 presents the desired feature.

That the underprediction of the scalar variance by the LES comes from the larger scales is demonstrated by Fig. 4.21 which shows the spectrum of the oxygen mass fraction: The energy in the smallest wave numbers is lower for the LES than the DNS. This results in a smaller magnitude of

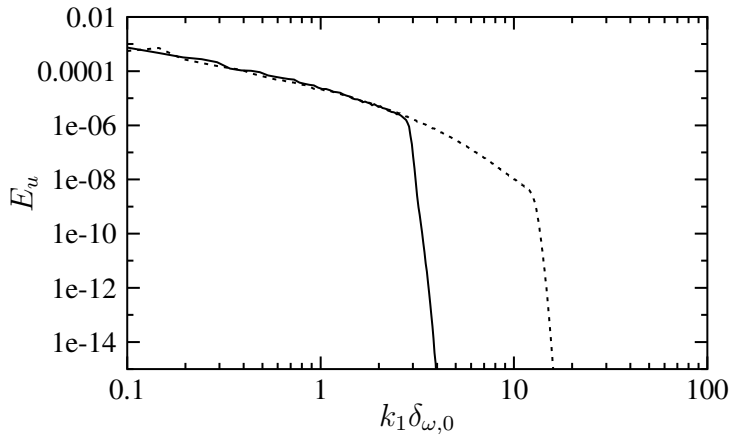

Figure 4.18: One-dimensional, streamwise spectrum of $u_1/\Delta u$ at the beginning of the self-similar state, solid: LES-inert-0.15-4, dotted: DNS-inert-0.15

the scalar variance peak even though there is a slight accumulation of spurious energy right before the cut-off wavenumber. This accumulation becomes even more evident in the one-dimensional spectrum of the scalar dissipation rate, evaluated as $k_1^2 \hat{Y}' \hat{Y}'^*$ in Fig. 4.22. However, since it is only small, no effect on the scalar dissipation profile is visible in Fig. 4.17 in which LES and i-f-DNS profile agree well. In Sect. 4.4.1.5, it is shown that a refinement of the grid alleviates the problem of energy accumulation.

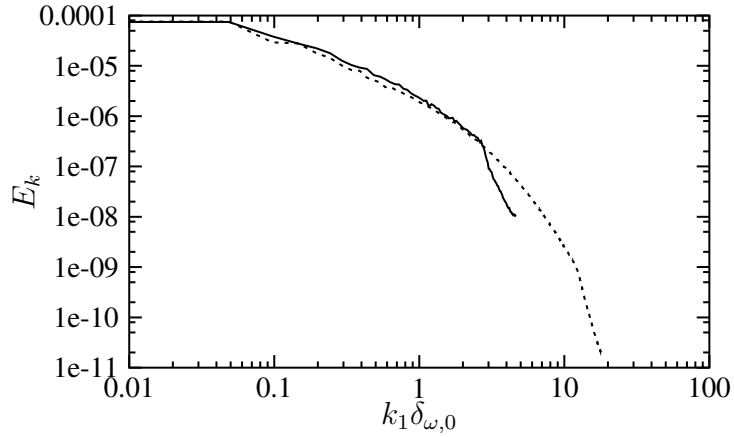

Figure 4.19: One-dimensional, streamwise spectrum of TKE $k/\Delta u^2$ at the beginning of the self-similar state, lines as in Fig. 4.18

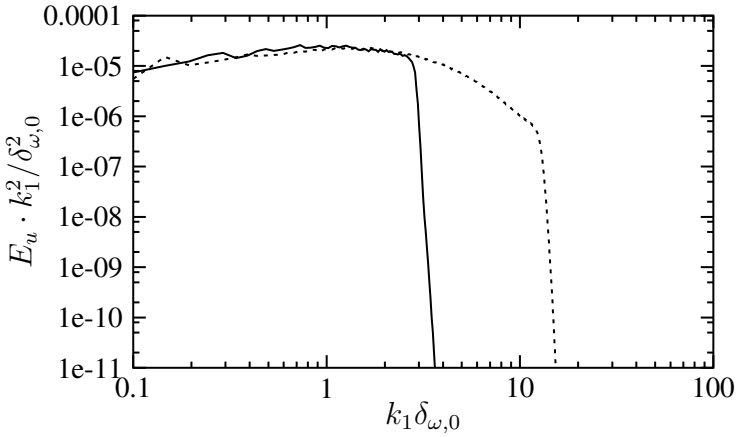

Figure 4.20: One-dimensional, streamwise dissipation spectrum (spectrum of $u_1/\Delta u$ multiplied with $(k_1\delta_{\omega,0})^2$) at the beginning of the self-similar state, lines as in Fig. 4.18

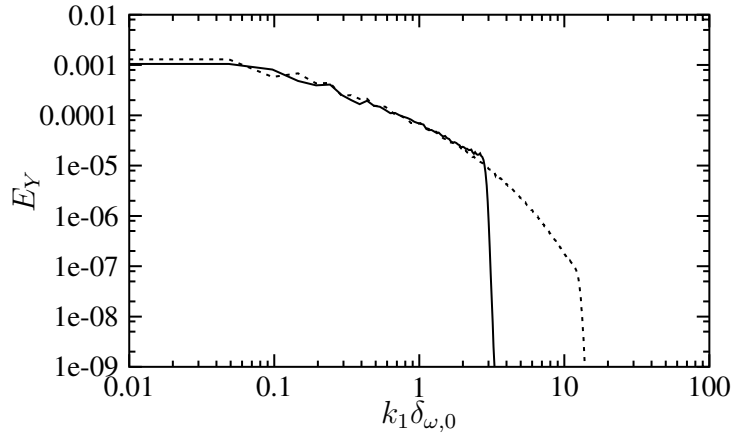

Figure 4.21: One-dimensional, streamwise spectrum of the mixture fraction z at the beginning of the self-similar state, lines as in Fig. 4.18

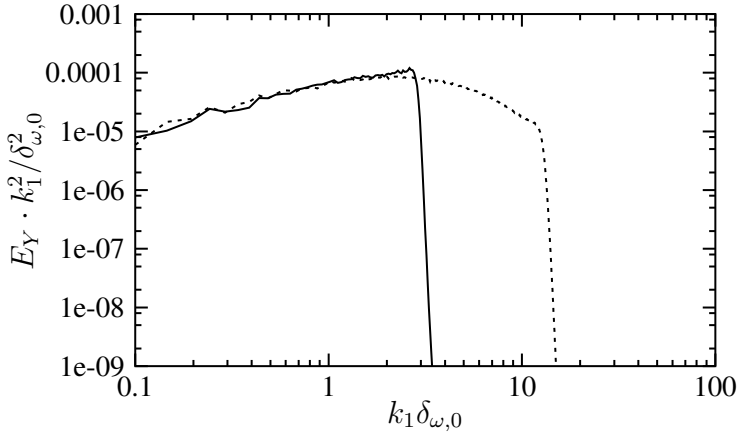

Figure 4.22: One-dimensional dissipation spectrum of the mixture fraction z (spectrum of z multiplied with $(k_1\delta_{\omega,0})^2$) at the beginning of the self-similar state, lines as in Fig. 4.18

4.4.1.4 Effect of filtering on dissipation rates

The subgrid part of the TKE dissipation rate, which is contained in the DNS data, but removed when these data are interpolated onto the coarser grid and filtered, can be interpreted as the difference between the dissipation rate profiles for the DNS and the i-f-DNS in Fig. 4.12. It has to be predicted somehow by the LES model, the EFM in the present case, in order to capture the development of the flow correctly. To see whether the filtering has the desired effect, a dissipation rate caused by the low-pass filter can be computed: After performing one iteration with and one without filtering on the LES grid, this filter dissipation rate is the difference of the resulting TKE profiles divided by the time step. The result at $\tau_\omega = 286$ is shown in Fig. 4.23 together with the instantaneous profiles of the actual dissipation rates in DNS and LES. Even though the filter dissipation rate is highly fluctuating it is clearly a sink term and has about the same magnitude as the dissipation rate of the filtering. Added together they approximately equate the dissipation rate of the DNS.

A similar procedure results in the filter scalar dissipation rate in Fig. 4.24 computed from the scalar (oxygen mass fraction) variance fields after one equation with and one without filtering. Since the scalar dissipation rate of the DNS is more than double the one of the LES, it is justified that the filter scalar dissipation profile has a larger magnitude than the LES dissipation profile. Added together, the total scalar dissipation in the LES, coming from actual scalar dissipation and filter scalar dissipation, has about the same size than the scalar dissipation rate of the DNS.

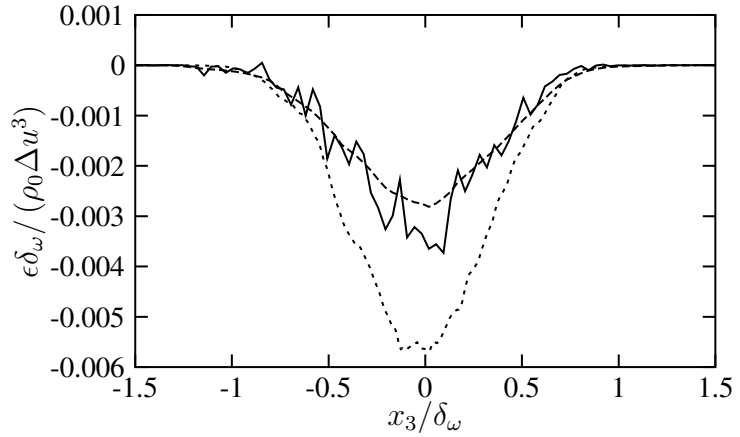

Figure 4.23: TKE dissipation rates at $\tau_\omega = 286$, normalized by $\rho_0\Delta u^3/\delta_\omega$, solid: effect of the filter, dashed: ϵ from LES-inert-0.15-4, dotted: ϵ from DNS-inert-0.15

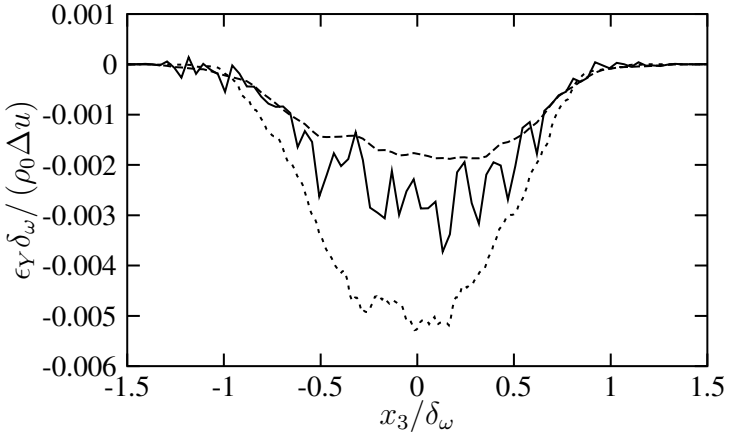

Figure 4.24: Scalar dissipation rates at $\tau_\omega = 286$, normalized by $\rho_0 \Delta u / \delta_\omega$, solid: effect of the filter, dashed: ϵ_Y from LES-inert-0.15-4, dotted: ϵ_Y from DNS-inert-0.15

4.4.1.5 Refinement of the grid

Reducing the DNS grid points by factor two in each direction only, as done in case LES-inert-0.15-2 improves the results compared to LES-inert-0.15-4, in particular those for scalar quantities. Figure 4.25 shows that the underprediction of the scalar variance is still there in simulation LES-inert-0.15-2, but it is less severe than in LES-inert-0.15-4 (cf. Fig. 4.10). Therefore, it can be expected that when increasing the number of grid points further, the LES profile will approach the i-f-DNS profile and also the DNS profile itself. By a refinement of the grid, the capturing of the scalar production rate is also improved as a comparison between Figs. 4.16 and 4.26 reveals. The energy content of the smallest wavenumbers, i.e. larger scales is about the same as in the DNS, and only a slight underestimation for intermediate wavenumbers is visible in the one-dimensional scalar spectrum in Fig. 4.27. Moreover, there is no spurious accumulation of energy in the wavenumbers right before the cut-off in both, the scalar spectrum and its dissipation rate spectrum (Fig. 4.28).

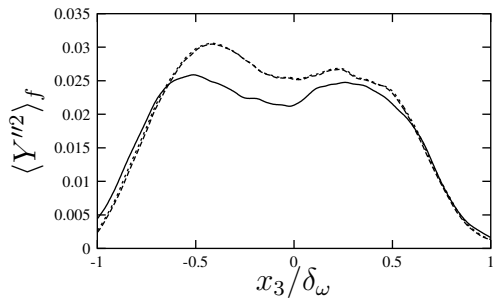

Figure 4.25: Variance of mixture fraction, solid: LES-inert-0.15-2, dashed: DNS-inert-0.15 interpolated to LES grid and filtered, dotted: DNS-inert-0.15

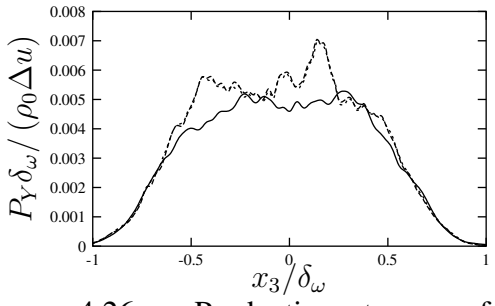

Figure 4.26: Production terms of the scalar variance transport equation, $P_Y = -\langle \rho Y_\alpha'' u_3'' \rangle \frac{\partial \langle Y_\alpha \rangle_f}{\partial x_3} - \frac{1}{2} \langle \rho Y_\alpha''^2 \rangle \frac{\partial \langle u_3 \rangle_f}{\partial x_3}$, normalized by $\delta_\omega / (\rho_0 \Delta u)$, lines as in Fig. 4.25

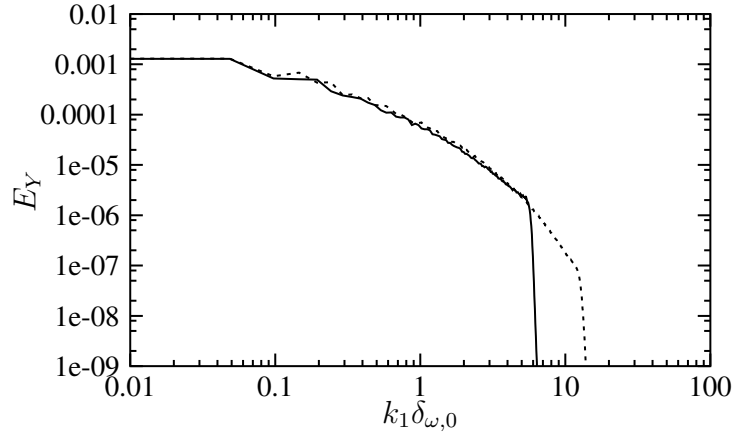

Figure 4.27: One-dimensional, streamwise spectrum of the mixture fraction z at the beginning of the self-similar state, solid: LES-inert-0.15-2, dotted: DNS-inert-0.15

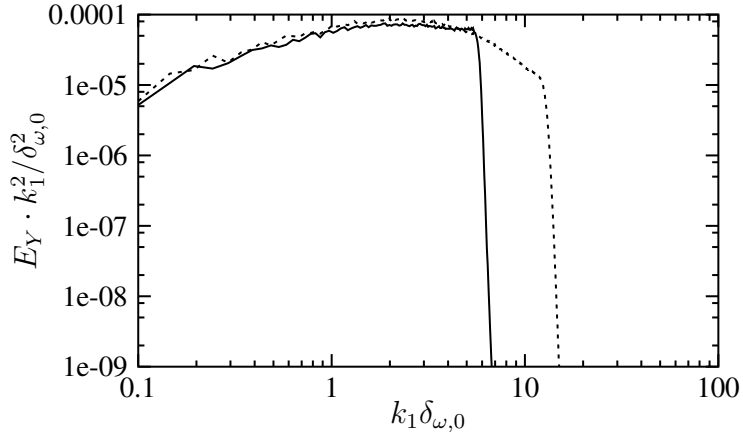

Figure 4.28: One-dimensional dissipation spectrum of the mixture fraction z (spectrum of z multiplied with $(k_1\delta_{\omega,0})^2$) at the beginning of the self-similar state, lines as in Fig. 4.27

4.4.2 Infinitely fast reacting mixing layers

4.4.2.1 Instantaneous fields

Most of the statements concerning the comparison of instantaneous DNS and LES scalar and scalar gradient fields of the inert mixing layers in Sect. 4.4.1.1 also apply to the corresponding fields of the reacting mixing layers. However, the scalar under investigation is now the mixture fraction instead of the oxygen mass fraction. Figures 4.29 and 4.30 show the instantaneous mixture fraction distribution at the beginning of the self-similar state. They are very similar, and there are even prominent ejections and intrusions that directly correspond to each other. This comes from the fact that the LES has been started from an instantaneous DNS field. However, the LES field is more blurred than the DNS field due to the coarser grid and the mixing layer boundaries of the LES are not as finely structured as those of the DNS. The same is true for the instantaneous temperature fields in Figs. 4.31 and 4.32. From the maximum value on the scales to the right of each image it can be seen that the extreme value of the LES is larger than the one of the DNS which indicates an overestimation of the temperature field that is also seen in its mean values and rms fluctuations (cf. Sect. 4.4.2.2).

Even more striking are the differences between the instantaneous mixture fraction gradient fields of DNS and LES in Figs. 4.33 and 4.34. As for the inert scalar gradient field, the maximum value in the LES is considerably smaller than in the DNS due to the lack of the smallest scales.

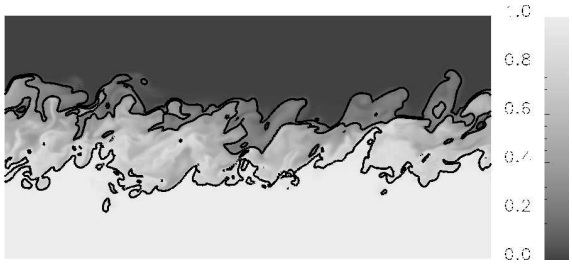

Figure 4.29: DNS-inf-0.15: Instantaneous mixture fraction field, x_1-x_3-plane in the middle of the computational domain at $\tau_\omega = 459$, isolines $z = 0.1$, $z = 0.3$ and $z = 0.9$ are shown

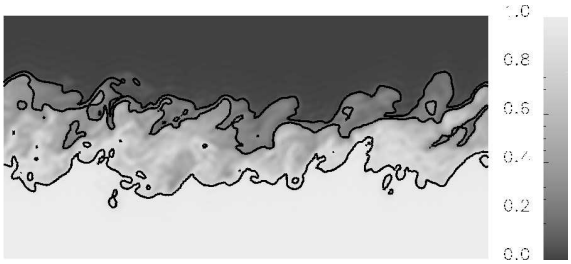

Figure 4.30: LES-inf-0.15-4: Instantaneous mixture fraction field, x_1-x_3-plane in the middle of the computational domain at $\tau_\omega = 459$, isolines $z = 0.1$, $z = 0.3$ and $z = 0.9$ are shown

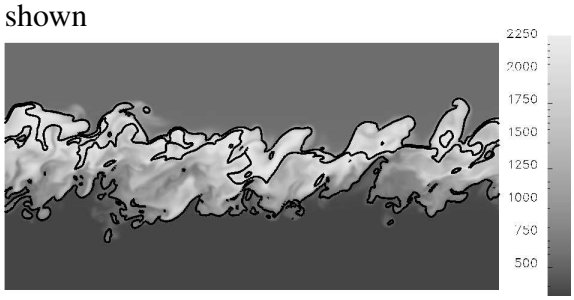

Figure 4.31: DNS-inf-0.15: Instantaneous temperature field, x_1-x_3-plane in the middle of the computational domain at $\tau_\omega = 459$, isolines $z = 0.1$, $z = 0.3$ and $z = 0.9$ are shown

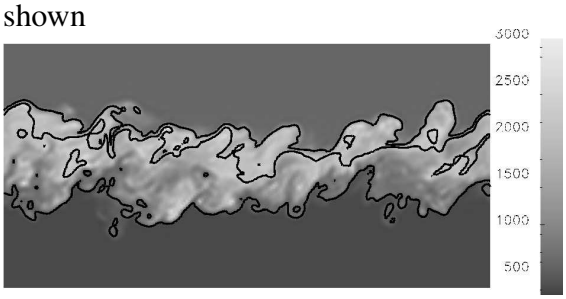

Figure 4.32: LES-inf-0.15-4: Instantaneous temperature field, x_1-x_3-plane in the middle of the computational domain at $\tau_\omega = 459$, isolines $z = 0.1$, $z = 0.3$ and $z = 0.9$ are shown

4.4.2.2 Profiles of averaged flow variables

The mean profiles of streamwise velocity, density and temperature are well predicted by the LES as the comparisons with the DNS and the i-f-DNS results in Figs. 4.35, 4.38 and 4.37 show. The averaged mixture fraction profile has slightly smaller gradients than the DNS and i-f-DNS ones (Fig. 4.36). A small overprediction of the temperature and a corresponding underprediction of the density are visible on the fuel-rich side of the mixing layer (Figs. 4.37 and 4.38).

The locations of the peak values of density and temperature fluctuations are also well predicted by the LES (Figs. 4.39 and 4.40), but the extreme values themselves are slightly exaggerated. The same is true to a smaller extent for the TKE in Fig. 4.41. The scalar variance in Fig. 4.42 is underpredicted by the LES but the underprediction is smaller than for the inert case (Fig. 4.10).

The weak underprediction of the TKE production rate in Fig. 4.43 by the LES does not seem to

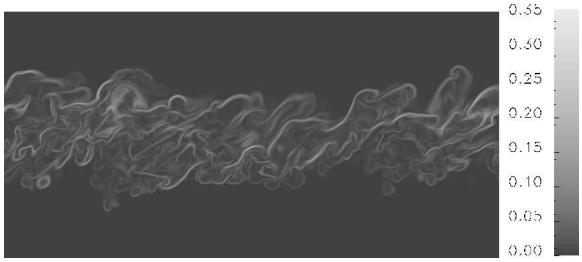

Figure 4.33: DNS-inf-0.15: Instantaneous mixture fraction gradient field, normalized by $\delta_{\omega,0}$, x_1-x_3-plane in the middle of the computational domain at $\tau_\omega = 459$

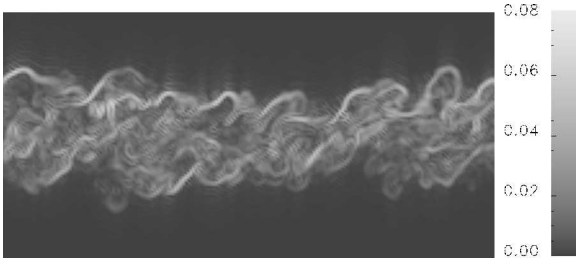

Figure 4.34: LES-inf-0.15-4: Instantaneous mixture fraction gradient field, normalized by $\delta_{\omega,0}$, x_1-x_3-plane in the middle of the computational domain at $\tau_\omega = 459$

have much effect on the relatively well predicted TKE value itself (Fig. 4.41). The agreement between the TKE dissipation rate of the LES and its counterpart from the i-f-DNS in Fig. 4.44 is excellent. If one compares Fig. 4.44 with Fig. 4.12 for the inert mixing layers, one can see that for the infinitely fast reacting mixing layers, there is a smaller part of the DNS dissipation rate suppressed when coarsening the grid than for the inert mixing layers. This is due to the smoothening effect of the heat release which leads to a scalar field with smaller fluctuations and less intermittency.

The scalar variance production rate is underestimated by the LES as shown in Fig. 4.45. Even though the magnitude of the major sink term in the scalar variance transport equation, namely the

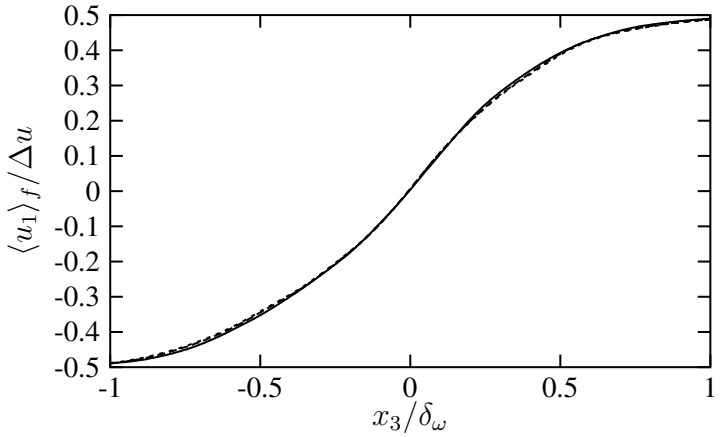

Figure 4.35: Favre averaged streamwise velocity, normalized by Δu, solid: LES-inf-0.15-4, dashed: DNS-inf-0.15 interpolated to LES grid and filtered, dotted: DNS-inf-0.15

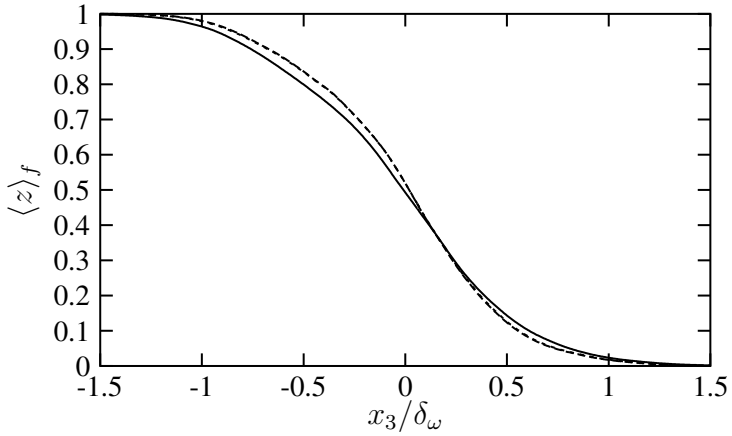

Figure 4.36: Favre averaged mixture fraction, solid: LES-inf-0.15-4, dashed: DNS-inf-0.15 interpolated to LES grid and filtered, dotted: DNS-inf-0.15

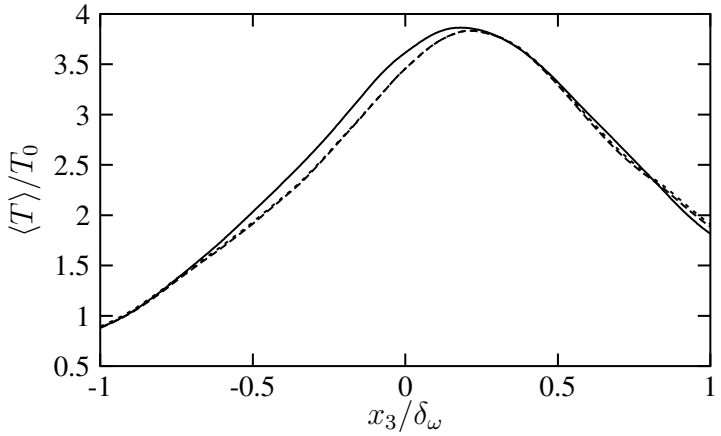

Figure 4.37: Averaged temperature, normalized by T_0, lines as in Fig. 4.35

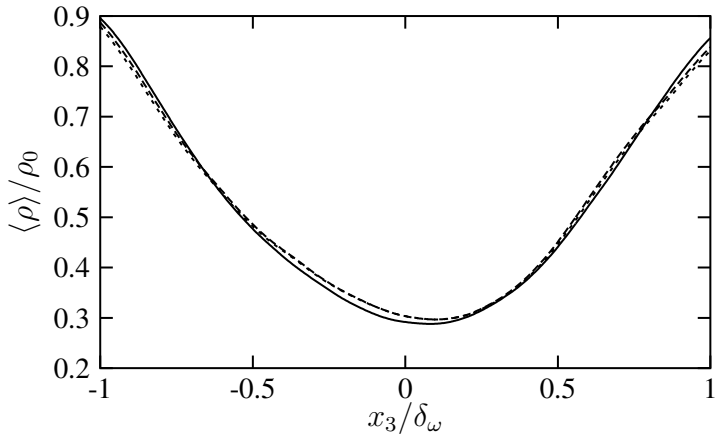

Figure 4.38: Averaged density, normalized by ρ_0, lines as in Fig. 4.35

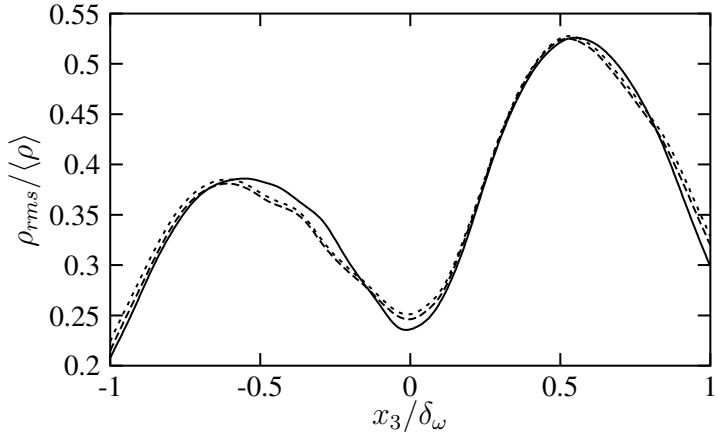

Figure 4.39: Rms value of the density fluctuations, normalized by $\langle\rho\rangle$, lines as in Fig. 4.35

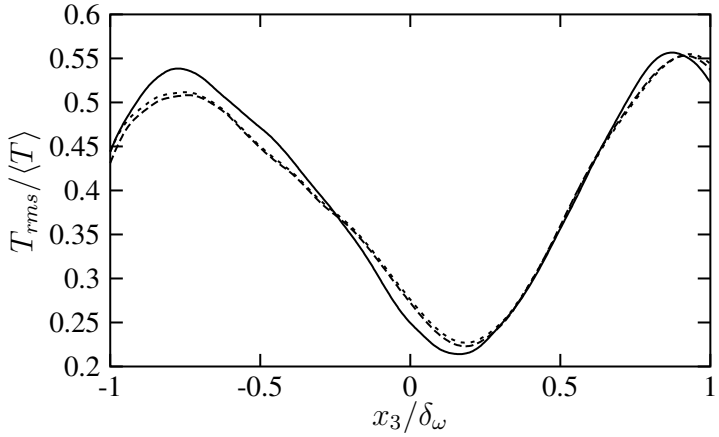

Figure 4.40: Rms value of the temperature fluctuations, normalized by $\langle T\rangle$, lines as in Fig. 4.35

scalar dissipation rate in Fig. 4.46, is also underestimated, both effects lead to a too small scalar variance. A refinement of the grid alleviates the problem partially and reduces the difference between LES and i-f-DNS (cf. Sect. 4.4.2.6).

4.4.2.3 The filtered heat release term

In this section, the modeling of the filtered heat release term by Eq. (4.25) is tested using a priori and a posteriori procedures. For the a priori tests, the DNS fields are interpolated onto the LES grid and filtered with a tophat filter. Then the terms in Eq. (4.25) are computed, whereby either the exact values or the models (cf. Sects. 4.2.4.1 and 4.2.4.3) for $(z^2)_{sg}$ and $\widetilde{\chi}$ are used. Averaging over the homogeneous directions as well as the self-similar state and comparing the exact profiles

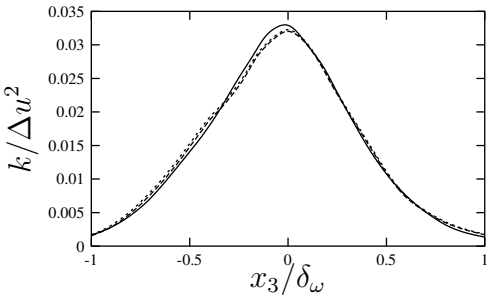

Figure 4.41: Turbulent kinetic energy, normalized by Δu^2, lines as in Fig. 4.35

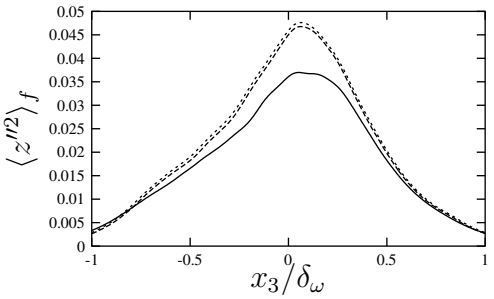

Figure 4.42: Variance of mixture fraction, lines as in Fig. 4.35

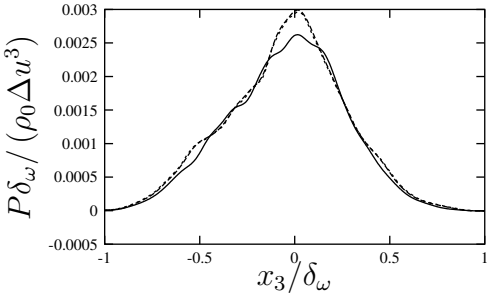

Figure 4.43: Production of TKE, normalized by $\delta_\omega / (\rho_0 \Delta u^3)$, lines as in Fig. 4.35

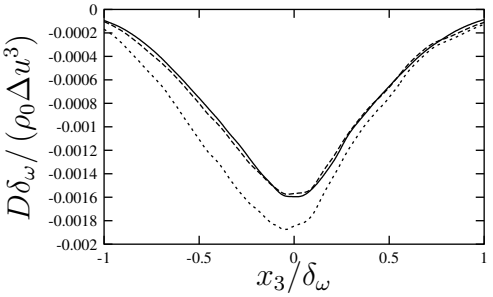

Figure 4.44: Dissipation rate of TKE, normalized by $\delta_\omega / (\rho_0 \Delta u^3)$, lines as in Fig. 4.35

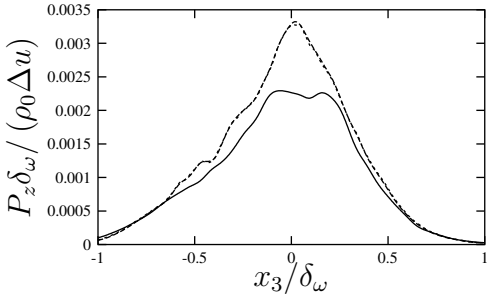

Figure 4.45: Production terms of the scalar variance transport equation, $P_z = -\langle \rho z'' u_3'' \rangle \frac{\partial \langle z \rangle_f}{\partial x_3} - \frac{1}{2} \langle \rho z''^2 \rangle \frac{\partial \langle u_3 \rangle_f}{\partial x_3}$, normalized by $\delta_\omega / (\rho_0 \Delta u)$, lines as in Fig. 4.35

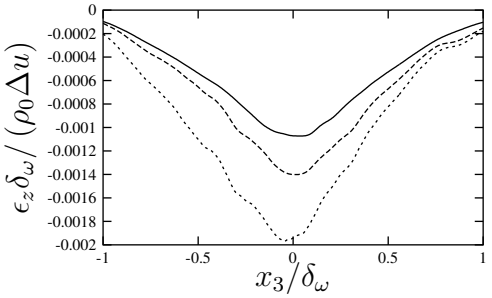

Figure 4.46: Scalar dissipation rate, $\epsilon_z = -\langle \frac{\mu}{Sc} \frac{\partial z}{\partial x_j} \frac{\partial z}{\partial x_j} \rangle$, lines as in Fig. 4.35

of $(z^2)_{sg}$ and $\widetilde{\chi}$ with the modeled ones, allows an optimal adaption of the model coefficients C_z^{GR} and C_χ^{GR}.

The first modeled quantity that the heat release term depends on is the subgrid scalar variance $(z^2)_{sg}$ which enters the beta-pdf. Figure 4.47 shows three profiles: the exact profile computed by Eq. (4.29) from interpolated and filtered DNS data, the profile that results when using gradient model, Eq. (4.30), a priori (i.e. with the exact gradient from the interpolated and filtered DNS data) and, finally, the a posteriori profile from the LES. The agreement between $(z^2)_{sg}$ from the LES and the corresponding value of the gradient model computed from DNS data is good for both, the peak value and the shape. The peak value is already well predicted in the a priori test which is due to the adaption of the model coefficient. Concerning the shape of the $(z^2)_{sg}$ profile, in particular on the fuel-rich side, the a posteriori test performs even better.

The model of the filtered heat release term depends on the beta-pdf via the factor $\widetilde{I}$, Eq. (4.38). Figure 4.48 shows a comparison between its exact profile and the a priori and a posteriori values. Besides $(z^2)_{sg}$, the filtered value $\widetilde{z}$ enters into the computation of $\widetilde{I}$. Even though the averaged LES fields of both $(z^2)_{sg}$ (Fig. 4.47) and $\widetilde{z}$ (LES curve in Fig. 4.36) agree quite well with the

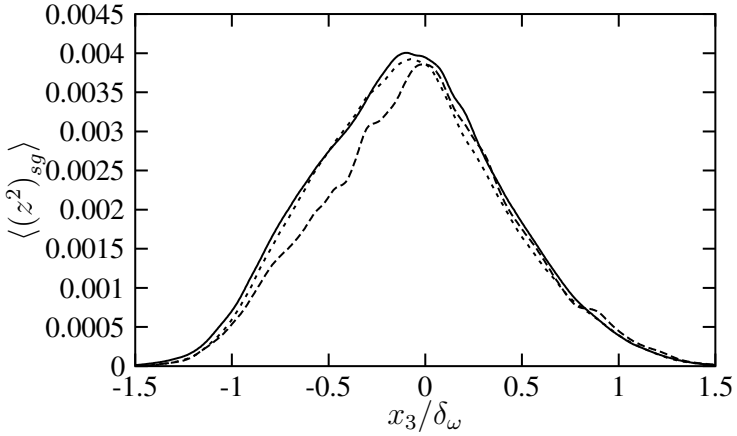

Figure 4.47: Subgrid scalar variance, solid: LES-inf-0.15-4, dashed: a priori test of model with data from DNS-inf-0.15, dotted: exact value from DNS-inf-0.15

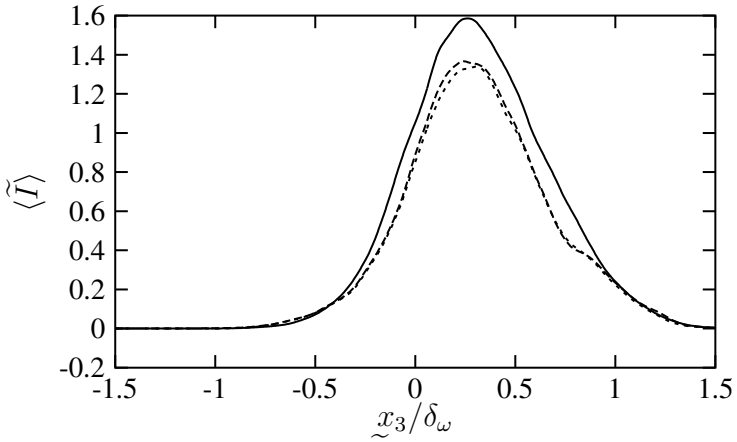

Figure 4.48: Integral $\widetilde{I}$, lines as in Fig. 4.47

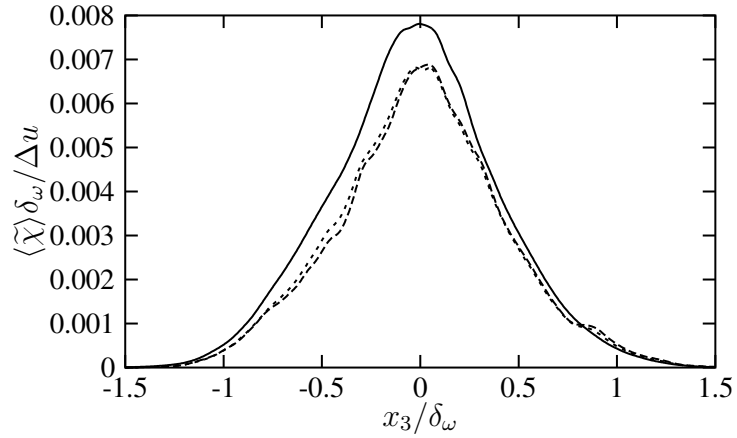

Figure 4.49: Filtered scalar dissipation rate, normalized by $\Delta u/\delta_\omega$, lines as in Fig. 4.47

DNS results, there must be differences in the higher moments of the mixture fraction between LES and DNS as the overestimation of $\widetilde{I}$ suggests. The a priori test of $\widetilde{I}$, however, is excellent.

The model of the filtered scalar dissipation rate is given by Eq. (4.44). A comparison of the exact averaged value of $\widetilde{\chi}$ with the a priori and a posteriori determined ones is shown in Fig. 4.49. Again, the model coefficient in Eq. (4.44) has been adapted such that the a priori test gives the best possible approximation of the exact $\widetilde{\chi}$. About $50\ \%$ of $\widetilde{\chi}$ are from its subgrid part $\chi_{sg} = \widetilde{\chi} - \chi_{ls}$ with χ_{ls} from Eq. (4.40). This is shown in Fig. 4.50 . The figure also demonstrates that the overestimation of $\widetilde{\chi}$ by the LES (Fig. 4.49) is mainly due to an overestimation of its subgrid part modeled by the gradient model.

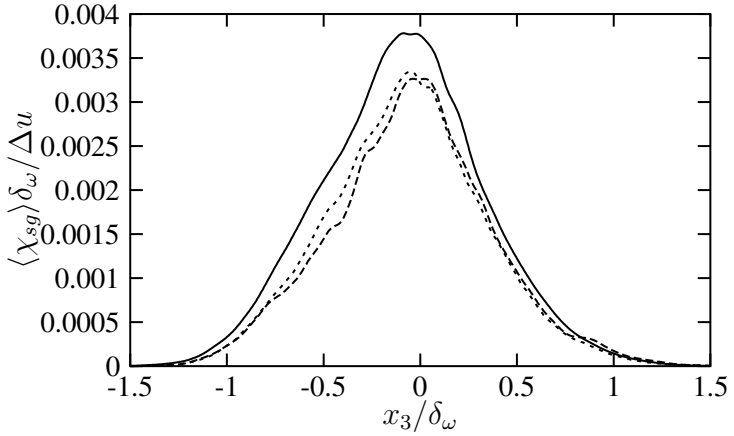

Figure 4.50: Subgrid part of scalar dissipation rate, normalized by $\Delta u/\delta_\omega$, lines as in Fig. 4.47

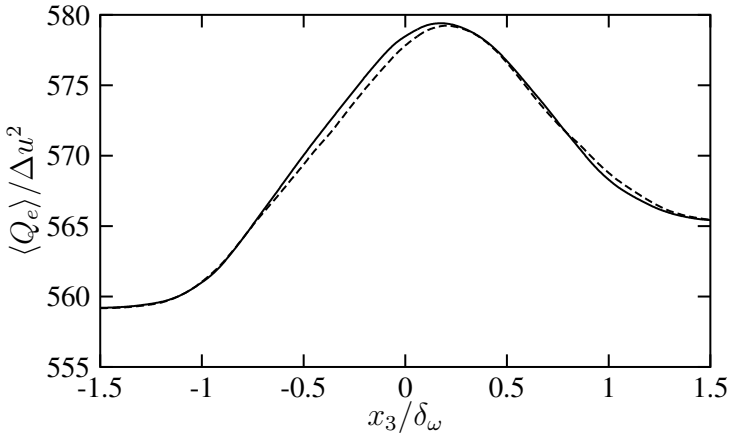

Figure 4.51: Heat release parameter Q_e, normalized by Δu^2, solid: LES-inf-0.15-4, dashed: data from DNS-inf-0.15

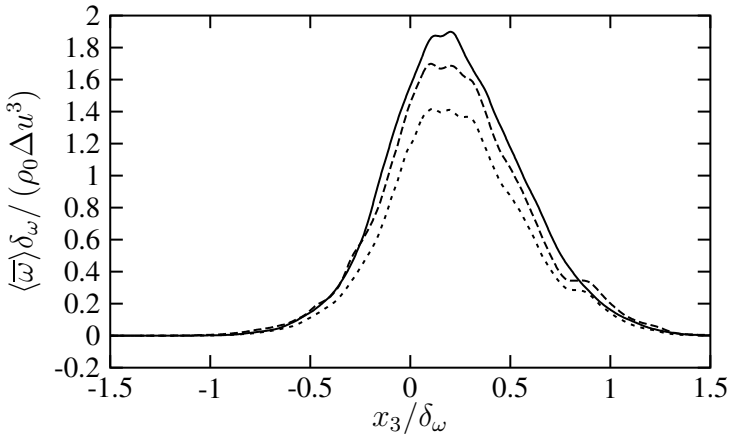

Figure 4.52: Filtered source term $\overline{\omega}$, normalized by $\rho_0 \Delta u^3/\delta_\omega$, lines as in Fig. 4.47

Since the remaining factor in the expression for $\overline{\omega}$, the heat release parameter Q_e (Eq. (4.26)) is well predicted by the LES, the overestimation of the heat release term itself (Fig. 4.52) can be mainly traced back to the overestimations of $\widetilde{I}$ and $\widetilde{\chi}$. However, the a priori computed source term $\overline{\omega}$ also overestimates the actual value. This leads to the conclusion that correlations between the factors in Eq. (4.25) play a role. The overestimation of $\overline{\omega}$, nevertheless, can be considered as tolerable when taking into account the good results for the averaged density and temperature profiles (Figs. 4.38 and 4.37).

4.4.2.4 Spectra

The agreement between various one-dimensional spectra of the reacting DNS and LES up to the cut-off wavenumber is very good (Figs. 4.53 to 4.55). No accumulation of energy in any of the resolved wavenumbers is visible.

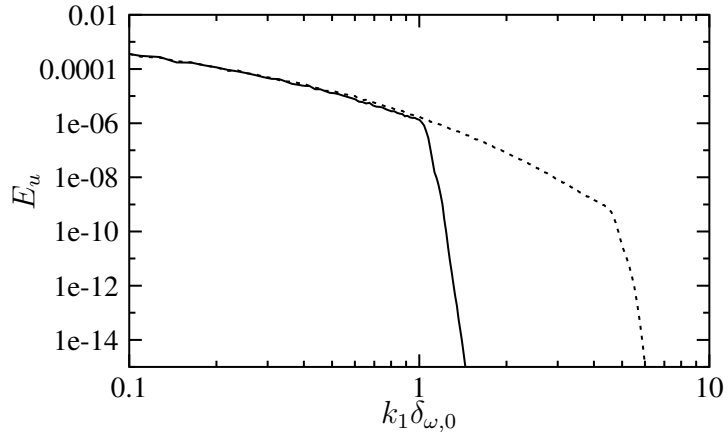

Figure 4.53: One-dimensional, streamwise spectrum of $u_1/\Delta u$ at the beginning of the self-similar state, solid: LES-inf-0.15-4, dotted: DNS-inf-0.15

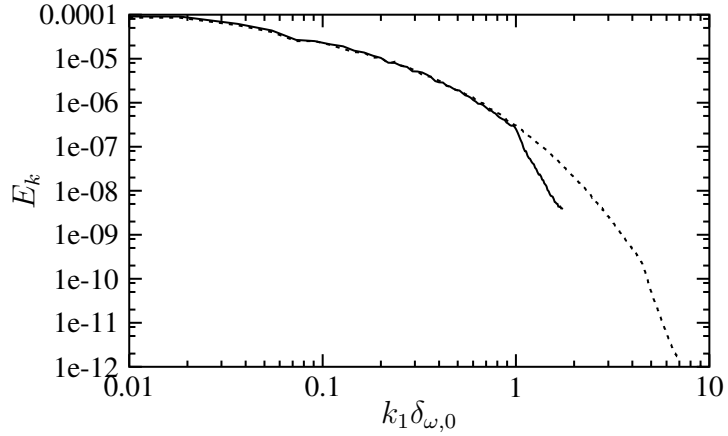

Figure 4.54: One-dimensional, streamwise spectrum of TKE $k/\Delta u^2$ at the beginning of the self-similar state, lines as in Fig. 4.53

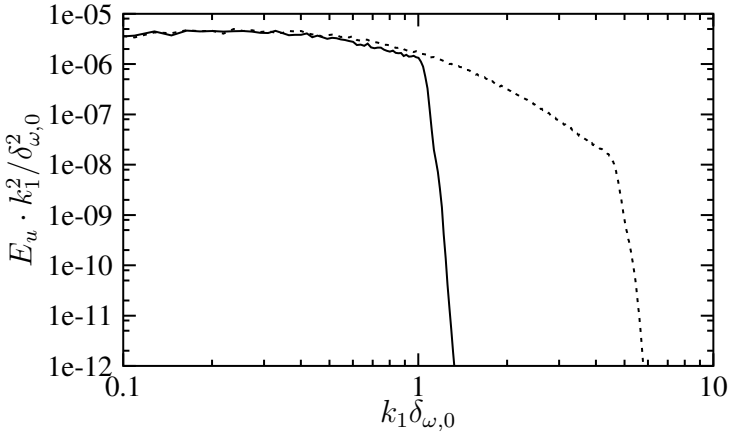

Figure 4.55: One-dimensional, streamwise dissipation spectrum (spectrum of $u_1/\Delta u$ multiplied with $(k_1\delta_{\omega,0})^2$) at the beginning of the self-similar state, lines as in Fig. 4.53

4.4.2.5 Effect of filtering on dissipation rates

In a procedure analogous to that for inert mixing layers in Sect. 4.4.1.4, instantaneous filter dissipation and scalar dissipation rates at the beginning of the self-similar state are computed for the reacting mixing layers. The results, as well as the actual scalar dissipation rates derived from LES and DNS data, are shown in Figs. 4.58 and 4.59. Added together, the filter dissipation rate and the LES TKE dissipation rate in Fig. 4.58 equate approximately the TKE dissipation rate of the DNS. The same is true for the scalar dissipation rates in Fig. 4.59.

4.4.2.6 Refinement of the grid

Quantities which were not perfectly captured by the LES when coarsening the DNS grid by factor four in each direction are better approximated when coarsening the DNS grid by factor two in each direction only. Two examples are shown in Figs. 4.60 and 4.61: The variance of the mixture fraction and the mean heat release term (compare with Figs. 4.42 and 4.61). For the latter one, we observe that the a priori computed profile and the a posteriori computed one collapse while the actual profile computed without any models from DNS results is below these curves. This leads to the conclusion that the remaining differences between LES and DNS concerning the profile of $\overline{\omega}$ are mainly due to correlations between the single factors in Eq. (4.25) since the a posteriori

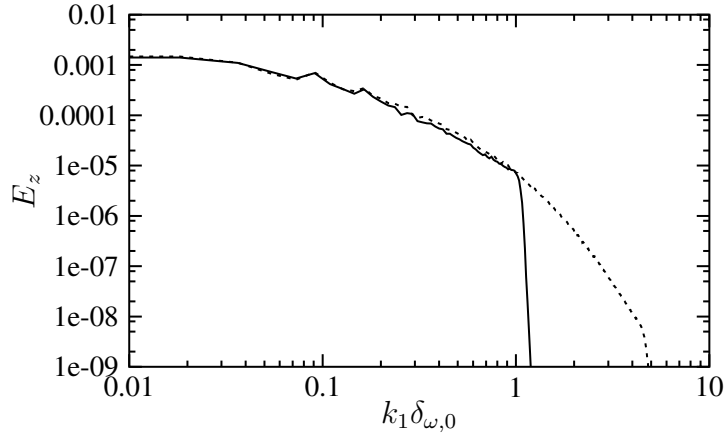

Figure 4.56: One-dimensional, streamwise spectrum of the mixture fraction z at the beginning of the self-similar state, lines as in Fig. 4.53

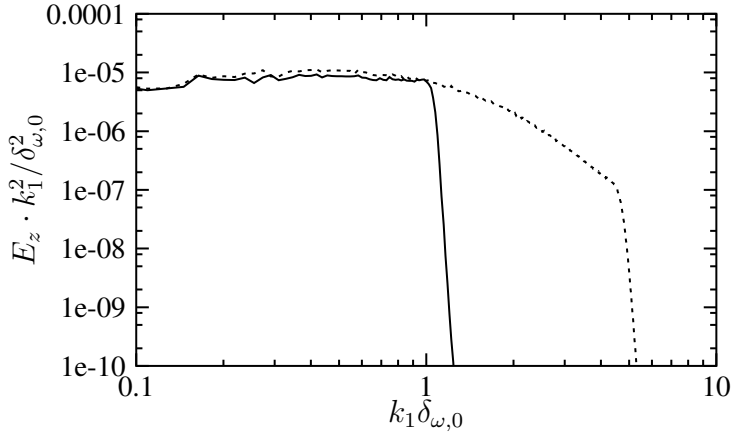

Figure 4.57: One-dimensional dissipation spectrum of the mixture fraction z (spectrum of z multiplied with $(k_1\delta_{\omega,0})^2$) at the beginning of the self-similar state, lines as in Fig. 4.53

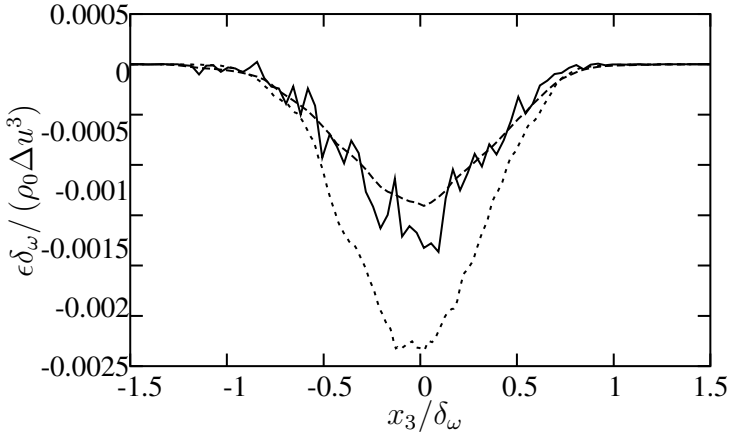

Figure 4.58: TKE dissipation rates at $\tau_\omega = 459$, normalized by $\rho_0\Delta u^3/\delta_\omega$, solid: effect of the filter, dashed: ϵ from LES-inf-0.15-4, dotted: ϵ from DNS-inf-0.15

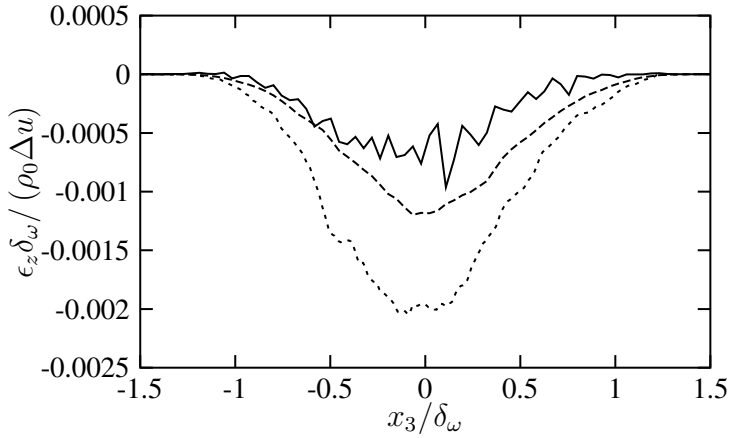

Figure 4.59: Scalar dissipation rates at $\tau_\omega = 459$, normalized by $\rho_0\Delta u/\delta_\omega$, solid: effect of the filter, dashed: ϵ_z from LES-inf-0.15-4, dotted: ϵ_z from DNS-inf-0.15

and a priori profiles match well with the latter one being the best possible approximation with the presently used models.

4.5 Summary and conclusions

A particular version of the Approximate Deconvolution Method (ADM) has been used for the LES of inert and reacting shear layers, and the results have been validated by comparison with DNS data. ADM aims at reconstructing turbulent flow fields from filtered ones by a deconvolution procedure. Except for the chemical source term, no additional models for subgrid terms are used during this purely mathematical procedure, and no knowledge about the flow physics is required beforehand. In the version of the ADM that is used in this work, the filtering and the deconvolution step are summarized into a single explicit filtering step. This particular variant of ADM is denoted here as EFM - Explicit Filtering Method. As already mentioned, the chemical source term in the simulation of the reacting shear layers cannot be treated by ADM or EFM since the chemical reactions take place nearly entirely in the smallest, unresolved scales. Hence, there is no chance of reconstructing them by deconvolution. In this chapter, the chemical source term has been modeled for infinitely fast, irreversible chemistry with the help of a beta-function for the mixture fraction fdf and gradient models for the mixture fraction subgrid variance and the filtered scalar dissipation rate. Furthermore, the filtered species mass fractions have also been

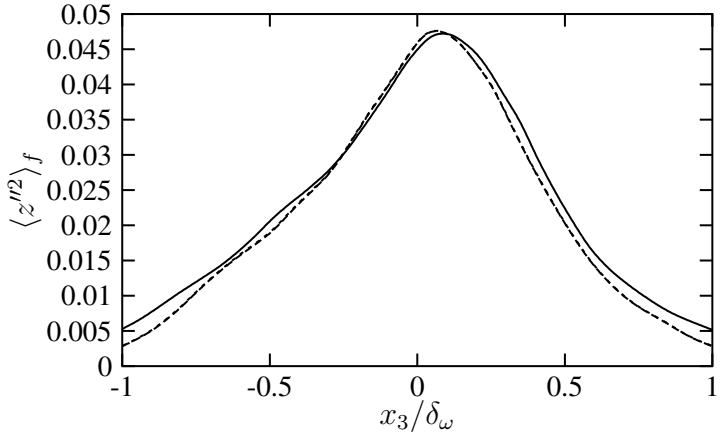

Figure 4.60: Variance of mixture fraction, solid: LES-inf-0.15-2, dashed: DNS-inf-0.15 interpolated to LES grid and filtered, dotted: DNS-inf-0.15

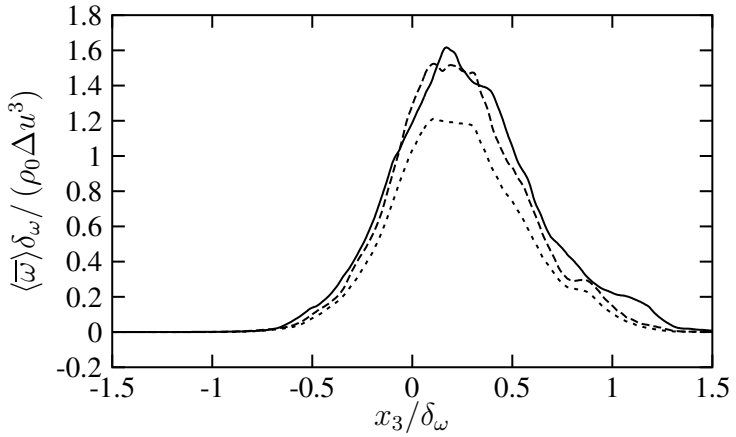

Figure 4.61: Mean filtered heat release term $\overline{\omega}$, normalized by $\rho_0\Delta u^3/\delta_\omega$, solid: LES-inf-0.15-4, dashed: a priori test of model with data from DNS-inf-0.15, dotted: exact value from DNS-inf-0.15

obtained by integration with a beta-fdf for the mixture fraction. Coefficients for the models have been adapted in a priori tests using DNS data.

The LES performed and analyzed are temporally evolving, turbulent mixing layers at $M_c = 0.15$, inert and infinitely fast reacting. They have been initialized well before the attainment of the self-similar state from corresponding DNS flow fields that had been interpolated to the coarser LES grid and filtered. Two different resolutions for the LES have been used: One with 8 times less grid points than the DNS and one with 64 times less grid points. A further coarsening of the grid would also be possible if only stability was the criteria for a successful LES and less quality of the results was allowed. This concerns in particular quantities that are dominated by small scales like the TKE dissipation rate and the scalar dissipation rate. However, computation on a grid as coarse as possible is not the goal of the present work, and we have opted for a compromise between computational effort and good results by chosing relatively fine LES grids. Statistics from the LES data were taken over the self-similar states of the mixing layers and compared to DNS data as well as DNS data that had been interpolated to the LES grid and filtered. A comparison of instantaneous scalar (mass and mixture fractions) and scalar gradient distributions have revealed that, while large structures have been successfully captured by the LES, this, as expected, has not been the case for small structures, and the LES fields appear consequently more 'blurred'. This is particularly strong for the intermittent scalar gradients, the highest values of which are situated in the smallest scales, that cannot be resolved in an LES.

For the inert mixing layers, an excellent capturing of flow dynamical quantities like the mean streamwise velocity and the turbulent kinetic energy (TKE) is observed, even for the resolution with 64 times less grid points than the DNS. Moreover, the most important terms in the TKE transport equation, namely production and the dissipation rates, are reproduced well, with a good agreement of the LES profiles and the profiles from the interpolated DNS data. The same is true for the pressure-strain correlations steering the re-distribution of energy from the streamwise Reynolds stress component to the spanwise and transverse ones. The one-dimensional spectra of the streamwise velocity, the turbulent kinetic energy and the dissipation rate show the expected behaviour: The LES spectra follow the DNS spectra up to the cut-off frequency, and no spurious accumulation of energy is visible in the highest resolved wavenumbers. However, a good capturing of scalar-related quantities seems to be more difficult, even for the inert mixing layers: Too small amplitudes of the LES profile compared to the filtered DNS profile for the mass fraction variances and their production rates have been observed. The one-dimensional scalar and scalar dissipation spectra show a slight accumulation of energy in the highest resolved wavenumbers. These difficulties are traced back to the fact that the scalar field is more sensitive to the small scales than the velocity field which complicates its modeling. However, the simulations with the finer grid (8 times less grid points than the DNS) show a significant improvement of the results.

For the LES of the reacting mixing layers, not only an excellent capturing of flow dynamical quantities (mean velocity, TKE), but also of thermodynamical quantities (mean temperature and density and the corresponding rms values) has been observed, even for the coarsest resolution that has been investigated. As for the inert mixing layers, scalar-related quantities, like the variance of the mixture fraction show discrepancies between the LES and the interpolated DNS profiles that are, however, reduced by a refinement of the LES grid. A priori and a posteriori tests of the filtered heat release term have also been performed. Its weak overestimation by LES has been led back to a slight overestimation of the subgrid scalar dissipation rate by the Smagorinsky model and to differences between LES and filtered DNS in higher moments of the mixture fraction. These deficiencies have been reduced when refining the LES grid. The mixture fraction subgrid variance has been captured excellently by the gradient model, even at the coarser resolution. Since the spectra for the reacting mixing layers are less dominated by the small scales than the inert ones, they are easier to reproduce (up to the cut-off frequency) by the LES, and no spurious accumulation of energy has been observed in the highest resolved wavenumbers, neither in the one-dimensional spectra for the streamwise velocity, the TKE and its dissipation rate, nor in the spectra for the scalar and the scalar dissipation rate.

Finally, it can be concluded that EFM (combined with proper heat release modeling for reacting flow) has been proven to be a successful and efficient LES model for inert and infinitely fast reacting turbulent mixing layers. As for any LES model, it is necessary to make compromises between the quality of the results and computational effort.

Even though only results for $M_c = 0.15$ have been shown in the present chapter, also inert and reacting shear layers at higher convective Mach numbers have been simulated successfully with EFM. However, since the following chapter deals with reacting mixing layers at the same low Mach number and shows an extension of the combustion model to include finite-rate chemistry and detailed diffusion, it has been decided not to extend the analysis of the present chapter to higher Mach numbers.

5 LES of shear layers with chemical kinetic and detailed diffusion effects

5.1 Introduction and literature survey

While in the previous chapters DNS and LES of reacting mixing layers with infinitely fast chemistry and simplified diffusion have been performed, the aim of this chapter is to take into account chemical kinetic and detailed diffusion effects by using an LES flamelet model. A classification of flamelet approaches within the range of combustion models has been provided in Sect. 4.1.

Besides a simplified treatment of chemistry, many existing turbulent combustion models also use simplified diffusion processes [73]. Multicomponent and thermal diffusion effects are only included in recent Direct Numerical Simulations (DNS) of turbulent combustion [40] and show mainly local influences on the flame structure. To our knowledge, only one attempt has been made to include these effects in a flamelet model for a Large Eddy Simulation (LES) [131]. In the present chapter, the formulation of the flamelet equations in physical space as well as the definition of the mixture fraction and its diffusivity is the same as in the work of Pierce & Moin [131], but the LES model is different. While Pierce & Moin apply eddy diffusivity and eddy viscosity models with dynamically evaluated coefficients, the LES model used in this work is a modified version of the approximate deconvolution method (ADM) [175, 176] and has already been presented in the previous chapter. In [131], Pierce & Moin mention the possibility to include different diffusion models in their flamelet model and show some LES results for a methane-fuelled coaxial jet combustor with different diffusion approximations. Based on these results, they argue that an accurate treatment of mass diffusion can be just as important as accurate modeling of chemical kinetics. The fact that the authors do not pursue the issue further, but concentrate instead on the advantages of a progress variable to capture unsteady, lifted flame dynamics [132], is one of the motivations to investigate detailed diffusion effects in the present work.

Most authors who considered effects of detailed diffusion in flamelets and laminar diffusion flames concentrated mainly on two species with different but constant diffusivities or Lewis numbers [34, 119] or neglected thermal diffusion [138]. Therefore, almost no data is available comparing different levels of approximation for the species diffusion fluxes and the heat flux with respect to multicomponent, Soret and Dufour effects. One aim of the present chapter is to see their influence in a basic configuration for non-premixed hydrogen combustion, namely a temporally evolving turbulent shear layer.

This chapter is organized as follows: Section 5.2 explains the essential features of the LES with a particular focus on the modeling of the filtered heat release term and the filtered species mass fractions. The computation and tabulation of the steady flamelets is dealt with in Sect. 5.3. It is also explained how the detailed chemistry is implemented and what different approximations of the diffusion fluxes and the heat flux vector are used. In Section 5.4, configuration, initialization

and essential parameters of the mixing layer LES are presented and related to the ones of test cases from other chapters of this work. Section 5.5 is dedicated to the results and their analysis: First, laminar flamelets with different diffusion approximations are compared with each other (Sect. 5.5.1). Then, the LES results are validated by comparison with DNS data (Sect. 5.5.2). Moreover, the differences between the LES results with detailed and simplified diffusion are assessed and contrasted with those encountered between the respective laminar flamelets. Conclusions are drawn in Sect. 5.6.

5.2 LES approach

5.2.1 LES equations and models

During the LES, the compressible transport equations for the pressure p, the Cartesian velocity components u_i, the temperature T and a passive scalar, which is the mixture fraction z, are integrated by using sixth-order compact central schemes for the spatial derivatives in all directions and a third order low-storage Runge-Kutta scheme for time integration. The transport equations for p, u_i and T are the same as given in Eq. (4.16). In the transport equation of z, the diffusivity of the mixture fraction, α_z, is used:

$$\frac{\partial z}{\partial t} = -u_i \frac{\partial z}{\partial x_i} + \frac{1}{\rho}\frac{\partial}{\partial x_i}\left(\alpha_z \rho \frac{\partial z}{\partial x_i}\right) \tag{5.1}$$

α_z depends on elemental diffusive fluxes and is therefore not constant. Its determination is explained in Sect. 5.3.3.

After each time integration step, an explicit filtering step (with the composite $(Q * G)^2$ filter) of the primitive flow variables as described in Sect. 4.2.1 is performed. This procedure implicitly models the subgrid terms arising from non-linearities when low-pass filtering and projecting the transport equations onto a coarse LES grid. Only the filtered heat release term

$$\overline{\omega} = -\sum_{\alpha} \overline{h_\alpha \omega_\alpha} \tag{5.2}$$

which appears in the transport equations of the pressure and the temperature has to be modeled separately. In Sect. 5.2.2, it is explained how this is done for finite-rate chemistry using a flamelet database.

Two additional quantities have to be modeled during the LES, since they are required for the retrieval of the filtered chemical source term and the filtered species mass fractions from the flamelet database (cf. Sect. 5.3): the subgrid variance of the mixture fraction,

$$\left(z^2\right)_{sg} = \widetilde{z^2} - \widetilde{z}^2 \tag{5.3}$$

and the filtered scalar dissipation rate,

$$\widetilde{\chi} = \alpha_z \widetilde{\left(\frac{\partial z}{\partial x_i}\right)^2}. \tag{5.4}$$

Both quantities, $\left(z^2\right)_{sg}$ and $\widetilde{\chi}$, are computed with gradient models which are given by Eqs. (4.30) and (4.44).

5.2.2 Filtered heat release term and filtered species mass fractions

As described in Chapter 4, the filtered heat release term, Eq. (5.2), resulting from the chemical reactions, is not captured by pure explicit filtering and has to be treated separately. The reason for this is that most of the chemical reactions are taking place in the unresolved scales. While $\overline{\omega}$ has been computed in Chapter 4 by Eq. (4.25), which is valid for an infinitely fast, irreversible global reaction, it is determined in the present chapter with the help of relations $\omega = \omega(z, \chi_0)$ which are tabulated in a flamelet database (cf. Sect. 5.3). The filtered species mass fractions $\widetilde{Y}_\alpha$ are computed based on corresponding relations, $Y = Y(z, \chi_0)$, and not by the Burke-Schumann equations as in Chapter 4. χ_0 is the average value of the scalar dissipation rate χ for a flamelet, with χ being defined as

$$\chi = \alpha_z \left(\frac{\partial z}{\partial x_i} \right)^2 . \tag{5.5}$$

To compute the filtered values $\widetilde{Y}_\alpha$ and $\overline{\omega}$ from the flamelet profiles, $Y_\alpha(z, \chi_0)$ and $\omega(z, \chi_0)$, integrations like

$$\widetilde{Y}_\alpha = \int_0^1 \int_{\chi_0^{min}}^{\chi_0^{max}} Y_\alpha(z, \chi_0) F(\chi_0) F(z) \, d\chi_0 dz \tag{5.6}$$

have to be performed using the filtered density functions (fdf) F of z and χ_0, respectively. χ_0^{min} and χ_0^{max} are the minimum and maximum values of χ_0 within the filter volume. In Equation (5.6), z and χ_0 are assumed to be statistically independent, i.e. the joint fdf $F(\chi_0, z)$ can be written as a product of the two marginal fdfs, $F(\chi_0) F(z)$. This assumption is justified by the fact that the scalar dissipation rate is constant for each flamelet individually (cf. Sect. 4). Following Cook et al. [33] and deBruynKops et al. [37], the integral (5.6) is simplified to

$$\widetilde{Y}_\alpha = \int_0^1 Y_\alpha(z, \widetilde{\chi}_0) F(z) \, dz \tag{5.7}$$

since Y_α is a weak, approximately linear function of χ_0. To obtain Eq. (5.7) from Eq. (5.6), $Y_\alpha(z, \chi_0)$ is approximated by the first two terms in the Taylor series expansion about the filtered value of χ_0, i.e.

$$Y_\alpha(z, \chi_0) \approx Y_\alpha(z, \widetilde{\chi}_0) + \left. \frac{\partial Y_\alpha}{\partial \chi_0} \right|_{\widetilde{\chi}_0} (\chi_0 - \widetilde{\chi}_0) . \tag{5.8}$$

Moreover, it is taken into account that

$$\int_{\chi_0^{min}}^{\chi_0^{max}} F(\chi_0) \, d\chi_0 = 1. \tag{5.9}$$

The fdf of the mixture fraction, $F(z)$, is approximated by a β-distribution (cf. Eq. (4.28)) depending on the filtered mass fraction $\widetilde{z}$ and its subgrid variance $(z^2)_{sg}$. The filtered mixture fraction is known during the LES by solving its transport equation, Eq. (5.1), while its subgrid variance and the mass-weighted filtered scalar dissipation rate, $\widetilde{\chi}_0$ are modeled (see Sect. 5.2.1). During the LES, $\widetilde{\chi}_0$ is equated to the actual dissipation rate in the flow, i.e. $\widetilde{\chi}_0 = \widetilde{\chi}$. As it is convenient to interpolate from pre-calculated tables, $\overline{\omega}$ and $\widetilde{Y}_\alpha$ are tabulated in the coordinates $\widetilde{z}$, $(z^2)_{sg}$ and $\widetilde{\chi}_0$ which means that the integrations, Eq. (5.7), are done before the actual LES simulation.

5.3 The flamelet database

Instead of computing the 1D flamelets in mixture fraction space [33, 128], they are computed in physical space (coordinate x) with zero velocity [131, 132]. Assuming constant pressure, which is justified by the low Mach number in the DNS and LES computations, the following 1D transport equations are obtained from the complete conservation equations for temperature, species mass fractions and a passive scalar:

$$\frac{\partial T}{\partial t} = \frac{1}{\rho c_v}\left[-\frac{\partial q_x}{\partial x} - \sum_\alpha \left(h_\alpha - \frac{\mathcal{R}}{W_\alpha}T\right)\left(-\frac{\partial \rho Y V_{\alpha x}}{\partial x} + \omega_\alpha\right)\right] \tag{5.10}$$

$$\frac{\partial Y_\alpha}{\partial t} = \frac{1}{\rho}\left(-\frac{\partial}{\partial x}\left(\rho Y_\alpha V_{\alpha x}\right) + \omega_\alpha\right) \tag{5.11}$$

$$\frac{\partial z}{\partial t} = \frac{1}{\rho}\frac{\partial}{\partial x}\left(\alpha_z \rho \frac{\partial z}{\partial x}\right) \tag{5.12}$$

The passive scalar z is the mixture fraction. Solving transport equations for this quantity and the species mass fractions, Y_α, simultaneously, allows to establish relations between z and Y_α which are later used for the tabulation of the flamelets. An alternative to solving the transport equation of z would be to compute z by its definition based on species mass fractions (see below: Eqs. (5.26) and (5.27)). However, as Pierce & Moin (2001) emphasize, this approach is equivalent to integrating Eq. (5.12) with an initial mixture fraction distribution given by Eq. (5.27).

The species diffusion flux $Y_\alpha V_{\alpha x}$ and the heat flux vector q_x in Eqs. (5.10) and (5.11) are evaluated as described in Sect. 5.3.2. either with detailed or with simplified diffusion.

The computation of the mixture fraction diffusivity, α_z is further detailed in Sect. 5.3.3.

5.3.1 Detailed reaction scheme and Arrhenius chemistry

The chemical production rates ω_α in Eqs. (5.10) and (5.11) are computed with full Arrhenius chemistry using the reaction scheme of Miller et al. [113] that is given in table 5.1. It involves 9 species, O_2, H_2, H_2O, N_2, O, H, OH, H_2O_2 and HO_2 and 19 elemental reactions. The same reaction scheme has been used by de Charantenay & Ern [40] for various premixed 2D H_2/O_2 flames with detailed diffusion.

Each elementary reaction in Table 5.1 can be written in the form

$$\sum_\alpha \nu'_{\alpha,irct} S_\alpha \leftrightarrow \sum_\alpha \nu''_{\alpha,irct} S_\alpha \tag{5.13}$$

with S_α denoting the chemical symbol of species α. For each reaction $irct$, mass conservation can be written with the help of the stoichiometric coefficients of the forward reaction, $\nu'_{\alpha,irct}$, and of the backward reaction, $\nu''_{\alpha,irct}$:

$$\sum_\alpha \nu'_{\alpha,irct} W_\alpha = \sum_\alpha \nu''_{\alpha,irct} W_\alpha \tag{5.14}$$

This can also be written as

$$\sum_{\alpha} \nu_{\alpha,irct} W_{\alpha} = 0 \tag{5.15}$$

with $\nu_{\alpha,irct} = \nu'_{\alpha,irct} - \nu''_{\alpha,irct}$. The mass reaction rate of species α that appears in Eqs. (5.10) and (5.11) is given by

$$\omega_{\alpha} = W_{\alpha} \sum_{irct} \nu_{\alpha,irct} w_{irct}. \tag{5.16}$$

It is the sum of contributions from the elementary reactions with the progress rates w_{irct},

$$w_{irct} = k_{f,irct} \Pi_{\alpha} C_{\alpha}^{\nu'_{\alpha,irct}} - k_{b,irct} \Pi_{\alpha} C_{\alpha}^{\nu''_{\alpha,irct}}. \tag{5.17}$$

The molar concentration of species α is denoted by $C_{\alpha} = \rho Y_{\alpha}/W_{\alpha}$ and the forward and backward constants of reaction $irct$ by $k_{f,irct}$ and $k_{b,irct}$. The forward constant of each elementary reaction is computed with the help of a semi-empirical Arrhenius law in the form

$$k_{f,irct} = A_{irct} T^{\beta_{irct}} \exp\left(-\frac{E_{irct}}{\mathcal{R}T}\right). \tag{5.18}$$

Table 5.1: Reaction scheme for H_2/O_2 combustion with pre-exponential factors A, temperature-dependence coefficients β and activation energies E [113]

	Reaction	A in (cm, mol, s)	β	E in cal/mol
(1)	$H_2 + O_2 \leftrightarrow 2OH$	$1.70 \cdot 10^{13}$	0.00	47780
(2)	$H_2 + OH \leftrightarrow H_2O + H$	$1.17 \cdot 10^{9}$	1.30	3626
(3)	$H + O_2 \leftrightarrow OH + O$	$2.00 \cdot 10^{14}$	0.00	16800
(4)	$O + H_2 \leftrightarrow OH + H$	$1.80 \cdot 10^{10}$	1.00	8826
(5)	$H + O_2 + M \leftrightarrow HO_2 + M$	$2.10 \cdot 10^{18}$	-1.00	0
	$H_2O/21/H_2/3.3/O_2/0.0/N_2/0.0$			
(6)	$H + O_2 + O_2 \leftrightarrow HO_2 + O_2$	$6.70 \cdot 10^{19}$	-1.42	0
(7)	$H + O_2 + N_2 \leftrightarrow HO_2 + N_2$	$6.70 \cdot 10^{19}$	-1.42	0
(8)	$OH + HO_2 \leftrightarrow H_2O + O_2$	$5.00 \cdot 10^{13}$	0.00	1000
(9)	$H + HO_2 \leftrightarrow 2OH$	$2.50 \cdot 10^{14}$	0.00	1900
(10)	$O + HO_2 \leftrightarrow O_2 + OH$	$4.80 \cdot 10^{13}$	0.00	1000
(11)	$2OH \leftrightarrow O + H_2O$	$6.00 \cdot 10^{8}$	1.30	0
(12)	$H_2 + M \leftrightarrow H + H + M$	$2.23 \cdot 10^{12}$	0.50	92600
	$H_2O/6/H/2/H_2/3$			
(13)	$O_2 + M \leftrightarrow 2O + M$	$1.85 \cdot 10^{11}$	0.50	95560
(14)	$H + OH + M \leftrightarrow H_2O + M$	$7.50 \cdot 10^{23}$	-2.60	0
	$H_2O/20$			
(15)	$H + HO_2 \leftrightarrow H_2 + O_2$	$2.50 \cdot 10^{13}$	0.00	700
(16)	$HO_2 + HO_2 \leftrightarrow H_2O_2 + O_2$	$2.00 \cdot 10^{12}$	0.00	0
(17)	$H_2O_2 + M \leftrightarrow OH + OH + M$	$1.30 \cdot 10^{17}$	0.00	45500
(18)	$H_2O_2 + H \leftrightarrow HO_2 + H_2$	$1.60 \cdot 10^{12}$	0.00	3800
(19)	$H_2O_2 + OH \leftrightarrow H_2O + HO_2$	$1.00 \cdot 10^{13}$	0.00	1800

Forward and backward coefficients of each reaction are linked by the equilibrium constant $K_{e,irct}$,

$$K_{e,irct} = \frac{k_{f,irct}}{k_{b,irct}}, \tag{5.19}$$

which is determined by [142]

$$K_{e,irct} = \left(\frac{p^0}{\mathcal{R}T}\right)^{\sum_\alpha \nu_{\alpha,irct}} \exp\left[\frac{\Delta\mathcal{S}^0_{irct}}{\mathcal{R}} - \frac{\Delta\mathcal{H}^0_{irct}}{\mathcal{R}T}\right] \tag{5.20}$$

with the entropy and enthalpy changes, $\Delta\mathcal{S}^0_{irct}$ and $\Delta\mathcal{H}^0_{irct}$, during reaction $irct$ at reference pressure $p^0 = 1013.25hPa$. In some reactions, like in reaction (5) in Table 5.1, a third compound denoted by M is involved. Elements present in the gas mixture act as such a third compound, the effective concentration of which is computed by

$$C_{M,irct} = \sum_\alpha \gamma_{\alpha,irct} C_\alpha. \tag{5.21}$$

The pre-factors $\gamma_{\alpha,irct}$ are mostly 1. Exceptions are given in Table 5.1 in the second line of the respective reaction, e.g. $\gamma_{H2O,5} = 21$. The progress of a reaction with a third compound involved is computed by

$$w_{irct} = C_{M,irct} \cdot \left(k_{f,irct}\Pi_\alpha C_\alpha^{\nu'_{\alpha,irct}} - k_{b,irct}\Pi_\alpha C_\alpha^{\nu''_{\alpha,irct}}\right). \tag{5.22}$$

5.3.2 Computation of detailed diffusion fluxes and of heat flux by EGlib

To establish the flamelet databases, detailed transport properties, and in particular the diffusion fluxes $Y_\alpha V_{\alpha x}$ and the heat flux q_x, are evaluated with the help of subroutines from the library EGlib [54]. EGlib uses an iterative method to obtain an approximate solution for the linear equations of the transport coefficients derived from kinetic theory. Truncation then provides, at a moderate computational cost, approximate expressions of desired accuracy for the transport coefficients. This is in contrast to the two 'traditional' approaches for evaluating transport coefficients, namely the direct numerical inversion of the linear equations, which is computationally expensive, and the use of empirical average expressions. The latter often leads to poorly accurate transport coefficients.

EGlib was first applied to laminar flames [55, 56], and it was shown that the accuracy of the transport coefficients severely influenced the flame properties. Later, de Charentenay and Ern [40] used it for various premixed 2D H_2/O_2 flames and found local modifications of turbulent flame properties by multicomponent transport that were much larger than those observed for laminar flames. In particular, the propagation velocity and the stretch in regions where the flame front experiences strong curvature effects were affected. Even though the impact on global flame properties was shown to be only moderate because of the smoothening induced by turbulent fluctuations, these authors concluded that for some types of flames (highly curved or with quenching phenomena), multicomponent transport plays a sufficiently relevant role to be included in accurate simulations.

In this chapter, results of computations performed with the detailed diffusion description given by Eqs. (2.8) to (2.10) are compared with those using a simplified description of diffusion and heat flux. In the simplified description, the thermodiffusive effects, namely the Soret and Dufour

effects, are neglected and the Hirschfelder-Curtiss approximation [74] for the species diffusion coefficients in the mixture is used. The simplified diffusion flux vector reads (in 3D)

$$Y_\alpha V_{\alpha i} = -\sum_\beta \mathcal{D}_{\alpha\beta,appr} d_{\beta i} \tag{5.23}$$

with the approximate flux diffusion matrix based on the diffusion coefficient of species α in the mixture, $D_{\alpha,m}$:

$$D_{\alpha,m} = \frac{\sum_{\beta\neq\alpha} Y_\beta}{\sum_{\beta\neq\alpha} X_\beta / D_{\alpha\beta}}. \tag{5.24}$$

As each species has just one diffusion coefficient in the mixture, which depends of course on the local conditions, namely temperature and species' composition, no cross-diffusion effects are taken into account. The use of $D_{\alpha,m}$, which is computed with the help of EGlib [53, 55], corresponds to the so-called Hirschfelder-Curtiss approximation [74] of scalar diffusion.

The simplified description of the heat flux is

$$q_i = \sum_\alpha \rho h_\alpha Y_\alpha V_{\alpha i} - \lambda \frac{\partial T}{\partial x_i} \tag{5.25}$$

with the thermal conductivity λ, which is also given by EGlib.

5.3.3 The mixture fraction and its diffusivity

Following Pierce & Moin [131, 132], the mixture fraction z is defined as an average mass fraction by combining the conserved elemental (atomic) mass fractions. The elemental mass fractions a_γ are given by

$$a_\gamma = \sum_\alpha Y_\alpha N_{\alpha\gamma} A_\gamma / W_\alpha, \tag{5.26}$$

where $N_{\alpha\gamma}$ is the number of γ atoms in each molecule of species α. A_γ are atomic weights and W_α molecular weights. After summing the elemental mass fractions and normalizing the result, the average mixture fraction is given by

$$z = \frac{\sum_\gamma |a_\gamma - a_{\gamma 1}|}{\sum_\gamma |a_{\gamma 2} - a_{\gamma 1}|}, \tag{5.27}$$

where $a_{\gamma 1}$ and $a_{\gamma 2}$ are the elemental mass fractions in the oxidizer and fuel streams, respectively. Elemental diffusive fluxes $a_{\gamma x}$ can be combined by

$$a_{\gamma x} = \sum_\alpha \rho Y_\alpha V_{\alpha x} N_{\alpha\gamma} A_\gamma / W_\alpha. \tag{5.28}$$

Finally, α_z is computed from

$$\rho \alpha_z \left| \frac{\partial z}{\partial x} \right| = \frac{\sum_\gamma |a_{\gamma x}|}{\sum_\gamma |a_{\gamma 2} - a_{\gamma 1}|}. \tag{5.29}$$

An analogous 3D expression, which is used to compute α_z during the LES, is easily obtained from Eq. (5.29).

The particular definition of the mixture fraction by Eq. (5.27), which is not only used for computing the flamelet database but also in the LES, is one feature that distinguishes the present flamelet computations from others, for example from Pitsch & Peters [138], where the mixture fraction is not related directly to any combination of the reactive scalars, but defined from the solution of a conservation equation with an arbitrary diffusion coefficient D_z and appropriate boundary conditions. Even though this approach allows to incorporate detailed diffusion effects into the flamelet database, while maintaining consistency in the mixture fraction evolution equation, it relies on the assumption that there exists a mixture fraction that is a conserved scalar and eliminates detailed diffusion by having the diffusion coefficient D_z. That the existence of such a mixture fraction is questionable has been shown for example by Sutherland [179]. Quantifications of detailed diffusion in experiments of turbulent, non-premixed jet flames of H_2 and CO_2 [170] were also performed with the help of elemental mixture fractions, the definition of which uses elemental mass fractions similar to Eq. (5.27), but with one particular element, the mixture fraction is based on. Other types of elemental mixture fractions were used for example by [5, 11]. However, the quantification of detailed diffusion that these mixture fractions provide is not unique as shown by [179] but depends essentially on the element, the elemental mixture fraction is based on. Contrarily, the present formulation, Eq. (5.27), has the advantage not to depend on such an explicit choice.

5.3.4 Steady flamelet solutions

After initialization with the solution from infinitely fast chemistry, Eqs. (5.10) to (5.12) are integrated with sixth-order central schemes in space and a third-order Runge-Kutta scheme in time up to the attainment of a steady state. The distinction in scalar dissipation rate between the single flamelets is caused by the domain length L. Dirichlet boundary conditions are imposed at the ends of the domain. They correspond to the free stream values of the shear layer computation. It can be seen from Eq. (5.12) that for $\partial z/\partial t = 0$ each steady flamelet solution is associated with a single, constant value of the mixture fraction diffusion:

$$\psi = \rho\alpha_z \frac{\partial z}{\partial x} \tag{5.30}$$

Using the definition of the scalar dissipation rate, Eq. (5.5), the relation between ψ and χ is given by

$$\rho\chi = \frac{\psi^2}{\rho\alpha_z} \tag{5.31}$$

from which we can define an average scalar dissipation rate for each flamelet,

$$\chi_0 = \frac{\psi}{\rho_0 L}, \tag{5.32}$$

by assuming $\psi \approx \rho_0\alpha_z/L$, which implies an averaged scalar gradient of $1/L$ and an averaged density ρ_0.

As the mixture fraction z is a monotonic function of the spatial coordinate x, the inverse function $x\,(z)$ can be obtained and used to remap all flamelet variables to the mixture fraction z. This is done in Figs. 5.1 to 5.4 for the mass fractions of H_2, H_2O, OH and the temperature for various flamelets which differ by a variation of the domain length L. Especially in Figs. 5.1 and 5.4,

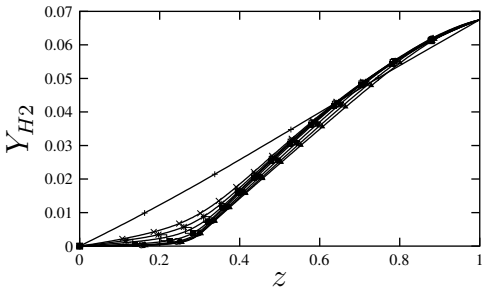

Figure 5.1: Flamelet profiles of Y_{H2} with different χ_0, mapped to mixture fraction space, $+$: $\chi_0 = 146.4s^{-1}$, $\times$: $\chi_0 = 173.5$, $*$: $\chi_0 = 135.7$, $\square$: $\chi_0 = 87.1$, $\blacksquare$: $\chi_0 = 35.6$, $\circ$: $\chi_0 = 7.7$, $\bullet$: $\chi_0 = 3.4$, $\triangle$: $\chi_0 = 1.9$, $\blacktriangle$: $\chi_0 = 1.2$

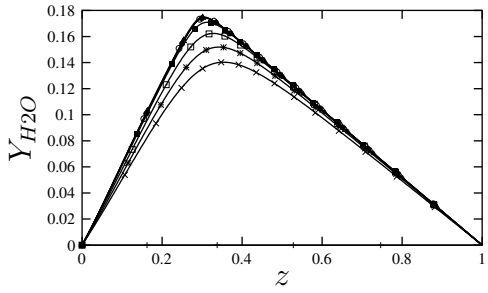

Figure 5.2: Flamelet profiles of Y_{H2O} with different χ_0, mapped to mixture fraction space, symbols as in Fig. 5.1

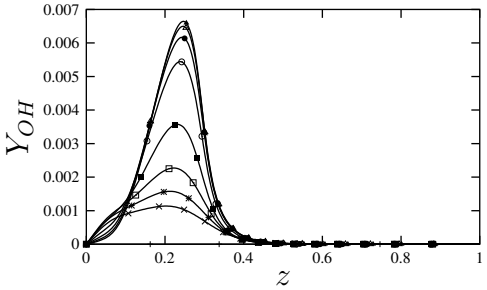

Figure 5.3: Flamelet profiles of Y_{OH} with different χ_0, mapped to mixture fraction space, symbols as in Fig. 5.1

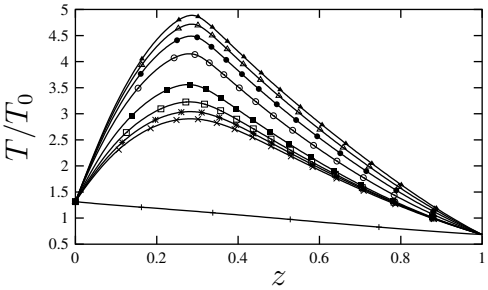

Figure 5.4: Flamelet profiles of T/T_0 with different χ_0, mapped to mixture fraction space, symbols as in Fig. 5.1

a flamelet with χ_0 higher than the extinction limit is clearly visible. It has a lower temperature profile than the others, a linear profile for Y_{H2} and no H_2O and OH. Within the flamelet library, we use the assumption of pure mixing between the fuel and the oxidizer stream for all profiles with χ_0 larger than the extinction limit. Fig. 5.1 shows that for $\chi \rightarrow 0$, the profile of Y_{H2} approaches asymptotically a profile that would be expected for infinitely fast chemistry, i.e. one with $Y_{H2} \approx 0$ for values of z smaller than the stoichiometric value (between $z = 0.2$ and $z = 0.3$ for the flamelets depending on the overlapping of the oxygen and the hydrogen mass fraction profiles) and a linear regime for larger values of z. The maximum values of Y_{H2O}, Y_{OH} and T/T_0 increase with decreasing χ_0.

The final flamelet library consists of tables with the relationships

$$Y_\alpha = Y_\alpha\left(z, \chi_0\right), \quad \omega = \omega\left(z, \chi_0\right). \tag{5.33}$$

An example is shown in Fig. 5.5. With respect to the asymptotic behaviour for $\chi_0 \rightarrow 0$ visible from the flamelet quantities (Figs. 5.2 to 5.4), we use the profile of the flamelet with the lowest χ_0 that converged within reasonable time for all smaller values of χ_0.

5.4 Test cases

The configuration of the mixing layers that are computed and analyzed in this chapter corresponds to the one of case inf-0.15 in Chapter 3. It is described in detail in Sect. 3.3. The resolution is

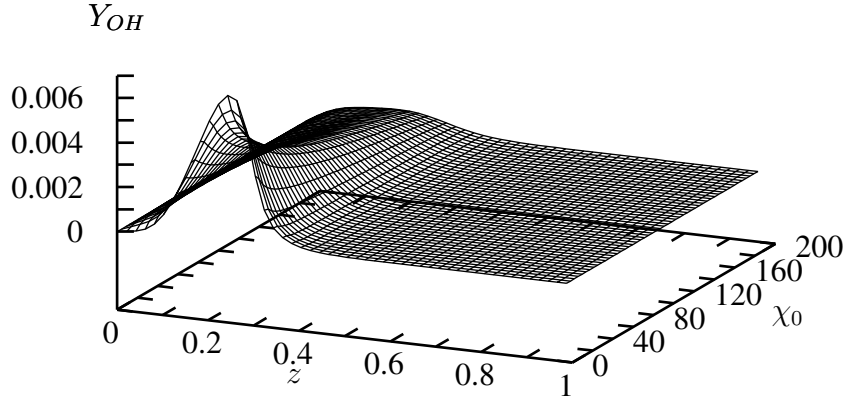

Figure 5.5: Tabulation of Y_{OH} in the coordinates χ_0 in $[s^{-1}]$ and z

the same as for the case LES-inf-0.15-4 in Chapter 4: 192 points in the streamwise direction, 48 in the spanwise direction and 108 points in the direction of the mean shear. The mixing layer is simulated twice: One time using a flamelet database computed with diffusion fluxes $YV_{\alpha x}$ and a heat flux q_x including Soret and Dufour effect, as well as multicomponent diffusion coefficients, $D_{\alpha\beta}$ (cf. Eqs. (2.8) to (2.10)) and another time without these effects, but with a Hirschfelder-Curtiss approximation [74] for the diffusion coefficients (cf. Eqs. (5.23) to (5.25)). The first database is referred to as dd (detailed diffusion) in the following and the second one as sd (simplified diffusion). It is evident that the diffusion fluxes and the heat fluxes in the LES (denoted by LES-dd and LES-sd) have to be computed with the same diffusion model as used in the corresponding flamelet database.

To be consistent with the LES with infinitely fast chemistry in Chapter 4, the LES with finite-rate chemistry are initialized by turbulent flow fields from the DNS with infinitely fast chemical reactions, which are interpolated onto the coarser LES grid and filtered with a tophat filter, the filter width of which is the LES grid spacing. This is done at a non-dimensional time $\tau_\omega = 290$ and therefore well before the beginning of the self-similar states (cf. Sct. 3.4.2).

The constants in the gradient models for $\left(z^2\right)_{sg}$ and $\widetilde{\chi}$ are set to the same values that have been found suitable during a priori tests with infinitely fast chemistry (cf. Sect. 4.3), namely $C_z^{GR} = 0.26$ and $C_\chi^{GR} = 0.06$.

5.5 Results and analysis

5.5.1 Flamelets with detailed and simplified diffusion

In this section, steady flamelet profiles computed with the flamelet equations (5.10) to (5.12) and different diffusion approximations (sd and dd) are compared to each other.

Figures 5.6 to 5.9 show a comparison of the source term, two species mass fractions and the temperature at two levels of χ_0. The source term ω of the dd flamelet is bigger than the source

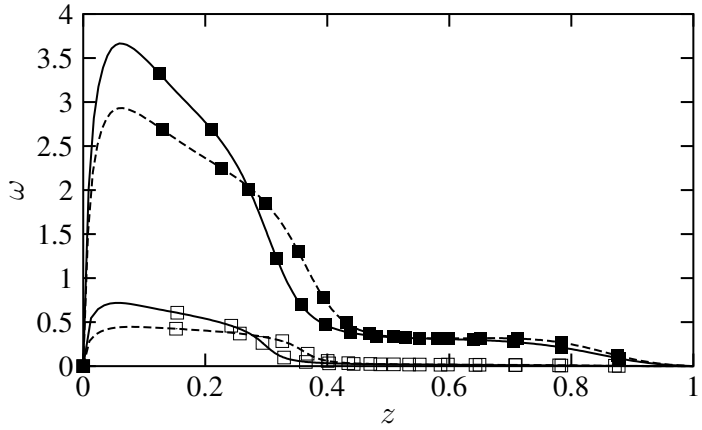

Figure 5.6: Flamelet profiles of ω in $[10^9 \cdot Jm^{-3}s^{-1}]$, ■, dashed: sd, $\chi = 88.4s^{-1}$, ■, solid: dd, $\chi = 87.1s^{-1}$, □, dashed: sd, $\chi = 7.7s^{-1}$, □, solid: dd, $\chi = 7.7s^{-1}$

term of the corresponding sd flamelet for mixture fraction values smaller than $z \approx 0.3$. ω is directly related to the diffusion fluxes by

$$\omega = -\sum_{\alpha} h_\alpha \omega_\alpha = -\sum_{\alpha} h_\alpha \frac{\partial}{\partial x} \left(\rho Y_\alpha V_{\alpha x}\right), \tag{5.34}$$

which becomes evident when setting the RHS of Eq. (5.11) to zero for the stationary state. Therefore, differences in the diffusion fluxes directly imply different source terms. An analytical determination of the location of the maximum for the source term in z-space is not possible due to the complicated relation between the diffusion fluxes, the mixture fraction and its diffusion coefficient α_z by Eq. (5.29). It would have been a welcome mathematical proof for the fact that

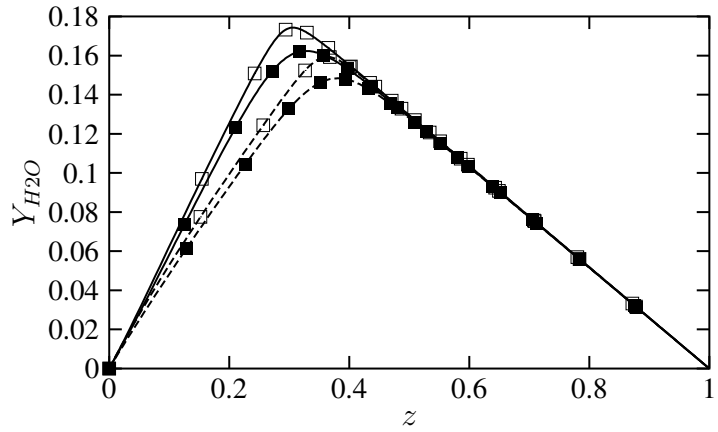

Figure 5.7: Flamelet profiles of Y_{H2O}, lines and symbols as in Fig. 5.6

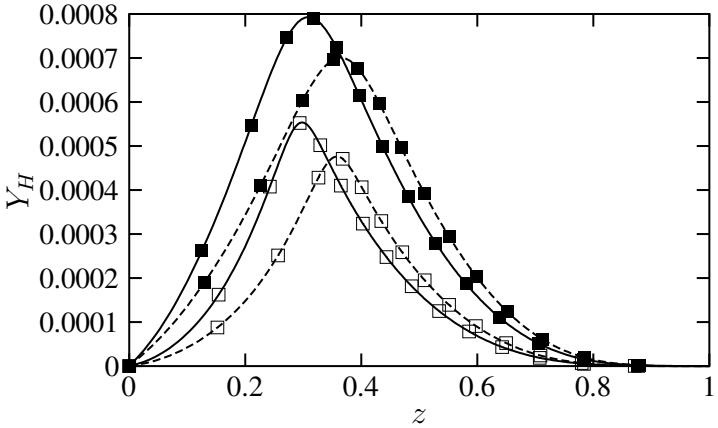

Figure 5.8: Flamelet profiles of Y_H, lines and symbols as in Fig. 5.6

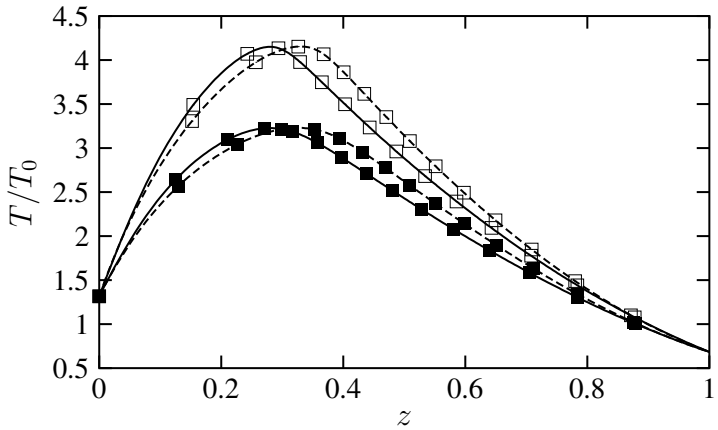

Figure 5.9: Flamelet profiles of T/T_0, lines and symbols as in Fig. 5.6

the peak position of ω is located to the left of the stoichiometric mixture fraction as seen in Fig. 5.6.

In agreement with the behaviour of the source term, the values of Y_H, Y_{H2O} and the temperature for flamelets with sd are lower than the ones for flamelets with dd for small values of z. For higher values of z, there are higher temperatures and there is more H for the flamelets with simplified diffusion. The mass fraction of H_2O is nearly the same for dd and sd in the fuel-rich region. The reason for this behaviour is that the Soret and Dufour effects on a species (here H_2O) become particularly intense where the temperature gradient is high (here on the oxygen-rich side). While the location of the peak value of ω is rather uninfluenced by the diffusion model, it is shifted to higher values for sd than for dd in the other profiles (Y_{H2O}, Y_H and T/T_0). Similar to the source term, the peak values of Y_H and Y_{H2O} are higher in the dd flamelets. The peak value of the temperature, however, is nearly the same for dd and sd, but the peak is found at a different location.

A further difference between the two databases is found in the extinction limit. In dd, it is at a χ_0-value which is about 45% higher than the extinction value of sd ($\chi_{ext} = 192\ s^{-1}$ for dd vs. $\chi_{ext} = 132\ s^{-1}$ for sd for our configuration).

Other authors noted similar influences of different diffusion models but direct comparisons with our results are not possible as the other authors compare different models without thermal diffusion [138] or as their models involve assumptions of constant Lewis numbers or constant diffusivities [34, 119] which are avoided in our simulations.

5.5.2 Evaluation of the LES results

In this section, the LES method is validated by comparing LES with DNS results (from case DNS-inf-0.15 in Chapter 3) that have been interpolated to the coarser grid and filtered. Even if the DNS uses a simplified diffusion model (constant Schmidt number $Sc = 0.7$) and infinitely fast chemistry (one-step irreversible reaction), mean quantities related to the velocity field and large scale structures are expected to be similar. To confirm this, instantaneous fields and temporally and spatially averaged quantities from the DNS and the LES with dd and sd are compared with each other.

Figure 5.10 shows the one-dimensional spectrum of the streamwise velocity component, $u_1/\Delta u$, at the beginning of the self-similar state, with the normalized wavenumber k_1 in the streamwise

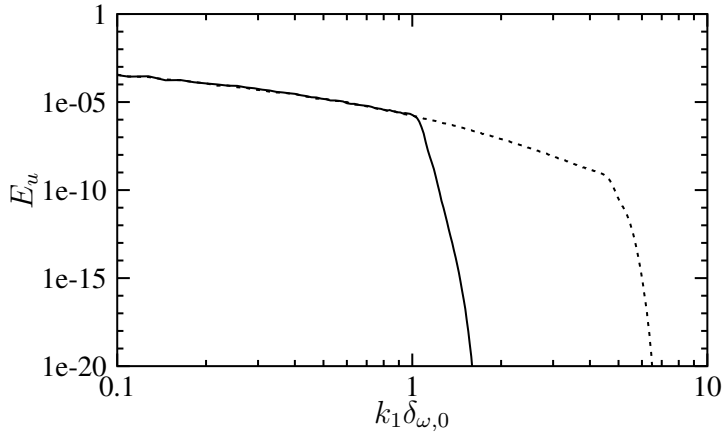

Figure 5.10: One-dimensional, streamwise spectrum of $u_1/\Delta u$ at the beginning of the self-similar state, solid: LES-dd, dotted: DNS

direction. In an ideal case, the spectra of the LES should follow the DNS spectra up to the cut-off wavenumber. This is the case for the spectrum shown in Fig. 5.10. No spurious accumulation of energy in the highest resolved wavenumbers is visible.

Figures 5.11 and 5.12 show profiles of the Favre averaged streamwise velocity and the turbulent kinetic energy, $k = 0.5\langle u_i u_i \rangle_f$. One can see that the LES and filtered DNS profiles match nearly perfectly which gives evidence that the LES method performs well. For other mean quantities, like temperature and density (Figs. 5.13 and 5.14), which are more related to the chemistry and therefore to the combustion model, differences between DNS, LES-dd and LES-sd arise:

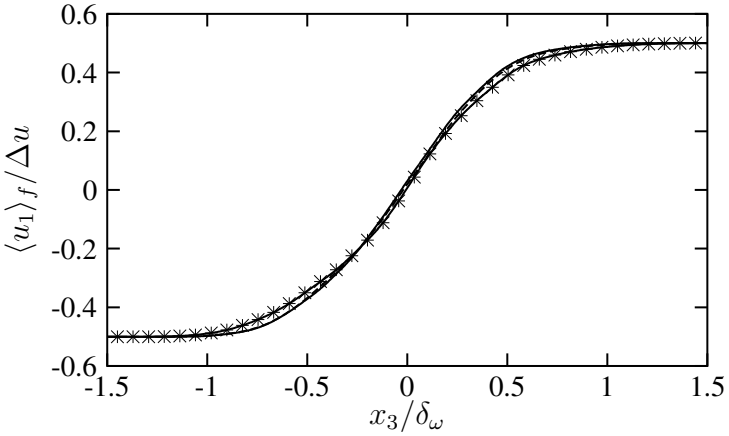

Figure 5.11: Favre averaged streamwise velocity, normalized by Δu, solid: LES-dd, dashed: LES-sd, solid with symbols: DNS interpolated to the LES grid and filtered

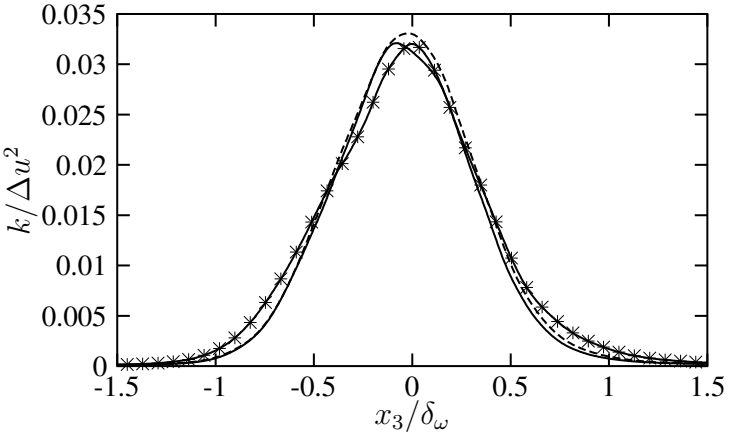

Figure 5.12: Turbulent kinetic energy, normalized by Δu^2, lines and symbols as in Fig. 5.11

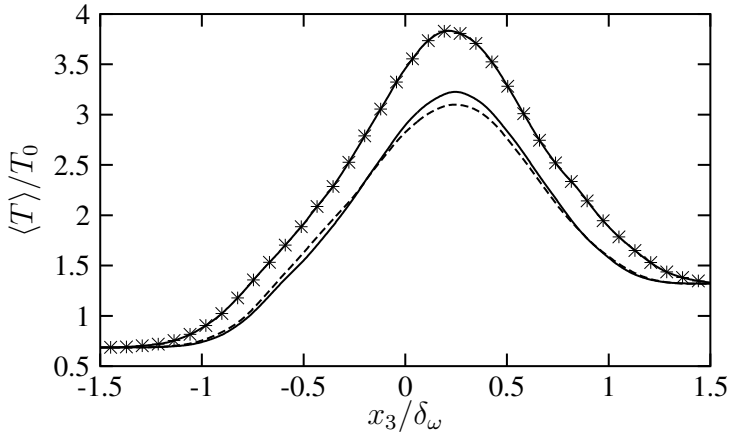

Figure 5.13: Averaged temperature, normalized by T_0, lines and symbols as in Fig. 5.11

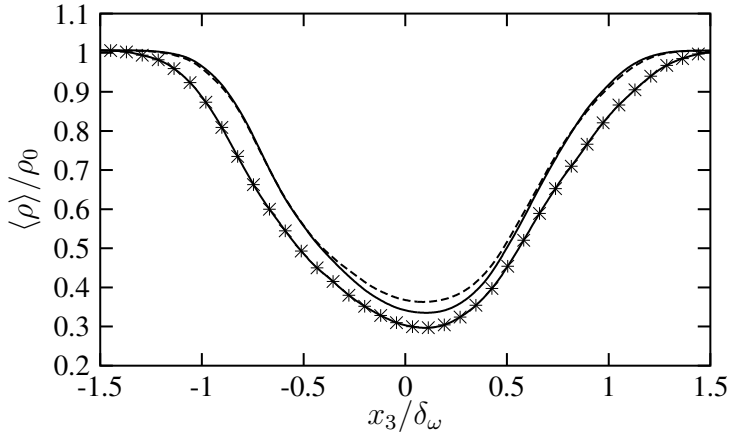

Figure 5.14: Averaged density, normalized by ρ_0, lines and symbols as in Fig. 5.11

Since the maximum temperatures in the flamelets with detailed chemistry at all χ_0 are lower than the maximum temperature resulting from infinitely fast chemistry (see Sect. 5.3), the peak of the averaged temperature is also higher for the DNS than for the LES and the minimum of the averaged density is consequently lower. The differences between the cases LES-dd and LES-sd come from differences in the flamelet temperature profiles, but also from differences in the extinction behaviour: The scalar dissipation rate at which extinction happens is lower for sd than for dd (see Sect. 5.5.1), why there is more colder, extinguished fluid in LES-sd. As a consequence, the averaged temperature in this LES is slightly lower and the density higher than in the case LES-dd.

Figure 5.15 presents instantaneous temperature fields LES-sd and the DNS. Such a comparison is quite illustrative, in particular since the LES has been started from an interpolated and filtered DNS field. Figure 5.15 shows that the large-scale structures in both cases are very similar, being successfully captured by the LES method. Nevertheless, differences are present. This can be seen

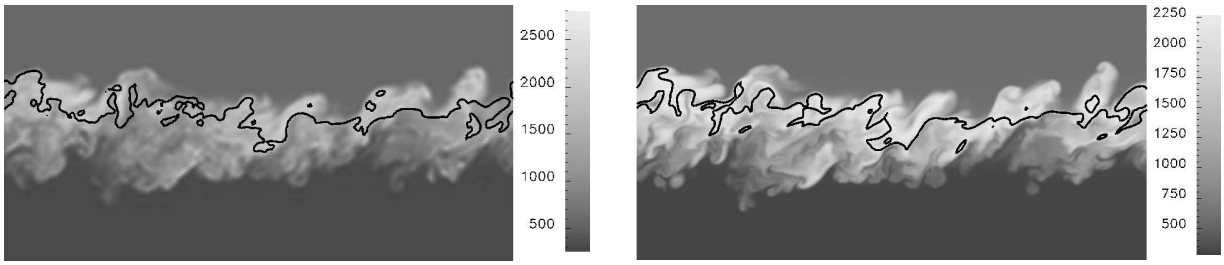

Figure 5.15: Instantaneous temperature fields at the beginning of the self-similar state, x_1-x_3-plane in the middle of the computational domain, left: LES-sd, right: DNS, black line: isoline at $z = 0.3$

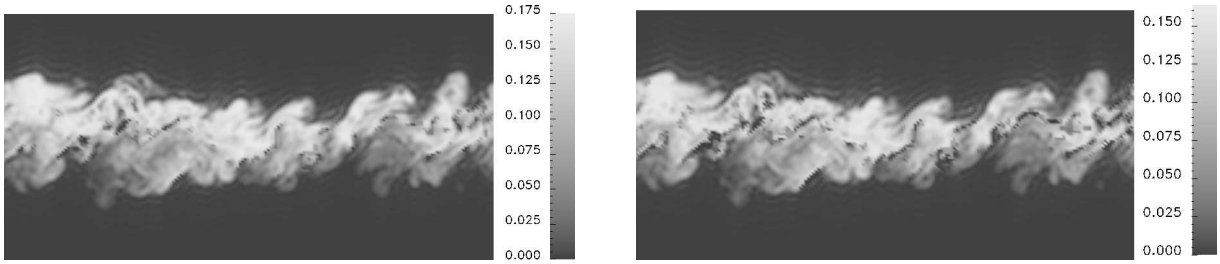

Figure 5.16: Instantaneous fields of Y_{H2O} at the beginning of the self-similar state, x_1-x_3-plane in the middle of the computational domain, left: LES-dd, right: LES-sd

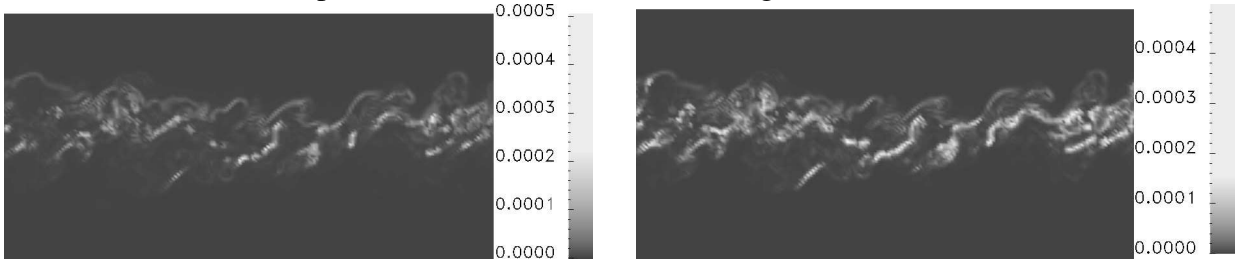

Figure 5.17: Instantaneous field of the scalar dissipation rate, normalized by $\Delta u/\delta_\omega$, at the beginning of the self-similar state, x_1-x_3-plane in the middle of the computational domain, left: LES-dd, right: LES-sd

for example by comparing the isoline at $z = 0.3$ which is the stoichiometric line and therefore the location of the flame and the highest temperature in the DNS. For this simulation, the isoline shows indentations on a finer scale than for the LES. Furthermore, the temperature field of the LES is more blurred than the one of the DNS due to the coarser resolution.

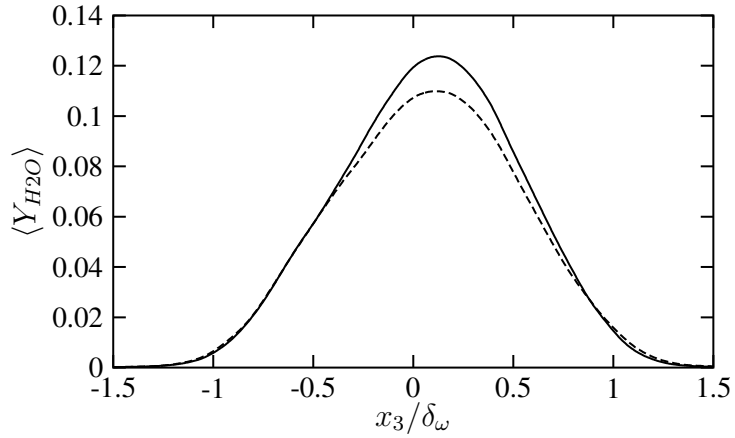

Figure 5.18: Averaged mass fraction of H_2O, solid: LES-dd, dashed: LES-sd

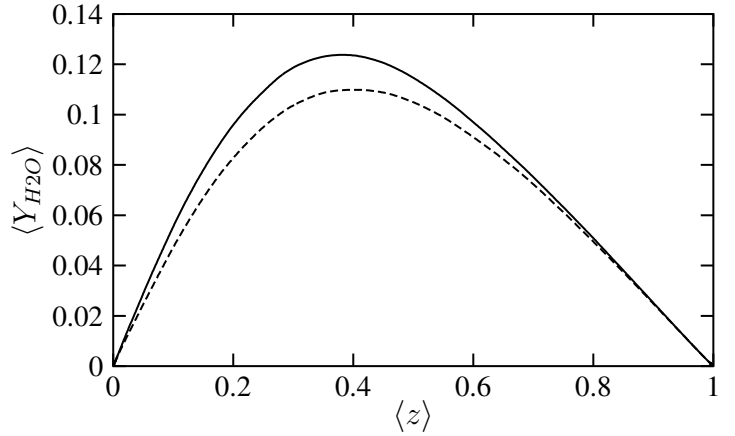

Figure 5.19: Averaged mass fraction of H_2O over $\langle z \rangle$, lines as in Fig. 5.18

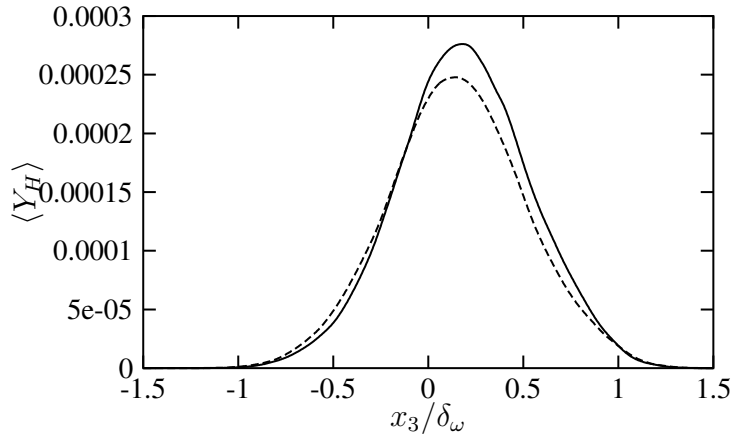

Figure 5.20: Averaged mass fraction of H, lines as in Fig. 5.18

An agreement concerning the size and shape of large-scale structures can also be observed when comparing instantaneous fields of LES-dd and LES-sd, e.g. $\widetilde{Y}_{H2O}$ in Fig. 5.16. The dark spots within the shear layer are regions where no reaction is taking place due to a scalar dissipation rate which is above the extinction limit. Figure 5.17 shows these scalar dissipation rates in white color, computed using the gradient model. The intermittent nature of $\widetilde{\chi}$ is clearly visible with the high scalar dissipation rates being organized in sheet-like structures. As the extinction limit for dd was found to be higher than that for sd, the white regions and dark spots are more pronounced in the right images of Figs. 5.17 and 5.16, respectively. This means that simple diffusion mechanisms promote extinction.

Regarding spatially and temporally averaged LES profiles, some features distinguishing dd from sd that have been detected when comparing the laminar flamelet profiles are still present. Others are smeared out by the turbulent fluctuations and the averaging procedure. One example, $\widetilde{Y}_{H2O}$, is shown in Fig. 5.18: The peak is lower for sd which is also the case for the flamelet profiles (Fig. 5.7), whereas a shift of the position of the peak can hardly be observed in Fig. 5.18. With $z = 1$ being located on the left-hand side of Fig. 5.20 (lower stream), the agreement of the two profiles on this side corresponds to the one on the right-hand side in Fig. 5.7. The shift of the peak is also weak when plotting the averaged mass fraction over the averaged mixture fraction as done in Fig. 5.19. These profiles have a rounder shape than the corresponding flamelet profiles. Statements similar to the ones for the profiles of Y_{H2O} (Fig. 5.18) can be made for the profiles of Y_H (Fig. 5.20). A lowering of the peak is also present here, while the shift visible in the flamelet profiles (Fig. 5.8) is smeared out to a great extent.

Differences between dd and sd are also evident when comparing higher central moments of the mass fractions, e.g. the variances in Figs. 5.21 and 5.22. These differences can be traced back to differences in the terms of the transport equation of $\langle \rho Y_\alpha''^2 \rangle$. This equation can be derived from the mass fraction transport equation

$$\frac{\partial Y_\alpha}{\partial t} + u_i \frac{\partial Y_\alpha}{\partial x_i} = \frac{1}{\rho} \left(-\frac{\partial}{\partial x_i} \left(\rho Y_\alpha V_{\alpha i} \right) + \omega_\alpha \right) \tag{5.35}$$

and the continuity equation by combining both linearily as described by their time derivatives:

$$\frac{\partial \rho Y_\alpha Y_\alpha}{\partial t} = 2 \rho Y_\alpha \frac{\partial Y_\alpha}{\partial t} + Y_\alpha^2 \frac{\partial \rho}{\partial t}. \tag{5.36}$$

A subsequent split-up into mean values and fluctuations, averaging and subtraction of the corresponding equations for the mean quantities results in the transport equation for $\langle \rho Y_\alpha''^2 \rangle$ in which

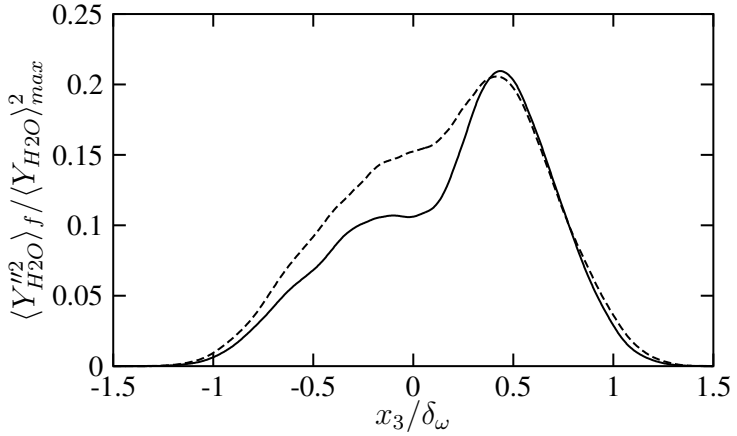

Figure 5.21: Variance of Y_{H2O}, normalized by $\langle Y_{H2O}\rangle^2_{max}$, lines as in Fig. 5.18

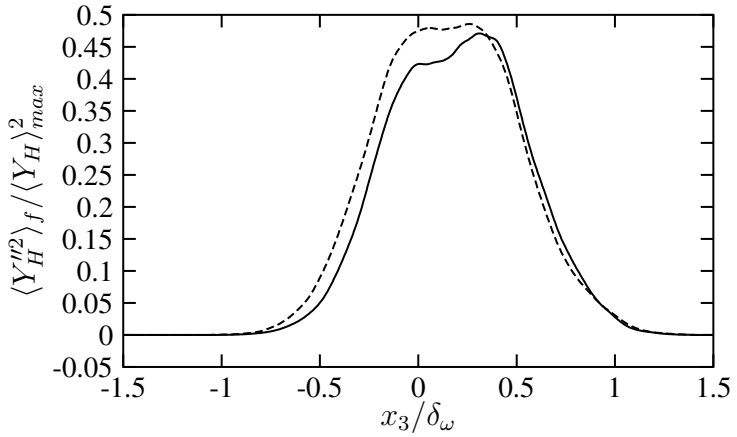

Figure 5.22: Variance of Y_H, normalized by $\langle Y_H\rangle^2_{max}$, lines as in Fig. 5.18

two terms depend explicitly on the diffusion fluxes: The diffusion term,

$$\Delta_\alpha = -2\frac{\partial}{\partial x_i}\langle \rho Y_\alpha Y''_\alpha V_{\alpha i}\rangle \tag{5.37}$$

and the dissipation rate,

$$\epsilon_\alpha = 2\langle \rho Y_\alpha V_{\alpha i}\frac{\partial Y''_\alpha}{\partial x_i}\rangle. \tag{5.38}$$

Results, which are not shown here, prove that the first one is negligible compared to the latter. The dissipation rate is presented for Y_{H2O} and Y_H in Figs. 5.23 and 5.24, respectively. It can be seen that the magnitude of the dissipation rate is larger for the simulations with sd. For H_2O, it is

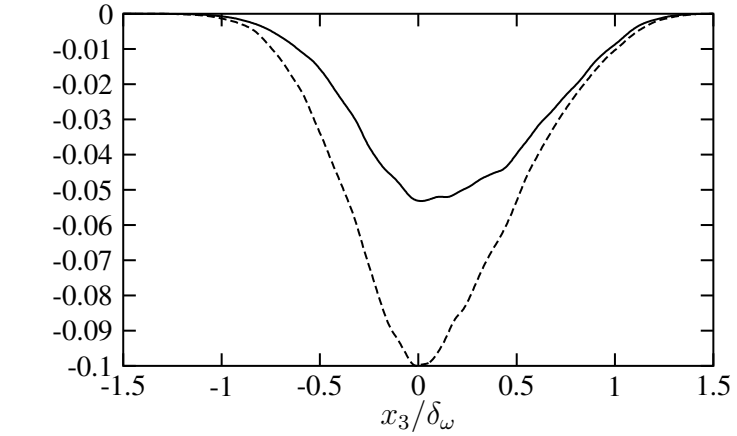

Figure 5.23: Dissipation term ϵ_{H2O}, Eq. (5.38), in the scalar variance transport equation of Y_{H2O}, normalized by $\rho_0 \Delta u \langle Y_{H2O}\rangle^2_{max}/\delta_\omega$, lines as in Fig. 5.18

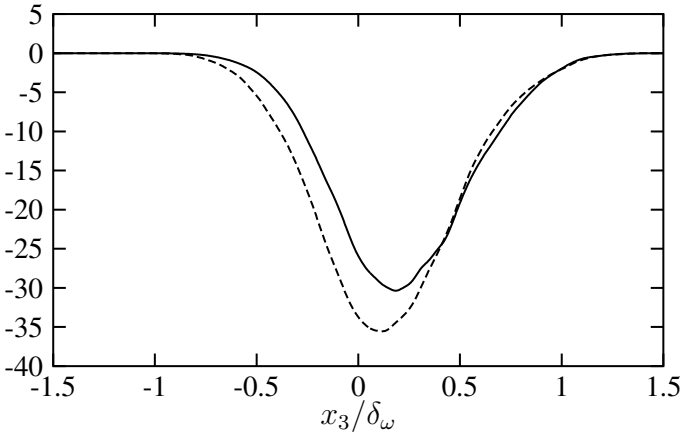

Figure 5.24: Dissipation term ϵ_H, Eq. (5.38), in the scalar variance transport equation of Y_H, normalized by $\rho_0 \Delta u \langle Y_H \rangle^2_{max}/\delta_\omega$, lines as in Fig. 5.18

even about double the size of that for the simulation with dd. This means that the flame dynamics is different due to the diffusion model. For the temperature variance, shown in Fig. 5.25, there is no such difference as for the mass fraction variances when results obtained with detailed (dd) and simplified diffusion mechanisms (sd) are compared. Correspondingly, the influence of the diffusion model on the terms in the transport equation for $\langle \rho T''^2 \rangle$ is expected to be small. This transport equation can be derived starting from the transport equation of the temperature

$$\frac{\partial T}{\partial t} + u_i \frac{\partial T}{\partial x_i} = \frac{1}{\rho c_v} \left[-p \frac{\partial u_i}{\partial x_i} + \phi - \frac{\partial q_i}{\partial x_i} - \sum_\alpha \left(h_\alpha - \frac{\mathcal{R}}{W_\alpha} T \right) \left(- \frac{\partial \rho Y V_{\alpha i}}{\partial x_i} + \omega_\alpha \right) \right]. \quad (5.39)$$

A linear combination of this equation with the continuity equation according to

$$\frac{\partial \rho T T}{\partial t} = 2 \rho T \frac{\partial T}{\partial t} + T^2 \frac{\partial \rho}{\partial t}, \quad (5.40)$$

and a similar procedure as described above leads to the transport equation for $\langle \rho T''^2 \rangle$. There are two terms in this equation that depend explicitly on the diffusion model: The term

$$T_q = -2 \langle \frac{T}{c_v} \frac{\partial q_i}{\partial x_i} \rangle - 2 \left(\langle T \rangle - 2 \langle T \rangle_f \right) \langle \frac{1}{c_v} \frac{\partial q_i}{\partial x_i} \rangle \quad (5.41)$$

that is related to the heat flux and the term

$$T_\alpha = 2 \langle \frac{T}{c_v} \sum_\alpha \left(h_\alpha - \frac{\mathcal{R}}{W_\alpha} T \right) \frac{\partial \rho Y_\alpha V_{\alpha i}}{\partial x_i} \rangle + 2 \left(\langle T \rangle - 2 \langle T \rangle_f \right) \langle \frac{1}{c_v} \sum_\alpha \left(h_\alpha - \frac{\mathcal{R}}{W_\alpha} T \right) \frac{\partial \rho Y_\alpha V_{\alpha i}}{\partial x_i} \rangle \quad (5.42)$$

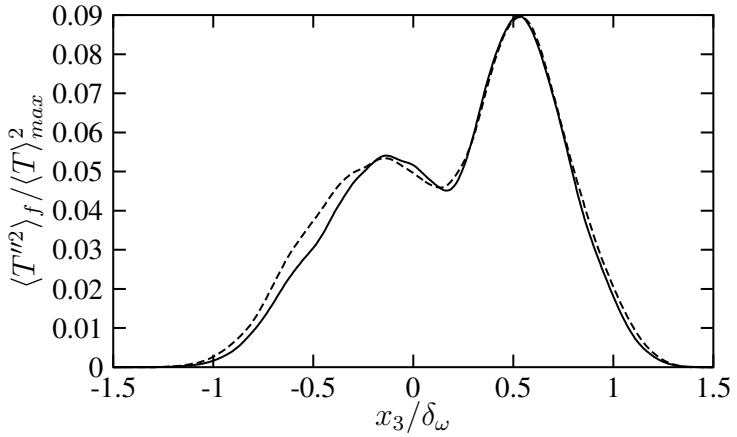

Figure 5.25: Variance of the temperature, $\langle T''^2 \rangle_f$, normalized by $\langle T \rangle^2_{max}$, lines as in Fig. 5.18

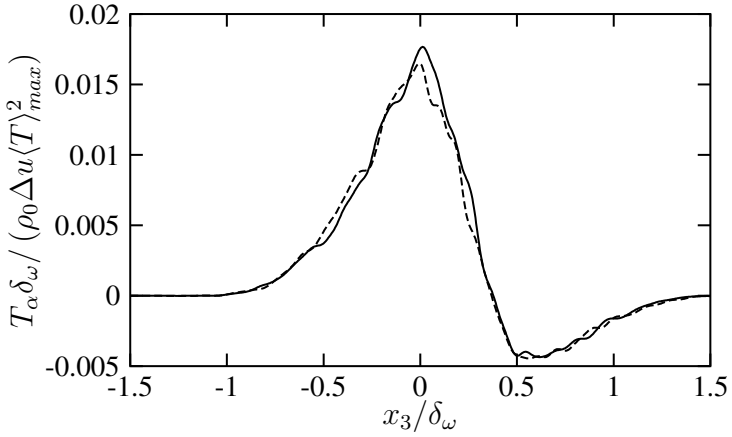

Figure 5.26: Term T_α, normalized by $\rho_0 \Delta u \langle T \rangle^2_{max}/\delta_\omega$, lines as in Fig. 5.18

that depends directly on the diffusion fluxes. T_q is small and need not be further discussed. T_α is shown in Fig. 5.26 and confirms the expectation that it is not of much importance for this term which of the two diffusion models is used.

Comparing the different sensitivities that $\langle Y''^2_\alpha \rangle$ and $\langle T''^2 \rangle$ and their transport equation terms reveal with respect to the diffusion models used, it can be concluded that a judgement whether detailed diffusion is important depends on the quantity under investigation and is not possible based on just arbitrary flow variables.

5.6 Summary and conclusions

LES of turbulent temporal shear layers with hydrogen combustion taking into account detailed chemical reactions and two different levels of diffusion approximation have been performed. The filtered heat release term has been determined with the help of pre-computed steady flamelet databases while all other subgrid-scale effects have been covered by an explicit filtering approach based on approximate deconvolution. A comparison with DNS data obtained using infinitely fast chemistry shows that this method is able to capture the large scale structures and averaged primitive flow variables successfully.

One flamelet database has been computed with multicomponent diffusion and the Soret and Dufour effects while in the other these effects have been neglected and a Hirschfelder-Curtiss approximation for the diffusion coefficients has been used. Both flamelet databases account for the extinguished state however with differences in the scalar dissipation rate at the extinction limit. This leads to differently pronounced extinguished zones in the LES. Further differences between the laminar flames resulting from different diffusion models have been found in the mass fraction, temperature and heat release profiles. Some of these differences are also present in the LES results, e.g. a lowering of the peak values of product and intermediate species mass fractions by simplified diffusion, while others are partly or completely smeared out by the turbulent fluctuations. Other quantities like the temperature variance proved to be rather insensitive towards the diffusion model. This is in contrast to the strong influence of the diffusion model on the scalar variances of the species mass fractions.

6 Conclusions and outlook

In this work, DNS and LES of inert and reacting, temporally evolving, turbulent shear layers have been performed. The DNS have been done at three different convective Mach numbers ($M_c = 0.15$, 0.7 and 1.1), corresponding to different levels of compressibility. The focus of their analysis has been on the consequences of compressibility and heat release for turbulent transport and scalar mixing. The emphasis of the LES study at low convective Mach number has been on the validation of a deconvolution approach in the form of a single explicit filtering step [106] as LES subgrid model and its performance in combination with different modeling approaches for the chemical source term. While the DNS have taken into account only infinitely fast chemistry, the LES have also included finite-rate chemistry: Multistep Arrhenius chemistry has been adopted in the framework of a flamelet model, allowing also to consider detailed diffusion mechanisms. In this context, results with two different approximations of the species diffusion fluxes and the heat flux vector have been compared: One LES has been performed with multicomponent diffusion and the Soret and Dufour effects, while in the other, these effects have been neglected and a Hirschfelder-Curtiss approximation for the diffusion coefficients has been used.

The relation of the present work to practical applications can be seen when considering, for example, ram- and scramjet engines. In both, the fuel, mostly hydrogen, is injected into the combustion chamber, and mixing layers develop between the fuel stream and the surrounding air flow. Thus, non-premixed combustion takes place, at subsonic speed in the ramjet and at supersonic speed in the scramjet. Since it is known that the combustion becomes less efficient the higher the Mach number is, a detailed understanding of the underlying mechanisms, in particular concerning the interaction of compressibility and heat release is required. The aim of this work has been to provide new insight into those phenomena.

Since there is a separate conclusion in every chapter, only the major highlights of the work are repeated in the following. They are assigned to the five basic questions that have been raised in the introduction (Chapter 1) to this thesis.

The first question was related to inert mixing layers at different M_c (Chapter 2):

- What are the effects of compressibility on turbulence and scalar mixing within inert mixing layers?

The answer can now be given as: With increasing M_c, the growth rate of the mixing layers reduces. This is related to the fact that the entrainment mechanism, i.e. the acquisition of external fluid, is hampered by compressibility, which has been shown with the help of fluid particles entering the mixing layer from outside. The smaller mixing layer growth rate is a consequence of reduced velocity fluctuations, i.e. reduced turbulent kinetic energy (TKE) and reduced Reynolds stresses. Their reduction with compressibility is traced back to a decrease of the production rate of the streamwise Reynolds stress and a reduction of the pressure-strain correlations. These

correlations steer the redistribution mechanism of turbulent fluctuating energy from the streamwise Reynolds stress component to the spanwise and transverse components. The pressure-strain correlations have been shown to play a crucial role concerning the stabilizing effect of compressibility. Changes in the fluctuating pressure field are mainly contributing to their reduction with increasing M_c. Instantaneous flow quantities, e.g. scalar (species mass fraction) distributions, further illustrate the consequences that compressibility has on the turbulence fluctuations: The fields are clearly smoothed, and an increase in the visible length scales of the wrinklings at the turbulence interface is observed. Smaller mass fraction variances are related to this. At low convective Mach number, more fluid parcels with scalar and vorticity values that are characteristic for freestream fluid can be found within the mixing layer, thus leading to higher intermittency. The engulfment events that are responsible for the presence of such fluid parcels become rarer when M_c rises. It has to be considered also that their contribution to the mixing layer growth rate is already small at low convective Mach numbers. Therefore, all inert mixing layers share the property that the acquisition of external fluid occurs mostly at the mixing layer boundaries. What increasing compressibility is concerned, it can be concluded that it is not benefitial for the turbulent mixing process.

The next two questions have been addressed in Chapter 3 of this work, which is dedicated to the infinitely fast reacting mixing layers at different M_c:

- How do the effects of compressibility change when heat release as a consequence of combustion is present?
- What effects does heat release have at different convective Mach numbers, i.e. different levels of compressibility?

The effects of compressibility on the momentum thickness growth rate and on most other statistical quantities (TKE, scalar variances etc.) of reacting mixing layers are not as strong as for the inert mixing layers. They are often masked by the much stronger consequences of heat release. Nevertheless, a reduction of mixing layer growth and turbulence activity is also observed when increasing M_c in the presence of heat release.

Heat release mostly acts in the same direction as compressibility, thus reducing turbulent fluctuations and mixing layer growth rates. The reduction is stronger at low M_c. Similar to compressibility, heat release has a smoothening effect on instantaneous flow fields, e.g. scalar fields and their isosurfaces. A closer investigation reveals that most consequences of heat release, in particular at low convective Mach number, can be traced back to the strong decrease in mean density as a consequence of the high temperatures in the vicinity of the flame sheets. Thus, these effects can be called 'direct mean density effects', which is not possible regarding compressibility effects. As for the reduction of the momentum thickness growth rate with compressibility, its reduction with heat release can also be related to a decrease of the pressure-strain correlations due to changes in the fluctuating pressure field. Solving the Poisson equation for the pressure fluctuations with the help of a Green function, after having checked the unimportance of acoustic effects, it has been shown that the reduction in mean density by heat release is mainly responsible for the reduction of the pressure fluctutations. Furthermore, the statement that acoustic effects are negligible turned out to be true at all convective Mach numbers under investigation. This has also been the case for the inert mixing layers. The explicit heat release term in the Poisson equation

for the pressure fluctuations when reaction takes place and affects density fluctuations, proved to play a rather minor role. Density and temperature fluctuations increase in the reacting mixing layers compared to the inert ones. These fluctuations are strongly correlated with each other and are mostly of entropic and not of acoustic nature. In accordance with a reduction of scalar fluctuations and intermittency, engulfment events, which have already been observed to be rather rare for the inert mixing layers, loose further importance in reacting layers. Fluid particles entering from the freestreams are carried along for a longer time at the edges of the mixing layer before they acquire vorticity and scalar concentrations that are typical of mixed fluid. This supports the general conclusion that heat release, similar to compressibility, is detrimental for mixing.

The next question concerns the LES of mixing layers at $M_c = 0.15$ which have been performed besides the DNS (Chapter 4 and 5):

- Is a realistic LES of reacting mixing layers possible with combinations of ADM (in the form of a single explicit filtering step) and different models for the chemical source term?

It has been shown that the implicit modeling of the subgrid terms by the filtering approach can be successfully combined with different models for the chemical source term taking into account an infinitely fast, irreversible global reaction or, alternatively, multistep Arrhenius chemistry with a flamelet approach. Direct comparisons with (interpolated and filtered) DNS data have revealed that both, flow dynamical quantities (e.g. mean velocity and turbulent kinetic energy), as well as thermodynamic quantities (e.g. mean density, mean temperature and their rms values) are captured well: While there is a good agreement between the infinitely fast reacting DNS and the LES with the same chemistry model, the LES with finite-rate chemistry shows differences which have been expected. They concern mainly thermodynamic quantities and manifest themselves in a lower mean temperature, higher mean density and lower temperature and density fluctuations.

The last question concerns the LES with finite-rate chemistry and different models for diffusion fluxes and heat flux (Chapter 5):

- What changes occur in mixing layers at low convective Mach number when taking into account finite-rate chemistry and different approximations for diffusion mechanisms?

Before analyzing the LES results with the two different diffusion models, the corresponding laminar flamelet profiles were compared with each other. Both flamelet databases account for the extinguished state however with differences in the value of the scalar dissipation rate at the extinction limit: The flamelets with simplified diffusion (no Soret and Dufour effects, Hirschfelder-Curtiss approximation for the diffusion coefficients) extinguished at a lower scalar dissipation rate than the ones with detailed diffusion (Soret and Dufour effects, multicomponent diffusion coefficients). Furthermore, differences mainly in peak values and peak positions of mass fraction, temperature and heat release profiles have been observed. Some of these differences are also present in the averaged LES data, e.g. a lowering of the peak values of product and intermediate species mass fractions by simplified diffusion, while others are partly or completely smeared out by the turbulent fluctuations. Some quantities like the temperature variance proved to be rather insensitive towards the diffusion model. The lower extinction limit of the flamelets with simplified diffusion has direct consequences for the corresponding LES, in which extinguished zones are larger and thus the mean density higher than in the LES with detailed diffusion.

One interesting possibility for future work, therefore, is to perform DNS of mixing layers with detailed chemistry and detailed diffusion. Since this results in the necessity of very small time steps when using an explicit time integration schemes, like the third-order Runge Kunge Kutta scheme in this work, the use of a semi-implicit scheme as given in [121] should be envisaged. With the results, a direct comparison between LES and DNS using the same detailed reaction mechanisms and diffusion models would be possible. Another topic that could be worked on in the future concerns an improvement of the flamelet model: Either an unsteady flamelet model [136] or the use of a progress variable [131] are imaginable. This would allow to capture unsteady phenomena like extinction and re-ignition processes, also with a view to more complicated configurations than the temporal mixing layer.

A Appendix: The characteristic form of the Navier-Stokes equations

A.1 The one-dimensional equations

Formulating the Navier-Stokes equations with the help of characteristics requires to write the transport equations for the pressure p, the velocity components u_i, the entropy s and the species mass fractions Y_α in a wave-like form. For a better understanding, this is first done for a one-dimensional case, involving only one velocity component, u.

The thermodynamic state of a gas, which consists only of one component or species is determined by two state variables. Therefore, one can write, for example for the pressure $p = p(\rho, s)$. However, if the gas is a mixture of various components, the mass fractions of the individual species are involved as well: $p = p(\rho, s, Y_\alpha)$. This leads to the total differential of the pressure:

$$dp = \mathcal{P}_\rho d\rho + \mathcal{P}_s ds + \sum_\alpha \mathcal{P}_\alpha dY_\alpha \tag{A.1}$$

with the partial derivatives as coefficients:

$$\mathcal{P}_\rho = \left(\frac{\partial p}{\partial \rho}\right)_{s,Y_\alpha} \qquad \mathcal{P}_s = \left(\frac{\partial p}{\partial s}\right)_{\rho,Y_\alpha} \qquad \mathcal{P}_\alpha = \left(\frac{\partial p}{\partial Y_\alpha}\right)_{\rho,s,Y_{\beta\neq\alpha}} \tag{A.2}$$

They depend on the kind of gas and are computed in Sect. A.4 for an ideal gas mixture. In a system with fluid motion, the substantial derivative replaces the total differential, viz:

$$\frac{Dp}{Dt} = \mathcal{P}_\rho \frac{D\rho}{Dt} + \mathcal{P}_s \frac{Ds}{Dt} + \sum_\alpha \mathcal{P}_\alpha \frac{DY_\alpha}{Dt} \tag{A.3}$$

When partially using $\frac{D}{Dt} = \frac{\partial}{\partial t} + u\frac{\partial}{\partial x}$, it follows that

$$\frac{\partial p}{\partial t} + u\frac{\partial p}{\partial x} - \mathcal{P}_\rho \left(\frac{\partial \rho}{\partial t} + u\frac{\partial \rho}{\partial x}\right) - \mathcal{P}_s \frac{Ds}{Dt} - \sum_\alpha \mathcal{P}_\alpha \frac{DY_\alpha}{Dt} = 0. \tag{A.4}$$

Using the continuity equation (2.1),

$$\frac{\partial \rho}{\partial t} + u\frac{\partial \rho}{\partial x} = -\rho\frac{\partial u}{\partial x}, \tag{A.5}$$

leads to

$$\frac{\partial p}{\partial t} + u\frac{\partial p}{\partial x} + \mathcal{P}_\rho \cdot \rho\frac{\partial u}{\partial x} - \mathcal{P}_s \frac{Ds}{Dt} - \sum_\alpha \mathcal{P}_\alpha \frac{DY_\alpha}{Dt} = 0. \tag{A.6}$$

Multiplying this equation with $\frac{1}{\rho\sqrt{\mathcal{P}_\rho}}$ and adding or subtracting, respectively, the momentum equation (2.2) multiplied by $\frac{1}{\rho}$ in the form

$$\rho\left(\frac{\partial u}{\partial t} + u\frac{\partial u}{\partial x}\right) + \frac{\partial p}{\partial x} - \frac{\partial \tau}{\partial x} = 0 \tag{A.7}$$

a wave-like form results:

$$\left(\frac{1}{\rho\sqrt{\mathcal{P}_\rho}}\frac{\partial p}{\partial t}+\frac{\partial u}{\partial t}\right)+\left(u+\sqrt{\mathcal{P}_\rho}\right)\left(\frac{1}{\rho\sqrt{\mathcal{P}_\rho}}\frac{\partial p}{\partial x}+\frac{\partial u}{\partial x}\right) - \frac{1}{\rho}\frac{\partial \tau}{\partial x}-\frac{\mathcal{P}_s}{\rho\sqrt{\mathcal{P}_\rho}}\frac{Ds}{Dt}-\sum_\alpha\frac{\mathcal{P}_\alpha}{\rho\sqrt{\mathcal{P}_\rho}}\frac{DY_\alpha}{Dt}=0 \tag{A.8}$$

$$\left(\frac{1}{\rho\sqrt{\mathcal{P}_\rho}}\frac{\partial p}{\partial t}-\frac{\partial u}{\partial t}\right)+\left(u-\sqrt{\mathcal{P}_\rho}\right)\left(\frac{1}{\rho\sqrt{\mathcal{P}_\rho}}\frac{\partial p}{\partial x}-\frac{\partial u}{\partial x}\right) + \frac{1}{\rho}\frac{\partial \tau}{\partial x}-\frac{\mathcal{P}_s}{\rho\sqrt{\mathcal{P}_\rho}}\frac{Ds}{Dt}-\sum_\alpha\frac{\mathcal{P}_\alpha}{\rho\sqrt{\mathcal{P}_\rho}}\frac{DY_\alpha}{Dt}=0 \tag{A.9}$$

The expression 'wave-like form' is justified because in the case of a friction-less flow (isentropic flow) of a one-component gas it follows from (A.8) und (A.9)

$$\left(\frac{1}{\rho\sqrt{\mathcal{P}_\rho}}\frac{\partial p}{\partial t}+\frac{\partial u}{\partial t}\right)+\left(u+\sqrt{\mathcal{P}_\rho}\right)\left(\frac{1}{\rho\sqrt{\mathcal{P}_\rho}}\frac{\partial p}{\partial x}+\frac{\partial u}{\partial x}\right)=0 \tag{A.10}$$

$$\left(\frac{1}{\rho\sqrt{\mathcal{P}_\rho}}\frac{\partial p}{\partial t}-\frac{\partial u}{\partial t}\right)+\left(u-\sqrt{\mathcal{P}_\rho}\right)\left(\frac{1}{\rho\sqrt{\mathcal{P}_\rho}}\frac{\partial p}{\partial x}-\frac{\partial u}{\partial x}\right)=0 \tag{A.11}$$

which is equivalent to the transport equations of a quantity Φ which is transported by a wave with speed c,

$$\left(\frac{\partial}{\partial t}\pm c\frac{\partial}{\partial x}\right)\Phi=0, \tag{A.12}$$

and satisfies the one-dimensional wave equation,

$$\frac{\partial^2\Phi}{\partial t^2}-c^2\frac{\partial^2\Phi}{\partial x^2}=\left(\frac{\partial}{\partial t}-c\frac{\partial}{\partial x}\right)\left(\frac{\partial}{\partial t}+c\frac{\partial}{\partial x}\right)\Phi=0. \tag{A.13}$$

The transport equation of a scalar in a fluid flow is of the same structure as (A.12). The speed c is replaced by the fluid velocity u. Therefore, the transport equation of the entropy can be written for an isotropic case as:

$$\frac{\partial s}{\partial t}+u\frac{\partial s}{\partial x}=0 \tag{A.14}$$

As the mass fractions Y_α are scalars as well, it follows when chemical reactions are absent:

$$\frac{\partial Y_\alpha}{\partial t}+u\frac{\partial Y_\alpha}{\partial x}=0 \tag{A.15}$$

If considering heat conduction, diffusion, friction and chemical reactions, source terms, σ and σ_α, have to be added:

$$\frac{\partial s}{\partial t}+u\frac{\partial s}{\partial x}=\sigma \tag{A.16}$$

$$\frac{\partial Y_\alpha}{\partial t}+u\frac{\partial Y_\alpha}{\partial x}=\sigma_\alpha \tag{A.17}$$

These source terms are further determined in Sect. A.3. Adding and subtracting the Eqs. (A.8) and (A.9) to and from each other, results in the system of the one-dimensional Navier-Stokes equations in a wave-like form,

$$\begin{aligned}
\frac{\partial p}{\partial t} &= -\frac{\rho\sqrt{\mathcal{P}_\rho}}{2}\left(X^+ + X^-\right) + \mathcal{P}_s\sigma + \sum_\alpha \mathcal{P}_\alpha\sigma_\alpha \\
\frac{\partial u}{\partial t} &= -\frac{1}{2}\left(X^+ - X^-\right) + \frac{1}{\rho}\frac{\partial \tau}{\partial x} \\
\frac{\partial s}{\partial t} &= -X^s + \sigma \\
\frac{\partial Y_\alpha}{\partial t} &= -X^\alpha + \sigma_\alpha,
\end{aligned} \tag{A.18}$$

with the wave amplitudes

$$\begin{aligned}
X^\pm &= \left(u \pm \sqrt{\mathcal{P}_\rho}\right)\left(\frac{1}{\rho\sqrt{\mathcal{P}_\rho}}\frac{\partial p}{\partial x} \pm \frac{\partial u}{\partial x}\right) \\
X^s &= u\frac{\partial s}{\partial x} \\
X^\alpha &= u\frac{\partial Y_\alpha}{\partial x}
\end{aligned} \tag{A.19}$$

The system can be completed by a transport equation for the temperature in order to circumvent the determination of the temperature from a non-linear polynomial expression relating the entropy with the temperature [66]. It is derived from a state relation $T = T\left(p, s, Y_\alpha\right)$:

$$\frac{\partial T}{\partial t} = \mathcal{T}_s\frac{\partial s}{\partial t} + \mathcal{T}_p\frac{\partial p}{\partial t} + \sum_\alpha \mathcal{T}_\alpha\frac{\partial Y_\alpha}{\partial t} \tag{A.20}$$

The coefficients are again partial derivatives,

$$\mathcal{T}_s = \left(\frac{\partial T}{\partial s}\right)_{p,Y_\alpha} \qquad \mathcal{T}_p = \left(\frac{\partial T}{\partial p}\right)_{s,Y_\alpha} \qquad \mathcal{T}_\alpha = \left(\frac{\partial T}{\partial Y_\alpha}\right)_{p,s,Y_{\beta\neq\alpha}}, \tag{A.21}$$

which are determined in Sect. A.4. It is obvious that when the temporal derivatives of pressure, entropy and mass fractions are known from Eqs. (A.18), the temporal derivative of the temperature can be computed from Eq. (A.20). Finally, the density can then be computed from the equation of state, in the present case Eq. (2.5) for an ideal gas.

A.2 The three-dimensional equations in Cartesian coordinates

The way to derive the three-dimensional transport equations corresponds to the one followed in Sect. A.1 for the one-dimensional equations. Therefore, only the result is given here with the coordinates denoted as x_1, x_2 and x_3 and the velocity components u_1, u_2 and u_3:

$$
\begin{aligned}
\frac{\partial p}{\partial t} &= -\frac{\rho\sqrt{\mathcal{P}_\rho}}{2}\left(X^+ + X^- + Y^+ + Y^- + Z^+ + Z^-\right) + \mathcal{P}_s\sigma + \sum_\alpha \mathcal{P}_\alpha\sigma_\alpha \\
\frac{\partial u_1}{\partial t} &= -\frac{1}{2}\left(X^+ - X^-\right) - Y^1 - Z^1 + \frac{1}{\rho}\frac{\partial \tau_{1j}}{\partial x_j} \\
\frac{\partial u_2}{\partial t} &= -\frac{1}{2}\left(Y^+ - Y^-\right) - X^2 - Z^2 + \frac{1}{\rho}\frac{\partial \tau_{2j}}{\partial x_j} \\
\frac{\partial u_3}{\partial t} &= -\frac{1}{2}\left(Z^+ - Z^-\right) - X^3 - Y^3 + \frac{1}{\rho}\frac{\partial \tau_{3j}}{\partial x_j} \\
\frac{\partial s}{\partial t} &= -X^s - Y^s - Z^s + \sigma \\
\frac{\partial Y_\alpha}{\partial t} &= -X^\alpha - Y^\alpha - Z^\alpha + \sigma_\alpha
\end{aligned}
\tag{A.22}
$$

with

$$
\begin{aligned}
X^\pm &= \left(u_1 \pm \sqrt{\mathcal{P}_\rho}\right)\left(\frac{1}{\rho\sqrt{\mathcal{P}_\rho}}\frac{\partial p}{\partial x_1} \pm \frac{\partial u_1}{\partial x_1}\right) \\
Y^\pm &= \left(u_2 \pm \sqrt{\mathcal{P}_\rho}\right)\left(\frac{1}{\rho\sqrt{\mathcal{P}_\rho}}\frac{\partial p}{\partial x_2} \pm \frac{\partial u_2}{\partial x_2}\right) \\
Z^\pm &= \left(u_3 \pm \sqrt{\mathcal{P}_\rho}\right)\left(\frac{1}{\rho\sqrt{\mathcal{P}_\rho}}\frac{\partial p}{\partial x_3} \pm \frac{\partial u_3}{\partial x_3}\right) \\
X^2 &= u_1\frac{\partial u_2}{\partial x_1} \qquad X^3 = u_1\frac{\partial u_3}{\partial x_1} \\
Y^1 &= u_2\frac{\partial u_1}{\partial x_2} \qquad Y^3 = u_2\frac{\partial u_3}{\partial x_2} \\
Z^1 &= u_3\frac{\partial u_1}{\partial x_3} \qquad Z^2 = u_3\frac{\partial u_2}{\partial x_3} \\
X^s &= u_1\frac{\partial s}{\partial x_1} \qquad Y^s = u_2\frac{\partial s}{\partial x_2} \qquad Z^s = u_3\frac{\partial s}{\partial x_3} \\
X^\alpha &= u_1\frac{\partial Y_\alpha}{\partial x_1} \quad Y^\alpha = u_2\frac{\partial Y_\alpha}{\partial x_2} \quad Z^\alpha = u_3\frac{\partial Y_\alpha}{\partial x_3}
\end{aligned}
\tag{A.23}
$$

A.3 The source terms in the transport equations

In order to determine the source terms σ and σ_α that appear in Eqs. (A.22) by relating them with the heat flux vector q_i, the stress tensor τ_{ij} and the diffusion velocity $V_{\alpha i}$, it is useful to start from the transport equation for the internal energy:

$$
\rho\frac{De}{Dt} = -p\frac{\partial u_i}{\partial x_i} + \tau_{ij}\frac{\partial u_i}{\partial x_j} - \frac{\partial q_i}{\partial x_i} \tag{A.24}
$$

This equation, valid for gas mixtures, is obtained when subtracting the momentum equation (2.2) multiplied by the velocity component u_i from the energy equation (2.3). As the continuity equa-

tion (2.1) can be transformed to

$$\begin{aligned} p\frac{\partial u_i}{\partial x_i} &= -\frac{p}{\rho}\left(\frac{\partial \rho}{\partial t} + u_i\frac{\partial \rho}{\partial x_i}\right) \\ &= -\frac{p}{\rho}\frac{D\rho}{Dt}, \end{aligned} \tag{A.25}$$

Eq. (A.24) can be reformulated as

$$\rho\left(\frac{De}{Dt} - \frac{p}{\rho^2}\frac{D\rho}{Dt}\right) = \tau_{ij}\frac{\partial u_i}{\partial x_j} - \frac{\partial q_i}{\partial x_i} \tag{A.26}$$

The left-hand-side (LHS) of this equation can rewritten with the help of the Gibbs fundamental equation. This equation is for a gas mixture:

$$de + pd\left(\frac{1}{\rho}\right) = Tds + \sum_\alpha \frac{\mu_\alpha}{W_\alpha} dY_\alpha \tag{A.27}$$

with the chemical potentials μ_α of the species (see Sect. A.4). Thus, in a system with fluid motions, the substantial derivatives are related by

$$\frac{De}{Dt} - \frac{p}{\rho^2}\frac{D\rho}{Dt} = T\frac{Ds}{Dt} + \sum_\alpha \frac{\mu_\alpha}{W_\alpha}\frac{DY_\alpha}{Dt}. \tag{A.28}$$

This is inserted into the LHS of Eq. (A.24). At the same time it is taken into account that it follows from Eqs. (A.16) und (A.17) that

$$\begin{aligned} \frac{Ds}{Dt} &= \frac{\partial s}{\partial t} + u_i\frac{\partial s}{\partial x_i} = \sigma \\ \frac{DY_\alpha}{Dt} &= \frac{\partial Y_\alpha}{\partial t} + u_i\frac{\partial Y_\alpha}{\partial x_i} = \sigma_\alpha. \end{aligned} \tag{A.29}$$

Thus,

$$\rho\left(T\sigma + \sum_\alpha \frac{\mu_\alpha}{W_\alpha}\sigma_\alpha\right) = \tau_{ij}\frac{\partial u_i}{\partial x_j} - \frac{\partial q_i}{\partial x_i} \tag{A.30}$$

from which an equation for the source term σ can be obtained:

$$\sigma = \frac{1}{T}\left(\frac{1}{\rho}\left(\tau_{ij}\frac{\partial u_i}{\partial x_j} - \frac{\partial q_i}{\partial x_i}\right) - \sum_\alpha \frac{\mu_\alpha}{W_\alpha}\sigma_\alpha\right) \tag{A.31}$$

The stress tensor τ_{ij} is given by Eq. (2.6) and the heat flux vector q_i by (2.10).

In order to determine the source terms σ_α, one starts with the transport equation of the species mass fractions (2.4), the LHS of which is simplified with the help of the continuity equation (2.1):

$$\begin{aligned} &\frac{\partial \rho Y_\alpha}{\partial t} + \frac{\partial \rho Y_\alpha u_i}{\partial x_i} \\ &= Y_\alpha\frac{\partial \rho}{\partial t} + \rho\frac{\partial Y_\alpha}{\partial t} + Y_\alpha\frac{\partial \rho u_i}{\partial x_i} + \rho u_i\frac{\partial Y_\alpha}{\partial x_i} \\ &= \rho\frac{\partial Y_\alpha}{\partial t} + \rho u_i\frac{\partial Y_\alpha}{\partial x_i} + Y_\alpha\left(\frac{\partial \rho}{\partial t} + \frac{\partial \rho u_i}{\partial x_i}\right) \\ &= \rho\frac{\partial Y_\alpha}{\partial t} + \rho u_i\frac{\partial Y_\alpha}{\partial x_i} \\ &= \rho\sigma_\alpha \end{aligned} \tag{A.32}$$

In the last step, Eq. (A.17) was used. Together with the RHS of the transport equation of the species mass fractions (2.4), the final result for the source terms σ_α is:

$$\sigma_\alpha = -\frac{1}{\rho}\frac{\partial}{\partial x_i}\left(\rho Y_\alpha V_{\alpha i}\right) \tag{A.33}$$

When taking into account chemical reactions, then

$$\sigma_\alpha = \frac{1}{\rho}\left(-\frac{\partial}{\partial x_i}\left(\rho Y_\alpha V_{\alpha i}\right) + \omega_\alpha\right) \tag{A.34}$$

with the mass production rate of species α, ω_α.

A.4 Specification of the transport equations for an ideal gas mixture

In this section, the partial derivatives (A.2) and (A.21), which are necessary for the integration of the transport equation, are evaluated for an ideal gas mixture.

Pressure and density are determined unambiguously by the density, the entropy and the species mass fractions: $p = p\left(\rho, s, Y_\alpha\right)$ and $\rho\left(p, s, Y_\alpha\right)$. The partial derivative of the pressure with respect to the density can be expressed with the help of the speed of sound c as:

$$\mathcal{P}_\rho = \frac{\partial p}{\partial \rho} = c^2 = \gamma\left(T\right) RT \tag{A.35}$$

$\gamma\left(T\right) = c_p\left(T\right)/c_v\left(T\right)$ is the ratio of the specific heat capacities $c_p\left(T\right)$ und $c_v\left(T\right)$ of the mixture at constant pressure and volume, respectively. The derivative of the pressure with respect to the entropy is transformed to:

$$\mathcal{P}_s = \frac{\partial p}{\partial s} = \frac{\partial p}{\partial T}\cdot\frac{\partial T}{\partial e}\cdot\frac{\partial e}{\partial s} = \rho R\cdot\frac{1}{c_v}\cdot\frac{\partial e}{\partial s} \tag{A.36}$$

In the last step, the ideal gas law (2.5) and the dependence of the internal energy on the temperature for constant mass fractions, $de = c_v dT$ was used. To determine its derivative with respect to the entropy, the Gibbs fundamental equation (A.27) is taken into account, which is simplified for constant density ρ and constant mass fractions to $de = Tds$. Thus, $\frac{\partial e}{\partial s} = T$ and

$$\mathcal{P}_s = \rho R\cdot\frac{1}{c_v}\cdot T = \frac{p}{c_v}. \tag{A.37}$$

To determine the partial derivative of the pressure with respect to each mass fraction, the Gibbs fundamental equation is used again, this time written with the specific enthalpy h:

$$dh = Tds + \frac{1}{\rho}dp + \sum_\alpha \frac{\mu_\alpha}{W_\alpha}dY_\alpha \tag{A.38}$$

Keeping the entropy and all but one mass fraction constant, $dh = \frac{1}{\rho}dp + \frac{\mu_\alpha}{W_\alpha}dY_\alpha$ or $dp = \rho\left(dh - \frac{\mu_\alpha}{W_\alpha}dY_\alpha\right)$ is obtained. It follows that

$$\mathcal{P}_\alpha = \frac{\partial p}{\partial Y_\alpha} = \rho\left(\frac{\partial h}{\partial Y_\alpha} - \frac{\mu_\alpha}{W_\alpha}\right) = \rho\left(h_\alpha + c_p\frac{\partial T}{\partial Y_\alpha} - \frac{\mu_\alpha}{W_\alpha}\right) \tag{A.39}$$

as the specific enthalpy is a function of both, the mass fractions and the temperature: $dh = c_p dT + \sum_\alpha h_\alpha dY_\alpha$. To compute the partial derivative of the temperature with respect to each mass fraction, the dependence of the specific internal energy on the temperature and the mass fractions is useful: $de = c_v dT + \sum_\alpha e_\alpha dY_\alpha$. Thus,

$$\frac{\partial T}{\partial Y_\alpha} = \frac{1}{c_v}\left(\frac{\partial e}{\partial Y_\alpha} - e_\alpha\right). \tag{A.40}$$

Together with the Gibbs fundamental equation (A.27), which is reduced to $de = \frac{\mu_\alpha}{W_\alpha} dY_\alpha$ when keeping the density and all mass fractions but one constant,

$$\frac{\partial T}{\partial Y_\alpha} = \frac{1}{c_v}\left(\frac{\mu_\alpha}{W_\alpha} - e_\alpha\right) \tag{A.41}$$

is obtained. The internal energy of each species, e_α, can be computed from the species enthalpy by $e_\alpha = h_\alpha - \frac{\mathcal{R}}{W_\alpha} T$. Substituting Eq. (A.41) into Eq. (A.39), the result for the partial derivative of the pressure with respect to each species is:

$$\mathcal{P}_\alpha = \rho\left(h_\alpha + \frac{c_p}{c_v}\left(\frac{\mu_\alpha}{W_\alpha} - e_\alpha\right) - \frac{\mu_\alpha}{W_\alpha}\right) \tag{A.42}$$

The partial derivative of the temperature with respect to the entropy is given by:

$$\mathcal{T}_s = \frac{\partial T}{\partial s} = \frac{\partial T}{\partial h} \cdot \frac{\partial h}{\partial s} = \frac{T}{c_p} \tag{A.43}$$

Here, the relation $dh = c_p dT$ for constant mass fractions is used, as well as the Gibbs fundamental equation (A.38) which is reduced to $dh = Tds$ for constant pressure and constant mass fractions. To determine the partial derivative of the temperature with respect to the pressure, $dh = c_p dT$ as well as the Gibbs fundamental equation (A.38), this time for constant entropy and constant mass fractions, namely $dh = \frac{1}{\rho} dp$, are needed:

$$\mathcal{T}_p = \frac{\partial T}{\partial p} = \frac{\partial T}{\partial h} \cdot \frac{\partial h}{\partial p} = \frac{1}{\rho c_p} \tag{A.44}$$

The last partial derivative is the one of the temperature with respect to each species mass fraction. Equation A.41 is not the relation that is asked for here, as it was obtained by keeping the density constant. Instead, the pressure has to be kept constant. Together with the assumption of constant entropy and all species but one mass fraction constant, the Gibbs fundamental equation (A.38) is reduced to $dh = \frac{\mu_\alpha}{W_\alpha} dY_\alpha$ or $\frac{\partial h}{\partial Y_\alpha} = \frac{\mu_\alpha}{W_\alpha}$. This is substituted into

$$\frac{\partial T}{\partial Y_\alpha} = \frac{1}{c_p}\left(\frac{\partial h}{\partial Y_\alpha} - h_\alpha\right) \tag{A.45}$$

resulting from the dependence of the specific enthalpy on temperature and species mass fractions, $dh = c_p dT + \sum_\alpha h_\alpha dY_\alpha$. The final result is

$$\frac{\partial T}{\partial Y_\alpha} = \frac{1}{c_p}\left(\frac{\mu_\alpha}{W_\alpha} - h_\alpha\right). \tag{A.46}$$

In the following, the chemical potentials μ_α, appearing in Eqs. A.31, A.42 and A.46 are determined for ideal gases. From the Gibbs fundamental equation, written for the free enthalpy G of a gas mixture in a control volume V with the mole numbers n_α of the individual components,

$$dG = -SdT + Vdp + \sum_\alpha \mu_\alpha dn_\alpha, \tag{A.47}$$

the relation

$$\mu_\alpha = \left(\frac{\partial G}{\partial n_\alpha}\right)_{p,T,n_{\beta\neq\alpha}} \tag{A.48}$$

is obtained. The free enthalpy of the mixture is given by

$$G = H - TS = \sum_\alpha n_\alpha \left(\mathcal{H}_\alpha - T\mathcal{S}_\alpha\right) \tag{A.49}$$

where $\mathcal{H}$ and $\mathcal{S}$ are the molar enthalpy and the molar entropy, respectively. H and S are the entropy and the enthalpy, and n is the total mole number of the mixture in the control volume. In Eq. (A.49), the entropy due to the mixing of the gas components is neglected. Only the entropies of the individual gas components, $\mathcal{S}_\alpha$ are taken into account. Computing the derivative of Eq. (A.49), leads to

$$\mu_\alpha = \left(\frac{\partial G}{\partial n_\alpha}\right)_{p,T,n_{\beta\neq\alpha}} = \mathcal{H}_\alpha - T\mathcal{S}_\alpha. \tag{A.50}$$

Thus, written in specific quantities, the chemical potentials are

$$\mu_\alpha = W_\alpha \left(h_\alpha - Ts_\alpha\right) \tag{A.51}$$

wherein the enthalpies h_α and the entropies s_α are computed as polynomials of the temperature [66].

A.5 Non-reflecting boundary conditions

Besides the periodic boundaries used in the streamwise and spanwise directions, only non-reflecting boundaries in the transverse direction are required for DNS and LES of temporally evolving shear layers. Their treatment is facilitated by the particular wave-like formulation of the Navier-Stokes equations (A.22). Wave amplitudes at the boundaries, the direction of which is into the computational domain, are set to zero. At the lower x_3-boundary, it is

$$\begin{aligned} &Z^+ = 0, \text{ if } u_3 + c \geq 0 \\ &Z^- = 0, \text{ if } u_3 - c \geq 0 \\ &Z^1 = Z^2 = Z^s = Z^\alpha = 0, \text{ if } u_3 \geq 0 \end{aligned} \tag{A.52}$$

and at the upper x_3-boundary

$$\begin{aligned} &Z^+ = 0, \text{ if } u_3 + c \leq 0 \\ &Z^- = 0, \text{ if } u_3 - c \leq 0 \\ &Z^1 = Z^2 = Z^s = Z^\alpha = 0, \text{ if } u_3 \leq 0. \end{aligned} \tag{A.53}$$

Bibliography

[1] Adams, N.A., Leonard, A., 1999, Deconvolution of subgrid-scales for the simulation of shock-turbulence interaction. In: *Direct and Large-Eddy Simulation III*, Eds: Voke, P., Sandham, N.D. and Kleiser, L.. Kluwer, Dordrecht, 201-212.

[2] Adams, N.A., Stolz, 2002, A sub-grid deconvolution approach for shock capturing, *J. Comput. Phys.* **178**, 391-426.

[3] Angelbergerer, C., Veynante, D., Egolfopoulos, F., 2000, LES of chemical and acoustic forcing of a premixed dump combustor, *Flow Turbul. Combust.* **65**, 205-222.

[4] Barlow, R.S., Fourguette, D.C., Mungal, M.G., Dibble, R.W., 1992, Experiments on the structure of an annular compressible reacting shear layer, *AIAA J.* **30**, 2244-2251.

[5] Barlow, R.S., Fiechtner, G.J., Carter, C.D., Chen, J.-Y., 2000, Experiments on the Scalar Structure of Turbulent $CO/H_2/N_2$ Jet Flames, *Combust. Flame* **120**, 549-569.

[6] Barre, S., Quine, C., Dussauge, J.P., 1994, Compressibility effects on the structure of supersonic mixing layers: experimental results, *J. Fluid Mech.* **259**, 47-78.

[7] Bell, J.H., Mehta, R.D., 1990, Development of a two-stream mixing layer from tripped and untripped boundary layers, *AIAA J.*, **28**, 2034-2042.

[8] Bilger, R.W., 1976, The structure of diffusion flames, *Combust. Sci. Technol.* **13**, 155-170.

[9] Bilger, R.W., 1980, Turbulent flows with nonpremixed reactants. In: *Topics in Applied Physics Number 44*, Eds: Libby, P.A, Williams, F.A., Springer, New York, 65-113.

[10] Bilger, R.W., 1993, Conditional moment closure for turbulent reacting flow, *Phys. Fluids A* **5**, 436-444.

[11] Bilger, R.W., Stårner, S.H., Kee, R.J., 1990, On reduced mechanisms for methane-air combustion in nonpremixed flames, *Combust. Flame* **80**, 135-149.

[12] Blaisdell, G.A., Mansour, N.N., Reynolds, W.C., 1991, Numerical simulation of compressible homogeneous turbulence, Report No. TF-50, Stanford University, Stanford, CA.

[13] Blaisdell, G.A., Mansour, N.N., Reynolds, W.C., 1993, Compressibility effects on the growth and structure of homogeneous turbulent shear flow, *J. Fluid Mech.* **256**, 443-485.

[14] Bogdanoff, D.W., 1983, Compressibility effects in turbulent shear layers, *AIAA J.* **21**, 926-927.

[15] Bonnet, J.P., Debisschop, J.R., Chambres, O., 1993, Experimental studies of the turbulent structure of supersonic mixing layers, *AIAA Paper* 93-0217.

[16] Bradshaw, P., 1977, Compressible turbulent shear layers, *Ann. Rev. Fluid Mech.*, **9**, 33-54.

[17] Branley, N., Jones, W., 2001, Large eddy simulation of a turbulent non-premixed flame, *Combust. Flame* **127**, 1914-1934.

[18] Breidenthal, R., 1981, Structure in turbulent mixing layers and wakes using a chemical reaction, *J. Fluid Mech.* **109**, 1-24.

[19] Browand, F.K., Troutt, T.R., 1985, The turbulent mixing layer: Geometry of the large vortices, *J. Fluid Mech.* **158**, 489-509.

[20] Brown, G., 1974, The entrainment and large structure in turbulent mixing layers. In: *5th Australasian Conf. on Hydraulics and Fluid Mechanics*, Eds: Lindley, D., Sutherland, A.J., 352-359.

[21] Brown, G.L., Roshko, A., 1974, On density effects and large structure in turbulent mixing layers, *J. Fluid Mech.* **64**, 775-816.

[22] Burke, S.P., Schumann, T.E.W., 1928, Diffusion flames, *Industrial and Engineering Chemistry* **20**, 998-1005.

[23] Bushe, W.K., Steiner, H., 1999, Conditional moment closure for large eddy simulation of nonpremixed turbulent reacting flows, *Phys. Fluids 11*, 1896- 1906.

[24] Calhoon, W., Menon, S., 1996, Subgrid Modeling for Reacting Large Eddy Simulations, *AIAA Paper* 96-0516.

[25] Chambres, O., Barre, S., Bonnet, J., 1998, Detailed turbulence characteristics of a highly compressible supersonic turbulent plane mixing layer, *J. Fluid Mech.*, submitted.

[26] Chen, J.Y., Kollman, W., Dibble, R.W., 1989, Pdf modeling of turbulent methane-air nonpremixed jet flames, *Combust. Sci. Technol.* **64**, 315-346.

[27] Clemens, N.T., Mungal, M.G., 1995, Large-scale structure and entrainment in the supersonic mixing layer, *J. Fluid Mech.* **284**, 171-216.

[28] Clemens, N.T., Paul, P.H., 1995, Scalar measurements in compressible axysymmetric mixing layers, *Phys. Fluids A* **7**, 1071-1081.

[29] Colucci, P.J., Jaberi, F.A., Givi, P., Pope, S.B., Filtered density function for large eddy simulation of turbulent reacting flows, *Phys. Fluids* **10**, 499-515.

[30] Cook, A.W., 1997, Determination of the constant coefficient in scale similarity models of turbulence, *Phys. Fluids* **9**, 1485-1487.

[31] Cook, A.W., Riley, J.J., 1994, A subgrid model for equilibrium chemistry in turbulent flows, *Phys. Fluids* **6**, 2868-2870.

[32] Cook, A.W., Riley, J.J., 1998, Subgrid-scale modeling for turbulent reacting flows, *Combust. Flame* **112**, 593-606.

[33] Cook, A.W., Riley, J.J., Kosály, G., 1997, A laminar flamelet approach to subgrid-scale chemistry in turbulent flows, *Combust. Flame* **109**, 332-341.

[34] Cuenot, B., Poinsot, T., 1996, Asymptotic and Numerical Study of Diffusion Flames with Variable Lewis Number and Finite Rate Chemistry, *Combust. Flame* **104**, 111-137.

[35] Day, M.J., Mansour, N.N., Reynolds, W.C., 2001, Nonlinear stability and structure of compressible reacting mixing layers, *J. Fluid Mech.* **446**, 375-408.

[36] Debisschop, J.R., Bonnet, J.P., 1993, Mean and fluctuating velocity measurements in supersonic mixing layers. In: *Engineering Turbulence Modelling and Experiments 2*, Eds: Rodi, W., Martelli, F., Elsevier.

[37] de Bruyn Kops, S.M., Riley, J.J., Kosály, G., 1998, Investigation of modeling for non-premixed turbulent combustion, *Flow Turbul. Combust.* **60**, 105-122.

[38] de Bruyn Kops, S.M., Riley, J.J., Kosály, G., 2001, Direct numerical simulation of reacting scalar mixing layers, *Phys. Fluids* **13**, 1450-1465.

[39] de Bruyn Kops, S.M., Riley, J.J., 2003, Large-Eddy Simulation of a Reacting Scalar Mixing Layer with Arrhenius Chemistry, *Computers and Mathematics with Applications 46*, 547-569.

[40] de Charentenay, J., Ern, A., 2002, Multicomponent transport impact on turbulent premixed H_2/O_2 flames, *Combust. Theor. Model.* **6** 439-462.

[41] DesJardin P.E., Frankel, S.H., 1998, Large eddy simulation of a nonpremixed reacting jet: Application and assessment of subgrid-scale combustion models, *Phys. Fluids* **10**, 2298-2314.

[42] Di Mare, F., Jones, W., Menzies, K., 2004, Large eddy simulation of a model gas turbine combustor, *Combust. Flame*, **137**, 278-294.

[43] Dimotakis, P., 1984, Two-dimensional shear layer entrainment, *AIAA J.* **24**, 1791-1796.

[44] Dimotakis, P.E., Brown, G.L., 1976, The mixing layer at high Reynold numbers: large structure dynamics and entrainment, *J. Fluid Mech.* **78**, 535-560.

[45] Dimotakis, P.E., Leonard, A., 1994, Chemical reactions in turbulent mixing flows, GALCIT Rep. 94-3,. California Institute of Technology, Pasadena, CA.

[46] Domaradzki, J.A., Adams, N.A., 2002, Direct modelling of subgrid scales of turbulence in large-eddy simulation, *J. Turbulence* **3**, 024.

[47] Dowling, A.P., 1992, Thermoacoustic Sources and Instabilities. In: *Modern Methods in Analytical Acoustics*, Eds: Crighton, D.G., Dowling, A.P., Ffowcs Williams, J.E., Heckl, M., Leppington, F.G., Springer, 378-405.

[48] El Baz, A.M., Launder, B.E., 1993, Second-moment modelling of compressible mixing layers. In: *Engineering, Turbulence Modelling and Experiments 2*, Eds: Rodi, W., Martelli, F., Elsevier.

[49] Elliott, G.S., Samimy, M., 1990, Compressibility effects in free shear layers, *Phys. Fluids A* **2**, 1231-1240.

[50] Elliott, G.S., Samimy, M., Arnette, S.A., 1993, Study of compressible mixing layers with filtered Rayleigh scattering based visualizations, *AIAA J.* **30**, 2567-2569.

[51] Emanuel, G., 1986, *Gasdynamics: Theory and Applications*, AIAA Education Series, New York.

[52] Erdos, G.S., Samimy, M., Arnette, S.A., 1992, Experiments on shear layer mixing at hypervelocity conditions, *AIAA Paper*, 92-0628.

[53] Ern, A., Giovangigli, V., 1994, *Multicomponent transport algorithms.* Springer.

[54] Ern, A., Giovangigli, V., 1995, Fast and accurate multicomponent transport property evaluation, *J. Comput. Physics* **120**, 105-116.

[55] Ern, A., Giovangigli, V., 1998, Thermal diffusion effects in hydrogen-air and methane-air flames, *Combust. Theory Model.* **2**, 349-372.

[56] Ern, A., Giovangigli, V., 1999, Impact of detailed multicomponent transport on planar and counterflow hydrogen/air and methane/air flames, *Combust. Sci. Tech.* **149**, 157-181.

[57] Faeth, G.M., Samuelsen, G.S., 1986, Fast reaction nonpremixed combustion, *Prog. Energy Combust. Sci.* **12**, 305-372.

[58] Fiedler, H., 1974, Transport of heat across a plane turbulent mixing layer, *Adv. Geophys.* **18A**, 93-109.

[59] Forkel, H., Janicka, J., 2000, Large-Eddy Simulation of a Turbulent Hydrogen Diffusion Flame, *Flow Turbul. Combust.* **65**, 163-175.

[60] Foysi, H., Sarkar, S., Friedrich, R., 2004, Compressibility effects and turbulence scaling in supersonic channel flow, *J. Fluid Mech.* **509**, 207-216.

[61] Foysi, H., 2005, Transport passiver Skalare in wandgebundener und isotroper kompressibler Turbulenz, Dissertation, TU München, Fakultät für Maschinenwesen, Germany.

[62] Frankel, S.H., Adumitroaie, V., Madinia, C.K., Givi, P., Large-eddy simulation of turbulent reacting flows by assumed PDF methods, In: *Engineering Applications of Large Eddy Simulations*, Eds: Ragab, S.A., Piomelli, U., ASME, New York.

[63] Freund, J.B., Lele, S.K., Moin, P., 2000, Compressibility effects in a turbulent annular mixing layer. Part 1. Turbulence and growth rate, *J. Fluid Mech.* **421**, 229-267.

[64] Freund, J.B., Moin, P., Lele, S.K., 2000, Compressibility effects in a turbulent annular mixing layer. Part 2. Mixing of a passive scalar, *J. Fluid Mech.* **421**, 269-292.

[65] Gao, F., O'Brien, E.E., 1993, A large-eddy simulation scheme for turbulent reacting flows, *Phys. Fluids A* **5**, 1282-1284.

[66] Gardiner, W., 1984, *Combustion chemistry.* Springer, New York.

[67] Givi, P., Madnia, C.K., Steinberger, C.J., Carpenter, M.H., Drummond, J.P., 1991, Effects of compressibility and heat release in a high speed reacting mixing layer, *Combust. Sci. Technol.* **78**, 33-68.

[68] Goebel, S.G., Dutton, J.C., 1991, Velocity measurements of compressible, turbulent mixing layers, *AIAA J.* **29**, 538-546.

[69] Girimaji, S.S., Zhou, Y., 1996, Analysis and modeling of subgrid scalar mixing using numerical data, *Phys. Fluids* **8**, 1224-1236.

[70] Hall, J.L., Dimotakis, P.E., Rosemann, H., 1991, Some measurements of molecular mixing in compressible turbulent shear layers, *AIAA Paper* 91-1719.

[71] Hall, J.L., Dimotakis, P.E., Rosemann, H., 1993, Experiments in nonreacting compressible shear layers, *AIAA J.* **31**, 2247-2254.

[72] Hermanson, J.C., Dimotakis, P.E., 1989, Effects of heat release in a turbulent, reacting shear layer, *J. Fluid Mech.* **199**, 333-375.

[73] Hilbert, R., Tap, F., El-Rabii H., Thévenin, D., 2004, Impact of detailed chemistry and transport models on turbulent combustion simulations, *Prog. Energy Combust. Sci.* **30**, 61-117.

[74] Hirschfelder, J.O., Curtiss, C.F., Bird, R.B., 1954, *Molecular theoury of gases and liquids.* Wiley, New York.

[75] Hussain, A.K.M.F., Zaman, K.M.B.Q., 1985, An experimental study of organized motions in the turbulent plane mixing layer, *J. Fluid Mech.* **159**, 85-104.

[76] Ihme, M., Cha, C.M., Pitsch, H., 2005, Prediction of local extinction and re-ignition effects in non-premixed turbulent combustion using a flamelet/progress variable approach, *Proc. Combust. Inst.* **30**, 793-800.

[77] Ihme, M., Pitsch, H., 2005, LES of a non-premixed flame using an extended flamelet/progress variable model, *AIAA Paper* 2005-0558.

[78] Island, T.C., 1997, Quantitative scalar measurements and mixing enhancement in compressible shear layers, Dissertation, Stanford University, Stanford, USA.

[79] Jaberi, F.A., Miller, R.S., Mashayek, F., Givi, P., 1997, Differential diffusion in binary scalar mixing and reaction. *Combustion and Flame* **109**, 561-577.

[80] Jaberi, F.A., Colucci, P.J., James, S., Givi, P., Pope, S.B., 1999, Filtered mass density function for large-eddy simulation of turbulent reacting flows, *J. Fluid Mech.* **401**, 85-121.

[81] Jackson, T.L., Grosch, C.E., 1989, Inviscid spatial stability of a compressible mixing layer, *J. Fluid Mech.* **208**, 609-637.

[82] Janicka, J., Sadiki, A., 2005, Large eddy simulation of turbulent combustion systems, *Proc. Combust. Inst.* **30**, 537-547.

[83] Jiménez, J., 1983, A spanwise structure in the plane shear layer, *J. Fluid Mech.* **132**, 319-336.

[84] Jiménez, J., Ducros, F., Cuenot, B., Bédat, B., 2001, Subgrid scale variance and dissipation of a scalar field in large eddy simulations, *Phys. Fluids* **13**, 1748-1754.

[85] Jiménez, J., Linán, A., Rogers, M.M., Higuera, F.J., 1997, A priori testing of subgrid models for chemically reacting non-premixed turbulent shear flows, *J. Fluid Mech.* **349**, 149-171.

[86] Kempf, A., Sadiki, A., Janicka, J., 2003, Prediction of finite chemistry effects using large eddy simulation, *Proc. Combust. Inst.* **29**, 1979-1985.

[87] Kempf, A., Lindtstedt, R.P., Janicka, J., 2006, Large-eddy simulation of a bluff-body stabilized nonpremixed flame, *Combust. Flame* **144**, 170-189.

[88] Kerstein, A.R., 1988, A linear-eddy model of turbulent scalar transport and mixing, *Combust. Sci. Technol.* **60**, 391-421.

[89] Kim, J., 1989, On the structure of pressure fluctuations in simulated turbulent channel flow, *J. Fluid Mech.* **205**, 421-451.

[90] Kim, W., Menon, S., Mongia, H., 1999, Large-eddy simulation of a gas turbine combustor flow, *Combust. Sci. Technol.* **143**, 25-62.

[91] Kim, S.H., Pitsch, H., 2005, Conditional filtering method for large eddy simulation of turbulent nonpremixed combustion, *Phys. Fluids*, in press.

[92] Klimenko, A.Y., 1990, Multicomponent diffusion of various admixtures in turbulent flow, *Fluid Dyn.* **25**, 3-10.

[93] Klimenko, A.Y., 2001, On the relation between the conditional moment closure and unsteady flamelets, *Fluid Dyn.* **25** 327-334.

[94] Klimenko, A.Y., Bilger, R.W., 1999, Conditional moment closure for turbulent combustion, *Prog. Energy Combust. Sci.* **25**, 595-687.

[95] Kovasznay, L.S.G., 1953, Turbulence in Supersonic Flows, *J. Aeronaut. Sci.* **20**, 657-682.

[96] Lasheras, J.C., Cho, J.S., Maxworthy, T., 1986, On the origin and evolution of streamwise vortical structures in a plane, free shear layer, *J. Fluid Mech.* **172**, 231-258.

[97] Lee, S., Lele, S.K., Moin, P., 1991, Eddy shocklets in decaying compressible turbulence, *Phys. Fluids A* **3**, 657-664.

[98] Lele, S.K., 1989, Direct numerical simulation of compressible free shear flows, *AIAA Paper*, 89-0374.

[99] Lele, S.K., 1992, Compact finite difference schemes with spectral-like resolution, *J. Comput. Phys.* **103**, 16-42.

[100] Libby, P.A., Williams, F.A., 1994, *Turbulent reacting flows.* Academic Press, New York.

[101] Lentini, D., 1994, Assessment of the stretched laminar flamelet approach for non-premixed turbulent combustion, *Combust. Sci. Technol.* **100**, 95-122.

[102] Lu, G., Lele, S.K., 1994, On the density effects on the growth rate of compressible mixing layer, *Phys. Fluids* **6**, 1073-1075.

[103] Mahesh, K., Constantinescu G., Apte, S., Iaccarino, G., Ham, F., Moin, P., 2005, Large-eddy simulation of reacting turbulent flows in complex geometries, *ASME J. Appl. Mech.*, in press.

[104] Masutani, S.M., Bowman, C.T., 1986, The structure of a chemically reacting plane mixing layer, *J. Fluid Mech.* **172**, 93-126.

[105] Mathew, J., Basu, A.J., 2002, Some characteristics of entrainment at a cylindrical turbulence boundary, *Phys. Fluids* **14**, 2065-2072.

[106] Mathew, J., Lechner, R., Foysi, H., Sesterhenn, J., Friedrich, R., 2003, An explicit filtering method for large eddy simulation of compressible flows., *Phys. Fluids* **15**, 2279-2289.

[107] Mathew, J., R., Foysi, H., Friedrich, R., 2006, A new approach to LES based on explicit filtering, *Int. J. Heat Fluid Flow* **27**, 594-602. w

[108] McMurtry, P.A., Riley, J.J., 1987, Mechanisms by which heat release affects the flow field in a chemically reacting, turbulent mixing layer, *AIAA Paper*, 87-0131.

[109] McMurtry, P., Riley, J., Metcalfe, R., 1989, Effects of heat release on the large-scale structure in turbulent mixing layers, *J. Fluid Mech.* **199**, 297-332.

[110] McMurtry, P.A., Menon, S., Kerstein, A.R., 1992, A linear eddy sub-grid model for turbulent reacting flows: Application to hydrogen-air combustion, *Proc. Combust. Inst.* **24**, 271-278.

[111] Mellado, J.P., Sarkar, S., Pantano, C., 2003, Reconstruction subgrid models for non-premixed combustion, *Phys. Fluids* **15**, 3280-3307.

[112] Messerschmith, N.L., Dutton, J.C., Krier, H., 1991, Experimental investigation of large scale structures in compressible mixing layers, *AIAA Paper* 91-0244.

[113] Miller, J.A., Mitchell, R.E., Smooke, M.D., Kee, R.J., 1982 Toward a comprehensive chemical kinetic mechanism for the oxidation of acetylene: comparison of model predictions with results from flame and shock tupe experiments *Proc. Combust. Inst.* **19**, 181-196.

[114] Miller, M.F., Bowman, C.T., Mungal, M.G., 1998, An experimental investigation of the effects of compressibility on a turbulent reacting mixing layer, *J. Fluid. Mech.* **356**, 25-64.

[115] Miller, R.S., Madnia, C.K., Givi, P., 1994, Structure of a Turbulent Reacting Mixing Layer, *Combust. Sci. and Tech.*, **99**, 1-36.

[116] Moin, P., Apte, S., 2005, Large-eddy simulation of realistic gas turbine combustors, *AIAA J.*, in press.

[117] Moin, P., Mahesh, K., 1998, Direct Numerical Simulation: A Tool in Turbulence Research, *Annu. Rev. Fluid. Mech.* **30**, 539-578.

[118] Mungal, M.G., Dimotakis, P.E., 1984, Mixing and combustion with low heat release in a turbulent shear layer, *J. Fluid Mech.* **148**, 349-382.

[119] Nilsen, V., Kosály, G., 1999, Differential Diffusion in Turbulent Reacting Flows, *Combust. Flame* **117**, 493-513.

[120] Pantano, C., 2000, Compressibility effects in turbulent nonpremixed reacting shear flows, Dissertation, University of California, San Diego, USA.

[121] Pantano, C., 2006, An additive semi-implicit Runge-Kutta family of schemes for nonstiff systems, , *Applied Numerical Mathematics*, in press.

[122] Pantano, C., Sarkar, S., 2001, A subgrid model for nonlinear functions of a scalar, *Phys. Fluids* **13**, 3803-3819.

[123] Pantano, P., Sarkar, S., 2002, A study of compressibility effects in the high-speed turbulent shear layer using direct simulation, *J. Fluid Mech.* **451**, 329-371.

[124] Pantano, C., Sarkar, S., Williams, F.A., 2003, Mixing of a conserved scalar in a turbulent reacting shear layer, *J. Fluid Mech.* **481**, 291-328.

[125] Papmoschou, D., 1995, Evidence of shocklets in a counterflow supersonic shear layer, *Phys. Fluids* **7**, 233-235.

[126] Papamoschou, D., Roshko, A., 1988, The compressible turbulent shear layer: an experimental study, *J. Fluid Mech.* **197**, 453-477.

[127] Passot, T., Pouquet, A., 1987, Numerical simulation of compressible homogeneous flows in the turbulent regime, *J. Fluid Mech.* **181**, 441-466.

[128] Peters, N., 1984, Laminar diffusion flamelet models in non-premixed turbulent combustion, *Prog. Energy Combust. Sci.* **10**, 319-339.

[129] Peters, N., 2000, *Turbulent combustion*, Cambridge University Press.

[130] Pierce, C.D., Moin, P., 1998, A dynamic model for subgrid-scale variance and dissipation rate of a conserved scalar, *Phys. Fluids* **10**, 3041-3044.

[131] Pierce C.D., Moin, P., 2001, Progress-variable approach for large eddy simulation of turbulent combustion, Report No. TF-80, Stanford University, Stanford, CA.

[132] Pierce, C.D., Moin, P., 2004, Progress-variable approach for large-eddy simulation of non-premixed turbulent combustion, *J. Fluid Mech.* **504**, 73-97.

[133] Pitsch, H., 2000, Unsteady flamelet modeling of differential diffusion in turbulent jet diffusion flames, *Combust. Flame* **123**, 358-374.

[134] Pitsch, H., 2002, Improved pollutant predictions in large-eddy simulations of turbulent non-premixed combustion by considering scalar dissipation rate fluctuations, *Proc. Combust. Inst.* **29**, 1971-1978.

[135] Pitsch, H., 2006, Large-Eddy Simulation of Turbulent Combustion, *Annu. Rev. Fluid. Mech.* **38**, 453-482.

[136] Pitsch, H., Chen, M., Peters, N., 1998, Unsteady flamelet modeling of turbulent hydrogen/air diffusion flames, *Proc. Combust. Inst.* **27**, 1057-1064.

[137] Pitsch, H., Ihme, M., 2005, An unsteady/flamelet progress variable method for LES of nonpremixed turbulent combustion, *AIAA Paper* 2004-557.

[138] Pitsch, H., Peters, N., 1998, A consistent flamelet formulation for non-premixed combustion considering differential diffusion effects, *Combust. Flame* **114**, 26-40.

[139] Pitsch, H., Steiner, H., 2000, Large-eddy simulation of a turbulent piloted methane/air diffusion flame (Sandia flame D), *Phys. Fluids* **12**, 2541-2554.

[140] Pitsch, H., Steiner, H., 2000, Scalar mixing and dissipation rate in large-eddy simulations of non-premixed turbulent combustion, *Proc. Combust. Inst.* **28**, 41-49.

[141] Planché, O.H., Reynolds, W.C., 1992, A numerical investigation of the compressible reacting mixing layer, Report No. TF-56, Stanford University, Stanford, CA.

[142] Poinsot, T., Veynante, D., 2001, *Theoretical and numerical combustion.* R.T. Edwards.

[143] Pope, S.B., 1985, PDF methods for turbulent reactive flows, *Prog. Energy Combust. Sci.* **11**, 119-192.

[144] Pope, S.B., 1990, Computations of turbulent combustion: progress and challenges, *Proc. Combust. Inst.* **23**, 591-612.

[145] Pope, S.B., 2000, *Turbulent Flows*, Cambridge University Press.

[146] Pope, S.B., 2004, Ten questions concerning the large-eddy simulation of turbulent flows, *New J. Phys.* **6**, 1-24.

[147] Ragab, S.A., Wu, J.L., 1989, Linear instabilities in two-dimensional compressible mixing layers, *Phys. Fluids A* **1**, 957-966.

[148] Red, R.C., Prausnitz, J.M, Poling, B.E., 1988, *The properties of gases and liquids.* McGraw Hill.

[149] Réveillon, J., Vervisch, L., 1996, Response of the dynamic LES model to heat release induced effects, *Phys. Fluids A* **8**, 2248-2250.

[150] Réveillon, J., Vervisch, L., 1996, Subgrid-scale turbulent micromixing: dynamic approach, *AIAA J.* **36**, 336-341.

[151] Riley, J.J., Metcalfe, R.W., Orszag, S.A., 1986, Direct numerical simulations of chemically reacting turbulent mixing layers, *Phys. Fluids* **29**, 406-422.

[152] Rogers, M.M., Moser, R.D., 1994, Direct simulation of a self-similar turbulent mixing layer, *Phys. Fluids* **6**, 903-923.

[153] Rotta, J.C., 1972, *Turbulente Strömungen*, Teubner-Verlag, Stuttgart.

[154] Sagaut, P., 2006, *Large Eddy Simulation for Incompressible Flows*, Springer, Berlin Heidelberg.

[155] Samimy, M., Elliott, G.S., 1990, Effects of compessibility on the characteristics of free shear layers, *AIAA J.* **28**, 439-445.

[156] Samimy, M., Reeder, M.F., Elliott, G.S., 1992, Compressibility effects on large structures in free shear flow, *Phys. Fluids A* **4**, 1251-1258.

[157] Sandham, N.D., Reynolds, W.C., 1991, Compressible mixing layer: Linear theory and direct simulation, *AIAA J.* **28**, 618-624.

[158] Sandham, N.D., Reynolds, W.C., 1991, Three-dimensional simulations of large-eddies in the compressible mixing layer, *J. Fluid Mech.* **224**, 133-158.

[159] Sandham, N.D., Yee, H.C., 1989, A numerical study of a class of TVD schemes for compressible mixing layers, *NASA Tech. Rep.* 102194.

[160] Sarkar, S., 1992, The pressure-dilatation correlation in compressible flows, *Phys. Fluids A* **2**, 2674-2682.

[161] Sarkar, S., 1995, The stabilizing effect of compressibility in turbulent shear flow, *J. Fluid Mech.* **282**, 163-186.

[162] Sarkar, S., 1997, On density and pressure fluctuations in uniformly sheared compressible flow. In: *IUTAM Symposium on Variable Density Low-Speed Turbulent Flows.*, Eds: Fulachier, L. et al., Kluwer, 325-332.

[163] Sarkar, S., 2002, The high-speed turbulent shear layer. In: *Variable Density Fluid Turbulence, Fluid Mechanics and its Applications.* **69**, Eds: Chassaing, P., Antonia, R.A., Anselmet, F., Joly, L., Sarkar, S., Kluwer, 235-259.

[164] Sarkar, S., Erlebacher, G., Hussaini, M.Y., 1991, Direct simulation of compressible turbulence in a shear flow, *Theor. Comput. Fluid Dynamics* **2**, 291-305.

[165] Saxena, V., Pope, S.B., 1998, Pdf calculations of major and minor species in a turbulent piloted jet flame, *Proc. Combust. Inst.* **27**, 1081-1086.

[166] Schmidt, H., Schumann, U., 1989, Coherent structure of the convective boundarylayer derived from large-eddy simulations, *J. Fluid Mech.* **200**, 511-562.

[167] Sesterhenn, J., 2000, A characteristic-type formulation of the Navier-Stokes equations for high order upwind schemes, *Computers & Fluids* **30**, 37-67.

[168] Sheikhi, M.R.H., Drozda, T.G., Givi, P., Pope, S.B., 2003, Velocity-scalar filtered density function for large eddy simulation of turbulent flows, *Phys. Fluids* **15**, 2321-2337.

[169] Shinjo, J., Mizobuchi, Y., Ogawa, S., 2003, LES of unstable combustion in a gas turbine combustor, *High Perform. Comput.* **2858**, 234-244.

[170] Smith, L.L., Dibble, R.W., Talbot, L., Barlow, R.S., Carter, C.D., 1995, Laser Raman Scattering Measurements of Differential Molecular Diffusion in Turbulent Nonpremixed Jet Flames of H_2/ CO_2 Fuel, *Combust. Flame* **100**, 153-160.

[171] Sommerer, Y., Galley, D., Poinsot, T., Ducruix, S., Lacas, F., Veynante, D., 2004, Large eddy simulation and experimental study of flashback and blow-off in a lean partially premixed swirled burner, *J. Turb.* **5**, 037.

[172] Spencer, B. W., Jones, B. G., 1971, Statistical investigation of pressure and velocity fields in the turbulent two-stream mixing layer, *AIAA Paper* 71-613.

[173] Sreenivasan, K.R., Meneveau, C., 1986, The fractal facets of turbulence, *J. Fluid Mech.* **173**, 357-386.

[174] Sripakagorn, P., Mitarai, S., Kosály, G., Pitsch, H., 2004, Extinction and reignition in a diffusion flame (a direct numerical study), *J. Fluid Mech.* **518**, 231-259.

[175] Stolz, S., Adams, N.A., 1999, An approximate deconvolution procedure for Large-Eddy simulation, *Phys. Fluids* **11**, 1699-1701.

[176] Stolz, S., Adams, N.A., Kleiser, L., 2001, An approximate deconvolution model for large-eddy simulation with application to incompressible wall-bounded flows, *Phys. Fluids* **13**, 997-1015.

[177] Stolz, S., Adams, N.A., Kleiser, L., 2001, An approximate deconvolution model for LES of compressible flow and its application to shock-turbulence interaction, *Phys. Fluids* **13**, 2985-3001.

[178] Stone, C., Menon, S., 2003, Open-loop control of combustion instabilities in a model gas turbine combustor, *J. Turb.* **4**, 020.

[179] Sutherland, J.C., 2004, Evaluation of mixing and reaction models for large-eddy simulation of nonpremixed combustion using direct numerical simulation. Dissertation, University of Utah, USA.

[180] Vervisch, L., Veynante, D., 1998, Direct numerical simulation of non-premixed turbulent flames, *Annu. Rev. Fluid Mech.* **30** 655-691.

[181] Veynante, D., Vervisch, L., 2002, Turbulent combustion modeling, *Prog. Energy Combust. Sci.* **28**, 193-266.

[182] Vreman, B., Kuerten, H., Geurts, B., 1995, Shocks in direct numerical simulation of the confined three-dimensional mixing layer, *Phys. Fluids* **7**, 2105-2107.

[183] Vreman, A.W., Sandham, N.D., Luo, K.H., 1996, Compressible mixing layer growth rate and turbulence characteristics, *J. Fluid Mech.* **320**, 235-258.

[184] Wall, C., Boersma, B.J., Moin, P., 2000, An evolution of the assumed beta probability density function subgrid-scale model for large eddy simulation of nonpremixed, turbulent combustion with heat release, *Phys. Fluids* **12**, 2522-2529.

[185] Wall, C.T., Moin, P., 2005, Numerical methods for large eddy simulation of acoustic combustion instabilities, Report No. TF-91, Stanford University, Stanford, CA.

[186] Westerweel, J., Fukushima, C., Pedersen, J.M., Hunt, J.C.R., 2005, Mechanics of the Turbulent-Nonturbulent Interface of a Jet, *Physical Review Letters* PRL 95, 174501.

[187] Williams, F.A., 1985, *Combustion theory.*, Addison Wesley.

[188] Williamson, J., 1980, Low-storage Runge-Kutta schemes, *J. Comput. Phys.* **35**, 48-56.

[189] Wygnanski, I., Oster, D., Fiedler, H., Dziomba, B., 1979, On the perseverance of a quasi-two-dimensional eddy-structure in a turbulent mixing layer, *J. Fluid Mech.* **93**, 325-335.

[190] Xu, J., Pope, S.B., 2000, PDF calculations of turbulent nonpremixed flames with local extinction, *Combust. Flame* **123**, 281-307.

[191] Yeung, P.K., Pope S.B., 1988, An algorithm for tracking fluid particles in numerical simulations of homogeneous turbulence, *J. Comput. Physics* **79**,373-416.

[192] Zeman, O., 1990, Dilatational dissipation - the concept and application in modelling compressible mixing layers, *Phys. Fluids A* **2**, 178-188.